Wu, Shuhao (2026) *Non-local resonant metasurface enhanced spectral filtering*. PhD thesis.

https://theses.gla.ac.uk/85822/

Copyright and moral rights for this work are retained by the author

A copy can be downloaded for personal non-commercial research or study, without prior permission or charge

This work cannot be reproduced or quoted extensively from without first obtaining permission from the author

The content must not be changed in any way or sold commercially in any format or medium without the formal permission of the author

When referring to this work, full bibliographic details including the author, title, awarding institution and date of the thesis must be given

Enlighten: Theses
https://theses.gla.ac.uk/
research-enlighten@glasgow.ac.uk

University of Glasgow

Non-local Resonant Metasurface Enhanced Spectral Filtering

Shuhao Wu

Submitted in fulfilment of the requirements for the Degree of

Doctor of Philosophy (PhD) by Research

James Watt School of Engineering

College of Science and Engineering

University of Glasgow

October 2025

To my mother Bilan Zhang,

And my father Shixian Wu

To my beloved aunt Shilan Wu,

Who loved and supported me always,

we love you forever.

ACKNOWLEDGEMENT

I am deeply grateful to my supervisor, Professor David R.S. Cumming, for the opportunity to pursue this research and for his guidance and support over the past four years, both academically and personally. I also thank my supervisor, Dr Vincenzo Pusino, for his invaluable help and mentorship throughout my work.

My time in Glasgow included many challenging periods, and I am especially thankful to colleagues in the MST Group — Chunxiao Hu, Khuetian Lai, Jinal Tapar, Thomas Nowack, James Daly, and many others — for their help and company. I am likewise grateful to the friends I met in Glasgow: Ang, Zhengxin, Qianxu, Weihao, Anqi, the West Village Room 160 “family” and all other friends.

Life at JWNC was demanding but rewarding. I was fortunate to have outstanding teammates — Simeng Zhu, Xiao Sun, Bocheng Yuan, Huihua Cheng, and others, with whom I shared many great moments. Also, would like to thank JWNC staff for their guidance and help.

I still kept in close contact with my old friends and occasionally share our thoughts in academic and pop music, Xu, Haomian, Xiaozhong, Yiru, wish you all the best in Switzerland and U.S..

A special thanks to Arsenal Football Club: supporting Arsenal was one reason I came to the UK, and the feeling of my first visit to the Emirates Stadium back in 2021 remains unforgettable, after all these years. Hope we will win the premier league this year.

Finally, I owe profound thanks to my parents, Shixian Wu and Bilan Zhang, and to my girlfriend, Jinglin, for their unwavering love and support.

我要感谢并纪念我亲爱的大姥吴诗兰女士。希望您在天堂能再当一次有父母陪伴的小女孩，开心快乐。

AUTHOR'S DECLARATION

I certify that the thesis presented here for examination for a PhD degree of the University of Glasgow is solely my own work and that the thesis has not been edited by a third party beyond what is permitted by the University's PGR Code of Practice. The copyright of this thesis rests with the author. No quotation from it is permitted without full acknowledgement. I declare that the thesis does not include work forming part of a thesis presented successfully for another degree. I declare that this thesis has been produced in accordance with the University of Glasgow's Code of Good Practice in Research. I acknowledge that if any issues are raised regarding good research practice based on review of the thesis, the examination may be postponed pending the outcome of any investigation of the issues.

Shuhao Wu

ABSTRACT

A metasurface is a quasi-two-dimensional micro-nano structure with subwavelength scale thickness. Owing to their compactness and the ability to integrate multiple functions, metasurfaces are seen as an excellent platform for optical field manipulation and photon-related experiments. In this thesis the focus of the research is the emerging concept of non-local resonant metasurfaces. Appearing in array form, they demonstrate narrowband wavelength-selective control of the optical field through collective non-local resonant modes. Two important parameters are spectral and polarisation control, and these are the main topics of study in the thesis. The ability to manipulate the spectral and polarisation selective properties of metasurfaces has applications in sensing and several novel devices in the visible and infrared wavelength range are proposed and demonstrated.

In the visible spectral range, a novel plasmonic metasurface filter with a periodic dimeric-aperture hole structure on a metal film is proposed. It integrates colour-dependent filtering and polarisation-dependent transmission, enabling two functions simultaneously. Simulations show that the structure has improved transmittance compared to a conventional monomeric-aperture structure, exceeding 30% in the blue, green, and red channels, and achieves an orthogonal polarisation extinction ratio greater than 1000. Fabricated devices made by electron-beam lithography and dry etching exhibited approximately 30% transmittance in red, green and blue channels, a filtering linewidth of about 100 nm, and an average polarisation extinction ratio exceeding 20. A polarisation–colour palette was made to observe simultaneous modulation of colour and polarisation, and a colour-gamut diagram was plotted to show vivid colours with more than 76% sRGB coverage. The simultaneous colour–polarisation modulation was further applied to polarisation-dependent encrypted displays and the reproduction of micro-structured artwork.

In the infrared spectral range, a novel narrowband filter based on quasi–bound states in the continuum (q-BIC) is proposed. The device is composed of periodic nano-disks with off-centre holes along orthogonal axes to realise dual symmetry-breaking perturbations. The device therefore enables resonance-related linear-to-linear cross-polarisation coupling. Unidirectional transmission enhancement is achieved by tuning the coupling between eigenmodes through adjusting the size of the holes, showing a transmission exceeding the theoretical limit value of 25% derived from temporal coupled mode theory for single-layer, single-excitation metasurface. By extracting the cross-polarisation transmission channel, narrowband filtering is realised in transmission mode. Multipolar decomposition and mode-

coupling related simulations explained the operating mechanism of the device. Devices fabricated using electron-beam lithography and dry-etching processes showed 30 % cross-polarisation conversion efficiency in Fourier-transform infrared microscope measurements. The experiments also exhibited a resonance linewidth of less than 60 nm at centre wavelength around 3500nm, corresponding to a quality-factor (Q) of approximately 60, which is an order of magnitude higher than previous experimental reports of free-space infrared filters based on plasmonic structures. The fabricated device was further applied to the reconstruction of infrared gas spectra. Experiments demonstrated real-time, in situ, spectral reconstruction of the semi-quantitative infrared absorption spectrum of butane gas, showing good agreement with the NIST ground-truth dataset.

A novel flat-band q-BIC metasurface working in the infrared spectral range is also proposed. High Q resonances are often accompanied by high sensitivity to the incident angle that is a limitation of non-local metasurfaces. In this study, band-structure engineering has been demonstrated through simulations. Using Brillouin-zone folding and symmetry breaking, strong coupling can be achieved between two modes that are not previously coupled because of a symmetry mismatch. The anti-crossing of the bands, because of the strong-coupling effect, adjusts the line shape of the band on which the mode lies in momentum space, thereby realising band-structure control hence exhibits a flat-band characteristic within an incident-angle range of approximately 15°. This new result presents opportunities for future experimental studies.

OUTCOMES OF THE RESEARCH ACTIVITY

Journal Publications:

1. **Polarisation-Controlled Transmissive Plasmonic Color Filter Using a Dimer-Aperture Array**. *Advanced Science* (2025, 12, 2501941*).*

Authors: Shuhao Wu*, Peter W.R. Connolly, Vincenzo Pusino, Gerald S. Buller, David R.S. Cumming

2. **A Linear-to-Linear Cross-Polarisation Conversion q-BIC Metasurface for Transmission Mode Mid-Infrared Spectral Filtering**. *Laser and Photonics Review* (2025, accepted for publication)

Authors: Shuhao Wu*, Simeng Zhu, Lianping Hou, Vincenzo Pusino, David R.S. Cumming

3. Ultra-High-Quality Factor Mid-infrared Flatband Metasurface. in preparation (2025)

Authors: **Shuhao Wu***, Simeng Zhu, Vincenzo Pusino, David R.S. Cumming

Conference Contributions:

1. High-quality factor mid-wave infrared metasurface for methane detection applications. (Invited oral presentation) *SPIE Sensors and Imaging @ Edinburgh, United Kingdom* (2024)

Authors: **Shuhao Wu***, Khue Tian Lai, Vincenzo Pusino, David R.S. Cumming

2. Narrow Linewidth Hybrid Plasmonic-Photonic Mid Wave Infrared Spectral Filter. (Oral presentation) *IEEE Photonics Conference @ Rome, Italy* (2024)

Authors: **Shuhao Wu***, Jinal Taper, Vincenzo Pusino, David R.S. Cumming

3. Schottky Au-InSb plasmonic photodiode for greenhouse gas detection. *SPIE Photonics West @ San Francisco, California, United States* (2025)

Authors: Jinal Tapar, **Shuhao Wu**, Khue Tian Lai, Maira Elksne, Nicholas Wood, David R. S. Cumming, Vincenzo Pusino

James Watt Nanofabrication Contributions:

1. Python + Layout for semi-automatic GDS Layout Generation (2023 JWNC Annual Conference)

2. Metasurface in JWNC (2024 JWNC Annual Conference)

TABLE OF CONTENTS

LIST OF FIGURES

LIST OF TABLES

ABSTRACT

A metasurface is a quasi-two-dimensional micro-nano structure with subwavelength scale thickness. Owing to their compactness and the ability to integrate multiple functions, metasurfaces are seen as an excellent platform for optical field manipulation and photon-related experiments. In this thesis the focus of the research is the emerging concept of non-local resonant metasurfaces. Appearing in array form, they demonstrate narrowband wavelength-selective control of the optical field through collective non-local resonant modes. Two important parameters are spectral and polarisation control, and these are the main topics of study in the thesis. The ability to manipulate the spectral and polarisation selective properties of metasurfaces has applications in sensing and several novel devices in the visible and infrared wavelength range are proposed and demonstrated.

In the visible spectral range, a novel plasmonic metasurface filter with a periodic dimeric-aperture hole structure on a metal film is proposed. It integrates colour-dependent filtering and polarisation-dependent transmission, enabling two functions simultaneously. Simulations show that the structure has improved transmittance compared to a conventional monomeric-aperture structure, exceeding 30% in the blue, green, and red channels, and achieves an orthogonal polarisation extinction ratio greater than 1000. Fabricated devices made by electron-beam lithography and dry etching exhibited approximately 30% transmittance in red, green and blue channels, a filtering linewidth of about 100 nm, and an average polarisation extinction ratio exceeding 20. A polarisation–colour palette was made to observe simultaneous modulation of colour and polarisation, and a colour-gamut diagram was plotted to show vivid colours with more than 76% sRGB coverage. The simultaneous colour–polarisation modulation was further applied to polarisation-dependent encrypted displays and the reproduction of micro-structured artwork.

In the infrared spectral range, a novel narrowband filter based on quasi–bound states in the continuum (q-BIC) is proposed. The device is composed of periodic nano-disks with off-centre holes along orthogonal axes to realise dual symmetry-breaking perturbations. The device therefore enables resonance-related linear-to-linear cross-polarisation coupling. Unidirectional transmission enhancement is achieved by tuning the coupling between eigenmodes through adjusting the size of the holes, showing a transmission exceeding the theoretical limit value of 25% derived from temporal coupled mode theory for single-layer, single-excitation metasurface. By extracting the cross-polarisation transmission channel,

narrowband filtering is realised in transmission mode. Multipolar decomposition and mode-coupling related simulations explained the operating mechanism of the device. Devices fabricated using electron-beam lithography and dry-etching processes showed 30 % cross-polarisation conversion efficiency in Fourier-transform infrared microscope measurements. The experiments also exhibited a resonance linewidth of less than 60 nm, corresponding to a quality-factor (Q) of approximately 60, which is an order of magnitude higher than previous experimental reports of free-space infrared filters based on plasmonic structures. The fabricated device was further applied to the reconstruction of infrared gas spectra. Experiments demonstrated real-time, in situ, spectral reconstruction of the semi-quantitative infrared absorption spectrum of butane gas, showing good agreement with the NIST ground-truth dataset.

A novel flat-band q-BIC metasurface working in the infrared spectral range is also proposed. High Q resonances are often accompanied by high sensitivity to the incident angle that is a limitation of non-local metasurfaces. In this study, band-structure engineering has been demonstrated through simulations. Using Brillouin-zone folding and symmetry breaking, strong coupling can be achieved between two modes that are not previously coupled because of a symmetry mismatch. The anti-crossing of the bands, because of the strong-coupling effect, adjusts the line shape of the band on which the mode lies in momentum space, thereby realising band-structure control hence exhibits a flat-band characteristic within an incident-angle range of approximately 15°. This new result presents opportunities for future experimental studies.

Chapter 1 Introduction and Motivation

Outline:

In this chapter, the outline of the thesis will be described. The underpinning concepts will be explained, especially the non-local resonant metasurfaces will be analysed and introduced, including the basic concept of metasurfaces (**Section 1**), the distinction between non-local and local metasurfaces (**Section 1**), and the types of resonances supported by non-local resonant metasurfaces involved in this research (**Sections 2** and **3**). Finally, the overall framework of this research will be presented in **Section 4**.

1.1 Introduction to Metasurfaces

Electromagnetic (EM) waves of different wavelengths may be one of the most important concepts from the physical world in modern life. We use radio-frequency electromagnetic signals to connect to the internet and make phone calls; we rely on the visible-light signals (that is, electromagnetic waves) received by our eyes to perceive the world; we heat food with microwaves; and we reconstruct the internal structure of the human body using X-rays. In this sense, EM waves are an objective reality, like water and fire. Likewise, just as humans have long sought ways to control water with pumps or fire with torches, their efforts to manipulate electromagnetic waves have a long history. Curtains can block light, which is fundamentally an example of amplitude modulation of light; The invention of spectacles can be traced back several centuries ago[1], where variations in lens thickness alter the phase distribution of the light wave, enabling a range of functions such as focusing and divergence of the light.

In the early 21st century, with advances in nanofabrication, many methods for controlling the EM wavefront at the micro- and nanoscale became feasible. One particularly prominent approach is so-called metamaterials[2-4]. Electromagnetic metamaterials generally refer to artificial materials with features at the subwavelength scale or comparable to the wavelength; these precise structures can influence many properties of EM waves. Beyond compactness and flexible control of different aspects of EM waves, they can also theoretically realise functionalities unattainable in bulk materials, such as the negative refractive index proposed by Professor John Pendry[5]. However, the fabrication of three-dimensional metamaterials remains challenging at present[6], and attention has therefore shifted to a two-dimensional form of metamaterials: metasurfaces.

The concept of metasurfaces originates from metamaterials [7], referring primarily to artificially engineered quasi-two-dimensional micro- and nano-scale subwavelength structures. These subwavelength structures enable the manipulation of electromagnetic wavefronts, including control over polarisation, amplitude, phase, and spin[8-14]. In this context, *quasi-two-dimensional* refers to the fact that the height of the micro or nano-scale structures is on a comparable scale to the wavelength. These compact yet highly versatile tools for controlling EM wavefronts have enabled many breakthroughs in portable devices compared with refractive lenses. Examples include ultra-compact, high-efficiency camera routing layers integrated into smartphone systems, or components that help generate structured light for facial recognition [15-17]; as well as metasurface-based waveguides and routing elements for AR near-eye displays[18, 19], and so on.

Wavefront control in metasurfaces mainly arises from the interaction between light and the nanostructures. From the perspective of material choice of the nanostructure, metasurfaces can be categorised as metallic (plasmonic), dielectric, or hybrid metasurfaces. These correspond to meta-atoms that are primarily metallic, entirely dielectric, or based on combined metal–dielectric structures, respectively, and each offers advantages in different application domains. Generally speaking, metallic metasurfaces more readily exhibit strong field confinement, enabling near-field electromagnetic hotspots, and can achieve pronounced resonant behaviour with relatively small thickness. Metallic electromagnetic metasurfaces are particularly attractive in the terahertz and microwave regimes, but in the visible and infrared bands their performance is constrained by ohmic loss. In addition, many metals are not compatible with standard CMOS etching processes. Therefore, for visible and infrared operation, designs must explicitly account for the impact of ohmic loss on device performance, as well as the overall complexity of the fabrication process. On the other hand, dielectric materials typically have negligible ohmic loss, allowing higher efficiency in transmission. As a result, they can also realise resonance-independent phase control through high–aspect-ratio designs. Moreover, the etching processes for many common dielectric materials—such as silicon, silicon nitride, aluminium oxide, and titanium dioxide—are well established and compatible with modern CMOS fabrication workflow. However, as dielectrics, their ability to manipulate optical fields is comparatively less-efficient, often requiring greater optical thickness. This, in turn, can reduce device mechanical robustness and make it harder to maintain precise structural fidelity. Hybrid metasurfaces sit between these two extremes; well-known systems such as metal–insulator–metal (MIM) and gap-plasmon structures are also frequently used in specialised metasurface designs[4, 20, 21].

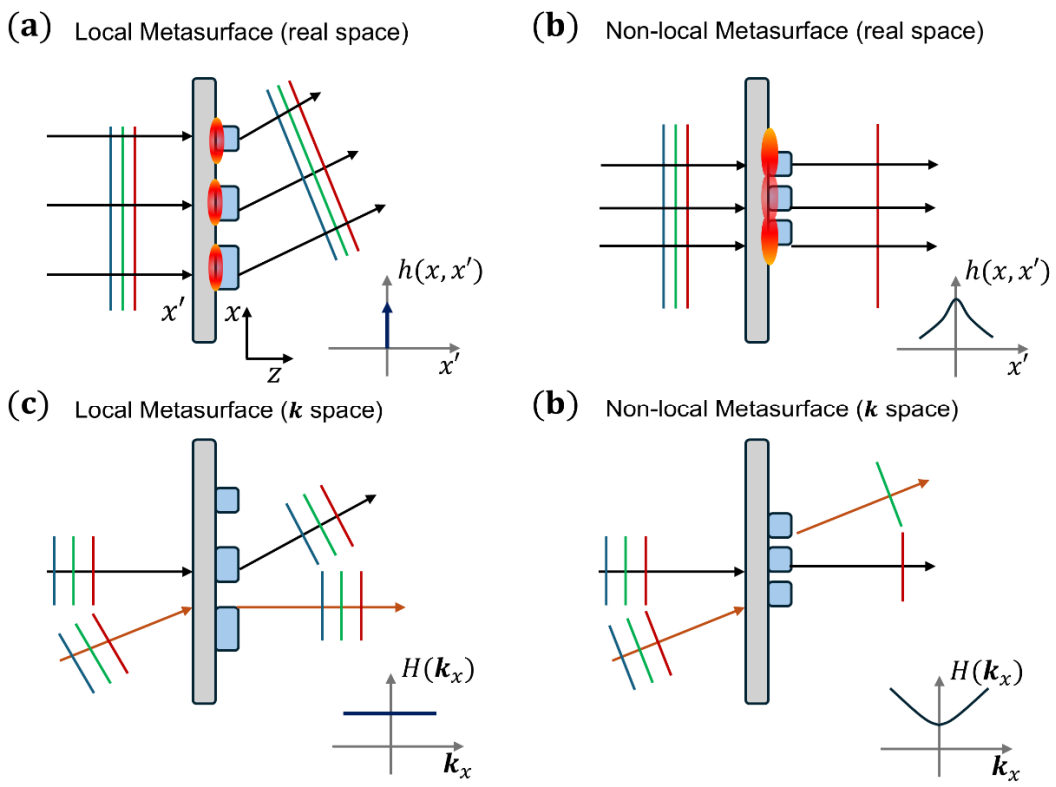

Figure 1-1 Comparison between local and non-local metasurfaces in real space and momentum space. (a) & (b) Illustration of the response function $\boldsymbol{h(x,x')}$ of local and non-local metasurface in real space. (c) & (d) Illustration of the response function $\boldsymbol{H(k_x)}$ of the two in momentum space

From the perspective of how light is manipulated, metasurfaces can be broadly categorised into two types[22]: (1) Local devices, which manipulate light using individual scatterers. (2) Non-local devices, whose responses originate from interactions among all neighbouring elements. Local metasurfaces typically shape the wavefront over a broad bandwidth by arranging meta-atoms on a surface while neglecting nearest-neighbour interactions. In contrast, non-local metasurfaces manipulate the spectrum by exploiting modes supported by the collective behaviour of many identical, adjacent meta-units. A schematic comparison of the two is shown in **Figure 1-1**. In a local metasurface, the optical response at each output point depends only on the input field at the same spatial location, resulting in a delta-function-like spatial impulse response $\boldsymbol{h(x,x')}$**.** In contrast, a non-local metasurface exhibits spatial coupling of many neighbouring elements, where the output at a point depends on a broader region of the input, characterised by a non-local spatial response function. The red spot in (a) and (b) represents the electric magnetic mode distribution. As shown in Figure 1-1 (c) and (d), In momentum space, a local metasurface corresponds to a flat transfer function

$\boldsymbol{H}(\boldsymbol{k_x})$, implying angle-independent behaviour. A non-local metasurface typically enables non-flat responses across transverse momentum components, resulting in a non-uniform $\boldsymbol{H}(\boldsymbol{k_x})$, which corresponds to angular dispersion.

A typical example of a local metasurface is the phase gradient metasurface, which deflects incident light into a desired diffraction order. The concept of achieving an artificially designed space-variant phase response through micro/nanostructures was widely proposed as early as the 20th century [23-27]. The control of the phase response can be various, such as Pancharatnam-Berry phase and propagation phase. Pancharatnam has showed that a cyclic change in the state of polarisation of the light is associated by a phase shift determined by the geometry of the cycle as represented on the Poincaré sphere[23, 28]. Space-variant polarisation-state manipulations are therefore accompanied by a phase modification that results from the Pancharatnam–Berry phase (PB-phase), which is also referred to as geometry phase. The propagation phase, on the other hand, relies on the variant meta-atom shape dependent phase retardations. These concepts can be found in early studies of nanophotonic systems such as diffractive optics and binary gratings[25-27, 29]. In recent years, in 2011, Yu et al. formally introduced the generalised Snell's law, an extension of traditional Snell's law, highlighting the role of phase gradients once again[30]. Recent advancements have enabled multifunctional local metasurfaces, such as broadband achromatic focusing[11, 12], polarisation control[31], and wavelength selective colour routers[32]. However, these devices generally suffer from limited spectral control: because the optical interaction with the meta-atoms is confined to deeply subwavelength structures, they typically exhibit broadband behaviour without distinct spectral features. As a result, for applications such as spectral sensing, local metasurfaces often lack sufficient design flexibility.

In contrast, non-local metasurfaces, which support collective resonant modes such as plasmonic resonances[33], guided mode resonances[34, 35], and bound states in the continuum (BICs)[36-38], can exhibit sharp, even ultra-narrow spectral features. These properties make them highly suitable for applications in free-space optical filtering, on-resonance sensing, and nonlinear signal enhancement[34, 39-44]. Such non-local metasurfaces that support these resonant modes are also referred as resonant non-local metasurfaces[22], highlighting the fact that supporting collective resonance is the key characteristic of this category. The emergence of such collective resonant modes can be achieved either by reducing the spacing between meta-atoms to induce near-field coupling, or by increasing the array period to introduce spatially extended modes[45], allowing electromagnetic waves to propagate in-plane. In

addition to in-plane geometrical parameters and periodicity, the height of the meta-atoms is also a key parameter that strongly influences nonlocality. Taking plasmonic metasurfaces as an example[46], substantial scaling of the height can lead to a pronounced transition between localised surface plasmon resonances (LSPRs) and surface plasmon polaritons (SPPs). Taller meta-atoms tend to correspond to more localised fields (manifested as spatial electric-field hotspots) and lower Q factors. It is worth noting that even meta-atoms that exhibit local metasurface behaviour within a certain spectral band (i.e., spatially independent phase/polarisation control) may still excite collective resonances at specific wavelengths[47]. This study focuses on structures that are unresponsive to external excitation over a certain band yet support collective resonances only at particular wavelengths.

Table 1-1 summarise the general differences between nonlocal and local metasurfaces in terms of typical geometries and properties[47-51].

Table 1-1-1 Comparison between non-local metasurface and local metasurface

	Non-local	Local
Height	Normally small ($<\lambda$)	Normally large ($>\lambda$)
Period	Normally smaller or comparable to diffraction limit ($\leq \lambda/2$)	Normally smaller Nyquist sampling but not too small to avoid near-field coupling
Fill factor	Normally big (meta-atoms or holes not too small compared to period)	Depend on phase modulation requirements
Q-factor	Large (>100)	Small (<10)

Together, these geometrical parameters determine whether nonlocal modes can be supported, and whether high-Q resonances can be achieved. Thanks to the resonance effects, non-local metasurfaces can achieve extremely narrowband filtering and enable wavelength-selective polarisation conversion, phase modulation, and other forms of multi-dimensional, narrowband wavefront control.

It is worth noting that, compared with more matured techniques used in modern display and camera systems, such as dye-based filter and multi-layer thin-film optics, filters based on such planar structures offer significant advantages in both form factor and fabrication workflow[52-54]. More importantly, these structures have the potential to integrate multiple modulation functions beyond spectral filtering[55-58], while still maintaining a compact

footprint—capabilities that are difficult to realise with optical thin films. Correspondingly, this thesis demonstrated the integration of spectral filtering and polarisation modulation. Beside the mentioned advantages, nonlocal metasurface-based filters inherently suffer from angular dispersion with respect to the angle of incidence[51]. In particular, the resonance wavelength associated with grating diffraction is especially sensitive to incident angle. This can, however, be a distinctive advantage in applications where enhanced angular dispersion is desirable (for example, edge detection[59-63]), but it is undesirable in more conventional scenarios such as hyperspectral imaging and the use of focused EM waves to strengthen light–matter interactions. In such cases, special management of the angle of incidence is required—namely, band-structure engineering of the resonant eigen-frequency. In this thesis, an example of band-structure engineering in nonlocal metasurfaces enabled by strong intermodal coupling has been demonstrated. Studies have also shown that such strong-coupling approach to band engineering can, in essence, be applied to reduce the angle sensitivity of thin films as well[64].

To highlight the contrast between nonlocal metasurface filters and thin-film optics, the differences in their respective properties are summarised below in the table below.

Table 1-2 Comparison between non-local (NL) metasurface based free-space optical filter and thin-film based optical filter

	NL-Metasurface	Thin film (TF)	Additional Notes
Size	Thin (~λ level) Flat optics	Thin (~$N \times \lambda$ level) Multi-layer optics	TF requires multiple stacked layers of high/low refractive index with precisely controlled thickness
Weight	Small	Larger	
Power	Passive device	Passive device	
Manufacturing Cost	Low Can be compatible with CMOS techniques and nano-imprinting techniques. Can be made with only single time lithography/deposition for different filtering wavelengths	High Requires multiple times lithography/deposition for different filtering wavelengths	

This thesis focuses primarily on two types of resonant modes that could help with narrow band filtering: plasmonic resonances and BICs. In nonlocal metasurfaces, plasmonic resonance typically refers to a propagating collective plasmonic mode—namely surface plasmon polariton (SPP)—in which the electromagnetic wave couples between unit cells and propagates in-plane. In momentum space, an SPP mode lies outside the light cone (i.e., it is phase-mismatched to free-space radiation), so it cannot be directly excited from the far field unless additional in-plane momentum is provided, for example via a grating that supplies an extra transverse wavevector component[65]. Bound state in the continuum (BIC) is likewise inaccessible to direct far-field excitation; however, it is distinctive in that it resides within the radiative continuum (inside the light cone) in momentum space yet remains non-radiative due to symmetry protection and/or destructive interference between radiation channels. Only when geometrical symmetry of the metasurface atoms is broken, or when other geometrical parameters are tuned such that the ideal BIC evolves into a quasi-BIC (see Section 1.3), can it couple to external illumination and become excitable. Both plasmonic resonances and BICs exhibit sensitive spectral responses. For plasmonic resonances, the feature stems from the strong frequency dependence of the additional grating momentum required for phase matching; for BICs, it arises because the characteristic frequency is highly sensitive to structural geometrical parameters. In this research, these features of plasmonic resonances and quasi-BICs will be exploited to design a new class of optical filters.

1.2 Plasmonic resonance

Plasmonic resonance refers to a type of resonance phenomenon that arises from strong interactions between light and the collective free electron fluctuation on a metal surface[33, 46, 66-69]. This resonance typically occurs in nanostructures located at the interface between a metal and a dielectric (such as air or glass) and is characterised by significant enhancement of the electromagnetic field at specific frequencies. In the case of non-local plasmonic resonance, the core physical mechanism lies in the excitation of surface plasmon polaritons (SPPs)[70-74]. SPPs are electromagnetic waves that propagate along the interface between a metal and a dielectric, originating from the coupling between incident light and the collective oscillation of free electrons in the metal.

Surface plasmon polaritons are a coupled mode of electromagnetic waves and collective oscillations of free electrons in a metal, confined strictly to the two-dimensional interface between a metal and a dielectric (such as air or glass). They can only be excited by transverse magnetic (TM) polarised light, and their field decays exponentially perpendicular to the interface. The propagation constant (wavevector) of the SPP, denoted k_{SPP}, satisfies the following dispersion relation[70, 73]:

$$k_{SPP} = k_0 \sqrt{\frac{\varepsilon_m \varepsilon_d}{\varepsilon_m + \varepsilon_d}} \tag{1.1}$$

Where:

- $k_0 = \frac{2\pi}{\lambda}$ refers to the wavevector in free space
- ε_m: the complex permittivity of the metal
- ε_d: the complex permittivity of the dielectric

This expression indicates that SPPs are not free-space waves; their wavevector is larger than that of light in free space at the same frequency. As a result, they cannot be excited directly by plane waves. Extra wavevector should be provided to satisfy momentum matching condition. When incident light satisfies the momentum matching condition through a coupling mechanism (such as a metallic grating, nanostructures, or prism coupling), that is:

$$k_{\parallel}^{\mathrm{inc}} + G = k_{SPP} \tag{1.2}$$

where G is the reciprocal lattice vector provided by the periodic structure, strong resonance absorption or transmission occurs at a specific wavelength. This is known as **plasmonic resonance**, corresponding to the most efficient excitation of SPPs and accompanied by intense electromagnetic field enhancement.

Plasmonic devices using noble metals like gold and silver have been extensively reported in the visible and near-infrared spectral bands due to their relatively low Ohmic losses[75-77]. However, gold suffers from interband transitions that impair colour performance below 500 nm (i.e. in the blue region), and silver is susceptible to surface sulphidation. Additionally, neither material is CMOS-compatible[78], limiting their utility in mainstream imaging system at the Back-of-End-of-the-Line level. By contrast, aluminium offers clear processing advantages: its etching commonly relies on chlorine-based chemistries that are well

established in semiconductor manufacturing, and aluminium generally provides more favourable deposition and adhesion behaviour. This makes it particularly attractive for integration with silicon-based detectors. As a result, aluminium-based plasmonic filters—offering low cost and ease of manufacturing—have attracted ongoing interest[33, 54, 79, 80].

Here, a comparison between Al and the commonly used noble metals Ag/Au is summarised in Table 1-3.

Table 1-3 Comparison among Aluminium, silver and gold for plasmonic filters.

	Al (Aluminium)	Ag (Silver)	Au (Gold)
Ohmic Loss	High	Low	Medium
Chemical Stability	Stable with surface oxidation	Surface sulphidation	Stable
CMOS Compatibility	Good	Bad	Bad
Price	Low	High	High
Risk	surface roughness scattering	Instable, requires specific protection	Interband transition at blue wavelengths

1.3 Bound States in the Continuum

In classical mechanics, an electron with sufficient kinetic energy is expected to escape its atomic system, entering the continuum of scattering states. However, experiments have shown that some high-energy electrons remain trapped within the system and do not escape the surrounding potential. This seemingly strange behaviour is explained by quantum mechanics. In 1929, John von Neumann and Eugene Wigner introduced the concept of Bound States in the Continuum (BIC) to describe such states[81, 82]. Since then, analogous phenomena have been observed across many systems that contains wave.

In optics, BICs have been widely studied in photonic platforms such as waveguides, photonic crystals, optical fibres, and metasurfaces[41, 82-86]. Conventionally, electromagnetic eigenmodes within the radiation continuum should radiate energy, while bound states should lie below the continuum. BICs challenge this view by existing within the radiation continuum yet remaining fully localised and non-radiative. Although their frequencies and momentum may match those of radiative modes in free space, BICs do not couple to the far

field[82]. In practice, perfect BICs cannot be realised or observed due to the complete decoupling with exciting light. Instead, quasi-BICs are more often manipulated, which exhibit weak coupling to the far field and small radiative leakage[38, 41, 83, 87]. By tuning parameters such as geometry, size, periodicity, or excitation wavevector, one can adjust the system to weakly couple a BIC to the environment, giving rise to quasi-BICs. These modes allow for precise control over radiation losses via interference between resonant pathways.

Consider a periodic dielectric slab in vacuum. The wavevector $\boldsymbol{k}$ of a radiative electromagnetic wave can be decomposed into vertical $\boldsymbol{k}_{\perp}$ and in-plane $\boldsymbol{k}_{\parallel}$ components. The wave's frequency satisfies $\omega = c|\boldsymbol{k}| > c|\boldsymbol{k}_{\parallel}|$, meaning the radiation continuum occupies the region $\omega > c|\boldsymbol{k}_{\parallel}|$ in the frequency-momentum domain ($\omega - \boldsymbol{k}$ space). Such region in the $\omega - \boldsymbol{k}$ space is also known as the light cone. Below this region lie discrete bound modes, determined by the eigenfrequencies of Maxwell's equations. Contrary to traditional assumptions, BICs stay inside the light cone but remain completely bound, with no energy leakage. This is illustrated schematically in Figure 1-2(a).

There are two main types of BICs:

1. Symmetry-protected BICs[88]: These arise when the structure possesses C_2 (or multi-fold) symmetry, allowing certain even-symmetry resonant modes to become orthogonal to odd-symmetry radiative modes, thus decoupling from the far field. Breaking the symmetry causes the BIC to couple and radiate, turning into a quasi-BIC. Symmetry-protected BIC (green dot in Figure 1-2 (a)) occurs at the high-symmetry $\boldsymbol{\Gamma}$ point because of mode symmetry mismatch with radiative channels.

2. Interference-induced BICs[89]: These BICs result from destructive interference between different resonant modes (e.g., Fabry–Pérot or Friedrich–Wintgen types) or between different components of the same mode. Adjusting structural parameters tunes the interference and thus the degree of radiative leakage, producing quasi-BICs when interference is incomplete. Because BICs are highly sensitive to structural conditions, they are often referred to as accidental BICs. Accidental BICs (red dots in Figure 1-2 (a)) arise away from $\boldsymbol{\Gamma}$, where destructive interference of radiation leads to complete decoupling from free-space modes.

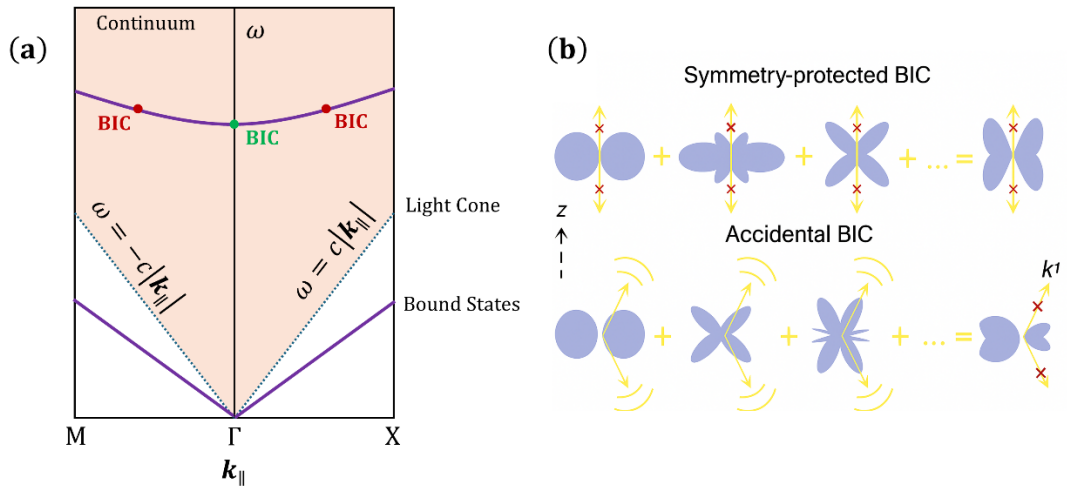

Figure 1-2 Bound States in the Continuum (BICs) in Photonic Systems. (a) Photonic band structure illustrating BICs in the continuum above the light cone. (b) Schematic illustration of the formation mechanisms of BICs from far-field multipolar analysis view. Top: In symmetry-protected BICs, any leakage of energy is forbidden in the normal direction if all the multipoles are not allowed to radiate along the z-axis, leading to a symmetry-protected BIC at the Γ point in the momentum space. Bottom: In accidental BICs, asymmetric mode components interfere destructively at specific in-plane wavevectors $\mathbf{k_1}$, suppressing radiation without relying on symmetry.

Symmetry-protected BICs are typically located at the centre of the first Brillouin zone in momentum space, i.e. the Γ point, and are ensured by the structural symmetry[88]. This type of BIC has been extensively studied in structures with in-plane geometry symmetry. Taking SP-BICs as an example to explain the formation of BICs, when the plane waves in free space are odd under a 180° (π) rotation around the z-axis (normal to metasurface plane), any eigen mode supported by the structure that is even symmetric under this operation is orthogonal to the radiation continuum. As a result, these modes cannot couple to free-space radiation and form BICs. However, when moving away from the Γ point, at least one component of the in-plane wavevector (either k_x or k_y) becomes non-zero. In this case, the π-rotation symmetry operation no longer preserves the in-plane wavevector, and the symmetry protection is broken. Consequently, the previously bound state begins to couple weakly to radiative modes, giving rise to a quasi-BIC with finite radiation leakage.

Here, a brief comparison among plasmonic resonances spanning the transition from local to nonlocal behaviour, and all-dielectric nonlocal quasi-BIC (q-BIC) modes is provided in Figure 1-3. A defining feature of local metasurfaces is that the sampling points (meta-units) can be treated as approximately spatially independent in shaping the wavefront. Consequently, both metallic metasurfaces based on localised surface plasmon resonances

(LSPRs) and dielectric metasurfaces based on local Mie resonances are well suited to Huygens metasurfaces and metalenses. A clear signature of modal localisation is weak sensitivity to the angle of incidence; correspondingly, such resonances typically exhibit relatively low Q factors. A SPP can be viewed as a propagating counterpart of an LSPR—i.e., a collective mode that still retains some LSPR-like characteristics. As a result, its angle sensitivity and Q factor generally lie between those of local resonances and q-BICs. Notably, even for arrays as small as only a few unit cells, SPP-type modes can still produce appreciable spectral modulation. By contrast, ultra-high-Q quasi-BIC modes operate on a completely different Q-factor scale and exhibit the strongest angle sensitivity among the three. This is a general characteristic of nonlocal states: changes in the in-plane wavevector directly modify the eigenmode wavelength and field profile, leading to resonance shifts and a reduction in Q factor. When low angular dispersion and localised wavefront control are required, q-BIC metasurfaces are therefore often not an ideal choice—for instance in metalenses and many nonlinear-optical implementations. Conversely, when very high-Q wavefront control is needed, local resonances often struggle to meet the requirement.

Based on the comparison and discussion above, a key question that has gained traction in recent years is whether the angular dispersion of q-BIC metasurfaces can be suppressed—in terms of both the real and imaginary parts of the eigenfrequency. This topic will be introduced in Chapter 2 and explored in detail in Chapter 6 of this thesis.

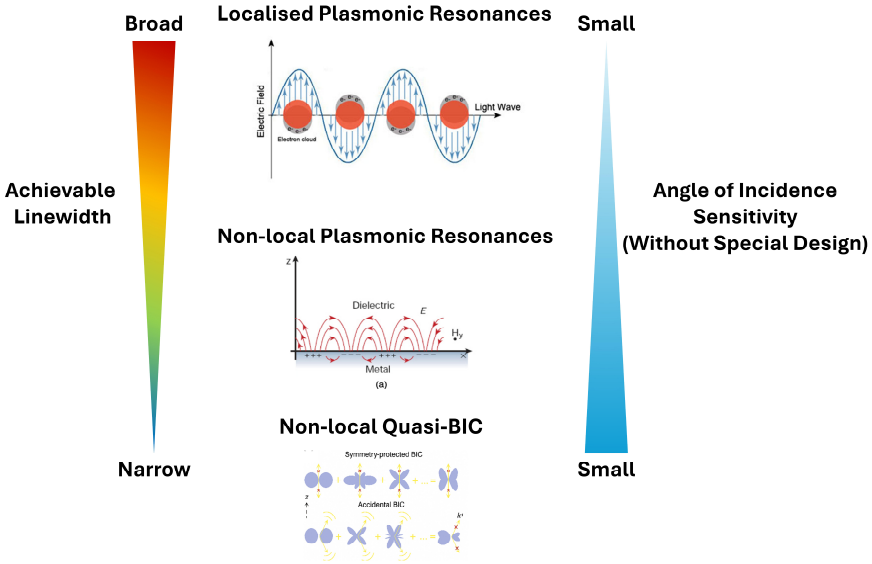

Figure 1-3 A general comparison among LSPR. SPP and Q-BIC.

1.4 Research outline

The following chapters in this thesis will contain following contents:

Chapter 2 provides a review and latest advances of the following areas:

1. Recent advances and state-of-the-art developments in nonlocal resonant metasurfaces supporting plasmonic resonances for colour filtering and structural colour.

2. The use of nonlocal resonant metasurfaces supporting BICs, with a particular focus on infrared sensing applications.

3. The current research frontiers in angular dispersion control of nonlocal resonant metasurfaces.

Chapter 3 introduces the main steps, tools, and methodologies involved in metasurface research, including numerical simulations, nanofabrication (in James Watt Nanofabrication Centre), and characterisation techniques. Special attention is given to the simulation principles and practical implementation of methods such as RCWA (Rigorous Coupled-Wave Analysis), FDTD (Finite-Difference Time-Domain), and FEM (Finite Element Method), a comprehensive comparison is presented and can serve as a guidebook for future users entering the field.

Chapter 4: The unique features of nonlocal resonant metasurfaces stem from the well-defined spectral responses provided by resonance. In the visible range, a typical application of such responses is colour filtering and detection. Colour is one of the most vital channels through which humans and many animals perceive their environment. Our ability to segment objects within a scene heavily relies on colour information[90, 91]. Consequently, how to detect colour is of considerable importance. Modern optical detectors often employ a Bayer-type pixel arrangement, where each 2×2 group of subpixels is equipped with red, green, and blue (RGB) filters (typically in an RGBG configuration), enabling full-colour detection. Early implementations of colour filters were based on dyes[92]. While they provided good colour purity, they were often environmentally unfriendly and involved complex manufacturing processes with the increasing reducing pixel size. Visible-band colour filters based on nonlocal metasurfaces represent a more promising approach. These single-layer structures can be fabricated using scalable semiconductor processing techniques. **Chapter 4** of this thesis shows the application of nonlocal plasmonic metasurfaces for colour filtering and

introduces a colour-polarisation filtering system capable of advanced, multidimensional detection of visible-light information.

Chapter 5: Beyond the visible spectrum, infrared (IR) wavelengths form another critical window for information perception. The infrared region is broadly divided into near-, mid-, and far-infrared bands (NIR, MIR, and FIR). The mid-infrared (mid-IR) is the most significant for thermal imaging because it includes the atmospheric transparency windows (3–5 μm and 8–14 μm), where absorption by water vapour is minimal—ideal for passive IR imaging. More importantly, this region encompasses the fundamental absorption peaks of molecular vibrations, making it highly relevant for the specific identification of chemical substances[93-95]. IR filters targeting these characteristic absorption bands are therefore crucial. In recent years, nonlocal metasurfaces supporting quasi-BIC (Bound States in the Continuum) modes have been widely adopted for mid-IR spectral analysis[39, 43, 96]. Quasi-BICs are high-Q resonant modes, enabling narrowband filtering with precise spectral selectivity. Additionally, their strong local field enhancement can facilitate strong coupling with vibrational modes or serve in nonlinear optical enhancement. **Chapter 5** presents nonlocal metasurfaces for multispectral mid-IR filtering and proposes a quasi-BIC-based metasurface architecture operable in transmission mode.

Chapter 6: Nonlocal metasurfaces are periodic structures where inter-element coupling gives rise to collective modes. As shown in Figure 1-1, their spectral responses are typically highly angle-dependent, a phenomenon known as angular dispersion. In some cases, this can be harnessed for tuneable filtering by varying the angle of incidence[97]. However, for applications requiring enhanced fields at specific frequencies—such as focused light excitation—angular dispersion becomes a limiting and unwanted factor[36]. Varying angles lead to a spread in resonant frequencies, thereby broadening the spectral linewidth. Therefore, designing nonlocal metasurfaces with low angular dispersion within a finite angular range is of practical importance, particularly for applications involving strong coupling or focused illumination. **Chapter 6** demonstrates such a flatband metasurface designed for on-resonance mid-IR sensing, exhibiting engineered low angular dispersion within a defined incidence range.

Chapter 7: Brief summary of completed work

Chapter 2 State of the Art of Non-local Resonant Metasurface

2.1 Nonlocal resonant metasurfaces supporting plasmonic resonances for colour filtering

In the field of nanophotonics, plasmonic metasurfaces have emerged as a transformative technology, enabling multidimensional control of light at the nanoscale [33, 68, 78, 80, 98-100]. These one- or two-dimensional arrays, composed of nanostructured metallic elements, exploit the unique optical properties of plasmonic materials such as noble metals (e.g., gold [Au] and silver [Ag]), as well as more cost-effective metals like aluminium (Al). Plasmonic metasurfaces can manipulate surface plasmon resonances (SPR) to achieve precise control over the phase, amplitude, and polarisation of light. This capability has paved the way for numerous applications, including beam deflection[101-103], metalenses[21, 104, 105], and holography[106-108]. A particularly compelling application is in the generation of structural colours, i.e., colour filtering[33, 68].

The use of metallic nanoparticles to produce vivid colours has a long history, dating back over 1,700 years to the famous Lycurgus Cup[109]. This phenomenon is primarily attributed to the surface plasmon resonance (SPR) effect. The localised resonant units, known as localised surface plasmon resonances (LSPR), exhibit strong field confinement and small mode volumes[110]. However, their ability to modulate the optical spectrum is generally limited, and the scattering intensity is often insufficient for clear observation under bright-field reflection microscopy[111]. A representative study by Karthik Kumar et al. firstly placed nanoparticle resonators above a metallic back-reflector to enhance their scattering intensity, achieving pixel sizes with an ultra-high spatial resolution of 250 nm[111]. While this approach still relies mainly on LSPR effects and successfully produces observable colour modulation, it operates in a subtractive colour mode and suffers from the relatively broad spectral features of LSPR, resulting in a narrow colour gamut. By transitioning from localised to nonlocal resonant modes, however, plasmonic metasurfaces can significantly improve linewidth narrowing and modulation depth in the spectrum (i.e. absolute peak transmission or reflection), thereby achieving well-defined spectral responses and a much broader colour gamut[33, 80, 112, 113].

Early studies predominantly focused on using nanohole arrays—structures supporting surface plasmon polariton (SPP) modes—for colour filtering. For instance, Chen et al. proposed a triangular periodic nanohole array that achieved RGB colour filtering with a peak transmission of approximately 30%[33]. This design incorporated a capping layer on the metallic nanohole film to retain symmetry between the top and bottom surfaces of the metal film, thereby enhancing the peak transmission, as illustrated in Figure 2-1 **(a)**. Similar structures have also been explored for direct integration with CMOS chips[100, 114], demonstrating their potential for large-scale fabrication and commercialisation, as shown in Figure 2-1**(b) / (c)**.

The size of the nanoholes is directly related to transmission efficiency and arrays achieving peak transmissions exceeding 70% have been reported when linewidth narrowing is not a primary consideration, as shown in Figure 2-1**(d)**[54]. Owing to their operation in transmission mode and their exceptionally high peak transmittance, such structures have also been integrated with single-photon avalanche detectors (SPADs) for colour reconstruction in ultra-low level of light environments. Compared to subtractive colour filters based on LSPR, these SPP-based designs offer narrower spectral features, making it easier to produce colours perceptible to the naked eye. Nevertheless, their colour gamut remains relatively narrow, and their functionality is still limited to basic filtering.

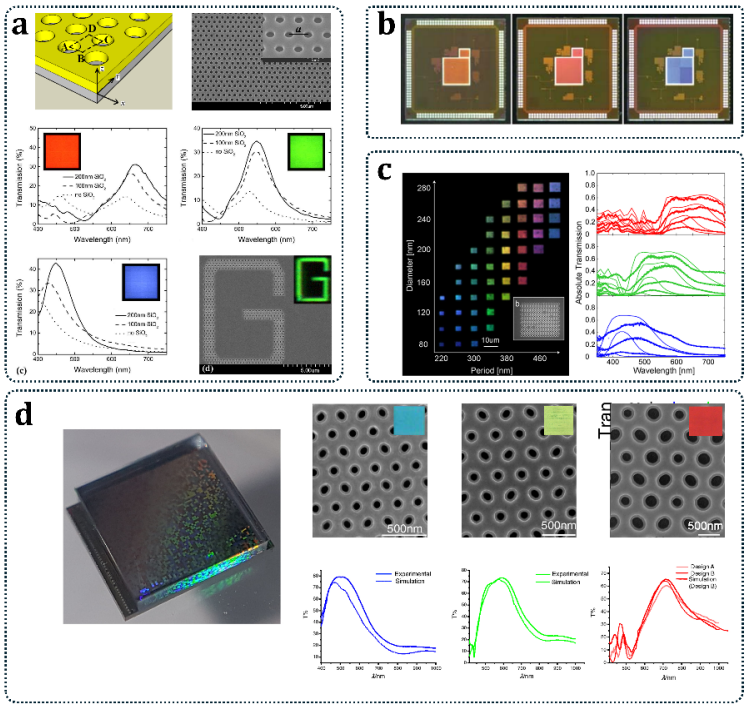

Figure 2-1 Periodic nanohole array plasmonic colour filters. (a) Tri-angular period of aluminium nanoholes, with 150nm of capping SiO2 layer on to the metal film. A clear transmission enhancement can be observed[33].

(b) Plasmonic colour filter fabricated on CMOS pixels, forming spectral-sensitive CMOS sensors[100]. (c) Colour palette made of plasmonic filters, achieving wide range of colour tunning by varying the size and period of the hold array[114]. (d) Left-hand side showed the integrated SPAD array with plasmonic mosaic colour filter array on top. Right-hand side showed the SEM image and the characterised spectral response of the 470, 570, 670nm centred filters, where a peak transmission larger than 70% was observed[54].

More advanced applications exploiting additional dimensions of light beyond spectral features have been explored. For example, as shown in Figure 2-2 (a), the integration of visible-light colour filters with other electromagnetic bands, such as the infrared and terahertz regions[115-117] , enables multi-band filtering and advanced functionalities such as simultaneous visible-light and thermal radiation cloaking.

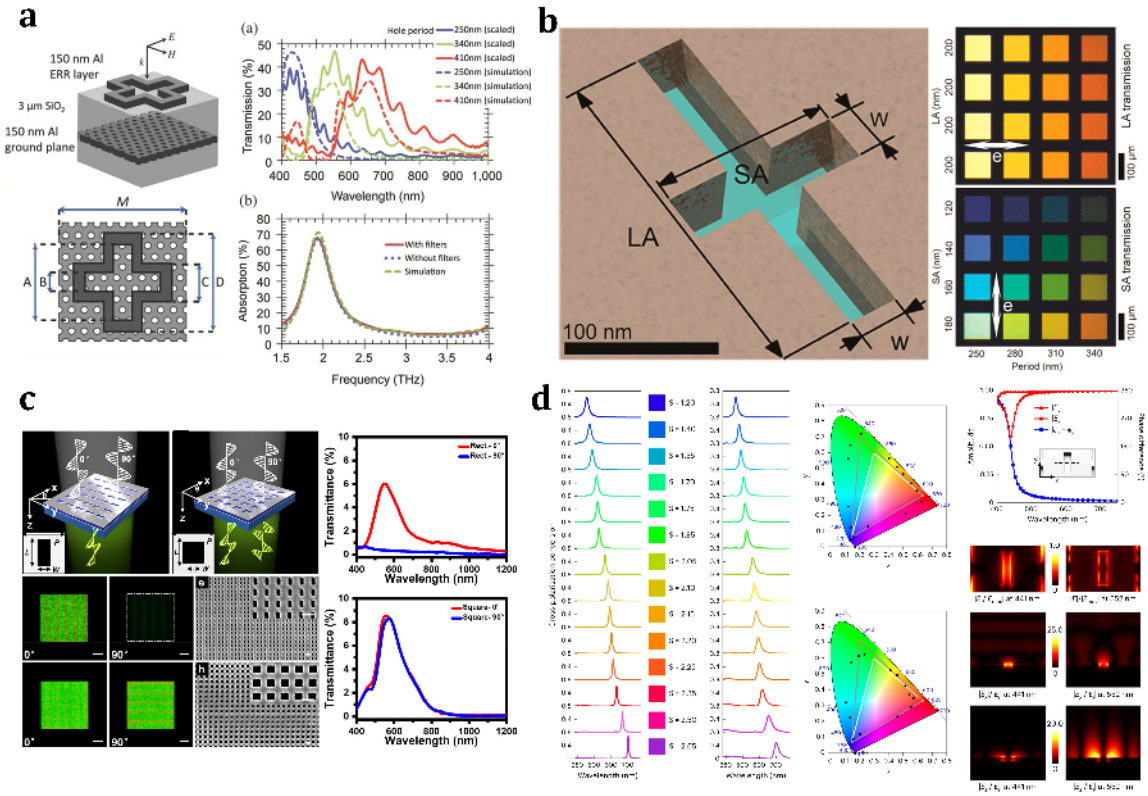

Figure 2-2 Advanced applications with plasmonic filters. (a) Hybridisation of visible plasmonic filter and Terahertz electric ring resonator (ERR), enabling dual band of operation. Right-hand side showed the visible characterisation and THz FTIR characterisation result of the fabricated dual layer metasurface[117]. (b) Dual polarisation multiplexed plasmonic filters. (c) Anisotropy enabled different response of plasmonic filter. By changing the ratio between two side-length, different polarisation distinction ratios can be obtained. For highly anisotropic rectangular design, a polariser was made as shown in the upper right corner, while a polarisation insensitive colour filter was made as shown in the bottom right corner[118]. (d) Plasmonic modes enabled half-wave plate for simultaneously-control of hue and colour [77].

In addition to spectral extension, the polarisation degree of freedom is also a key consideration in filter design. In 2017, Li et al. proposed a cross-shaped nanohole array, enabling spectral responses dependent on orthogonal linear polarisations, which could be used for polarisation-encoded micro/nano-images[119], as shown in Figure 2-2 (b) The layout on the left-hand side demonstrated the design of the cross-shaped hole in a unit cell. The short-arm (SA) direction and long-arm (LA) direction will support different plasmonic modes, and different colours were therefore made for x-polarised and y-polarised incidence light. Similarly, other studies [79, 118] reported rectangular nanohole arrays with varying aspect ratios, demonstrating transitions from polarisation-independent to polarisation-extinction behaviour, as shown in Figure 2-2 (c). However, these designs typically exhibited peak transmissions below 10%, due to the reduced fill factor of the holes when introducing polarisation selectivity, which inherently limits transmittance. A recent study [77] adopted a completely different strategy by using the anisotropy of periodic rectangular nanoholes. The device proposed introduced a 180° phase delay difference between the x- and y-polarised electric fields, effectively forming nano-hole-controlled half-wave plates with high spatial resolution. Using a cross-polarisation microscopy setup, the rotation of the rectangular nanoholes with respect to z axis enabled different intensities for orthogonal polarisation reflection peaks. Experiments demonstrated an orthogonal polarisation conversion efficiency exceeding 70%, achieving multiple functionalities including colour filtering, hue control, and polarisation encoding. Nevertheless, this device operates in reflection mode, and the correct rendering of colours relies on an optical setup with orthogonal polarisations. Figure 2-2 (d) demonstrates the cross-polarisation spectrum, and the colour palette showed the wide colour gamut supported by such a design. The performance was enabled by anisotropic phase and amplitude response of the rectangular hole towards the incident electric field.

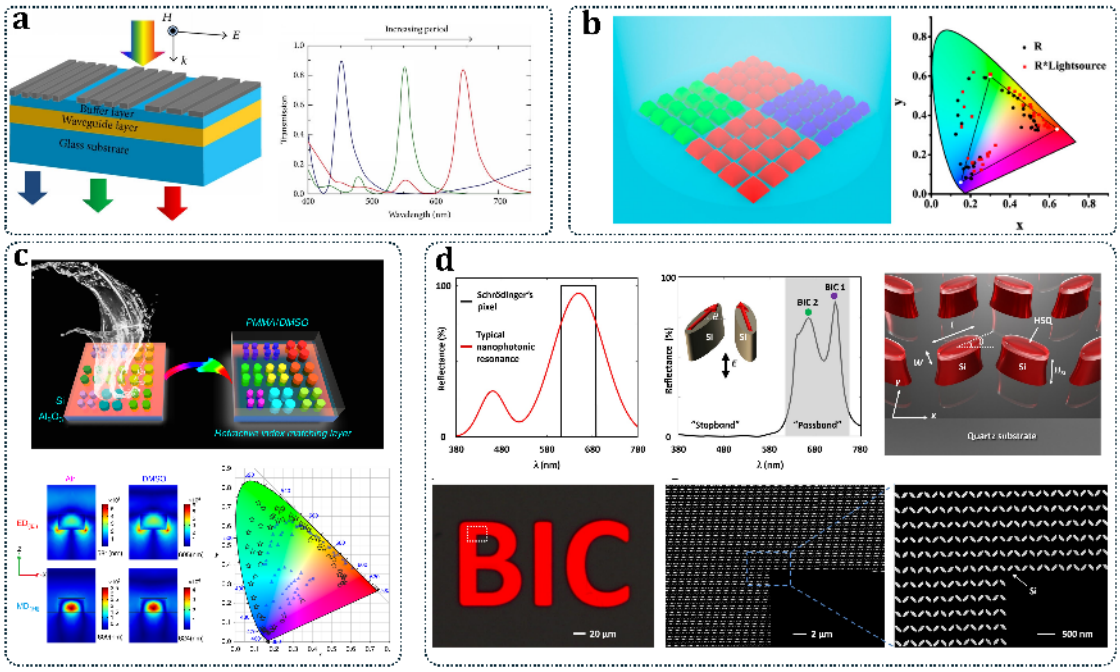

Figure 2-3 Nonlocal metasurface and nanophotonic device for structural colour generation other than SPP modes. (a) A guided mode resonance type hybrid metal-dielectric filter[120]. (b) Full-colour coverage structural colour using TiO2 metasurface. The structure was designed to be TiO2 squares on sapphire substrate to enable polarisation insensitivity at normal incidence. Collective Mie resonance contributes to the spectral response[121]. (c) Si metasurface using Mie resonance for high-saturation, high resolution and CMOS-compatible structural colour generation. A PMMA or DMSO layer was applied on top of the silicon resonators to serve as a refractive index matching layer, effectively suppressing the resonances at unwanted bands. The device therefore showed enlarged colour gamut coverage, as shown in the bottom right area[122]. (d) Schrödinger's red pixel (S-red) made of BIC metasurface. A dimer ellipse structure with tilted angle was made, to convert symmetry-protected BIC into quasi-BIC, leaking a sharp resonance with small radiative loss. Unlike conventional Mie-resonance type metasurface, such a design effectively suppressed the higher order resonance at shorter wavelengths for red pixel, making a purer red colour[123].

In addition to the nonlocal modes dominated by SPPs in metallic nanohole arrays, there have also been many reports on hybrid metal-dielectric guided mode resonance (GMR) structures, narrow-linewidth Mie resonance-based all-dielectric metasurfaces, and high-quality-factor (high-Q) nonlocal modes such as those supporting BICs for colour filtering. In 2011, Alex F. Kaplan *et al.* proposed colour filters fabricated using nanoimprint lithography that support guided mode resonances[120]. As shown in Figure 2-3 (a), in their design, a thin buffer layer was adapted in between the gratings and the waveguide layer. The buffer layer, waveguide layer and the glass substrate formed a sandwiched structure with low-high-low refractive index distribution, forming a waveguide structure. The waveguide structure and the metallic gratings on top combined formed guide mode resonance, filtering specific colours. Their design successfully achieved narrow-linewidth filters with over 80% peak transmittance

under normal incidence, and by rationally tuning the buffer layer thickness, they realised multi-band filtering across the visible spectrum within the same overall thickness. However, GMR structures inherently involve guided modes with strong dispersion, making their colour filtering and display highly incident angle dependent, limiting their practical applications.

More recently, the group led by S. Xiao *et al.* has proposed several designs for structural colours based on Mie resonances[112, 121, 122]. In these designs, the structural colour is achieved via collective Mie resonances in dielectric materials, offering advantages over plasmonic types such as lower radiative losses, narrower linewidths, and broader colour gamut coverage. In 2017 and 2020, they respectively demonstrated narrow-linewidth, wide-gamut structural colours using silicon nitride as the resonator material and silicon resonators with a refractive index matching layer, as shown in Figure 2-3 (b) and (c). Notably, these structural colours function effectively under bright-field illumination. Another important advancement was the demonstration of structures capable of producing "Schrödinger red" — the purest red in the colour gamut, as shown in Figure 2-3 (d). Traditional Mie resonance-based designs often suffer from interference caused by short-wavelength higher-order resonances when fabricating red pixels, which reduces colour purity[123]. To suppress the influence, BIC-based structures and machine-learning techniques were employed. These structures operate in a different periodicity regime than conventional Mie resonators, and through careful tuning of size and periodicity, the impact of higher-order Mie resonances can be eliminated. To further optimize performance — balancing colour purity and peak reflectance — the authors also integrated machine learning methods to refine the structural design.

On the design methodology side, the application of advanced machine learning techniques[124-127] for inverse structural design has received considerable attention in recent years. Approaches range from directly using convolutional neural networks (CNNs) for spectral prediction[128] to employing cascaded neural networks for inverse retrieval of structures from target spectra [124]. These methods have made the design of colour filters more directional and efficient, moving beyond traditional brute-force numerical searches.

A primary limitation of such Mie resonance or BIC-based structures is that they operate in reflection mode. As a result, they can only be used for structural colour display and are not suitable for direct integration with detectors as transmissive filters. This phenomenon can be understood as the fact that Mie/Fano resonances and qBIC resonances supported by

dielectric structures typically act as strong scattering features superimposed on a broadband transmission background spectrum. In the vicinity of a resonance, the phase undergoes a rapid flip (relative $\varphi(\omega)$ changes from π to $-\pi$). there must exist a frequency at which the resonant contribution interferes destructively with the original background transmission, leading to a redistribution of energy between transmission and reflection. Because these dielectric metasurfaces naturally exhibit a broad transmission background, introducing a resonator-mediated spectral response commonly results in an energy redistribution opposite to the transmission background—manifesting as a transmission dip and a corresponding reflection peak. However, if one could engineer the background spectrum to be reflective, the resonance would instead appear as a transmission peak (for instance, electromagnetic induce transmission (EIT)-like line shape). However, designing broadband, low-loss reflection using dielectric or hybrid dielectric–metal materials is almost impossible in practice. High-performance transmissive metasurface structural colours/filters are therefor hard to make and rarely reported.

In summary, achieving relatively higher transmittance while maintaining narrow linewidths, as well as incorporating additional functionalities such as polarisation control, remains a key challenge for plasmonic metasurface-based colour filters. This is also the focus of Chapter 4 in this study.

2.2 Nonlocal resonant metasurfaces for mid-infrared sensing

In the visible light spectrum, colour conveys a wealth of information that assists with recognition and classification. However, in the invisible light spectrum, such as ultra-violet, infrared and terahertz range, the recognition and classification of the material and objects more rely on the direct analysis of the spectral characteristics. The infrared (IR) region is one of the most important bands for sensing applications, comprising the near-infrared, mid-infrared, and far-infrared ranges. Among these, the mid-infrared is particularly critical for sensing, as the intrinsic vibrational absorption peaks of many chemical bonds lie within this region[93, 95]. Absorption peaks arising from different excitations produce rich characteristic fingerprints, thereby enabling the detection of specific molecules, the enhancement of infrared signals. Tools for infrared spectral analysis have therefore attracted considerable interest. A popular optical filter platform, multi-layer thin films can be used for spectral filtering and sensing. However, at large angles of incidence, thin-film filters are primarily affected by changes in the effective optical path length, which in turn shifts the Fabry–Pérot (FP) modes; by contrast, for non-local (NL) metasurfaces the dominant mechanism is the change in the in-plane wavevector, leading to different eigen resonance frequencies. Nevertheless, metasurfaces offer distinct additional design opportunities. For example, if a BIC or quasi-BIC is placed on an intrinsic quasi-flat band structure (often associated with Mie-type, localised resonances), then, aside from a degradation in the Q factor, its centre wavelength does not substantially shift, as demonstrated by the structure proposed in Chapter 5 of this thesis and in [129]. Alternatively, one may deliberately engineer a flat band so as to realise high-Q resonances on that flat band, that will be discussed in section 2.3. Multilayer metasurfaces are, in turn, more readily able to achieve angle-insensitive transmission via angular-dispersion compensation or by artificially creating Moiré flat bands[84, 130-132]. Admittedly, some of these design principles can be transferred to thin-film filter design[64]; however, in terms of both flexibility and achievable Q factor, thin-film approaches still fall short of the upper limits attainable with metasurfaces. Nonlocal metasurfaces can act as infrared filters and media for surface-enhanced spectroscopy that would contribute to infrared spectroscopy, owing to the strong near-field enhancement and frequency selectivity of nonlocal modes.

For frequency selectivity, the nanohole design introduced in Section 2.1.1 can similarly be extended to the infrared region[115, 133]. In the mid-infrared range, noble metals such as gold and silver are regarded as excellent plasmonic materials because of their superior plasmonic properties and relatively lower losses. Numerous studies have reported mid-infrared filters based on gold or silver. For example, Ang Wang *et al.* first experimentally demonstrated a multispectral mid-infrared filter[115]. The structure consists mainly of gold nanoholes embedded in a Ge layer, where the Ge layer functions analogously to the SiO_2 substrate and capping layer commonly used in the visible spectrum. Their experiments achieved full width at half maximum (FWHM) on the order of several hundred nanometres and peak transmittance exceeding 60%. Such nanohole arrays can serve as the filtering layer in multispectral thermal imaging systems[133], as illustrated in the system shown in Figure 2-4(b). In another report, several Au-on-GaAs plasmonic metasurface filters of large areas were fabricated to provide field-of-view coverage, enabling multispectral long-wave infrared imaging.

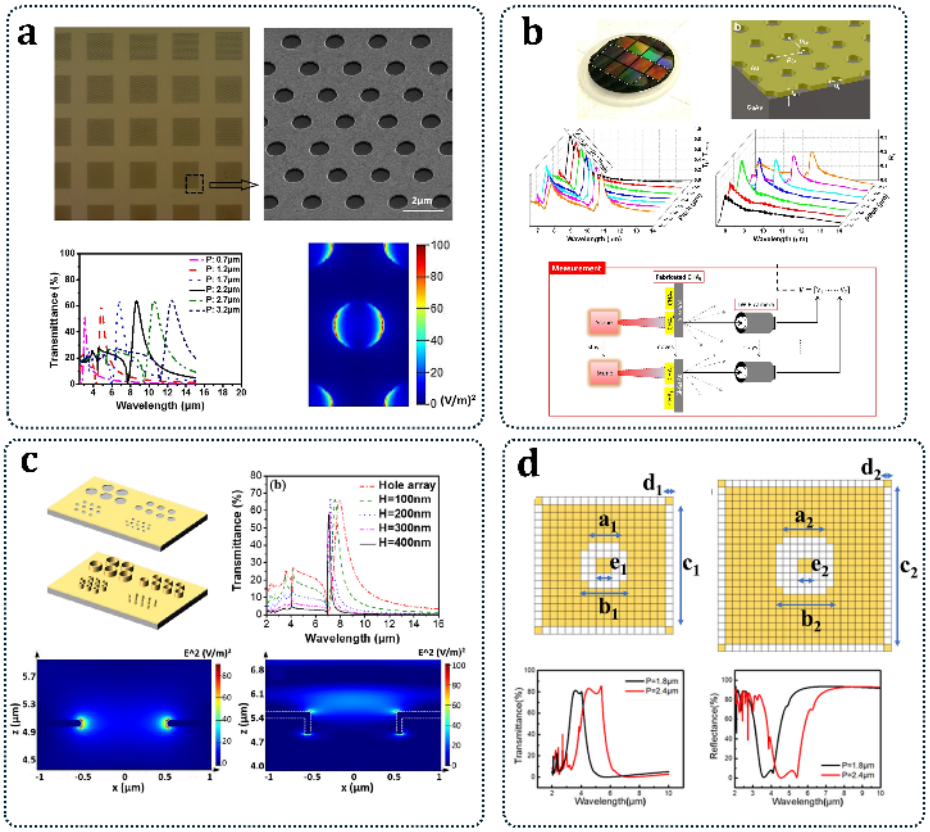

Figure 2-4 Plasmonic filters in infrared range. (a) Au nanoholes buried in Ge layer, forming periodic hole structure supporting SPP mode. The FTIR characterised spectral transmission response of the fabricated sample was shown in the bottom left side, which showed maximum exceeding 60%[115]. (b) Similar nanohole array

design in Au film on top of GaAs. Top-left showed the fabricated large area sample, which can be applied to multi-spectral thermal imaging applications as shown in the bottom part[133]. (c) Micropipe plasmonic filters for linewidth reduction. A micropipe structure was applied, to split the SPP modes supported by top metal-dielectric and bottom metal-dielectric. The simulated transmission spectrum was shown in the top right corner, it can be seen that with the increasing height of the micro-pipe structure, the linewidth of the transmission spectrum of the device was reduced[134]. (d) Machine learning enabled hole-structure optimisation. The unit cell of the plasmonic metasurface was discretised into $\mathbf{m} \times \mathbf{n}$ pixels. The transmission spectrum was monitored and optimised with varying structural parameters including the size of the hole and unit cell side length[135].

It is worth noting, however, that the linewidths achieved in such works tend to be relatively large, which limits the number of supported spectral channels. To reduce the linewidth, Xu *et al.* proposed the use of a micro-pipe structure instead of traditional nanoholes[134]. This design increases the vertical distance between the top and bottom metal-dielectric interfaces, fully separating the two plasmonic modes supported on these surfaces and thereby narrowing the transmission peaks. Beyond system-level structural optimisations, the shape of the holes themselves also has a significant impact on the transmission properties[71, 136, 137]. Recently, Dan *et al.* proposed a gradient optimisation of hole geometries using deep learning techniques. As shown in the upper side of Figure 2-4(d), their design discretizes and binarizes the hole patterns: each unit cell is divided into $m \times n$ pixels (corresponding to sides *c* and *d*), where regions assigned a value of zero represent holes. Using neural networks and other computational tools, they optimized hole geometries to achieve the target spectra[135].

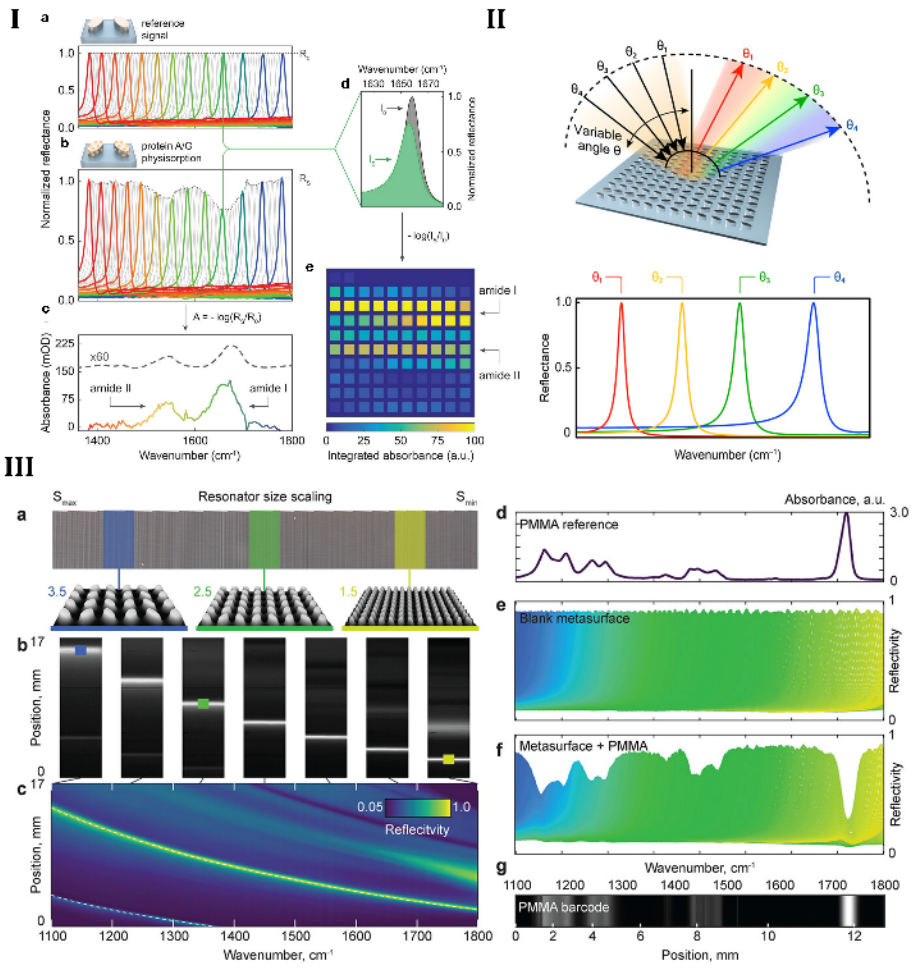

Figure 2-5 BIC-metasurface for mid infrared sensing. (I) Pixelated q-BIC metasurface, the metasurface pixel respectively supported a q-BIC mode, giving a reflection peak in the MIR range[43]. By scaling the unit size, the central peak wavenumber can be tuned, as shown in **a.** When applied the protein A/G on top of the metasurface, the reflection peak was reduced because of the absorption of the protein, as shown in d. The influence of the protein absorption will be enhanced owing to the strong near field enhancement of q-BIC mode. e. showed the pixelated metasurface array, from which the classification and quantification of the protein can be conducted in a spectrometer-less configuration. (II) Angle-multiplexed single-pixel metasurface. The reflection peak can be effectively tunned through the change of the incidence angle[97]. The MIR range can be therefore covered with just single pixel metasurface area. (III) Continuous encoding of the reflection peak of the metasurface[138]. Gradient size change of the adjacent unit pixel in spatial space was applied to the array design, the reflection peak was therefore mapped continuously instead of pixelation or highly discretion, therefore increased the spatial-spectral channel density.

Despite extensive optimisation efforts, metallic nanohole arrays remain fundamentally limited in achieving narrow linewidths due to Ohmic losses. To further realize high-quality-factor (high-Q) mode generation and narrowband filtering, increasing attention has been directed towards all-dielectric metasurfaces, particularly those supporting bound states in the

continuum (BIC) modes. A. Leitis and his group have conducted a series of pioneering studies in this area[43, 97, 139]. They proposed a pixelated metasurface platform based on BIC modes to develop a novel approach for detecting characteristic molecular fingerprints of various surface-adsorbed molecules. The design utilizes resonator units composed of two slightly tilted amorphous silicon or germanium ellipses, breaking the C_2 geometric symmetry of the system to support convert symmetry protected BIC into quasi-BIC modes. Each super-pixel exhibits strong frequency selectivity and, through scaling of the entire structure, can provide high-Q resonances at specific wavenumbers within the target spectral range. This establishes a mapping between spatial information (the location of super-pixels in the array) and spectral information (the associated resonance positions). When a thin layer of protein A/G biomolecules was deposited, the authors observed a pronounced reduction and broadening of the super-pixel resonance amplitudes associated with molecular vibrational bands (Fig. 2-5 I, bottom). Owing to the high-Q resonances and spectrally well-defined line shapes, it became possible to read out chemically specific absorption signals even under broadband illumination and detection. This enabled the generation of image-based molecular fingerprint representations suitable for further analysis using pattern recognition and machine learning methods[43]. These so-called 'molecular barcodes' have been demonstrated for detecting compounds across diverse fields such as biology, environmental monitoring, and materials science, and the approach has been extended to both the visible[42], near infrared[140] and terahertz[141] regimes. Furthermore, the density of spectral channels can be increased by introducing gradient designs into the super-pixels. In the design illustrated in Fig. 2-5(III), the concept of discrete super-pixel arrays is abandoned. Instead, the authors introduced size scaling gradients between adjacent units. This results in continuous variations of characteristic reflection wavelengths, forming a continuous relation between space and reflection peak wavenumber[138, 139]. Beyond spatial multiplexing, angular multiplexing has also shown promising potential[97]. As reported in Fig. 2-5(II), researchers discovered a clear functional relationship between the incident angle and the reflection peak wavelength owing to the highly dispersive nature of the proposed quasi-BIC modes. This one-to-one correspondence allows the reflection peak wavelength to be tuned by altering the incident angle, enabling broadband detection even with a single pixel. Here, the number of spectral channels depends only on the curvature of the quasi-BIC dispersion and the sensitivity of the detector, rather than the fabrication precision. These works are all based on one-dimensional mappings between spectrum -spatial position or spectrum-angle.

Recently, however, several studies have demonstrated two-dimensional mappings between spectrum and position.

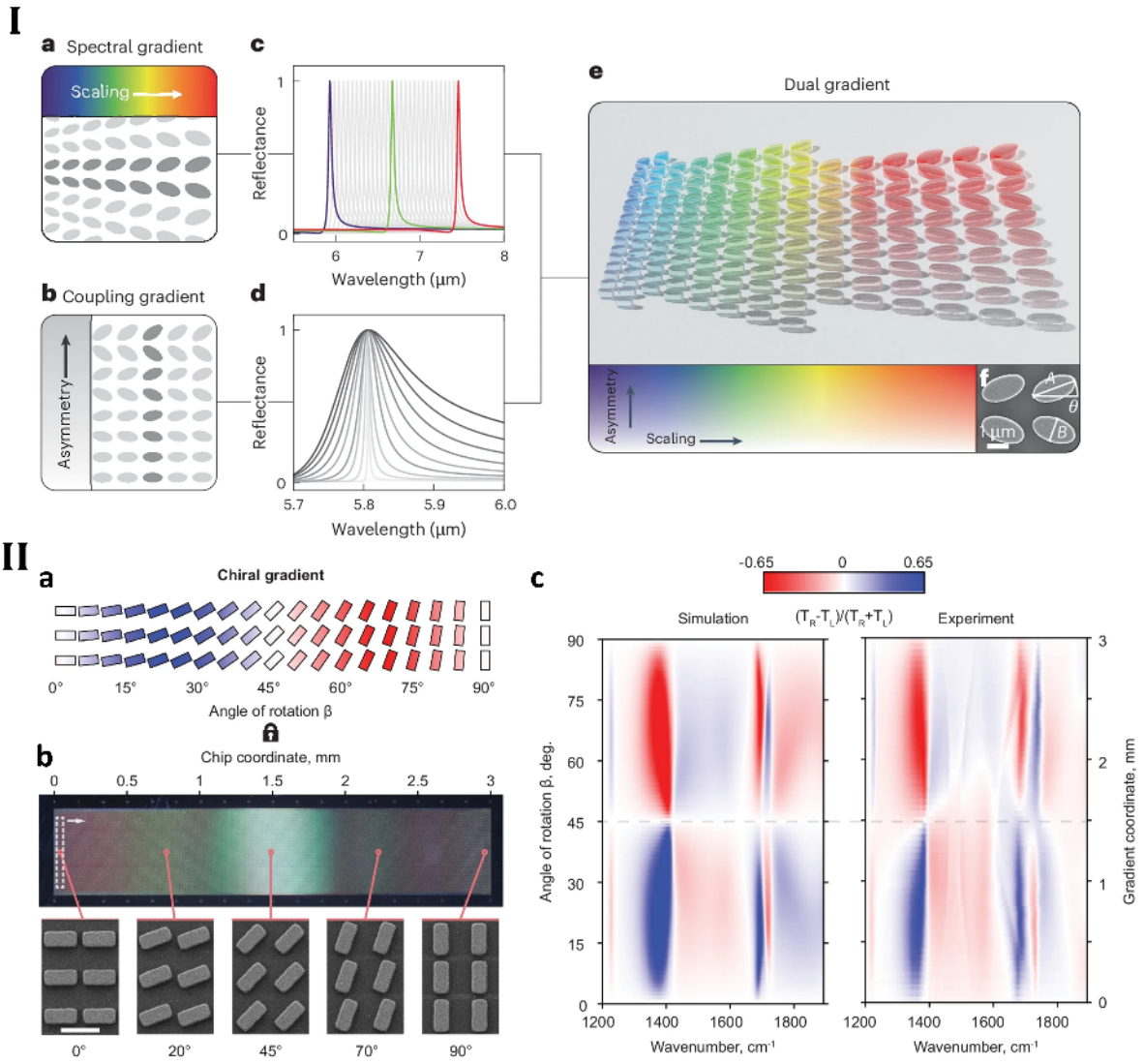

Figure 2-6 Advanced gradient MIR metasurface. (I) Dual gradient q-BIC metasurface. The scaling gradient (corresponds to resonant mode centre wavelength) and coupling gradient (refers to different quality factor) were introduced into the adjacent units in horizontal direction and vertical direction respectively[139]. (II) Chirality gradient metasurface. In a similar configuration to gradient q-BIC metasurface, the chirality gradient can also be introduced through continuously change of rotation angle of nano bricks[142].

A. Leitis *et al.* introduced the concept of dual gradients in spectrum -spatial position encoded q-BIC metasurface. In this design, two systematic parameters varied with gradients[139]. The first is size scaling, as proposed in their earlier work, where a continuous variation in the unit cell sizes along the x-axis (in spatial position) allows tuning of the reflection peak wavenumbers. Beyond this, they introduced a second gradient along the y-axis (in spatial position), referred to as the coupling gradient. In the dimer ellipse structure that supports

symmetry-protected BICs, a slight relative rotation between the ellipses is key to transitioning from a non-radiative state to a radiative state that can couple to free-space radiation. The gradually increasing relative rotation angle led to greater radiative loss and thus lower Q-factors. In theory, the coupling strength gradient corresponds to a continuous variation of the rotation angle. However, in these zig-zag-type BIC structures, a notable characteristic is that changes in the rotation angle also shift the resonance peak wavelength. Therefore, in their practical design, the authors implemented not only angle variations but also a combined tuning of angle and size to achieve spectral alignment. This alignment ensures that the reflection peak wavenumbers of q-BICs with different Q-factors within the same x-position occur at the same wavenumber in spectral response. Together with the size variation along the x-direction, the authors achieved a dual-gradient design enabling continuous variation of both the characteristic peak wavenumbers and the Q-factors. This two-dimensional spatial-spectral encoding effectively enriches the spectral features: it increases the spectral channel density and allows the intuitive mapping of q-BIC modes with different Q-factors on a 2D encoded image. This, in turn, facilitates observation of how resonances with different Q-factors interact with biochemical samples under test. Recently, another report demonstrated a different type of encoding by introducing chirality[142]. As shown in Figure 2-6(II), a continuous variation in the rotation angles of unit nanobricks enables chirality to be encoded into spatial position. The fabricated metasurface covered an area approximately 3 mm in length, with nanobricks in adjacent periods having different rotation angles and thus different chiral responses. Figure 2-6(II)(c) illustrates the relationship between rotation angle and spatial position, as well as experimental results showing the continuous change of chirality across the surface. Collectively, these studies have profoundly inspired research into high-Q infrared metasurfaces.

The zig-zag dimer ellipse structure is inherently polarisation-sensitive and operates under polarised illumination. In contrast, W. Adi *et al.* applied the concept of band folding from photonic crystals to design mid-infrared metasurfaces capable of operating under unpolarised illumination[96]. In their design, a silicon thin film with periodically arranged holes forms a photonic crystal. A perturbation was introduced by varying the hole sizes in adjacent units, effectively modifying the periodicity and folding the structure's first Brillouin zone. As a result, certain forbidden modes with ultra-high Q factors that originally lay below the light cone were folded into the radiation continuum, forming quasi-guided modes. These modes exhibit extremely high Q-factors and very low radiative losses, with the Q-factor inversely proportional to the square of the perturbation magnitude—characteristic of quasi-

BIC behaviour. These band-folding-induced quasi-BIC modes are also referred to as BZF-BICs[143]. A key advantage of this design is its polarisation insensitivity under normal incidence. Additionally, the concept of freestanding BICs was introduced by removing the substrate and using air as a 'virtual substrate' This maximises the refractive index contrast between the resonators and the substrate, thereby enhancing the modulation efficiency of the resonators. The freestanding metasurface design has also been applied to multi-functional infrared sensing[39] and dynamic tuning via photothermal effects[144], demonstrating the promising potential of this approach.

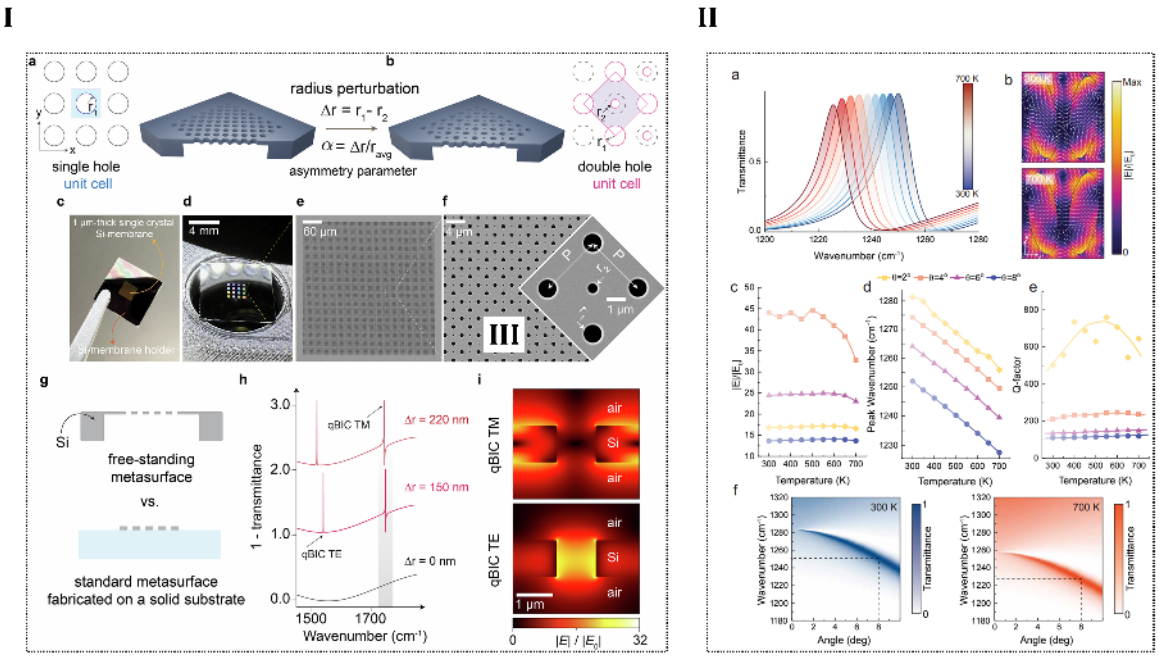

Figure 2-7 Free-standing membrane q-BIC metasurface. (I) Polarisation angle-insensitive (for normal incidence) membrane q-BIC metasurface[96]. (a) and (b) illustrate the design of the unit cells. Asymmetry parameter Δr that refers to the radius difference between adjacent holes was introduced. The period of the structure was therefore changed, correspondingly the first Brillouin zone was folded, forming a q-BIC mode at **Γ** point. (c-f) showed the optical image and SEM image of the proposed structure, respectively. (g) illustrated the concept of freestanding membrane, where no solid substrate was applied. h and i respectively showed the transmission spectrum and near-field E-field enhancement of TE and TM mode q-BIC (II) Tuneable q-BIC metasurface based on thermal expansion of the membrane film[144]. (a), (d), (e) showed the dynamic change of the transmittance peak wavenumber and quality factor in response to temperature change, while (e) and (f) showed the spectrum change with respect to relative rotation angle of the dimer ellipse.

In practice, fabrication errors can significantly affect the Q-factor of q-BICs. J. Kühne *et al.* conducted a detailed comparison of the fabrication tolerance of different dimer unit-cell q-BIC metasurface structures[145]. They found that among the various dimer models shown in

Figure 2-8(I), the zig-zag type demonstrated the best fabrication robustness. This conclusion was based on how the Q-factor degradation depends on fabrication errors. Another study reviewed a series of structures, including both metallic and dielectric materials[36], and complementary shapes such as nanobricks and nanoholes. This work again highlighted the superior performance of zig-zag binary metasurfaces in terms of Q-factor and modulation depth.

Nevertheless, these designs still have a notable limitation: they operate in reflection mode, where the spectral features appear as reflection peaks or transmission dips. With special designs mentioned above[39], it is possible to shift the BIC resonance into the transmission dips of leaky modes, resulting in EIT-like spectral features. However, such designs often introduce sidelobes and lack a clean spectral background, making them difficult to use as filters. Transmission-mode filters have a natural system-level advantage because they can be directly integrated with detectors without the need for complex signal processing. Chapter 5 of this study focuses on addressing this issue — specifically, how to achieve the application of BIC narrowband modes in transmission mode.

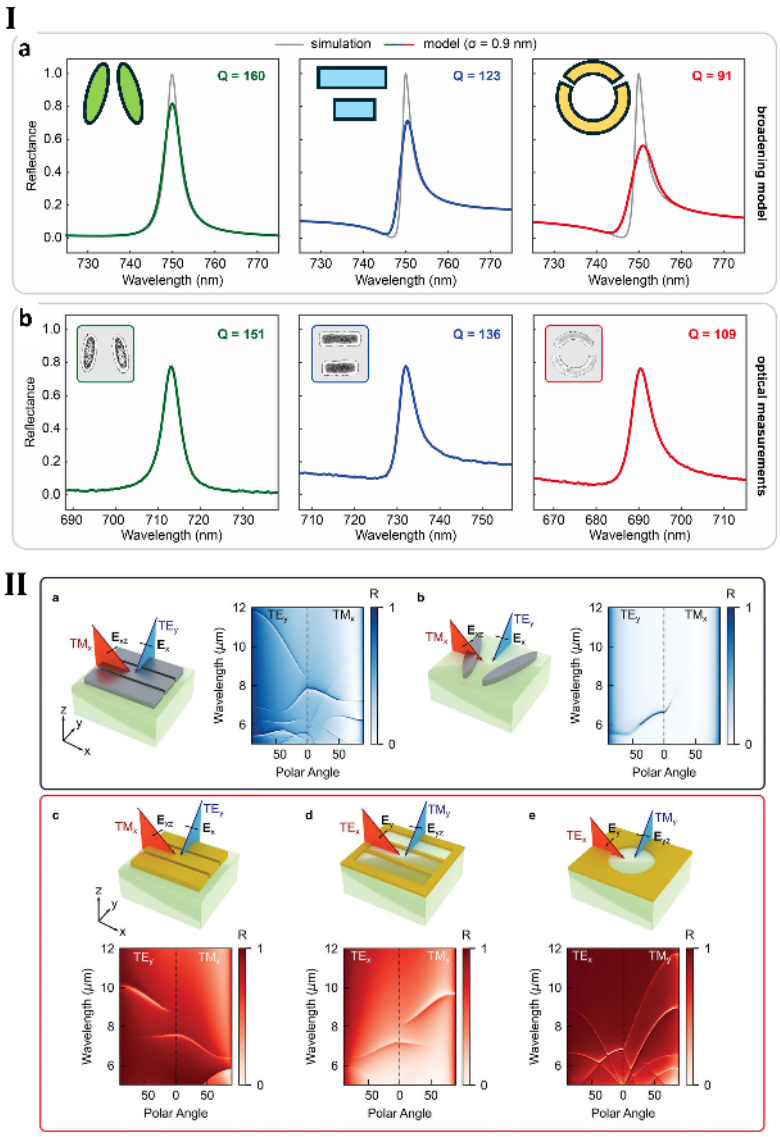

Figure 2-8 Comparison of the spectrum change of different typers of SP-BIC metasurface that indicates the fabrication robustness[145]. The coloured lines indicate the spectrum taking the fabrication error (**σ**) into account. **σ** refers to the symmetry relative error in breaking perturbation parameter. It can be seen that the dimer ellipse has the highest robustness against **σ**, as shown in **a** and **b**. (II) Discussion on the incidence angle sensitivity of different type of q-BIC metasurface[36]. The polar angle resolved spectrum can be seen as a method to evaluate the band structure of the radiative modes. It can be seen that all the structures are incidence angle and polarisation sensitive, while the dimer ellipse shows a clean spectrum with just q-BIC modes.

2.3 Angular dispersion engineering for non-local high-Q metasurface

Although nonlocal metasurfaces, as previously discussed, have shown remarkable performance in infrared sensing in terms of refractive index sensing[94, 146], strong coupling with chemical absorption bonds[39, 147], imaging[39, 115], and so on, most frequency-domain manipulations have only been simulated and validated under normal incidence., most frequency-domain manipulations have only been simulated and validated under normal incidence. In contrast, angular dispersion of the device is often overlooked. In reality, angular dispersion is a critical issue that must be carefully addressed across different application scenarios—particularly in those that require efficient utilisation of optical energy, such as surface-enhanced infrared sensing[39, 148, 149] and experiments involving optical nonlinear components generation enhancement[38, 41, 150, 151] via metasurfaces. In these applications, signal enhancement primarily stems from enhanced interaction between the electromagnetic field and the material. Concentrating the electromagnetic field into a smaller region to maximise the field strength on a macroscopic scale can significantly enhance the signal. For this reason, systems involved in such applications often incorporate focusing optics such as lenses or microscopes to concentrate the light beam onto the metasurface.

However, beam focusing inherently introduces a wide range of oblique incident angles in addition to normal incidence. For nonlocal metasurfaces exhibiting angular dispersion—that is, where the characteristic frequency of the optical structure varies significantly with in-plane momentum $k_{\parallel}$ or different incident angles correspond to different resonance frequencies. This causes the optical energy to spread across multiple modes, rather than being confined within the specifically designed resonance mode intended for material interaction or nonlinear enhancement. To address the issue, there is growing interest in designing flatband photonic structures—structures whose dispersion near the **Γ**-point is nearly flat, implying near-zero group velocity and extremely high density of optical states[152, 153]. Such designs offer a solution to angular dispersion, enabling efficient light-matter interaction across a broad angular range.

Flatband photonic lattices—periodic media with at least one Bloch band exhibiting zero dispersion—have been known since the 1980s[154-156], though their realisation was long hindered by fabrication limitations. In principle, the most direct way to create a flat band is to take the Hamiltonian $H(k)$ of any periodic system, compute its band structure, and divide it by the momentum-dependent energy $E(k)$ of one of the bands to obtain a new Hamiltonian

$H'(k) = H(k)/E(k)$. While the newly constructed Hamiltonian indeed exhibits a perfectly flat band, its real-space counterpart that can be obtained via Fourier transformation, typically involves complex structures, including finely tuned long-range couplings, rendering it impractical for physical implementation.

Recently, the physics community has witnessed a growing number of photonic flatband models based on simple, short-range connectivity. The advancements in nanofabrication have enabled experimental realisation of such precise structures[153, 157, 158]. This has re-motivated the interest in the study of photonic flatband. A 2018 perspective[154] categorised flatband photonic systems into three types based on their origin:

1. Symmetry-protected flatband, associated with local "dark" states that are decoupled from propagating channels.
2. Topologically protected flatband.
3. Accidental flatband, which arise through fine-tuning of system parameters.

The third category—accidental flatband—does not stem from the inherent geometry or topology of the system but rather emerges from precise tuning of parameters such as coupling strengths, external fields, or other variables, resulting in a locally flattened band within part of the Brillouin zone. However, such bands are highly sensitive to parameter variations, and any deviation from optimal values can reintroduce dispersion.

With the rise of advanced nanofabrication techniques, an increasing number of these finely tuned flatband systems are being both theoretically designed and experimentally realised. In general, as the mode volume of optical resonators decreases and the resonances become more localised[159-161], the angular dependence of the resonant modes tends to diminish. However, this localisation also typically increases the number of available radiative channels, thereby lowering the quality factor of the resonance. Thus, the challenge of realising photonic flatband structures that support high-Q resonant modes remains both significant and valuable.

One possible scheme is to merge BICs on a quasi-flat band in order to achieve high Q-factors over a certain range of momentum space[129]. This idea is based on exploiting the topological characteristics of BICs[162-164]. BICs have been confirmed to be polarisation singularities in momentum space, known as eigenmodes of optical systems where the far-field polarisation direction is undefined. As the vortex centres of linearly polarised far fields in momentum

space, BICs carry an integer topological charge $\boldsymbol{q}$. Conservation of topological charge implies that BICs can move within reciprocal space without breaking the system's symmetry. Therefore, by carefully adjusting structural parameters, multiple isolated BICs can be tuned to the same wavevector, thereby constructing merged BICs. H. Chen et al. demonstrated the concept of merging BICs on a low angular dispersion band through simulation[129]. By precisely tuning the period and height of photonic crystal pillars, they brought multiple BICs close together in momentum space, allowing them to merge. As shown in Figure 2-9 I (a), when the period of the photonic crystal *a* equals 1090nm to 1137nm, 5 BICs tends to merge, therefore maintain high Q in specific [$\boldsymbol{kx, ky}$] range. While for a = 1261nm, the BICs are isolated. The high Q-factor characteristic was maintained across a wider region in momentum space as a result. Furthermore, fine-tuning of structural parameters made the merging behaviour take place on a quasi-flat band inherently supported by the system, thereby achieving angle-insensitive peak resonance and high Q-factors over a certain range of incidence angles. Figure 2-8(I) clearly shows the comparison between the merged BIC obtained after structural parameter optimisation and isolated BICs without such optimisation. Under specific choices of the lattice constant-to-height ratio (a/h), the structure exhibits both angle insensitivity within the 0–12° incidence range and high-Q features within a certain momentum range. This kind of parameter tuning involves two-dimensional control of the BICs' positions in momentum space (i.e., merging on a quasi-flat band), which requires nanometre-level precision in both the height and radius. As such, fabrication errors at the nanoscale can significantly shift the BICs from their optimal locations that limits its realisation.

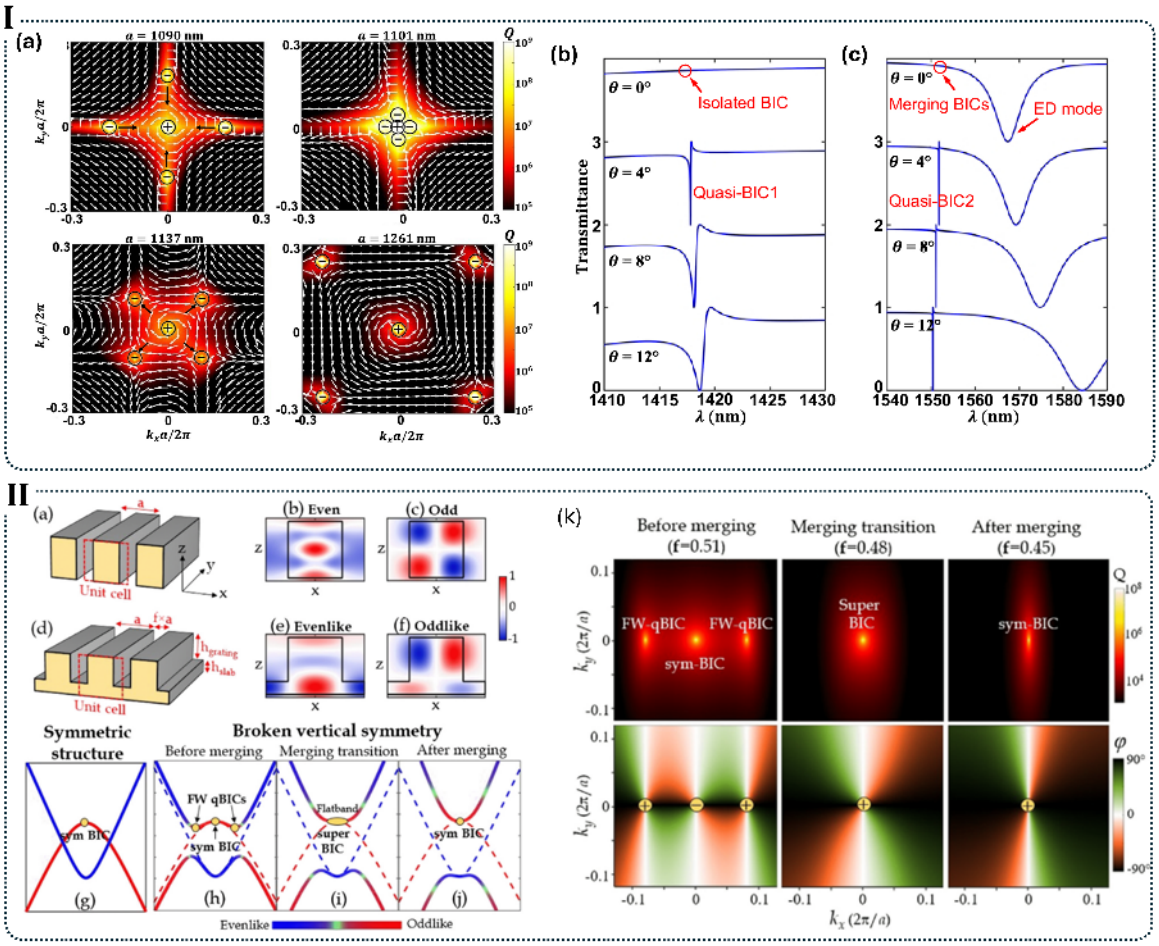

Figure 2-9 Merging multiple BICs to achieve high Q in a specific range in momentum space. (I) (a) showed the merging transitions with different period value a. (b) and (c) demonstrated the simulation results for isolated BIC and merging BICs with different angle of incidence[129]. (II) Comb-like structures for merging BICs and flatband formation[165]. (a) and (d) showed the geometrical differences of a 1D grating and comb-like grating, where a slab was added underneath the grating. The existence of the slab converted the even/odd modes in xz plane into even-like and odd-like modes, thus breaking the vertical symmetry. (g)-(j) showed the effect of vertical symmetry breaking (k) illustrated the forming of merging BIC. With increasing fill factor f, the relative distance in momentum space of the SP-BIC and FW-BIC changed.

N. D. Le recently proposed a structure based on a similar concept, using band engineering and BIC merging to realise ultra-high Q-factors with flatband characteristic[158, 165]. Their theoretical analysis shows that by carefully adjusting geometric parameters—including duty cycle and height—of a one-dimensional amorphous silicon grating on a silicon slab, a symmetry-protected BIC at the *Γ* point and a Friedrich–Wintgen BIC (FW-BIC) away from the **Γ** point can be merged, resulting in high Q-factors over a range of momentum values. This merging process evolves with changes to the geometrical parameters, mainly the fill

factor of the 1D grating, transitioning from isolated BICs, to merged BICs, and finally to various band structures such as multi-valley, flatband, and Dirac-shaped dispersions.

Figure 2-9(II) (g) shows the band diagram of a symmetric grating structure (as illustrated in **II(a)**), which contains two crossing band, indicating no coupling between the two modes. When symmetry-breaking parameters are introduced into the system—specifically, by adding a slab beneath the 1D grating to form a "comb" structure—vertical symmetry is broken; while the fill factor of the binary grating (which effectively defines the relative width and position difference between adjacent grooves) breaks in-plane symmetry. Without these symmetry-breaking perturbations, the blue and red lines corresponding to the TE modes cannot couple due to even–odd mode mismatch. After symmetry breaking is introduced, a bandgap opens because of the anti-crossing of the two bands in the band diagram. The broken vertical symmetry led to the strong coupling between the two odd/even mismatched modes (blue and red curve in (g)). Such strong coupling led to anti-crossing at the two sides and created extra two FW-BICs. By changing the fill factor of the grating, the relative position of the SP-BIC and FW-BIC can be tuned relatively, creating flatband with high Q. The blue and central red segments together form a multi-valley band structure, containing a symmetry-protected BIC at **Γ** point and two FW-BICs at anti-crossing points.

By finely tuning the system parameters, the three BICs move relative to each other in momentum space and form a so-called super BIC region near the **Γ**-point. In this region, high Q-factors and a relatively flat band are simultaneously achieved. Although the structure still relies heavily on fine-tuning, once the multi-valley band structure—close to a flat band—is established through symmetry breaking, the height can be fixed. After that, only minor adjustments to the period are needed to finalise the flatband design. Experimentally, the authors fabricated a series of samples with gradually increasing fill factor, observing multi-valley and Dirac-like dispersions, and identifying the sample corresponding to a flatband structure for experimental measurement. Some structures achieve flat bands by breaking vertical symmetry, such as the fishbone design[158, 166]. However, the comb structure offers a significant advantage in that it is relatively simpler to fabricate. In practical fabrication, the authors employed a very thin layer of silicon dioxide inserted between the grating and the slab as an etch-stop layer. This design and fabrication approach can be extended to other wavelength ranges. Recently, there have been reports of such one-dimensional comb gratings designed for flat bands in the visible spectrum. Using the same

design principle, the authors achieved flatband structures at visible wavelengths by finely tuning the fill factor[167], as shown in Figure 2-10(I).

One possible application of these high-Q flatband structures is to use them as absorbing layers in photodetectors, enabling frequency-selective absorption that is weakly dependent on the angle of incidence[168]. In their work, as shown in Figure 2-10 (II), the authors directly fabricated silicon nitride gratings of approximately 180 nm in height on InGaAs absorbing layers to enhance light absorption. By slightly adjusting the fill factor, they created asymmetric gratings and fine-tuned the band structure, ultimately realising a flatband structure at around 780 nm in the near infrared, with angular tolerance of approximately 18°. This flatband structure enabled the external quantum efficiency (EQE) of the detector to increase from below 25% to above 60%.

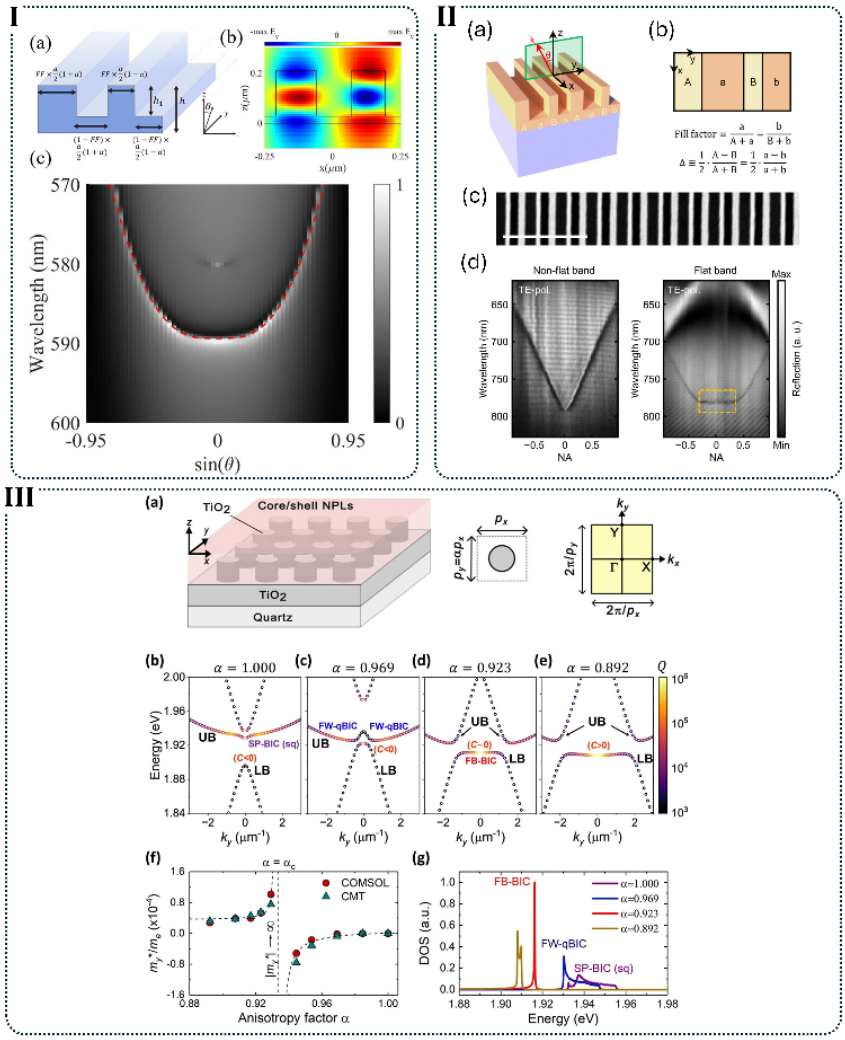

Figure 2-10 (I) Observation of photonic flatband in the visible spectrum. A comb-like structure with asymmetric 1D gratings were made for flatband creation. GaP was used because of its high refractive index and low loss in the visible range. A near-zero group-velocity dispersion and a Q factor of about 750 was

obtained at around 590nm within 10-degree angle of incidence[167]. (II) Comb-like structures for enhanced photon-detection. A similar design of 1D grating on slab, made of a-Si was made to create flatband with high Q characteristic[168]. (d) compared the different angle-resolved reflection spectrum of the two structures. With a flat spectral response, the external quantum efficiency of the device can be largely enhanced. (III) Room temperature lasing assisted by flatband metasurface design[169]. Low-loss $\mathbf{TiO_2}$ nanorods on the slab were used to make the meta-atoms, in which the ratio between y-direction lattice constant and x-direction lattice constant can effectively influence the anti-crossing between the lower-band mode (LB) and upper-band mode (UB) in the band diagram. By carefully design the ratio $\boldsymbol{\alpha}$, flatband BIC (FB-BIC) was obtained. The calculation results (f) and (g), showed the infinite effective mass of the coupled mode, and higher density of the states feature of the designed flatband structure.

In addition to the one-dimensional comb-like structures built on slabs, similar designs can also be constructed using two-dimensional gratings, as shown in Figure 2-10(III). Unlike the duty cycle tuning used in 1D gratings, a recent study demonstrated how adjusting the anisotropy of a square lattice can be used to control the coupling strength between modes, thereby achieving different anti-crossing strengths[169]. This form of band engineering can likewise produce high-Q flatband. Since the coupling strength in the design is determined solely by the ratio of lattice constants in the y- and x-directions, its fabrication may offer improved robustness. The authors applied this design to the realisation of room-temperature lasing. In the work, a rectangular array of TiO_2 nanopillars served as the photonic crystal layer, supporting two intersecting modes. By varying the ratio of the lattice periods along orthogonal directions—defined as $\alpha = Py/Px$ also referred to in the paper as the anisotropy factor—band engineering was achieved. Compared to conventional BIC lasers, this flatband design clearly exhibits higher energy utilisation efficiency and a denser optical density of states. As a result, the authors experimentally achieved a lasing threshold pump power of 295 kW/cm², which is four times lower than that of non-flatband BIC lasers.

Some structures that do not explicitly involve BIC merging have also been reported; these structures mainly used guided-mode resonances or band folding and anti-crossing to realise flatband structures. A recent report demonstrated the realisation of flatband resonances through fine-tuning of the band structure of guided-mode resonances and applied the design into laser generation[170]. The waveguide layer used in the work, including a two-dimensional grating and slab, was made of α-Si. By precisely adjusting geometric parameters such as the lattice constant, radius, and heights of the slab and nanopillars, the band structure changes

shown in Figure 2-11 (I) f–h emerge. These correspond to two low-dispersion bands. As the period Pxincreases, the quasi flatband shift towards lower photon energies points and the low-dispersion features expand over a broader range of momentum space.

K. Sun et al. recently reported a series of binary metasurface structures that realise mode hybridisation and anti-crossing via band folding[171]. Overall, the proposed structures consist of binary nano-disk arrays; notably, their structures do not necessarily involve a slab—the functional layer is only a single planar layer. In-plane lattice doubling perturbations cause the guided mode that originally appeared near the band edge along the $\Gamma - M$ direction to be folded into the first Brillouin zone above the light line along $\Gamma - Y$, becoming a quasi-guided mode. This newly introduced mode exhibits anticrossing with the original mode containing the $\Gamma - \mathrm{BIC}$. Through a combination of lattice perturbation and in-plane symmetry breaking, the strength of the mode coupling responsible for the anti-crossing can be modified, thereby enabling the generation of flatband photonic structures. The authors further applied the design to rainbow free thermal emitter design. In the work shown in Figure 2-11 (II), the authors realised a narrowband mid-infrared thermal emitter with a bandwidth as small as 23 nm. The structure consists of Ge on an Al_2O_3 buffer layer; the thickness of the Ge and Al_2O_3 layers is primarily used to adjust impedance matching, in order to achieve optimal emissivity. Since thermal radiation in this design is non-directional, the flatband design helped to maintain a constant centre wavelength across a wide angular range for energy collection. More recently, this design has been further applied to near-infrared resonant nonlinear enhancement[172].

What has not been widely discovered in the existing reports is how a single-layer structure can simultaneously achieve high Q factors across the entire band and enable flat-band engineering. Chapter 6 of this thesis proposed a novel flat-band design scheme and demonstrates its key performance.

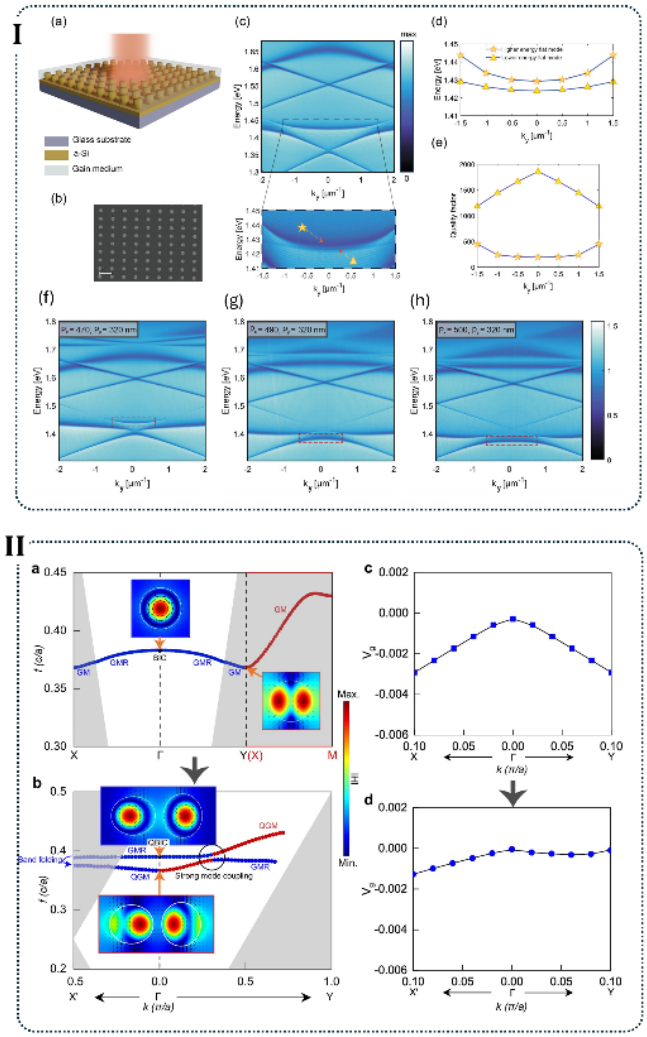

Figure 2-11 (I) Flatband photonic structures for low threshold lasing[170]. Periodic α-Si nanorods were fabricated on top of silicon slab, two quasi flatband modes were observed, as shown in (c) red-dashed rectangle part and inset. The Q factors of the two modes are shown in (d) and (e). (II) Rainbow-free thermal emitter formed by band-folding and anti-crossing[171]. (a) illustrates the band structure of a single-disk array, where a quasi-guide mode that contains a symmetry protected BIC at **Γ** point was the band to be engineered. By symmetry breaking and relative moving closer, which effectively doubled the lattice constant, the band that represented the guide mode in **X** − **M** path was folded into **Γ** − **Y** path, and the strong coupling happened between the folded GM (forming new QGM in **Γ** − **Y** path) and the original QGM containing BIC. By precisely changing the coupling strength, the lower group velocity dispersion can be obtained compared to original GVD, as shown in (c) and (d).

Chapter 3 Methodology: Fabrication, Simulation and Characterisation

In this chapter, the main methods and software used in the key stages of metasurface research—simulation, fabrication, and characterisation—will be introduced.

3.1 Metasurface Research Workflow

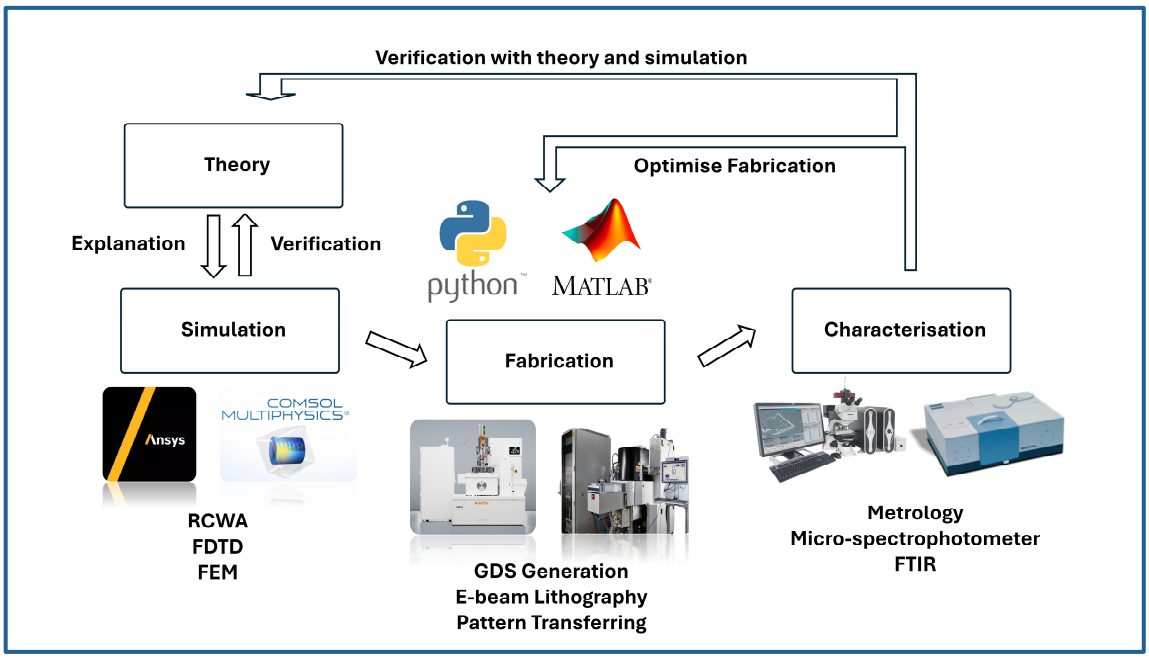

Figure 3-1 Schematic workflow of metasurface research workflow.

The research process for metasurfaces can be categorised into the conceptual flowchart shown in Figure 3-1, including theoretical analysis, simulation, fabrication, and characterisation. Simulation of metasurfaces primarily relies on commercial software platforms such as Ansys Lumerical and COMSOL Multiphysics, which help conduct semi-analytical or numerical calculations. The calculations of electromagnetic-response are based on the rigorous coupled-wave analysis (RCWA) method, Finite-Difference Time-Domain (FDTD) and Finite Element Method (FEM). These commercial software platforms and calculation methods offer highly integrated, multifunctional simulation capabilities and provide user-friendly computer-resource management interfaces and a large community of users, making them more accessible than custom-coded simulations.

The fabrication of the metasurface micro/nanostructures discussed in this work mainly depends on electron beam lithography (EBL) and subsequent physical or chemical etching techniques to transfer the designed patterns onto the functional metasurface layers.

Finally, the fabricated metasurfaces are inspected using various microscopy tools, including optical microscopes and scanning electron microscopes (SEMs). The spectral responses of the metasurface studied are mainly tested using microspectrophotometers and Fourier transform infrared spectrometers (FTIR).

3.2 Simulation Based on Lumerical/COMSOL

As mentioned earlier, nonlocal metasurfaces primarily focus on periodic structures and the resonant effects arising from collective responses. Simulations of these periodic structures will mainly use RCWA, FDTD, and FEM methods. These numerical and simulation approaches are already integrated into commercial software.

Both Lumerical and COMSOL have large user communities and extensive tutorial resources, and a wide range of simulation settings are already integrated into their GUIs. Users can, for example, rely on parallel viewports to inspect the construction of the geometry, the resulting mesh discretisation, and the planning/allocation of computational resources (for Lumerical FDTD only) in a more interactive manner. This is particularly important for beginners, and it represents a key advantage of these commercial packages over some open-source codes available online, such as MEEP. However, it is also undoubtful that free, open-source frameworks such as MEEP and Legume have made tremendous contributions to the field.

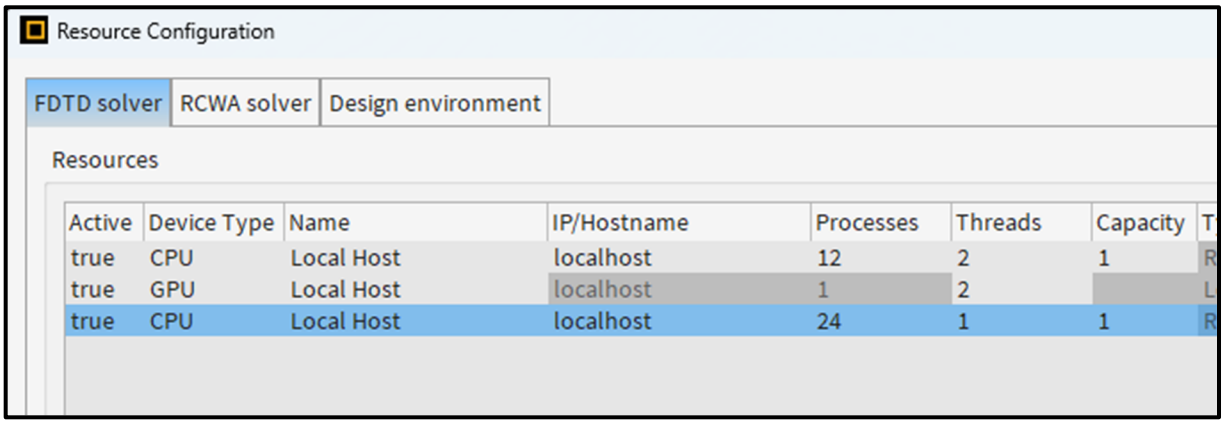

Figure 3-2 Screenshot of computational resources management user interface in Ansys Lumerical software. One can customise and optimise the environmental configuration to improve the simulation efficiency.

In this section, the basic principles of RCWA, FDTD, and FEM, as well as the user interfaces (GUI) of Lumerical and COMSOL, will be thoroughly discussed. While explaining the principles, the software interfaces will be correspondingly introduced, highlighting the key simulation settings and their theoretical underpinnings, helping readers gain a deep understanding of what simulation parameters to focus on and underlying reasons.

Finally, a comparison of the advantages and disadvantages of these three simulation methods across different scenarios will be presented, outlining the application contexts best suited to each method.

3.2.1 RCWA

3.2.1.1 Overview of RCWA

RCWA is an algorithm designed for solving periodic electromagnetic field problems. It is primarily used in the analysis of diffraction characteristics in various periodic structures, such as gratings and metasurfaces[173-176]. RCWA is particularly well-suited for studying polarisation-dependent transmission in dielectric metasurfaces, because—unlike FDTD and FEM methods discussed later—it provides an analytical solution, offering superior speed and accuracy.

In the RCWA method, the electromagnetic fields are expanded into spatial harmonics (i.e., Fourier series), which is why RCWA is also referred to as the Fourier Modal Method (FMM). Although each discrete spatial harmonic does not individually satisfy the wave equation, their superposition does.

The typical RCWA procedure consists of three steps:

I. Fourier expansion of the permittivity and permeability of the structure.

II. Plane wave expansion of the incident, transmitted, and grating (metasurface) regions. The expansion in the grating region is substituted into Maxwell's equations, leading to a set of coupled wave eigenvalue equations to be solved.

III. Applying tangential boundary conditions of the electromagnetic fields to derive the scattering matrix, from which diffraction characteristics such as reflectance, transmittance, field distribution, and diffraction efficiencies can be obtained.

By utilising the RCWA module in Ansys Lumerical, one can efficiently compute transmission, reflection, and phase shifts of metasurfaces.

3.2.1.1 Derivation of RCWA

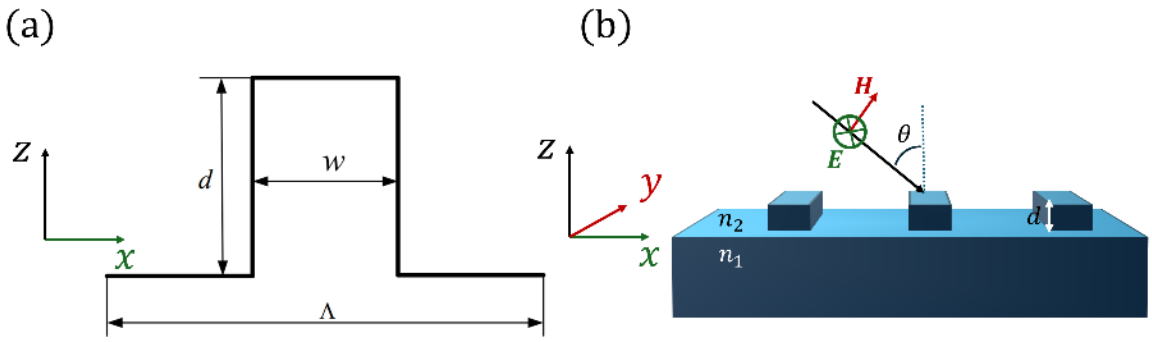

Figure 3-3 (a) definition of 1D rectangular grating. (b) illustration of the incidence angle and parameter definition.

In this section, the steps described in 3.2.1.1 are followed to derive the reflection and transmission coefficients using the RCWA method considering diffraction for a one-dimensional rectangular grating, as shown in in Fig 3.3(a). An arbitrary light beam incident on the grating surface, as illustrated in Fig. 3.3(b), will be used as an example to illustrate the RCWA derivation. The calculation of metasurface is the 2D extension of 1D example[174, 177]. The parameters are defined as follows:

$\boldsymbol{\Lambda}$ **:** grating period, $\boldsymbol{d}$**:** groove depth, $\boldsymbol{f}$**:** duty cycle, **X-axis:** perpendicular to the grating lines, **Y-axis:** along the grating lines, **Z-axis:** normal to the grating surface, $\boldsymbol{\theta}$**:** angle between the incident beam and the Z-axis.

The entire space is divided into three regions: Incident/Reflected region, grating region, and transmitted region. The refractive indices of the incident/reflected and transmitted regions are denoted as $\boldsymbol{n_1}$ and $\boldsymbol{n_2}$, respectively. The grating region consists of a periodic distribution of dielectrics with refractive indices $\boldsymbol{n_1}$ and $\boldsymbol{n_2}$.

In typical grating systems, the incident beam can have two types of polarisations: TE (Transverse Electric) and TM (Transverse Magnetic). In this context, TE polarisation is defined as the case where the electric field component of the incident wave is perpendicular to the plane of incidence. The following derivation focuses on the RCWA formulation for a TE-polarised incident wave interacting with a 1D rectangular grating.

The two media with refractive indices $\boldsymbol{n_1}$ and $\boldsymbol{n_2}$are periodically distributed in the grating region, and their relative permittivity $\boldsymbol{\varepsilon(x)}$ can be expanded into a Fourier series as:

$$\varepsilon(x) = \sum_{h=-\infty}^{\infty} \varepsilon_h \exp\left(j\frac{2\pi}{\Lambda}hx\right) \tag{3.1}$$

The expansion coefficient $\boldsymbol{\varepsilon_h}$ is:

$$\varepsilon_h = \frac{1}{\Lambda}\int_0^{\Lambda} \varepsilon(x) \exp\left(-j\frac{2\pi}{\Lambda}hx\right) dx \tag{3.2}$$

In the incident region, the normalised electric field vector can be expressed as:

$$E_{\text{inc}} = \exp[-jk_0 n_1(\sin\theta x + \cos\theta z)] \tag{3.3}$$

In the equation, $k_0 = \frac{2\pi}{\lambda_0}$ is the wave vector of the incident light, and λ_0 is the wavelength of the incident light.

The electric field vectors in the reflection and transmission regions are expressed respectively as:

$$E_{1,y} = E_{\text{inc}} + \sum_i R_i \exp\left[-j\left(k_{x_i}x + k_{1,z_i}z\right)\right] \tag{3.4}$$

$$E_{2,y} = \sum_i T_i \exp\left\{-j\left[k_{x_i}x + k_{2,z_i}(z-d)\right]\right\} \tag{3.5}$$

In the equations, $\boldsymbol{R_i}$ and $\boldsymbol{T_i}$ represent the normalised amplitude of the $i-th$ order reflected and transmitted electromagnetic fields, respectively.

According to Floquet's theorem, k_{x_i} and $k_{L,zi}$ are given by the following expressions:

$$k_{x_i} = -k_0 n_1 \sin\theta - i\frac{2\pi}{\Lambda} \tag{3.6}$$

$$k_{L,zi} = \begin{cases} k_{l,z_i} = +\left(k_0^2 n_l^2 - k_{x_i}^2\right)^{1/2}, & k_{x_i}^2 \le k_0^2 n_l^2 \\ k_{l,z_i} = -\left(k_{x_i}^2 - k_0^2 n_l^2\right)^{1/2}, & k_{x_i}^2 > k_0^2 n_l^2 \end{cases} ;\ L = 1,2 \tag{3.7}$$

When the incident light is TE-polarised, the electromagnetic field vectors in all regions have only the electric field in the Y-direction and magnetic fields in the X and Z directions being non-zero, while all other components are zero. Under these conditions, Maxwell's equations can be simplified as follows:

$$\frac{\partial E_{gy}}{\partial z} = j\omega\mu_0 H_{gx} \tag{3.8}$$

$$\frac{\partial H_{gx}}{\partial z} = j\omega\varepsilon_0\varepsilon(x)E_{gy} + \frac{\partial H_{gz}}{\partial x} \tag{3.9}$$

$$\frac{\partial E_{gy}}{\partial z} = -j\omega\mu_0 H_{gz} \tag{3.10}$$

Here, the subscript g denotes the grating region. In the grating region, the electric field in the Y-direction and the magnetic field in the X-direction are expanded into Fourier series and expressed in the form of spatial harmonic fields as follows:

$$E_{gy} = \sum_i S_{y_i}(z)\exp\left(-jk_{x_i}x\right) \tag{3.11}$$

$$H_{gx} = \left(\frac{\varepsilon_0}{\mu_0}\right)^{1/2}\sum_l U_{x_i}(z)\exp\left(-jk_{x_i}x\right) \tag{3.12}$$

In the equations, $\boldsymbol{\varepsilon_0}$ is the vacuum permittivity, $\boldsymbol{\mu_0}$ is the vacuum permeability, $\boldsymbol{S_{yi}(z)}$ is the amplitude of the $i-th$ order electric field component in the Y-direction, and $\boldsymbol{U_{x_i}(z)}$ is the amplitude of the $i-th$ order magnetic field component in the X-direction.

By substituting equations 3.11 and 3.12 into Maxwell's equations 3.8, 3.9, and 3.10 and simplifying, the coupled-wave equations can be obtained:

$$\frac{\partial S_{y_i}(z)}{\partial z} = k_0 U_{x_i}(z) \tag{3.13}$$

$$\frac{\partial U_{x_i}(z)}{\partial z} = \left(\frac{k_{x_i}^2}{k_0} - k_0\right)S_{y_i}(z) - k_0\sum_p \varepsilon_h{}^p S_{y_i-p}(z) \tag{3.14}$$

Equations 3.13 and 3.14 can be simplified and expressed in the following matrix form:

$$\begin{bmatrix}\partial S_{y_i}(z)/\partial z \\ \partial U_{x_i}(z)/\partial z\end{bmatrix} = \begin{bmatrix}0 & k_0 I \\ A/k_0 & 0\end{bmatrix} \tag{3.15}$$

By differentiating both sides of Equation 3.13 with respect to z, the term $U_{x_i}(z)$ can be eliminated, simplifying the equation to:

$$\frac{\partial^2 S_{y_i}(z)}{\partial z^2} = AS_{y_i}(z) \tag{3.16}$$

In the equation 3.15, $\boldsymbol{A} = \boldsymbol{K_x^2} - \boldsymbol{K_0^2 E}$. I is the identity matrix, and E is the Toeplitz matrix composed of the dielectric Fourier coefficients ε_h. K_x is the diagonal matrix composed of k_{xi}, defined as: $K_x = \mathrm{diag}\left(k_{x,-N}, \ldots, k_{x,0}, \ldots, k_{x,N}\right)$

The dimensions of the above matrices are all $n \times n$, where n is the number of Fourier expansion orders. By applying the eigenvalue method to solve the coefficient matrix $\boldsymbol{A}$on the right-hand side of Equation 3.16, the formal solution $\boldsymbol{S_y}$ can be expressed using its eigenvalues and eigenvectors as:

$$S_{y_i}(z) = \sum_{m=1}^{n} w_{i,m}\{c_m^+ \exp[q_m(z-d)] + c_m^- \exp(-q_m z)\} \tag{3.17}$$

In the equation, $\boldsymbol{q_m}$ is the positive square root of the eigenvalue of matrix $\boldsymbol{A}$, $\boldsymbol{w_{i,m}}$ is the corresponding eigenvector, and $\boldsymbol{c_m^{\pm}}$ are undetermined coefficients.

By differentiating both sides of Equation 3.17 with respect to z, and using Equation 3.13, one can obtain:

$$U_{x_i}(z) = \frac{1}{k_0}\sum_{m=1}^{n} w_{i,m}\{q_m c_m^+ \exp[q_m(z-d)] - q_m c_m^- \exp(-q_m z)\} \tag{3.18}$$

For convenience, Equations 3.17 and 3.18 are expressed in a simplified form as follows:

$$S_y = WX^{z-d}C^+ + WX^{-z}C^- \tag{3.19}$$

$$U_x = \frac{1}{k_0}WQX^{z-d}C^+ - \frac{1}{k_0}WQX^{-z}C^- \tag{3.20}$$

Where $\boldsymbol{W}$ is the eigenvector matrix of matrix $\boldsymbol{A}$, $\boldsymbol{Q}$ is a diagonal matrix whose diagonal elements are the positive square roots of the eigenvalues of $\boldsymbol{A}$, and $\boldsymbol{X}$ is a diagonal matrix whose diagonal elements are the exponential functions appearing in Equations 3.17 and 3.18.

At the interfaces between the incident, the grating region and the transmission region, the boundary conditions must be satisfied. By solving the set of boundary condition equations, the reflection coefficient $\boldsymbol{R}$ and transmission coefficient $\boldsymbol{T}$ can be obtained.

At the boundary between the incident/reflection region and the grating region, i.e., at $Z = 0$, the boundary conditions are:

$$\begin{cases} \delta_{i_0} + R = WX^{-d}C^{+} + WC^{-} \\ jk_0\delta_{i_0}\cos\theta + jK_{1,z}R = WQC^{-} - WQX^{-d}C^{+} \end{cases} \tag{3.21}$$

Similarly, at the boundary between the grating region and the transmission region, i.e., at $Z = d$, the boundary conditions are:

$$\begin{cases} WC^{+} + WX^{-d}C^{-} = T \\ WQX^{-d}C^{-} - WQC^{+} = jK_{2,z}T \end{cases} \tag{3.22}$$

The four sets of equations in Equations 3.21 and 3.22 are used to solve four unknown parameters: $\boldsymbol{R}, \boldsymbol{T}, \boldsymbol{C}^{+}$ and $\boldsymbol{C}^{-}$. From this, the reflection coefficient $\boldsymbol{R}$ and transmission coefficient $\boldsymbol{T}$ can be obtained. Finally, the diffraction efficiencies for each order under TE polarisation for the rectangular grating are calculated using the definitions given in Equations 3.23 and 3.24:

$$DE_{r_i} = R_i R_i^{*}\,\mathrm{Re}\left(\frac{k_{1,z_i}}{k_1\cos\theta}\right) \tag{3.23}$$

$$DE_{t_i} = T_i T_i^{*}\,\mathrm{Re}\left(\frac{k_{2,z_i}}{k_1\cos\theta}\right) \tag{3.24}$$

TM incidence will be similar to TE incidence, and 2D gratings (which is the case for metasurfaces) can be calculated using a similar process but modifying Equations 3.1-3.5 into two dimensions. The next section shows how using Ansys Lumerical can greatly simplify the calculation of reflection and transmission coefficients.

3.2.1.2 Ansys Lumerical RCWA Setup

In this research, the RCWA calculations are performed using the Ansys Lumerical platform. In the software setup, aside from defining the geometric structure of the metasurface, the following key aspects of the RCWA algorithm need to be specified:

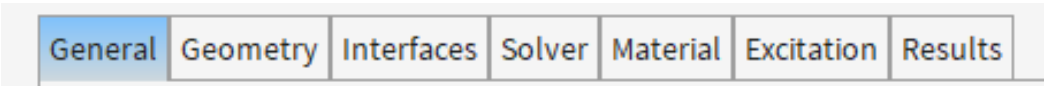

Figure 3-4. Screenshot of User-interface tabs for RCWA definition in Ansys Lumerical.

The **General** tab primarily involves the definition of the incident direction and the background refractive index, as shown in Figure 3-5(a). This corresponds to the definition of the XYZ axes, and the background refractive index described in Section 2.1.1.

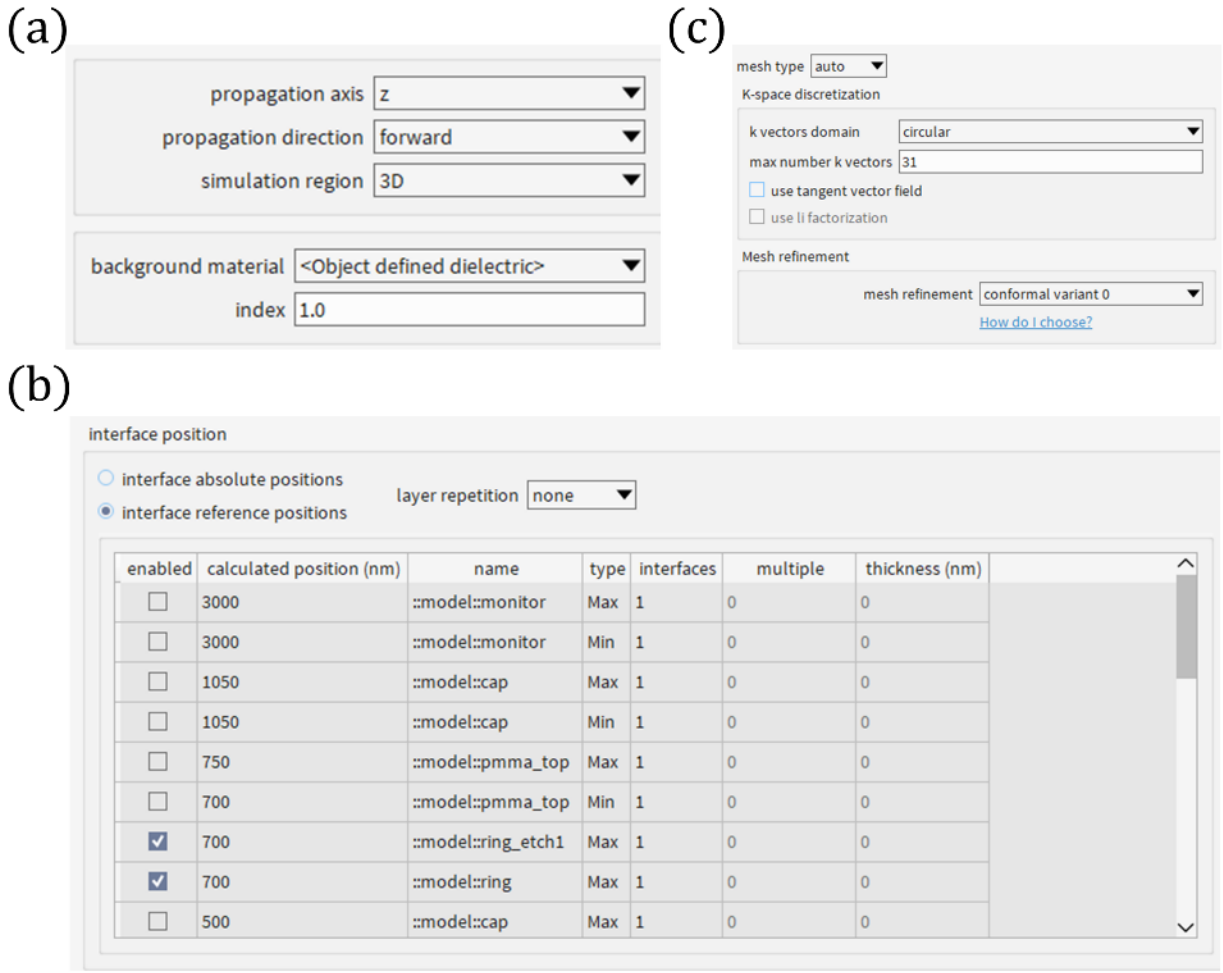

Figure 3-5 Screenshot of RCWA configuration. (a) General settings. (b) Interfaces Settings. (c) Solver settings.

The **Interfaces** (Figure 3-5(b)) and **Solver** (Figure 3-5(c)) tabs, which are closely related to the Fourier expansion, also need to be defined. The **Interfaces** correspond to the boundaries between different regions as described in Section 2.1.0 and 2.1.1. These interfaces are the locations where boundary conditions are applied, as explained in Section 2.1.1, enabling the continuous calculation of the transfer matrix across multiple layers. In general, an interface should always be inserted between any two layers with different refractive indices. In the **Solver** settings, two aspects are defined. On one hand, the in-plane mesh size is set, which corresponds to the discretisation of the metasurface's in-plane geometry. On the other hand, the K vectors domain shape refers to the shape of the sampling grid in reciprocal space. It determines how the in-plane wavevector components (k_x , k_y) are arranged and how many diffraction orders are considered during the simulation. This setting controls how the spatial harmonics (Fourier modes) are selected and organised. It corresponds to the k -vectors in the x and y directions discussed in Section 2.1.1 and directly affects both the simulation accuracy and computational cost. Generally, for structures with low spatial anisotropy, the

circular domain is most commonly used and tends to converge the fastest. The maximum number refers to the total number of spatial harmonics (diffraction orders) used in the Fourier expansion, corresponding to the harmonic number n in Section 2.1.1.

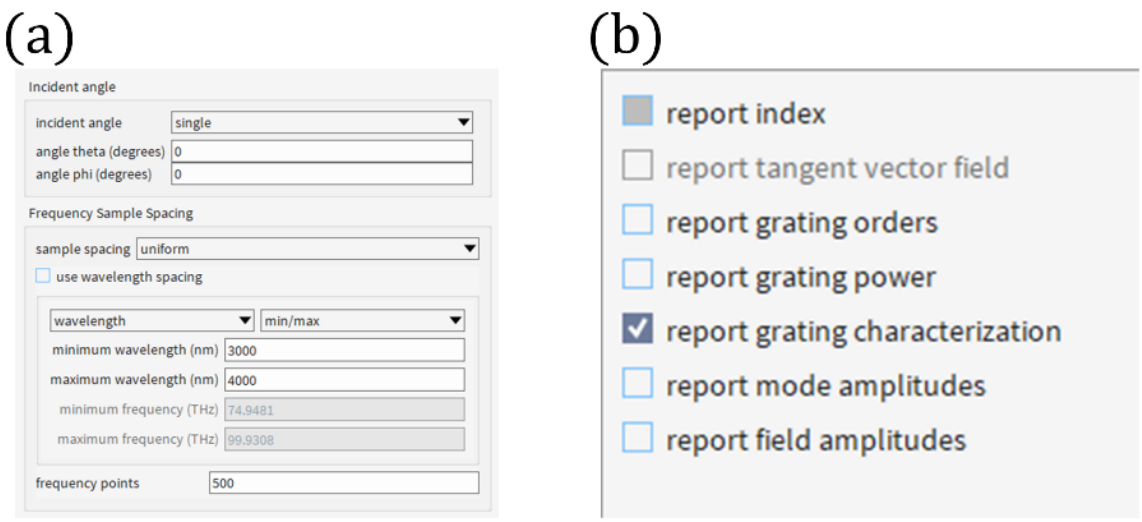

Figure 3-6. Screenshot of RCWA source/results configuration. (a) Excitation source definition settings. (b) Results to be recorded settings.

Finally, it is necessary to define the **incident angle** and **azimuthal angle** of the incoming wave as shown in Figure 3-6. Although the azimuthal angle was not considered in the earlier derivations, it only introduces an azimuth-dependent correction in the calculation. By setting both the incident angle and azimuthal angle, it is possible to simulate complex TE/TM definitions under oblique incidence.

The **Frequency Sampling Spacing and Range** determine the frequency range and resolution of the simulation. After the RCWA calculation, the variables shown in Figure 3-6(b) can be selectively recorded. Generally, the main focus is on:

Grating Power: related to total energy, used for calculating transmission and reflection coefficients.

Grating Characterisation: includes detailed transmission matrix data, such as the amplitude and phase of both co-polarisation and cross-polarisation components in transmission and reflection.

3.2.2 Finite-Difference-Time-Domain (FDTD) method

3.2.2.1 Overview of FDTD

The key advantage of FDTD method lies in its time-domain nature that enables broadband electromagnetic response analysis through a single simulation. This makes it well-suited for scenarios such as nonlinear response enhancement, and other applications requiring broadband spectral characterisation of metasurfaces. FDTD method was first proposed by K. S. Yee in 1966[178]. The idea of FDTD method is to discretise the differential form of Maxwell's equations using finite differences, applying a central difference scheme to represent the first-order partial derivatives of electric/magnetic field quantities in space and time. By discretising the continuous spatial and temporal domains into a meshed grid and incorporating proper boundary conditions, FDTD method transforms the continuous electromagnetic problem into a discrete difference equation solving problem, enabling numerical simulation and computation of electromagnetic fields[179, 180].

The successful implementation of the FDTD method depends on three key aspects, which will be introduced in this section:

I. Finite-difference Discretisation: This refers to the choice of finite-difference expressions for both the spatial and temporal derivatives in Maxwell's equations, which forms the foundation of the numerical model.

II. Numerical Stability: It is crucial to ensure that the selected time and space steps meet stability conditions to avoid inaccuracies or numerical instability in the simulation results. In software platform, various parameters in FDTD simulation settings

III. Boundary Conditions: This involves handling the simulation domain boundaries in a way that allows electromagnetic waves to reflect and propagate correctly within the domain, while minimizing unwanted reflections and edge effects.

These three components are fundamental to the FDTD method and play a vital role in the accurate and efficient simulation of electromagnetic fields. The following section will briefly introduce each of these aspects.

3.2.2.2 Finite-difference Discretisation

For a non-magnetic, isotropic medium, the curl forms of Maxwell's equations are:

$$\nabla \times \boldsymbol{E} = -\mu_0 \frac{\partial \boldsymbol{H}}{\partial t} \tag{3.25}$$

$$\nabla \times \boldsymbol{H} = \varepsilon \frac{\partial \boldsymbol{E}}{\partial t} + \boldsymbol{J} \tag{3.26}$$

Where $\boldsymbol{H}$ refers to magnetic field vector, $\boldsymbol{E}$ is electric field vector, $\boldsymbol{\varepsilon}$ is permittivity of the medium, μ_0 refers to permeability of free space (here non-magnetic medium is discussed), $\boldsymbol{J} = \sigma \boldsymbol{E}$ refers to electric current density vector, and σ is electrical conductivity.

In broadband FDTD simulations, material dispersion $\varepsilon(\lambda)$ is an issue that requires particular attention. In Lumerical, dispersion is handled using a so-called *multi-coefficient model* fitting approach, in which frequency-domain data of ε are converted into a time-domain response that can be evaluated recursively. Although Lumerical does not explicitly disclose the underlying algorithm (as a commercial proprietary implementation), it is widely recognised that incorporating dispersion introduces additional computational overhead [181].

Consequently, for materials that exhibit very weak dispersion across the simulated band (e.g., refractive-index variations below ~0.1), the polynomial fitting—under Lumerical's default tolerance—often converges towards an effectively constant response anyway. For this reason, much of the literature adopts a constant refractive index for low-dispersion materials within the band of interest as a more efficient and sufficiently accurate approximation; examples include silica in the visible (RI $\approx$ 1.46) and CaF_2 in the mid-infrared (RI $\approx$ 1.4).

In Cartesian coordinates, equations (3.25) and (3.26) can be rewritten into Faraday's Law form:

$$\begin{cases} \dfrac{\partial E_x}{\partial y} - \dfrac{\partial E_y}{\partial x} = -\mu_0 \dfrac{\partial H_z}{\partial t} \\ \dfrac{\partial E_y}{\partial z} - \dfrac{\partial E_z}{\partial y} = -\mu_0 \dfrac{\partial H_x}{\partial t} \\ \dfrac{\partial E_z}{\partial x} - \dfrac{\partial E_x}{\partial z} = -\mu_0 \dfrac{\partial H_y}{\partial t} \end{cases} \tag{3.27}$$

And Ampère–Maxwell Law form:

$$\begin{cases} \dfrac{\partial H_x}{\partial y} - \dfrac{\partial H_y}{\partial x} = \varepsilon \dfrac{\partial E_z}{\partial t} + \sigma E_z \\ \dfrac{\partial H_y}{\partial z} - \dfrac{\partial H_z}{\partial y} = \varepsilon \dfrac{\partial E_x}{\partial t} + \sigma E_x \\ \dfrac{\partial H_z}{\partial x} - \dfrac{\partial H_x}{\partial z} = \varepsilon \dfrac{\partial E_y}{\partial t} + \sigma E_y \end{cases} \tag{3.28}$$

Next, equations (3.27) and (3.28) are discretised using finite-difference methods. For any point (x, y, z) in a Cartesian coordinate system, within an infinitesimally small region centred at that point, the electric and magnetic fields can be considered approximately constant. Let $u\ (x, y, z, t)$ represent a specific component of either E or H, after discretising in both time and space domains, $u\ (x, y, z, t)$ can be expressed as:

$$u(x, y, z, t) = u(i\ \Delta x, j\ \Delta y, k\ \Delta z, n\ \Delta t) = u^{n(i,j,k)} \tag{3.29}$$

Where i, j, k are indices in the x, y, z directions respectively, n is the time step index, $\Delta x, \Delta y, \Delta z$, are the spatial step sizes, Δt is the temporal step size, $u^{n(i,j,k)}$ represents the value of the field component at grid point (i, j, k) at time step n. The finite-difference expressions for the first-order partial derivatives with respect to space and time can be written as follows:

$$\left.\frac{\partial u}{\partial t}\right|_{i,j,k}^{n} \approx \frac{u^{n+1}(i,j,k) - u^{n-1}(i,j,k)}{2\Delta t} \tag{3.30}$$

$$\begin{cases} \left.\dfrac{\partial u}{\partial x}\right|_{i,j,k}^{n} \approx \dfrac{u^{n}(i+1,j,k) - u^{n}(i-1,j,k)}{2\Delta x} \\ \left.\dfrac{\partial u}{\partial y}\right|_{i,j,k}^{n} \approx \dfrac{u^{n}(i,j+1,k) - u^{n}(i,j-1,k)}{2\Delta y} \\ \left.\dfrac{\partial u}{\partial z}\right|_{i,j,k}^{n} \approx \dfrac{u^{n}(i,j,k+1) - u^{n}(i,j,k-1)}{2\Delta z} \end{cases} \tag{3.31}$$

Figure 3-7 illustrates the spatial distribution of electric and magnetic field components after FDTD discretisation, commonly referred to as the Yee cell. In this structure, each electric/magnetic field component is surrounded by four corresponding magnetic (or electric) field components. The electric field components $\boldsymbol{E_x, E_y, E_z}$ are positioned along the edges of the cell, while the magnetic field components $\boldsymbol{H_x, H_y, H_z}$ are located at the centres of the corresponding faces. Each field component is staggered in space by half a grid step relative to the others, enabling accurate coupling through Maxwell's curl equations..

By sampling the electric and magnetic fields at staggered intervals—specifically offset by half a time step—and substituting these samples into Maxwell's curl equations, a set of explicit finite-difference equations can be derived. These equations enable time-domain iterative solving of the electromagnetic fields. Using the known values of the electric or magnetic field at the previous time step, the corresponding magnetic or electric field at the next time step can be calculated. This spatial sampling strategy for field components not

only facilitates accurate finite-difference solutions of Maxwell's equations, but also effectively preserves the physical characteristics of electromagnetic wave propagation.

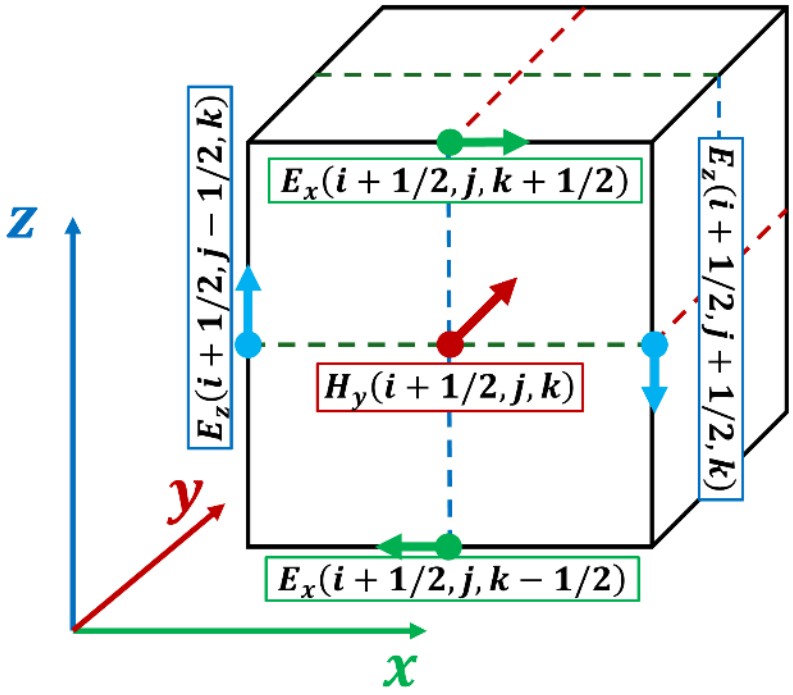

Figure 3-7 Spatial distribution of electric $\boldsymbol{E}$ and magnetic $\boldsymbol{H}$ field components in a Yee cell used in FDTD.

Figure 3-7 illustrates the Yee cell and visualises the update process of the electromagnetic fields. The Yee cell achieves this by spatially staggering the components of $\boldsymbol{E}$ and $\boldsymbol{H}$. The FDTD method updates the fields in a time-staggered order—first updating the magnetic field based on the known electric field, and then updating the electric field based on the updated magnetic field. Each component update uses the surrounding circulating field values, based on the discretised form of the curl equations. Given the initial fields and boundary conditions, the propagation of electromagnetic waves can be computed step-by-step in time domain. For example, the update of $\boldsymbol{H_x}$ can be derived from equations (3.30)– (3.31) as follows:

$$H_x^{n+\frac{1}{2}}(i+1/2,j,k)$$

$$= H_x^{n-\frac{1}{2}}(i+1/2,j,k) - \frac{\Delta t}{\mu_0}\left(\frac{E_z^n(i+1/2,j+1,k) - E_z^n(i+1/2,j,k)}{\Delta y}\right.$$

$$\left. - \frac{E_y^n(i+1/2,j,k+1) - E_y^n(i+1/2,j,k)}{\Delta z}\right) \qquad (3.32)$$

3.2.2.3 Numerical Stability

Unlike the RCWA method which obtains an analytical solution, FDTD obtains numerical solutions by discretising and iteratively solving Maxwell's curl equations. In FDTD simulations, convergence and stability are the most critical considerations, as they determine whether valid and meaningful results can be obtained. Convergence refers to the property that, as the discrete time step approaches zero, the solution of the finite-difference equation at any point in space and time approaches the exact solution of the original differential equation. Stability refers to the existence of certain conditions on the discretisation intervals under which the numerical solution of the difference equation remains bounded in its deviation from the exact solution. Lumerical FDTD adopts the Courant–Friedrichs–Lewy (CFL) condition that is one of the criteria in numerical analysis for determining the stability[182]. Its core idea is that in each time step, the distance over which information propagates must not exceed one mesh grid cell. This ensures that electromagnetic waves cannot 'skip over' adjacent grid points, which would otherwise lead to numerical instability such as divergence or oscillation. CFL condition can be expressed as follows:

$$\Delta t \leq \frac{1}{c\sqrt{\left(\frac{1}{\Delta x^2}+\frac{1}{\Delta y^2}+\frac{1}{\Delta z^2}\right)}} \tag{3.33}$$

The upper limit of the time step is typically denoted as Δt_{CFL}. In general, a scaling factor is introduced in FDTD simulations to further ensure numerical stability and reduce potential discretisation errors. Accordingly, the actual time step used in the simulation is given by:$\Delta t = S \cdot \Delta t_{\mathrm{CFL}}, S \in (0, 0.99]$.

Another important consideration in FDTD simulations is numerical dispersion, where the propagation speed of electromagnetic waves, dependent on frequency or propagation direction, deviates from the actual physical wave velocity and gradually distorts the simulated waveform. Unlike physical dispersion (e.g., material dispersion), numerical dispersion is a non-physical artifact introduced by discretisation. FDTD uses finite-difference approximations to represent partial derivatives, and these approximations become increasingly inaccurate at higher frequencies or when waves propagate at oblique angles. For example, the phase velocity of a wave may vary depending on the direction of propagation. The higher the frequency, or coarser the spatial grid, the more significant the numerical error becomes. Therefore, refining the mesh in FDTD is not only essential for

accurately capturing geometric features, but also for reducing numerical dispersion. A commonly accepted guideline is to ensure that the grid size is smaller than $\lambda/10$.[181, 183]

3.2.2.4 Boundary Conditions

The real world is infinite, but simulation domains are necessarily finite—otherwise, infinite computational resources would be required. Moreover, in most cases, large portions of space are not of interest in the simulation. Specific boundary conditions therefore must be applied at (or even within) the boundaries of the finite simulation domain to truncate the computational space and reduce the computational resources required. Improper boundary settings can result in unreliable results, such as artificial reflections caused by boundary layers. In Lumerical FDTD, commonly used boundary conditions include Perfect Electric Conductor (PEC), Periodic Boundary Conditions (PBC), Perfectly Matched Layer (PML), as well as symmetric and antisymmetric boundary conditions.

- Perfect Electric Conductor (PEC): At PEC boundaries, the tangential electric field satisfies $\boldsymbol{E_{\mathbf{tangent}} = 0}$ and the magnetic field is normal to the boundary. This condition is commonly used to model ideal metal reflectors. In Lumerical FDTD, such condition can be applied either in boundary condition settings or in material settings.
- Periodic Boundary Condition (PBC): PBC enforces periodic repetition of field distributions on opposing boundaries and are typically applied when simulating periodic structures, such as metasurface and photonic crystals.
- Perfectly Matched Layer (PML): PML is currently the most widely used and effective absorbing boundary condition. A layer of artificial material is added outside the simulation domain to absorb outgoing waves without reflection, preventing them from reflecting back into the simulation region.
- Symmetry Boundary Conditions: These include symmetric and antisymmetric boundaries. The two symmetry boundary types are summarised in Table 3-1**,** and are primarily applied to nanophotonic structures exhibiting spatial symmetry, typically corresponding to symmetric electromagnetic responses. For an electromagnetic field that exhibits mirror symmetry, symmetric or antisymmetric boundary conditions can be imposed along the symmetry axis to effectively reduce the simulation domain by half, thereby significantly saving computational resources.

Table 3-1 Electric and magnetic field settings for symmetric and anti-symmetric boundary conditions respectively.

	Symmetric Boundary Condition	Anti-symmetric Boundary Condition
normal electric field	Non-zero	0
tangential electric field	0	Non-zero
normal magnetic field	0	Non-zero
tangential magnetic field	Non-zero	0

3.2.2.5 Ansys Lumerical FDTD Setup

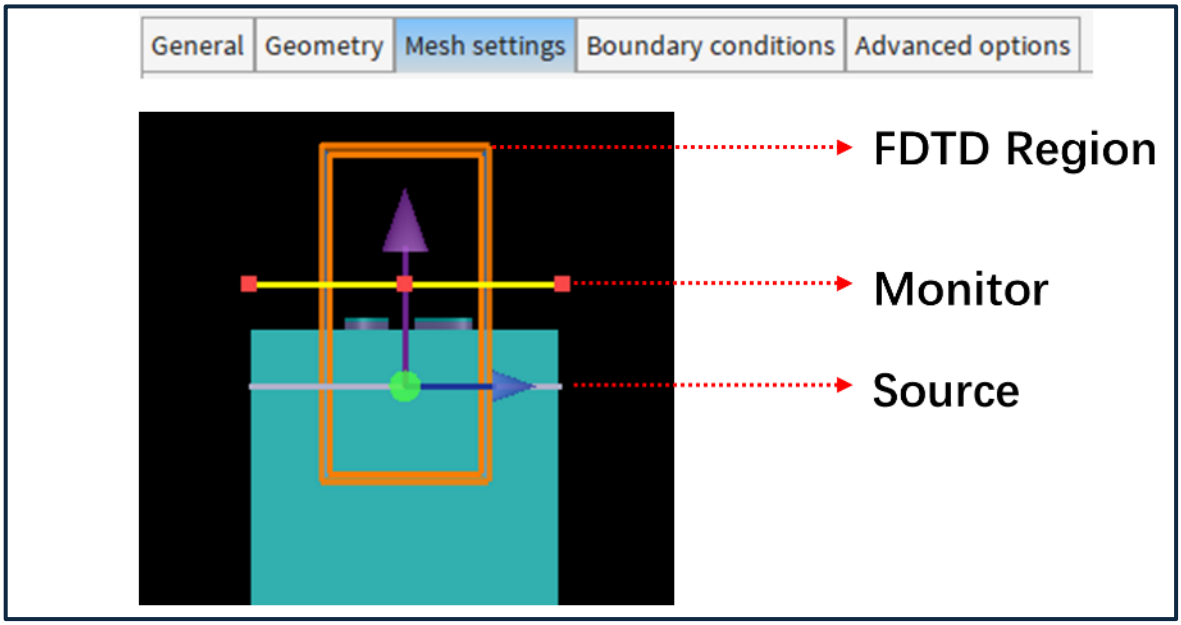

Figure 3-8 FDTD Simulation setup overview.

The setup of Ansys Lumerical FDTD primarily consists of three key components, as shown in Figure 3-8: the FDTD Region, Monitors, and Source. Among these, the most critical component is the FDTD Region, which contains five advanced configuration tabs, as illustrated in the upper side of Figure 3-8. In the simulations of periodic metasurface structures, a fundamental principle is that both the Source and Monitor should extend beyond the boundaries of the FDTD Region. The simulation engine will automatically truncate these objects to fit within the region and apply the specified boundary conditions accordingly.

Moreover, when calculating far-field transmission and reflection, it is essential to position the source and monitors at least one wavelength away from the metasurface. This ensures the exclusion of any evanescent near-field components, which could otherwise interfere with the accuracy of the far-field analysis. As for configuring the FDTD Region, the two most important aspects are the Mesh Settings and the Boundary Conditions, whose key attributes are shown in Figure 3-9.

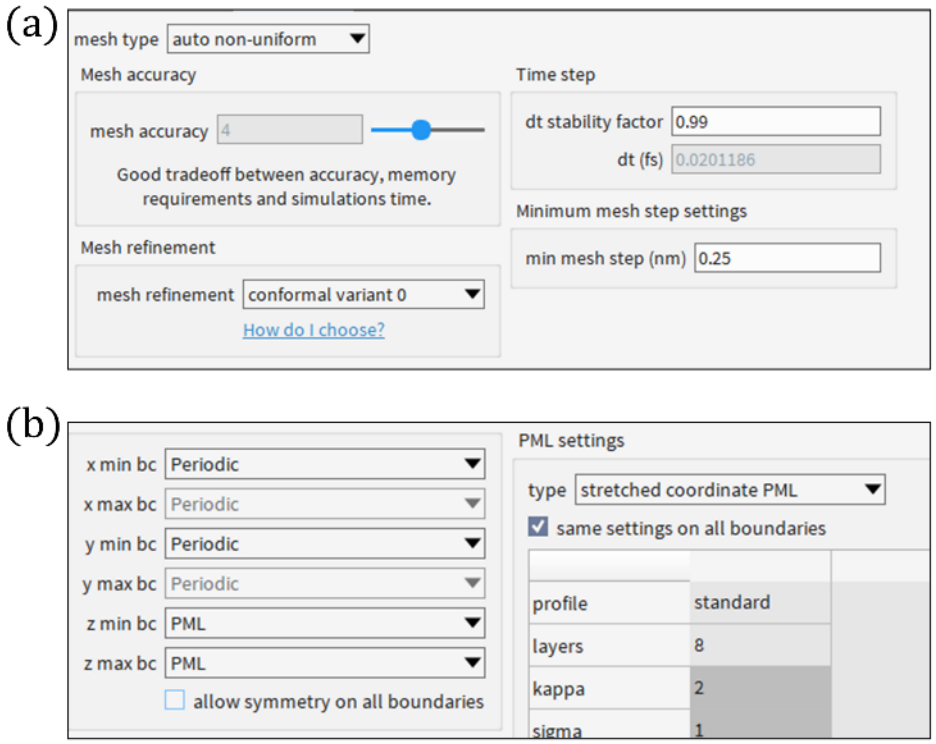

Figure 3-9 Screenshot of user interfaces of (a) mesh settings tab and (b) boundary conditions settings tab

Figure 3-9(a) shows the Mesh Settings panel. The Mesh accuracy setting controls the fineness of the mesh grid. In general, higher mesh accuracy leads to finer discretisation and improved numerical precision/stability, as discussed previously in Section 2.2.2. However, in 3D simulations, increasing mesh resolution can cause a substantial rise in computational size and cost. Therefore, convergence testing is often necessary to ensure that the chosen mesh level provides sufficient accuracy without excessive resource usage. The dt stability factor corresponds to the scaling factor introduced in Section 2.2.2. Its default value is 0.99 in the software. Reducing the scaling factor improves numerical stability but also increases the total simulation time. The Mesh refinement option is typically set to the default value

"conformal variant 0". Lumerical's Conformal Mesh Technology (CMT) uses a rigorous physical description of Maxwell's integral equations near interfaces between two materials that is able to incorporate Lumerical's Multi-Coefficient Materials[184]. The CMT can handle interfaces between arbitrary dispersive media. In general, this provides greater accuracy for a given mesh size or make it possible to run jobs much faster without sacrificing accuracy. When metal structures are present in the simulation, it is recommended to switch this setting to 1 for better accuracy. Figure 3-9(b) illustrates the Boundary Conditions settings. For Perfectly Matched Layers (PML), users can manually conFigure advanced properties such as the number of layers, PML type, and profile shape. As shown in the Figures, periodic boundaries are typically set in the x and y directions for 2D metasurface, while PML boundaries are used in the z (propagation) direction.

3.2.3 Finite Element Method with COMSOL

3.2.3.1 Overview of FEM

Physical laws involving both space and time are typically described by partial differential equations (PDEs). In most cases, approximate models can be constructed by applying various discretisation schemes, which transform the original PDEs into numerical model equations that can be solved using computational methods. The solutions to these numerical models then serve as approximations to the true solutions of the original PDEs.

The finite element method (FEM) is one such approach designed to compute these approximate solutions. In the context of electromagnetic field problems, FEM relies on the variational principle, solving a weak formulation of Maxwell’s equations to obtain a finite element solution. FEM is fundamentally different from the FDTD method, even though their software implementations may share several operational similarities—for example, spatial domain discretisation, and the use of boundary conditions to truncate the simulation region. To clarify the distinctions between these two methods and highlight the core principles of FEM, Table 3-2 provides a side-by-side comparison between FEM and FDTD.

	FEM	FDTD
Basic Principle	Transforms the problem into a variational (weak) form and solves it using basis function expansions	Directly discretises Maxwell's curl equations in time and space using finite differences
Form	**Weak form** (integral formulation with basis functions and weighted residuals)	**Strong form** (directly discretizes the differential equations)
Field Values representations	Fields are treated as continuous functions and expanded using basis functions within each element	Field values (***E*** or ***H***) are directly represented at discrete grid nodes

Table 3-2 Comparison of FEM and FDTD from theoretical basis.

3.2.3.2 Workflow of FEM

FEM is not the primary simulation method used in this research; it is employed as a supplementary tool to support certain results. Therefore, this section provides only a brief overview of the basic workflow of the FEM. FEM can be interpreted as consisting of the following key steps:

I. The computational domain is divided into many small, non-overlapping subregions, referred to as finite elements or mesh elements.
II. Within each element, the solution is approximated using local basis functions.
III. The governing partial differential equations are then expressed in their weak form and discretised over each element to obtain local element matrices.
IV. These local matrices are subsequently assembled into a global system matrix, which is then solved to obtain the numerical solution.

Here the governing partial differential equation mainly refers to the frequency-domain Maxwell's equation for the electric field in a linear, isotropic, and source-free medium:

$$\nabla \times \left(\frac{1}{\mu}\nabla \times \boldsymbol{E}\right) - \omega^2 \varepsilon \boldsymbol{E} = 0 \tag{3.34}$$

Equation 3.34 is also referred as the *curl-curl form* of the frequency domain Maxwell's function. Basis functions (also referred to as shape functions in COMSOL) are mathematical functions used to approximate the distribution of physical fields. They represent a continuous field within each small finite element as a linear combination of local functions. In electromagnetic simulations, curl-conforming basis functions—also known as edge elements (Nédélec Edge Elements)—are commonly used. This is because the formulation in Equation (3.34) involves the curl operator, which requires appropriate treatment of field continuity. These edge-based basis functions ensure tangential continuity of the electric field across element boundaries, while allowing for possible discontinuities in the normal component. Compared to standard nodal basis functions, they provide a more physically accurate representation of the electric field behaviour in FEM calculations.

3.3 Comparison of the three methods

3.3.1 Features of the methods

Based on extensive experience, the characteristics of several electromagnetic simulation methods available in commercial software for metasurface analysis are summarised, as shown in Table 3-3.

Method characteristic	RCWA	FDTD	FEM
Solution Type	**Semi-analytical**	**Numerical**	**Numerical**
Single band Speed	**Fastest**	**Fast**	**Fast**
Broadband Speed	**Fastest**	**Moderate**	**Slow**
Oblique Angle-incidence Speed	**Fastest**	**Slow**	**Slow**
High-Q resonance Speed	**Fastest**	**Not Suitable**	**Moderate**
Finite-size Calculation Speed	**No**	**Fastest with GPU**	**Fast**
Eigenmode Calculation	**No**	**No**	**Yes**

Polarisation Conversion Calculation	**Only Linear Polarisation**	**Complex**	**Yes, for Linear and Circular**
Metal Calculation Convergency	**Low, needs modification**	**Good**	**Good**
Nonlinearity Calculation	**Not Suitable**	**Yes**	**Yes, but slow**
Multipole Expansion Calculation	**Not Suitable**	**Yes, but complex**	**Yes**

Table 3-3 Comparison of electromagnetic simulation methods used in this work.

The characteristics listed in the table are defined and explained below:

- Solution Type: The type of solution, mainly divided into analytical and numerical solutions. The solution provided by RCWA is approximately analytical, from which the transmission and reflection of metasurfaces are obtained directly through analytical formulas. When considering the solution under finite diffraction orders and limited in-plane mesh numbers, it is not a fully analytical solution, and it is referred to as "semi-analytical". For the same number of in-plane mesh elements, RCWA offers the fastest and most accurate computation compared to the other methods.
- Single-Frequency Speed: The computational speed for electromagnetic response at a single frequency (i.e., single-wavelength illumination). In this case, the incident wave is a Dirac delta function in the frequency domain. Owing to its semi-analytical nature, RCWA is a lot faster than FDTD and FEM in single-frequency calculations, while the latter two have comparable speeds in such calculation. For instance, RCWA field monitor for single-wavelength electric field or magnetic field distribution calculation will take seconds in RCWA while might take hours for FDTD. The actual speed is task-related, but generally it took less than a second for RCWA simulation for mode-profiles for single-wavelength, seconds/minutes for FEM, while minutes/hours for FDTD. The tested hardware was using 24 core CPU Intel Core 13900 with 128GB RAM.
- Broadband Speed: Computation under broadband illumination. Because of its advantages in single-frequency computation, RCWA remains significantly faster than other methods. FEM, on the other hand, conducts multiple single-frequency

simulations rather than time-domain computation like FDTD, making it the slowest in this context.

- Oblique Angle-incidence Speed: Computation of electromagnetic response under oblique incidence. Angular dispersion of metasurfaces is one of the most important aspects to consider. Again, owing to its analytical formulation, RCWA only requires oblique-angular corrections of the incident wave to obtain angular dispersion, thus it is much faster than FDTD and FEM in this regard.
- High-Q Resonance Speed: Computation speed of the spectral response of metasurface with high quality factor (high-Q) resonances. In time-domain simulations, it is necessary to wait for the resonance energy to decay. Since for high-Q resonances the energy dissipation in the simulation is inherently slow, the convergence of the FDTD calculation is also slow, thus FDTD is not suitable for high-Q calculations. RCWA and FEM each have their own advantages for high-Q calculations: RCWA is fast, while FEM can directly compute the Q-factor owing to its inherent nature: since FEM solves the weak form of Maxwell's equations discretised into matrix eigenvalue problems it directly computes the real and imaginary **parts of** eigenfrequencies. The real part is the eigenfrequency, while the imaginary part is the Q-factor — both parameters that we often aim to extract from the spectral response.
- Finite-size Calculation Speed: Computation for metasurfaces with finite dimensions. For nonlocal metasurfaces, the size of the metasurface becomes an important consideration[46, 185]. In the extreme case of 1×1 unit cell, collective resonance modes do not exist. On the other extreme, with an infinite number of unit cells—implied by periodic boundary conditions—a nonlocal metasurface reaches an ideal infinitely periodic state, where each unit cell is equivalent. However, it is impossible to fabricate an infinitely large metasurface in reality. Determining the minimum number of unit cells or the size beyond which the spectral response begins to converge thus becomes an important issue. RCWA is based on Fourier expansion and, in principle, does not support simulations of metasurfaces with finite size. FDTD and FEM, however, can achieve such finite-size simulations simply by removing the periodic boundary conditions. Notably, Ansys Lumerical versions from 2024 onward have added GPU interfaces for electromagnetic computation with non-periodic boundaries. Similar to how GPUs accelerate deep learning[186, 187], using GPU can

significantly (by more than 10,000 times, depending on GPU performance) increase the computational speed compared to CPU-based simulations.

- Metal Calculation Convergency: When devices involve plasmonic modes supported by metals, computational stability is affected. This is because of the existence of evanescent waves of surface plasmon polariton (SPP) modes at the metal–dielectric interface, which can result in false reflection/transmission, or incorrect absorption spectra[188]. The transfer matrix in Section 2.1 must be corrected to mitigate the influence of evanescent field. Ansys Lumerical RCWA performs poorly in this respect. For simulations involving plasmonic modes, FDTD or FEM should therefore be used instead of RCWA.
- Nonlinearity Calculation: Computation of optical nonlinear effects. While in principle the framework of RCWA can be extended to include nonlinear effects[173, 189], the RCWA is generally considered not suitable for calculation of optical nonlinearities, with FDTD and FEM preferred. Both FDTD and FEM support flexible definitions of nonlinear permittivity. When using FDTD for nonlinear simulations, one must define a custom time-domain pulse shape. Owing to time-domain nature, FDTD maintains higher computational efficiency than FEM in non-linear optics calculation.
- Multipole Expansion Calculation: When analysing the far-field contributions of resonances, multipole expansion is a commonly used method[190-192]. The FEM method in COMSOL supports user-defined regions and arbitrary-order multipole expansions, making it highly capable for such analysis.

Based on the above experience and the official software documentation, the use of the methods can be concluded as:

- **RCWA (*Ansys Lumerical*):** Extremely suitable for spectral calculations of all-dielectric, **high-Q** non-local metasurfaces, including both normal and **oblique incidence**. It is particularly well-suited for computing the transmission efficiency and phase of Huygens-type metasurface unit structures. It is not suitable for the simulation of non-periodic structures (such as the spectral and phase response of finite-aperture metasurfaces). Therefore, the RCWA method in Lumerical is our primary tool for analysing the transmission and reflection amplitudes, phase, and linear polarisation conversion of dielectric metasurfaces.

- **FDTD** (***Ansys Lumerical***): A numerical method suitable for **low-Q** spectral calculations involving **metallic plasmonic modes**, under both normal and oblique incidence. For broadband oblique incidence, broadband sources cannot be directly used; the built-in BFAST source must be used, or a single frequency with multi-angle scan must be performed. Under non-periodic boundary conditions, **GPU**-accelerated computation is available, which greatly enhances simulation speed, making it especially suitable for finite-size metasurface calculations. However, for ultra-high-Q resonances, convergence is very difficult to achieve, thus FDTD is not suitable for simulating such cases.

- **FEM** (***COMSOL Multiphysics***): A numerical method suitable for electromagnetic response calculations of **arbitrary Q values and arbitrary materials**, including both dielectrics and metals. Because it allows convenient definition of custom partial differential equations and desired physical parameters, it is particularly suitable for advanced physical parameters computations, such as calculating polarisation conversion efficiency, phase, and performing multipole decomposition. Additionally, FEM supports the most flexible meshing, making it capable of generating more accurate mesh grids for irregular geometries (regular refers to shapes such as square, rectangular, or circular shapes).

- As detailed in chapter 4,5 and 6, this project involved simulations of both metallic and dielectric metasurfaces. The RCWA methods was mainly used for angular resolved transmission/reflection spectrum, while the FEM methods were used for eigenfrequency calculations. FDTD is used for verification and spectral response simulation for structures involving metals.

3.3.2 A simulation example using the three methods

To visualise the difference of the methods, especially in terms of the computational time, two examples are shown in this section. However, for FDTD, RCWA and FEM, the meshing strategy and convergence criteria varies a lot. The comparison is therefore not completely fair, but the computational time magnitude can be well estimated. The computer used for the simulation was equipped with following hardware configurations on my personal PC: CPU = AMD Ryzen 5 7600. GPU = NVIDIA RTX 3060 12GB. RAM = Crucial 32GB 5200MT/s. Such configuration is a regular personal PC; the simulations are therefore expected to be faster on high-performance PCs.

A simple symmetry-breaking structure that contains a q-BIC feature in the spectrum was simulated using three methods. In FDTD and RCWA, the in-plane mesh cell numbers are kept the same as $\lambda/150$, and the free tetrahedral mesh size in COMSOL is kept smaller than $\lambda/80$ for meta-atom area. The x-y view of the mesh results is shown in Figure 3-10(b). RCWA and FDTD have same in plane mesh grids and therefore only RCWA is shown. Symmetric conditions were applied in FDTD and FEM to fasten the simulation but not shown here for clearer visualisation. Spectral sample points intervals are the same. The simulated transmission spectrum is shown in Figure 3-10 (c).

Example: Broadband transmission spectrum simulation

Table 3-4 Time consumption comparison between CPU/GPU based FDTD and CPU-based RCWA/FEM for broadband simulation.

	CPU time	GPU time	Autoshut level Criteria
FDTD	**1034s**	**314s**	**1e-6**
RCWA	**4.8s**		
FEM	**5822s**		

Table 3-4 shows the time used when the simulation reaches the convergence criteria. It is worth noting that as the meshing of FEM is more flexible and better represents the geometry of the meta-atom, the mesh size of FEM can be set much larger to $\lambda/10$ and obtain similar results only using 600 seconds (here it was set smaller to be comparable to FDTD), while it still took double the time than GPU-FDTD. In this example, RCWA shows different level of speed with almost same results with FEM.

It can be seen in the simulated spectrum in Figure 3-10(c) that the convergence of the FDTD for such high-Q resonance is the worst, as it contains damping energy, showing spikes on the spectrum. The resonance centre differs between FDTD and RCWA, while RCWA and FEM shows identical resonance wavelength. The difference in spectrum results among the methods mainly originates from the meshing strategy around the interfaces. From this example, it is not difficult to see that for high-Q resonance simulations, FDTD is rather unsuitable in terms of both accuracy and efficiency. Admittedly, with the aid of GPU, the

disadvantage in efficiency has been largely remedied; however, the accuracy does not necessarily improve, unless a finer mesh and a smaller autoshut level are employed – which in turn would substantially increase the computational cost.

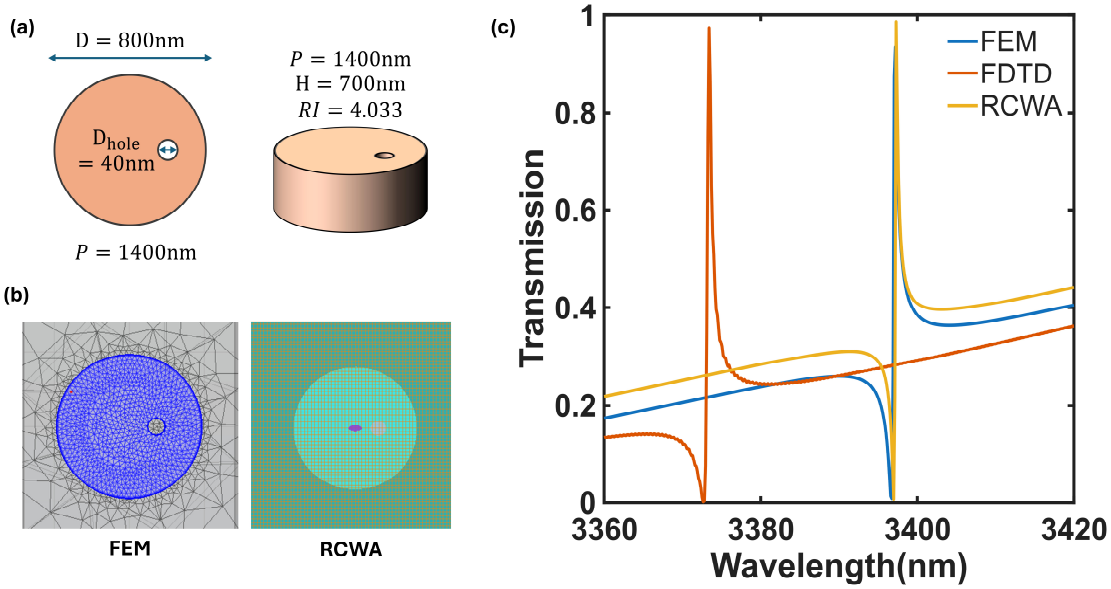

Figure 3-10 A simulation example (quoted from chapter 5 of this thesis).

3.4 Nanofabrication based on EBL and Dry-etch

In this section, the fabrication of metasurfaces based on electron beam lithography and dry etching will be introduced.

3.4.1 EBL for mask definition

3.4.1.1 Overview of EBL

To define a pattern in a material at the micro- or nano-scale, first the sample is coated with a substance called “resist”, whose molecular structure changes upon illumination with UV light (in photolithography) or with a beam of electrons (in electron beam lithography). Once the desired pattern is defined in the resist, it is usually transferred to the underlying material through etching techniques.

The metasurfaces involved in this research are single-layer structures, with unit cell sizes mostly ranging from several hundred nanometres to 2 micrometres. The James Watt Nanofabrication Centre (JWNC), the main cleanroom at the University of Glasgow, has

photolithography tools with maximum resolution of approximately 1 μm, and electron beam lithography (EBL) tools whose resolution can achieve few nm. Because of the requirements of metasurface fabrication that has dimensions smaller than 100nm, EBL was preferred for pattern definition, while photolithography in JWNC was not used in this research. EBL uses a highly focused electron beam with an extremely short wavelength to directly expose and write micro/nanostructures on the surface of an electron-sensitive resist, in accordance with the design pattern. EBL systems offer high resolution (with a minimum feature size <10 nm) and flexible patterning (direct writing without the need for a mask). The main drawbacks of EBL include low exposure throughput and complex process control, and for these reasons EBL is mostly used in mask fabrication, advanced prototype development, and nanoscale scientific research.

At JWNC, the EBL workflow involves users designing the pattern to be transferred onto the resist, setting parameters for the beam scanning process, spin-coating the resist onto the sample, and submitting it to staff for placement and coarse alignment. The Raith EBPG5200 system then performs the writing process based on the user-defined parameters. This process is summarised in the schematic diagram shown in Figure 3-11.

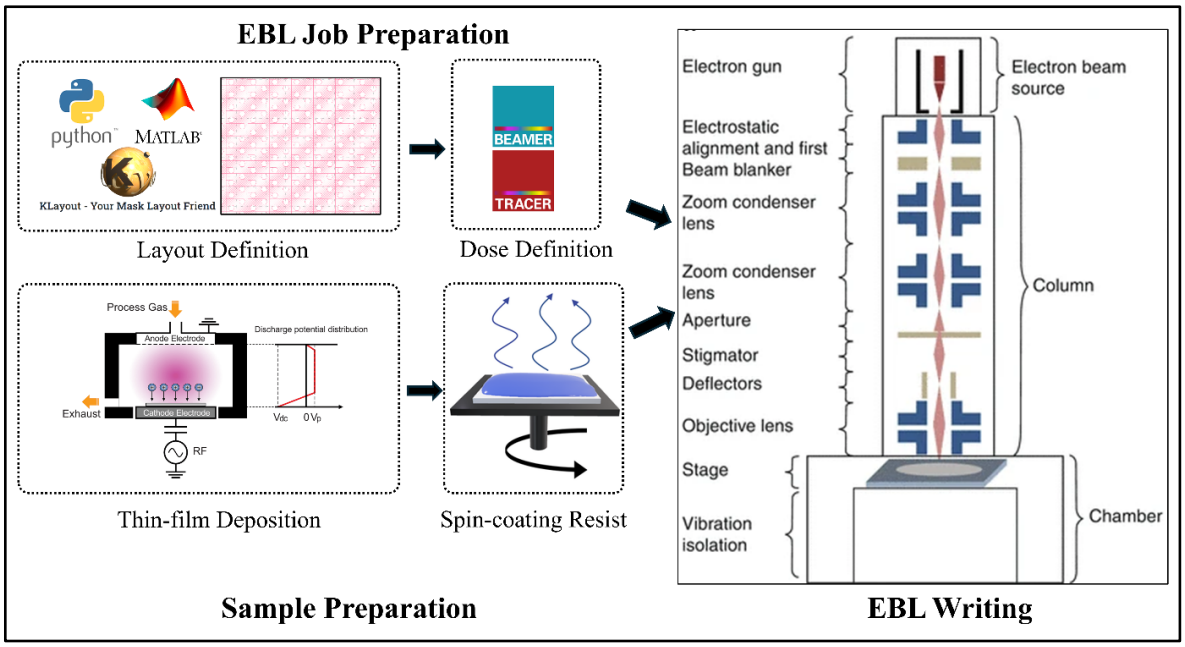

Figure 3-11 Schematic workflow of preparing a sample for EBL in JWNC.

3.4.1.2 Components of EBL

EBL is a prime example of a modern maskless resist exposure system. It utilises a high-energy electron beam for direct pattern writing, transferring designed structures onto an electron-sensitive resist layer. The electron beam has an extremely short wavelength. For

example, the de Broglie wavelength of a 100 keV electron beam, without relativistic correction, can be estimated as:

$$\lambda = \frac{h}{\sqrt{2m_e eV}} = \frac{1.227}{\sqrt{100000}} \approx 0.004nm \tag{3.34}$$

Where m_e is the mass of the electron, and h is the plank constant. Here a often-used constant $\frac{h}{\sqrt{2m_e e}} = 1.227\ nm \cdot V\text{^}(\frac{1}{2})$ is applied for quick estimation. The diffraction limit is therefore not a primary factor to consider in EBL. Instead, the achievable resolution is predominantly limited by factors such as aberrations in the electron optical system, electron scattering within the resist, and backscattering from the substrate. These effects constrain the resolution limit to approximately 10 nm. Consequently, designing pattern features with dimensions below this threshold offers limited practical benefit. The primary advantage of EBL in research settings lies in its direct-write capability, which eliminates the need for photomasks as required in deep ultraviolet (DUV) lithography.

A typical EBL writer system is detailed in Figure 3-12. Its structure closely resembles that of a scanning electron microscope (SEM).

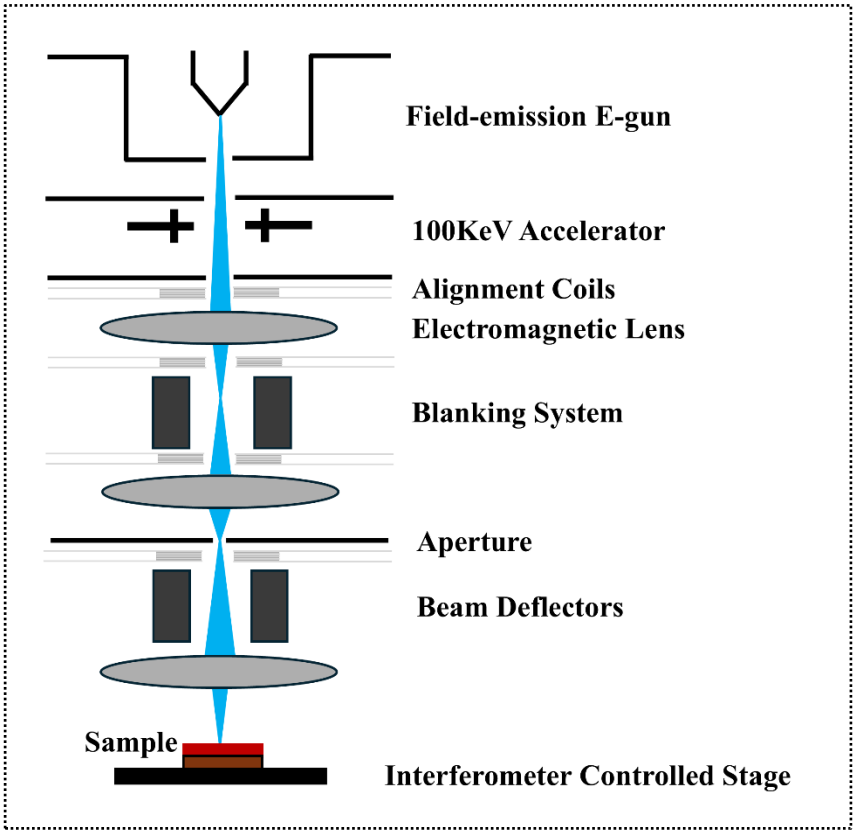

Figure 3-12 Schematic illustration of the key components in an EBL writer system.

The field-emission electron gun is responsible for generating a high-brightness, highly stable electron beam, which is then accelerated by an accelerator. In the EBPG system at JWNC, the default beam energy is 100 keV. The electron beam is subsequently shaped and focused by alignment coils and lenses. The blanking system employs deflectors to deflect the beam to blocking positions, effectively switching it off when scanning over non-patterned regions. The aperture in the system controls the beam spot size and blocks off-axis electrons. In general, the theoretical beam spot size on the sample is determined by a combination of the aperture size and the beam current. At the base of the system, the sample stage is a high-precision, nanometre-scale positioning platform controlled by an interferometer.

3.4.1.3 Job preparation

The final file read by the EBL writer is a vendor-specific project file format, which includes both the pattern data and the writing parameters. In the Raith system, this project file has an extension .cjob, and it is generated using software tools Layout Beamer and Cjob.

From the user's perspective, the primary task is pattern definition. Non-local metasurfaces typically consist of periodically repeated unit cells, so the design process generally starts with defining a single unit, which is then replicated into an array. This workflow can be accomplished through a graphical user interface (GUI) in commercial software such as LEdit. However, LEdit is relatively expensive, and its user base is limited compared to many free open source software. In this research, pattern definition is carried out using KLayout, which offers significant advantages, most notably, the ability to define patterns programmatically via Python scripting, including parametrised control over unit cell repetition. This approach greatly facilitates design adjustments and is particularly essential for tasks in this work that require large-scale pattern generation through code. The relevant code used in this research is provided in the appendix and will be discussed in detail in subsequent chapters. The defined patterns are stored in the GDSII format, which remains the most widely used standard. GDSII, short for Graphic Design System, is a data format used for the exchange of integrated circuit or layout data in Electronic Design Automation (EDA). Although the more advanced OASIS format offers advantages across nearly all aspects, GDSII is still the mainstream choice within the industry. Considering that it is straightforward to move between GDSII and OASIS formats, and that all software used in this work is compatible with both, the two formats will not be explicitly distinguished and will be considered equivalent in the following.

Once the pattern is defined, it is processed using Beamer, a software developed by GenISys, to convert the file into GPF (General Pattern Format) format, which is recognised by the Raith system. In Beamer, users can define parameters such as the relative dose distribution and step size used during the writing process. The absolute dose value will be defined within the Raith CJob software.

3.4.1.4 Sample preparation

The metasurface functional layers studied in this work generally consist of one or more thin films deposited on a transparent substrate with a low refractive index. Another promising material platform, Ge-on-Si, has attracted considerable attention in recent years, particularly for detectors and absorbers operating from the near-infrared into the short-wavelength mid-infrared[193, 194]. In the present case, the primary objective is to make transmission-mode devices, and a large refractive-index contrast between the meta-atoms and the substrate is desired in order to maximise the modulation efficiency for a given thickness. Accordingly, a low-index substrate such as CaF_2 represents a more suitable choice in this example. By contrast, for reflective and/or absorptive metasurface designs, Ge-on-Si remains a compelling option.

These films may be either metallic or dielectric and thus require specific deposition tools to achieve epitaxial growth. The JWNC is home to several electron beam (E-gun) metal evaporators which were used for metals and germanium. For dielectric materials such as SiN_x and SiO_2, plasma-enhanced chemical vapour deposition (PECVD) was used instead.

After the film deposition, bake-out and resist spin-coating are performed. The spin-coating process ensures the resist layer is both thinned and uniformly distributed. This is followed by a secondary bake to remove any potential bubbles or residual solvents within the resist. The patterns written by EBL are not directly transferred to the functional layer of the metasurface but are first written into a resist layer. Electron beam-sensitive resists operate on a principle similar to that of conventional photoresists, except that the exposure source is an electron beam rather than UV light. The electron beam changes the molecular structure of the resist. Depending on the so-called “tone” of the resist, the electron beam either makes it soluble in a particular solvent (called developer) in the exposed areas or cross-links the resist molecules and prevents dissolution in the exposed areas. In the former case the resist is known as a “positive tone” resist, while the latter is a “negative tone” resist.

The tone of the resist must be known when designing the pattern, since in positive resists the exposed areas are dissolved and removed but in negative resists the exposed areas remain, effectively producing an inverse pattern. Common positive resists include Polymethyl methacrylate (PMMA), a 1:1 copolymer of α-chloromethacrylate and α-methylstyrene commercially known as ZEP, and Chemical Semi Amplified Resist (CSAR), all of which are organic polymers. Upon electron beam exposure, the irradiated regions become more soluble in certain solvents and can be easily removed. The unexposed regions remain, serving as masks for subsequent chemical or physical etching processes — hence the term “resist”.

Among these, PMMA is the most widely used and cost-effective resist, although it exhibits poor resistance under certain high voltage/high power dry etching conditions. CSAR and ZEP are generally considered more suitable for high-energy etching environments.

The most commonly used negative resist is Hydrogen silsesquioxane (HSQ), which enables high-resolution pattern definition under high exposure doses. However, it is difficult to remove, requires complex development procedures, and is expensive and sensitive to storage conditions. In this work, only positive resists are used. Similar to photolithography, EBL requires a development step to remove the exposed regions of the positive resist. The development process involves the use of specific solvents to dissolve selected areas of the resist, allowing the transferred pattern to be accurately revealed. The specific developers used in this study will be detailed in later sections.

3.4.2 Reactive Ion etching based pattern transferring

Once the defined pattern is transferred onto the resist, the resist can then act as a mask for subsequent etching, allowing the pattern to be transferred onto the functional thin film to form the metasurface. Etching techniques can be broadly classified into two categories: wet etching and dry etching, depending on whether liquid-phase chemical reagents are involved. Wet etching relies on chemical solutions to etch the material, and is generally isotropic, that is it etches at the same rate in all directions. However, for certain crystalline materials, anisotropic etching can be achieved by exploiting differences in the etch rates of different crystal planes[195, 196]. Wet etching is inexpensive and simple to implement, but it is difficult to precisely control the sidewall profile and reaction time. Dry etching, by contrast, uses gaseous species or plasma under high-vacuum conditions to achieve etching through chemical reactions and/or physical ion bombardment. It allows precise control over etching conditions through the regulation of gas flow and reaction-by-product removal, but care has

to be taken to ensure ion bombardment and reaction byproducts do not result in material damage and contamination, respectively , highly anisotropic dry etch can be achieved by introducing inert gases to enhance directionality or by depositing sidewall passivation layers to protect against lateral etching. A detailed comparison of wet and dry etching methods is summarised in Table 3-4.

Aspect	Dry etching	Wet etching
Etching Medium	Gas phase / plasma (e.g. Cl_2, SF_6, O_2)	Liquid chemicals (e.g. HF, KOH, HCl)
Etching Principle	Physical and/or chemical interaction of ions and radicals in plasma	Chemical reaction between material and liquid etchant
Anisotropy	Highly anisotropic (vertical profiles achievable)	Mostly isotropic
Etch Precision	High; suitable for nm-scale features	Lower; undercutting is common
Equipment Requirement	High (requires vacuum systems, plasma sources, RF power)	Low (simple chemical baths)
Etch Rate	Moderate to fast; highly controllable	Usually fast, but less controllable
Material Selectivity	Adjustable via gas chemistry and parameters	Often great, depending on chemical selectivity
Typical Applications	Metasurfaces, FinFETs, photonic crystals, hard masks	MEMS structures, sacrificial layer removal, isotropic bulk etching

Table 3-5 Comparison between dry-etching and wet-etching.

Based on the characteristics listed in the table above, this research mainly uses dry etching. The use of dry etching includes two main steps: the transfer of patterns from the resist mask onto the functional thin film, and the subsequent oxygen-based removal of the residual resist. The two types of dry etching used in this work are Reactive Ion Etching (RIE) and Inductively Coupled Plasma (ICP) etching.

In an RIE etching tool, schematically shown in Fig. 3-13 **a**, the etching gases are ionised under the influence of a single high-frequency electric field, generating a plasma. The active species within the plasma (such as ions, electrons, and free radicals) exhibit high chemical reactivity and interact with the surface atoms of the target material to form volatile reaction products, thus enabling chemical etching. Simultaneously, high-energy ions are accelerated in the vicinity of the cathode and bombard the wafer surface vertically. This physical bombardment not only enhances the surface chemical reaction rate but also facilitates the desorption of the reaction by-products, thereby improving the overall etch rate. The presence of ion bombardment allows RIE to achieve anisotropic etching, i.e., directionally selective material removal. Inert gases such as argon (Ar) are often added to the gas mixture to further enhance the etch directionality.

ICP etching is a high-density dry etching technique. Compared with conventional RIE, ICP offers significantly higher plasma densities, enabling faster and more anisotropic etching, along with improved independent control over both the etch rate and directionality. As shown in Figure 3-13 **b**, an ICP system typically employs two separate RF power sources: one coupled to the top inductive coil to generate a high-density plasma, and another applied to the lower electrode (Bias) to control the ion acceleration energy and bombardment direction. This configuration allows users to independently regulate plasma density and ion energy, enabling better tuning of etch anisotropy, etch selectivity, and resist durability. It is worth noting that, in the actual fabrication process, the ICP system was operated using only the lower Bias power, while keeping the ICP (primary) power set to zero. This was because the structures involved in this study were relatively shallow (typically <1000 nm) with low aspect ratios and no stringent requirements on etch rate. Considerations about structure falling and sidewall profile should be taken if the structures have large aspect ratios. On the other hand, surface quality of the metasurface layer was a primary concern. Therefore, disabling the primary RF source helped to minimise damage to both the resist and the sample surface.

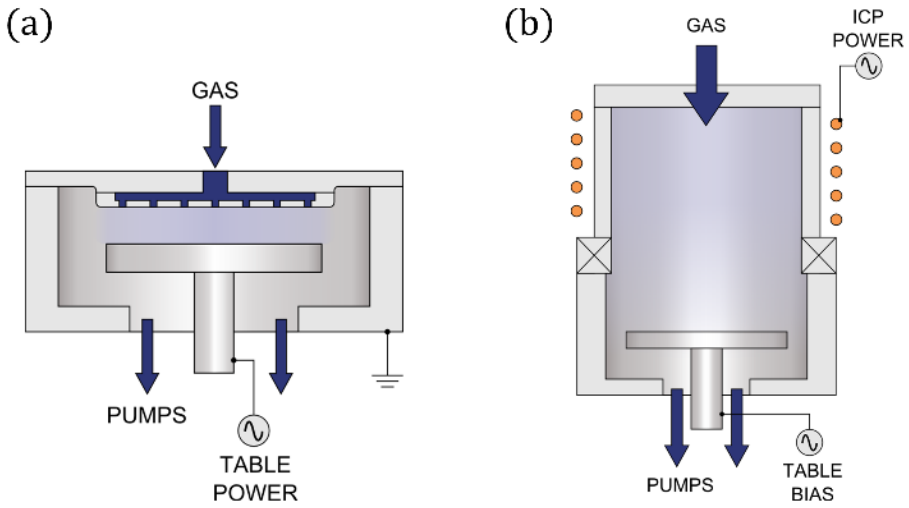

Figure 3-13. Schematic of key components of (a) RIE etching tool and (b) ICP etching tool.

The details of the fabrication flow developed to make the metasurface in this research can be found in following chapters in chapter 4 and 5.

3.5 Characterisation of metasurface

The fabricated metasurface were extensively characterised, and this section will introduce the main characterisation tools involved. The characterisation of metasurfaces in this research focuses on two primary aspects: the first is morphological characterisation, while the second is the investigation of the spectral response of the metasurfaces.

3.5.1 Scanning Electron Microscopy

For morphological characterisation, given the sub-micron feature sizes involved in the metasurface design and fabrication, Scanning Electron Microscopy (SEM) was mainly used. The structure of an SEM system is very similar to that of the EBL system described in the previous section, and the underlying principles are closely related. Both rely on the extremely short wavelength of electrons (as derived in Equation 3.34), which makes the diffraction limit negligible compared to visible-light optical microscope systems. As a result, SEM can achieve resolution far beyond that of a light microscope. A schematic comparison between light microscopy and SEM is shown in Figure 3-14(a). The imaging pathways of both systems are conceptually similar; however, in SEM, the imaging medium is not light but electrons, and thus, the lenses and detectors are designed specifically for electron optics.

Moreover, unlike optical microscopes which use wide-field imaging, SEM operates via a scanning probe mechanism. The image is formed by raster-scanning a finely focused electron beam across the surface, acquiring signals point-by-point and line-by-line. This principle is illustrated in Figure 3-14(b), where the deflection lens and final lens work together to steer and focus the electron beam onto different positions on the sample, enabling high-resolution image construction.

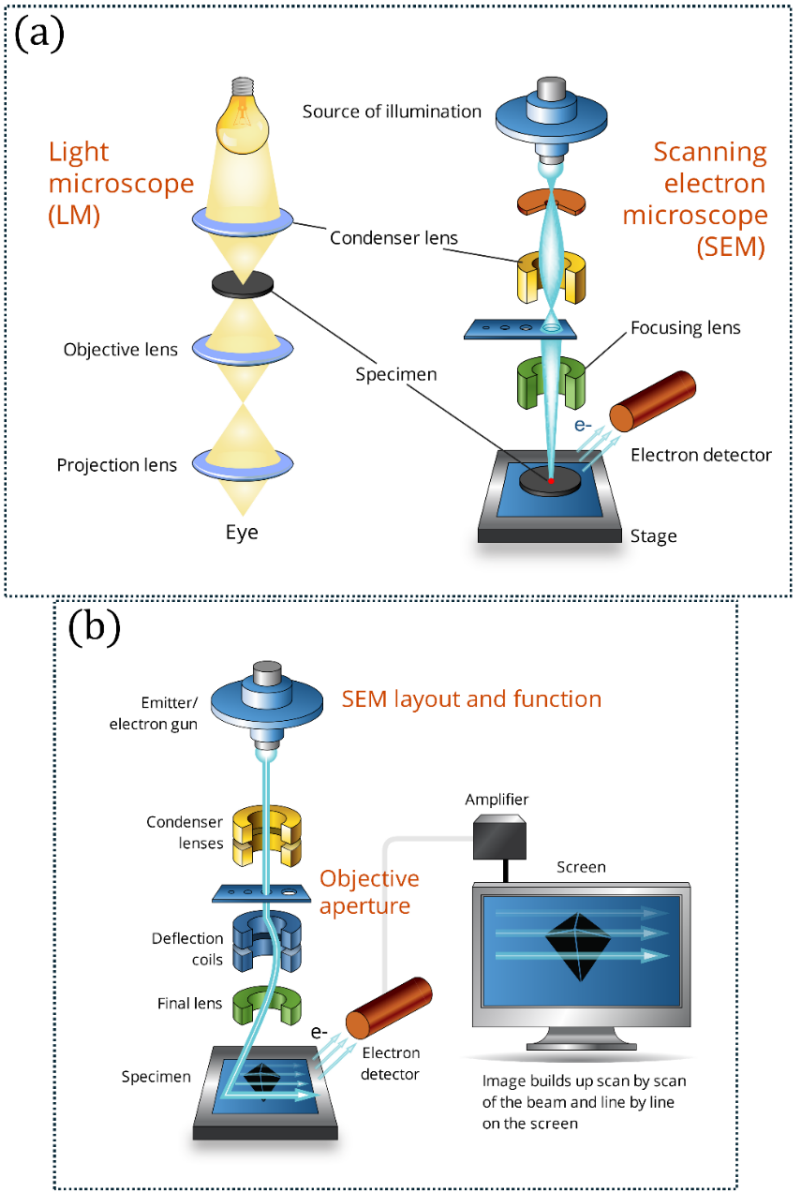

Figure 3-14 (a) Schematic illustration of the relation between conventional optical light microscope and SEM (b) Key components and workflow of SEM.

In SEM, the primary signal acquisition modes are Secondary Electron (SE) imaging and Backscattered Electron (BSE) imaging. Secondary electrons are generated when a high-

energy incident electron beam strikes the sample surface and undergoes inelastic scattering with the electrons in the sample atoms. This interaction excites low-energy electrons from the outer atomic shells, which are emitted from the sample as SE. Because of their shallow origin and low energy, SEs are highly sensitive to surface topography, making them ideal for high-resolution imaging of fine surface structures.

In contrast, BSEs are produced through approximately elastic scattering. When incident electrons interact with the atomic nuclei of the sample without significant energy loss, a portion of them is reflected toward the surface. These reflected, high-energy electrons form the BSE signal and can indicate the nuclei information. Compared to SEs, BSEs are less sensitive to surface morphology and provide lower axial resolution. As a result, SE imaging is more commonly used for characterising metasurfaces. Some material can be affected by "charging" and need special SEM techniques, such as dielectric and oxides that cannot transport electrons smoothly, but charging was not problematic for the metasurfaces in this work as the material mainly used are metals and semiconductors (germanium).

The primary SEM system used in this study at JWNC is the Hitachi SU8200 series, an industry-leading Cold Field Emission SEM known for its ultra-high-resolution capabilities. Cold field emission involves operating the electron gun in ultra-high vacuum (UHV) and cryogenically cooled conditions, offering several advantages:

- High brightness → Smaller beam spot size, sharper images, especially beneficial at high magnification and low accelerating voltages
- Low energy spread → Improved energy resolution for techniques like EDS (Energy Dispersive Spectroscopy) and EELS (Electron energy loss spectroscopy), and higher precision in EBSD (Electron Backscatter Diffraction) and crystallographic analysis
- Narrow beam divergence & small emission source size → Enables ultra-fine probes for nanoscale imaging and analysis

In the SU8200 series, SE signals are collected using two detectors:

- Upper Secondary Electron Detector [SE(U)] – positioned just above the objective lens; ideal for capturing fine surface detail because of proximity to the beam impact point.

- Lower Secondary Electron Detector [SE(L)] – a conventional Everhart–Thornley detector, typically mounted on the chamber wall or below the sample. It provides a wider field of view and better sidewall information and is less affected by sample charging. However, due to the detector's greater distance from the beam impact point, its spatial resolution is generally lower than SE(U).

In Hitachi SEMs, these two modes can be used simultaneously, and the optimal imaging configuration depends on the sample geometry and the desired observation angle.

3.5.2 Microspectrophotometer

For the investigation of the spectral response of nonlocal metasurfaces, an important experimental technique is the use of a microspectrophotometer.

A microspectrophotometer refers to a system that integrates a spectral analysis module into a conventional optical microscope. This allows for spectral decomposition of light using techniques such as grating-based dispersion or Fourier transform spectroscopy.

The schematic configuration of the microspectrophotometer used in this study is shown below:

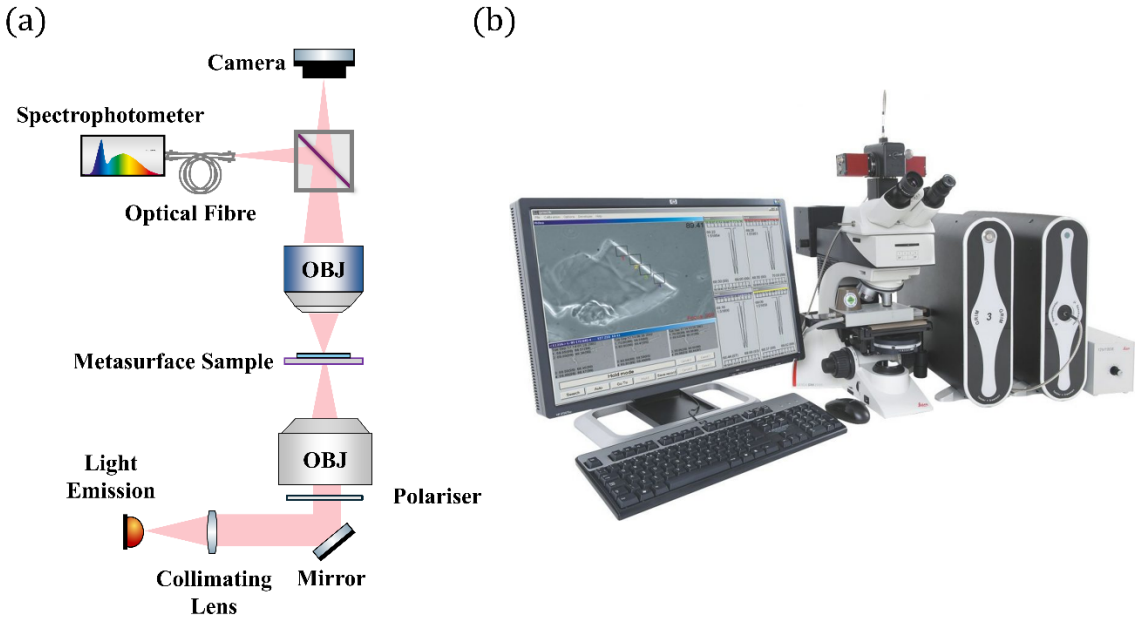

Figure 3-15 (a) Schematic illustration of a micro-spectrophotometer system working in transmission mode; (b) Photograph of the micro-spectrophotometer system used in this work.

In the visible wavelength range, the microspectrophotometer system employed in this study uses grating-based spectral dispersion in combination with a high-performance CCD

detector array, enabling simultaneous detection of different frequency components. The detection range of such a system primarily depends on the light source and the performance of the diffraction grating. For visible light, inexpensive and durable sources such as tungsten filament lamps are most commonly used. High-quality grating systems have also become commercially available and widely adopted.

However, for the infrared (IR) spectral range, achieving broad-band detection using diffraction gratings presents significant challenges. In such cases, a Fourier-transform infrared (FTIR) spectrometer is more commonly used. While the particular FTIR used will be discussed in detail in Section 4.3, the following will describe the principles and key components of FTIR spectroscopy.

3.5.3 Fourier Transform Infrared Spectroscopy

The FTIR Spectrometer is a widely used instrument in modern infrared spectral analysis. It acquires information about a sample's absorption, transmission or reflection of infrared light through an interferometric process and then reconstructs the corresponding spectrum using a Fourier transform of the resulting interferogram.

The key component of an FTIR system is the Michelson interferometer, and the basic structure includes the following elements:

- **Infrared light source**: Emits broadband infrared radiation.
- **Beamsplitter**: Divides the incoming beam between two optical paths. It is commonly made of CaF_2 or KBr in the infrared range.
- **Mirrors**: two mirrors, one fixed and another moving back and forth.
- **Sample compartment**: where the recombined beam passes through the sample after being reflected by the mirrors and recombining in the beamsplitter.
- **Detector**: Measures the light intensity as a function of the optical path difference, resulting in an interferogram.

A schematic diagram of this setup is shown in Figure 3-16. Mirrors M1 and M2 represent the fixed and moving mirrors, respectively, and together with the beamsplitter (BS), form the Michelson interferometric path.

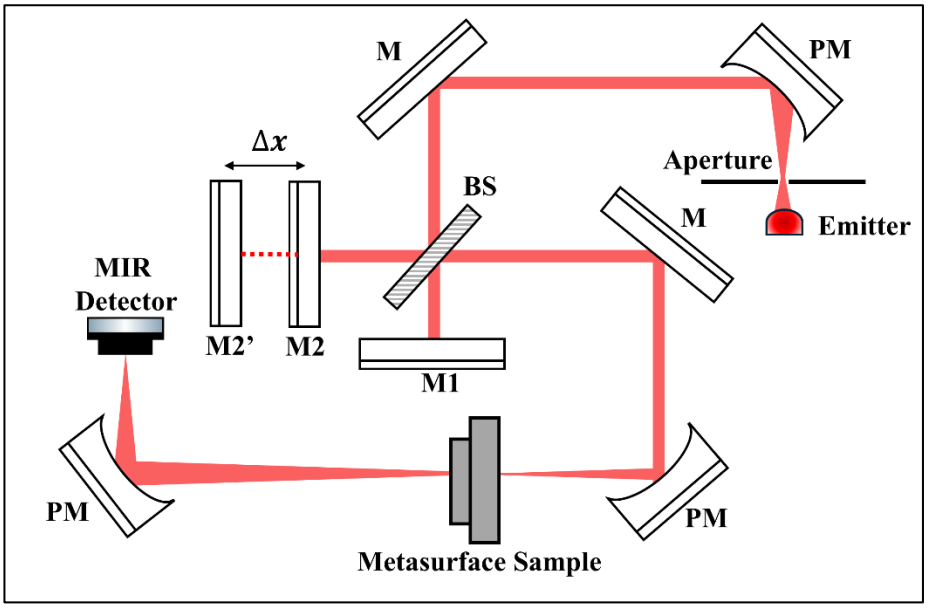

Figure 3-16 Schematic illustration of the key components in a FTIR. **M** represents metal based broadband mirror; **PM** refers to parabolic mirror which can reflect and focus infrared beam; **BS** refers to Beamsplitter.

The path difference introduced by the moving mirror is denoted as $\boldsymbol{\Delta x}$, and the corresponding optical path difference is given by $\boldsymbol{\Delta L = 2n\Delta x}$, where $\boldsymbol{n}$ the refractive index of the medium inside the interferometer.

Assuming the infrared source is a broadband continuous source composed of multiple frequency components; its intensity can be described as a function of frequency. The spectral intensity of the source at frequency $\boldsymbol{\nu}$ is therefore described as $\boldsymbol{I(\nu)}$.

The intensity recorded by a Michelson interferometer (note as interferogram) is the result of interference between two beams and depends on the optical path difference $\boldsymbol{\Delta L}$. The interfered intensity is given by:

$$I(\Delta L) = \int_0^{+\infty} I(\nu)cos(2\pi\nu\Delta L)d\nu \tag{3.35}$$

Which is a cosine Fourier transform of the source spectrum. The resulting interferogram is the superposition of interferograms from individual monochromatic components of the source. A single monochromatic component shows a single peak in the frequency, domain, corresponding to a cosine-shaped interferogram as shown in Fig. 3.16 **a.** For a broadband continuous wave in the frequency domain, however, all monochromatic components interfere constructively only at zero optical path difference (OPD), yielding a maximum intensity. Away from zero OPD, the phase differences among various frequency components cause constructive or destructive interference, leading to partial cancellation. As a result, the

interferogram exhibits a central peak with rapid decay on both sides, forming a symmetric pattern, as shown in Figure 3-16(b). The function with respect to optical path difference essentially represents a time-domain signal, as the optical path difference corresponds directly to a temporal delay. Therefore, in Figure 3-17, the horizontal axis labelled “Mirror Position” on the right-hand side is equivalent to time.

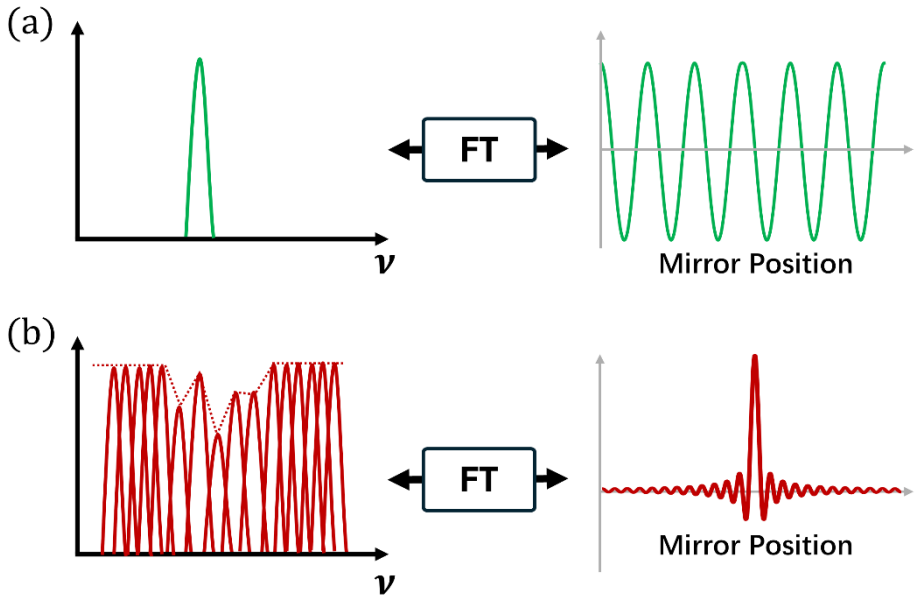

Figure 3-17 Schematic illustration of the Fourier Transform/ inverse Fourier Transform pair of (a) monochromatic wave (b) broadband continuous wave in frequency domain and in time (mirror position) domain respectively.

Furthermore, as the spectral bandwidth of the source increases (i.e., more monochromatic components are added), the central peak of the interferogram becomes sharper and stronger, and the side lobes decay more quickly. This reflects the improved localisation of the interference signal in the spatial domain.

According to the inverse Fourier transform formula, the original spectral intensity $I(\nu)$ can be recovered from the interferogram using:

$$I(\nu) = \int_{-\infty}^{+\infty} I(\Delta L)\cos(2\pi\nu\Delta L)\ d(\Delta L) \tag{3.36}$$

This means that as long as the interferogram is accurately recorded, the spectrum can be fully reconstructed via Fourier transformation.

In practice, this operation is performed by a computer. The mirror position, sensor, and computer involved in the system cannot fully sample a continuous signal but require some discrete sampling and a truncated range. At the same time, because of the limited physical size of the instrument, the range of the optical path difference is also not infinite. Therefore, the Fourier transform becomes a discrete Fourier transform (DFT) or fast Fourier transform (FFT). Assume that the interferogram is sampled at a finite number of N odd points over the interval $[-\Delta L_{max}, +\Delta L_{max}]$, where the n-th sampling point is $\Delta L_n = n \cdot \delta\Delta$ and $\delta\Delta = \frac{2\Delta L_{max}}{N}$, Then, the interferogram becomes a discrete signal:

$$I_n = I(\Delta L_n), n = -\frac{N-1}{2}, -\frac{N-1}{2} + 1, \ldots, \frac{N-1}{2} \tag{3.37}$$

Its DFT can be written as Equation (3.38), where the subscript n is replaced with $[0, N-1]$, the more commonly used range in computing:

$$S_k = \sum_{n=0}^{N-1} I_n \cdot e^{-2\pi ikn/N}, \quad k = 0,1, \ldots, N-1 \tag{3.38}$$

As I_n is a segment taken from an infinite sequence, equivalent to multiplying the original signal by a rectangular window function, it introduces sidelobes (spectral leakage). To compensate for the sidelobes caused by this truncation, it is common to apply a window function to suppress them. Therefore, the actual signal used for the DFT operation is expressed as Equation (3.39).

$$S_k = \sum_{n=0}^{N-1} I_n \cdot w(n) \cdot e^{-2\pi ikn/N} \tag{3.39}$$

Here, $w(n)$ represents the window function. One commonly used window function is the Blackman–Harris 3-term window, as demonstrated in equation 3.40[197]:

$$w(n) = 0.42323 - 0.49755 \cos\left(\frac{2\pi n}{N-1}\right) + 0.07922 \cos\left(\frac{4\pi n}{N-1}\right) \tag{3.40}$$

It provides excellent sidelobe suppression, which means a lower likelihood of false peaks appearing. In this thesis, all results involving FTIR use the Blackman–Harris 3-term window function that can be defined in the FTIR data processing software OPUS, provided by the supplier Bruker.

The core advantage of FTIR lies in its ability to detect broadband signals in the time domain and rapidly retrieve corresponding spectral information via Fourier transformation. It does not rely on broadband diffraction gratings or filter-detector arrays, but instead uses only a single detector, achieving very high photon energy utilisation efficiency. As a result, the requirements on the light source are relatively low—a standard Globar source is often sufficient. The primary limitations on the detectable spectral range usually come from the detector's response range and the bandwidth of the beamsplitter.

Chapter 4 Plasmonic colour filter with polarisation selection

4.1 Introduction and motivation

The colour or spectral characteristics of an object within the visible range (400–700 nm) convey vital image information to both human observers and machine vision systems. Polarisation, another key property of light, is less intuitively perceived but holds valuable cues such as surface reflectivity and contour variation. Various organisms in nature have evolved the ability to perceive polarisation[198, 199], and when this ability is combined with spectral selectivity, it enables a rich, information-dense visual experience. Polarisation awareness is essential for numerous imaging functions, including passive underwater observation[200], edge enhancement for three-dimensional visualisation[201], image dehazing[202], and medical diagnostics[203]. As a result, imaging technologies capable of concurrently resolving both polarisation and colour have attracted considerable interest from researchers and industry alike [204-207]. Conventionally, such colour-polarisation cameras adopt a two-layer filtering system, as shown in Figure 4-1(a), comprising a thin-film stack for colour discrimination and a secondary grating structure for polarisation filtering, which often necessitates sophisticated fabrication and alignment procedures. To improve integration and performance, there is growing interest in leveraging the capabilities of metasurfaces. Besides enabling multiple optical functionalities on a single planar platform, metasurfaces offer compatibility with standard CMOS processes and can be directly integrated with imaging sensors, making them suitable for compact spectral-polarisation filter systems.

Metasurface-based colour filters have been widely studied[54, 68, 112, 113, 121-123, 208-210]. These devices reshape the optical wavefront using quasi-planar subwavelength architectures to perform selective spectral filtering. High-efficiency, high-saturation colour filters based on all-dielectric resonant metasurfaces have received significant attention [121-123, 210-213]. Compared with metallic or plasmonic structures, dielectric metasurfaces offer inherently lower optical losses, enabling narrow-band and efficient structural colour filtering. A number of these platforms exploit collective resonance phenomena, such as multi-order Mie resonances, guided-mode resonances, and quasi-bound states in the continuum (q-BIC). These effects generally require extended periodicity to fully develop and amplify the modes [112]. Prior work has demonstrated that TiO_2 metasurfaces can reduce the reliance on

periodicity by utilising magnetic dipole (MD) modes excited by individual resonators, thereby achieving high spatial resolution colour filters[121]. Employing semiconductors such as silicon as the resonator material can also produce angle-stable MD modes under s-polarised illumination. Moreover, by introducing an index-matching overlayer, such resonator-based structures have been shown to yield highly saturated colours and fine spatial resolution [122]. Although striking colour effects have been achieved with reflection-mode devices, experimental demonstrations of **transmission-mode** metasurface filters remain limited, apart from a few studies using subtractive colour concepts[20, 214, 215]. Without adding computational overhead, transmission-mode filters offer straightforward integration benefits for practical colour imaging systems. Some such designs also rely on CMOS-compatible materials and processing methods [78, 100, 114, 208], making them promising candidates to replace traditional dye-based or multilayer thin-film Bayer filters currently used in CMOS image sensor (CIS) arrays.

Plasmonic colour filters using metal apertures can operate efficiently within just a few lattice periods, making them well-matched to the typical pixel dimensions (micron scale) of image sensors. Hence, they present a viable alternative for camera filter elements[77, 113, 215, 216]. These plasmonic arrays have also been explored for applications in fluorescence microscopy[217] and high-speed single-photon imaging[218]. Polarisation-dependent colour filtering can be achieved through structural anisotropy, either in aperture geometry or in the periodic arrangement[72, 79, 219], especially through tailoring aperture dimensions. Plasmonic devices using noble metals like gold and silver have been extensively reported in the visible and near-infrared spectral bands due to their relatively low Ohmic losses[75-77]. However, gold suffers from interband transitions that impair colour performance below 500 nm (i.e. in the blue region), and silver is susceptible to surface sulphidation. Additionally, neither material is CMOS-compatible[78], limiting their utility in mainstream imaging. As a result, aluminium-based plasmonic filters—offering low cost and ease of manufacturing—have attracted ongoing interest[33, 54, 79, 80]. Nevertheless, the inherently low quality-factor (Q-factor) of aluminium resonators presents challenges for accurate colour reproduction. Moreover, designs that rely on anisotropy in aperture shape or lattice symmetry to enable polarisation filtering often involve trade-offs between peak transmission, linewidth, and polarisation extinction ratio. Although current structures can exhibit differing polarisation responses[119, 220, 221], achieving strong polarisation extinction while preserving spectral sharpness remains a key challenge. There is therefore a clear need to explore approaches for

simultaneously obtaining narrow linewidth and high polarisation extinction without compromising transmission in aluminium-based spectral-polarisation filters.

In response to this need, a plasmonic metasurface based on a dimer-elliptical aluminium aperture array was proposed and experimentally realised, as illustrated in Figure 4-1(a). Two specific design innovations are introduced to simultaneously improve the linewidth and polarisation extinction ratio of aluminium-based filters without significant loss of peak transmission. First, the use of dimer apertures enables approximately double the transmission compared to monomer configurations, while maintaining polarisation extinction performance. Second, deep etching into the SiO_2 substrate reduces the resonance linewidth with only minimal transmission loss (less than 5%). By combining these two design principles, the proposed polarisation-sensitive colour filter achieves a peak transmission of ~30%, a polarisation extinction ratio surpassing commercial polarising films in the blue spectral range (>150 at 465 nm), and over 76% coverage of the RGB colour gamut (CIE 1931, 2° observer).

It is worth noting that Professor David Cumming has produced a substantial body of highly influential work in this field. The Microsystem Technology Group, led by David Cumming, was the first to propose the design of adding a SiO_2 capping layer on triangular-lattice plasmonic colour filters[33] to achieve match the SPP modes respectively emerging at upper and lower metal–dielectric interfaces, thereby significantly improving transmission efficiency with high colour purity. Building on this concept, the group demonstrated the integration of plasmonic metasurfaces with CMOS photodetectors[100]. More recently, they have further shown flip-chip adhesive integration of plasmonic filters with SPADs, enabling colour reconstruction under low-light conditions[54]. These polarisation-insensitive micro-/nano-scale filters have convincingly demonstrated the viability of this technological route. Motivated by this, after joining the group I initiated the development of plasmonic filters for higher-dimensional imaging modalities. In this section, the focus is on filters designed for simultaneous colour and polarisation sensing.

To validate the structure's polarisation selectivity and colour generation capabilities, I experimentally demonstrate both micron-scale structural colour images and polarisation-encoded imagery using the proposed transmissive filter in a coded-array format. Fabrication involves a single lithography exposure followed by chlorine-based dry etching[222]. While electron-beam lithography (EBL) is used in this work for proof-of-concept fabrication, the

design dimensions are compatible with scalable methods such as photolithography or nanoimprint lithography for mass production.

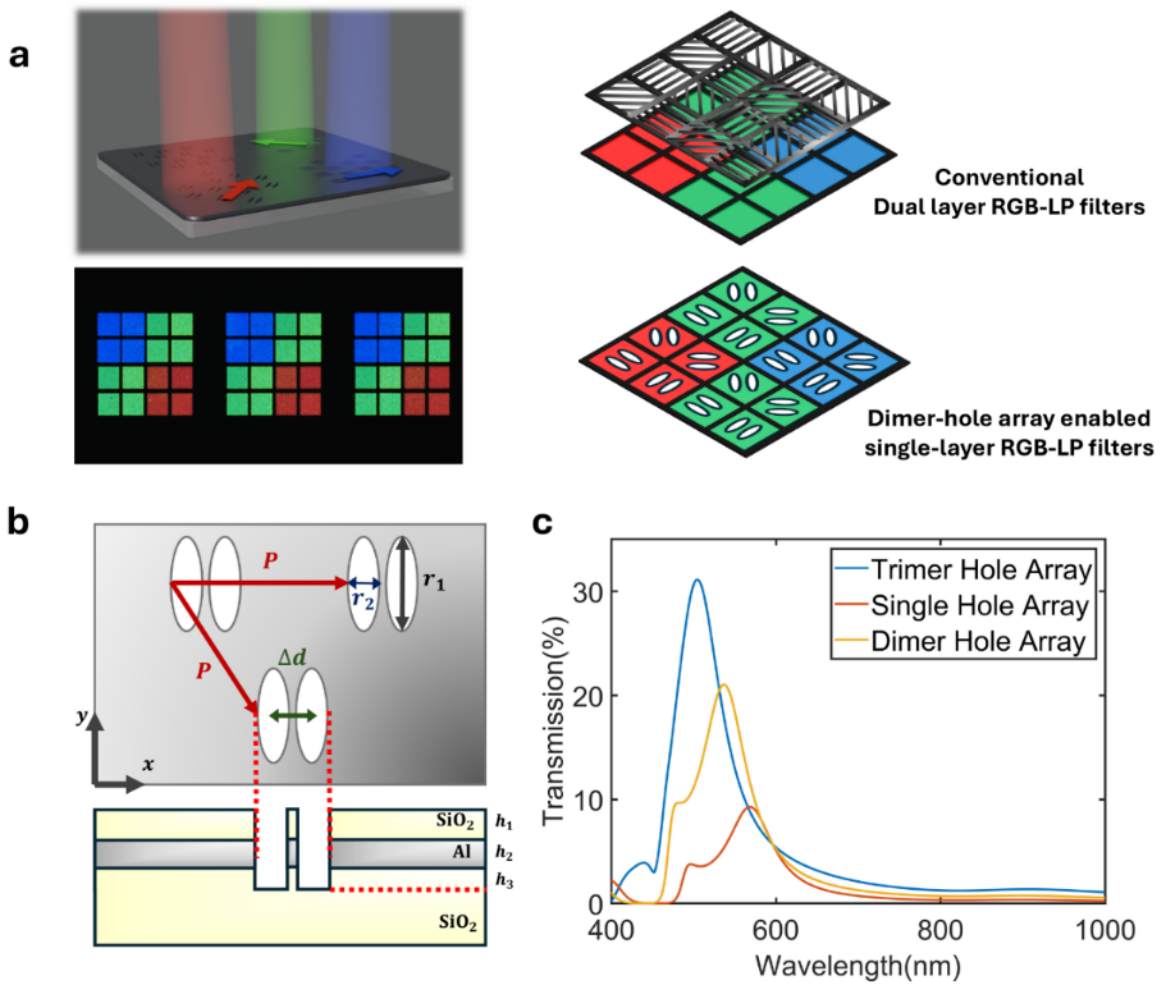

Figure 4-1. Design of the proposed polarisation controlled transmissive aluminium plasmonic metasurface filter. **a.** An illustration of the filter function and optical photomicrograph of fabricated RGB-LP array (under unpolarised illumination). The size of the colour filter pixel shown here is 10 **µm** x10 **µm**. The metasurface serves as both a linear polarizer and a colour filter with single-layer periodic aperture in an aluminium film. **b.** The geometrical structure of the metasurface filter. **P** refers to the period of the triangular lattice, while $\mathbf{r_1}, \mathbf{r_2}$ refers to the major and minor axes of the ellipse. $\mathbf{\Delta d = P * g}$ refers to the distance between the dimer apertures. The dimensions are $\mathbf{h_1 = 150nm}$, $\mathbf{h_2 = 150nm}$, $\mathbf{h_3 = 100nm}$. **c.** Transmission enhancement of the multi elliptical aperture array. Multiple aperture array enhanced the transmission without broadening the linewidth of colour filtering.

4.2 Design and modelling

4.2.1 Simulation Methods

A three-dimensional finite-difference time-domain (FDTD) simulation (ANSYS, Lumerical FDTD) was employed to evaluate the transmission characteristics of monomer, dimer, and trimer aperture arrays. A plane-wave source covering 400–1000 nm was placed within the substrate. Perfectly matched layers (PML) were assigned to the top and bottom simulation boundaries. Anti-symmetric and symmetric boundary conditions were applied to the directions of the electric (E-field) and magnetic (M-field) components of the incident wave, respectively, to reduce computational time.

The optical constants for aluminium were taken from the Palik material database, and the refractive index of the PECVD-deposited SiO_2 capping layer was set to 1.46, in accordance with characterisation data obtained from the James Watt Nanofabrication Centre, University of Glasgow. A power monitor was positioned 2 μm above the capping layer to eliminate near-field artefacts and to record the far-field transmission spectrum.

For oblique incidence simulations, the source was replaced with the broadband fixed-angle source technique (BFAST), and boundary conditions were adjusted to periodic in the lateral directions. The colorimetric response was derived from the simulated spectra using CIE standard colour matching functions. A flat-spectrum illumination source was used to generate the corresponding CIE colour plots. MATLAB scripts, partially adapted from those shared by the MATLAB user community[223], were used in the processing pipeline.

4.2.2 Colour filtering

The phenomenon known as extraordinary optical transmission (EOT) has been effectively employed to explain and thereby enable the fabrication of transmissive filters[33, 75, 78, 80, 216, 224, 225]. These filters are composed of periodic arrays of subwavelength apertures etched into a thin metallic film. When the periodic lattice vector of these apertures offsets the wavevector of the surface plasmon polariton (SPP) under normal incidence, the resulting wavelength, referred to as λ_{SPP}, can act as a predictor for the spectral location of the transmission window[216], as expressed in Equation (4.1):

$$\lambda_{\mathrm{SPP}} = \frac{p}{\sqrt{\frac{4}{3}(i^2 + ij + j^2)}} \sqrt{\frac{\varepsilon_m \varepsilon_d}{\varepsilon_m + \varepsilon_d}} \tag{4.1}$$

Here, (i, j) denotes the diffraction order, and ε_m and ε_d represent the permittivity of the metal and the adjacent dielectric medium, respectively. A triangular lattice was selected as it provides a denser aperture arrangement than a square lattice, along with a larger spectral separation between the (1, 0) and (1, 1) order surface plasmon wavelengths, λ_{SPP}, which facilitates improved colour filtering performance and superior out-of-band suppression. In this study, the filter design targets the (1, 0) diffraction mode. In previous models and implementations, metallic periodic aperture arrays were typically patterned directly onto a substrate to form a diffraction grating. Such gratings offer an additional in-plane momentum component, enabling the incident wave that originates from the substrate to couple into the SPP mode. The resulting plasmonic wave then interferes either constructively or destructively with the wave transmitted directly through the aperture into free space. Constructive interference between the SPP and the transmitted mode results in a transmission maximum in the far-field spectrum. Although this peak generally exhibits a red shift due to an additional phase delay introduced by the apertures[70, 71], Equation (1) still offers a reliable approximation for the onset (rising edge) of the transmission peak. An increase in aperture radius raises the overall transmission across all wavelengths, thus boosting the peak transmittance. However, since the SPP field is strongest at the metal-dielectric interface, particularly near the aperture edge, enlarging the aperture also admits more non-resonant transmission that is unrelated to the SPP. As the aperture area scales quadratically with radius, this leads to increased broadband leakage, thereby broadening the spectral linewidth. Based on these principles, I designed and modelled a series of plasmonic colour filters.

To enhance spectral selectivity while simultaneously increasing peak transmission, a multi-aperture unit design was introduced. Accordingly, structures comprising one, two (dimer), and three (trimer) apertures per unit cell were investigated. The multi-aperture configurations yielded more favourable results than the single-aperture configuration (see Fig. 4-1). Although the trimer-aperture structure exhibited better colour characteristics in the green wavelength range, it suffered from performance issues in the red channel. As shown in Figure 4-2, the trimer structure in the red band is affected by higher-order resonances at shorter wavelengths, introducing unwanted transmission components that degrade red colour purity. In addition, the trimer structure displays significantly poorer near-infrared (NIR) cutoff and generates more sidebands. A strong NIR cutoff is desirable for imaging applications, especially when used with modern CMOS sensor chips, which are typically sensitive to near-infrared wavelengths. For these reasons, the dimer configuration was

selected for demonstration, in order to highlight the advantages of the multiple-aperture design.

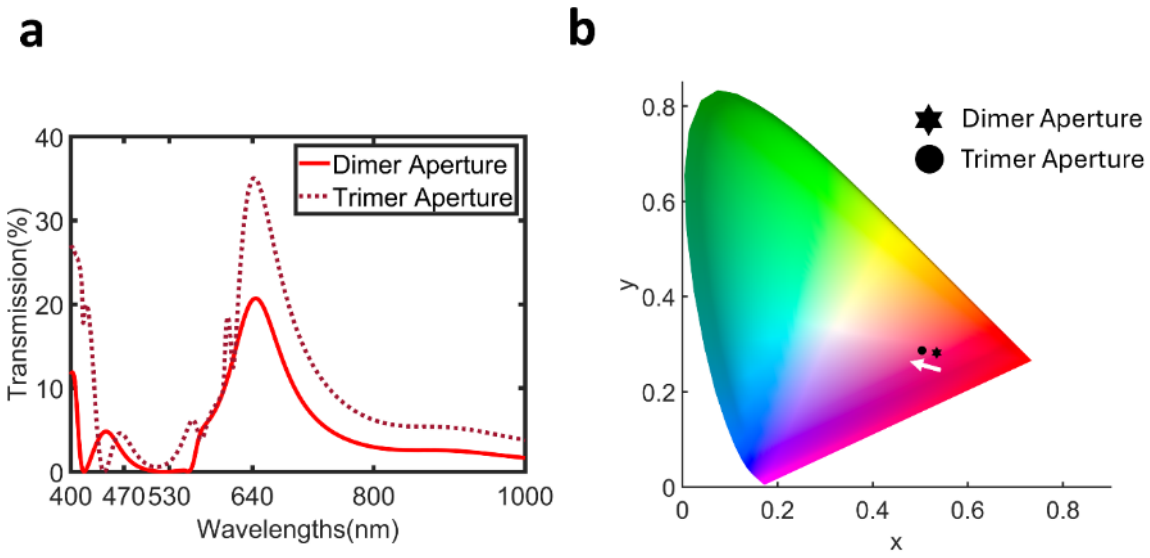

Figure 4-2 a. red channel filter transmission for dimer aperture configuration and trimer aperture configuration. **b.** converted results of the transmission spectrum in a on CIE 1931 colour gamut.

In the dimer-aperture array plasmonic filter, the structure can be interpreted as a superposition of two triangular lattice arrays (each with period P), offset by a distance Δd. Provided that $\Delta d << P$, the system still be effectively treated as a grating with period PPP, so Equation (1) continues to provide an accurate prediction of the transmission wavelength.

As further described in Section 4.2.3, the incorporation of elliptical apertures is essential for achieving polarisation sensitivity. Two key design parameters govern the optical response: the aspect ratio of the ellipses e (defined as the ratio of the major to minor axes, r1/r2), and the relative spacing ratio g, which relates to the offset by $\Delta d = P \cdot g$. In this study, the parameters were fixed to $e = 4,\ g = 0.3$. The detailed influence of these parameters is discussed in later sections. Using the green-channel filter as a representative example, the adoption of a dimer unit led to a significant improvement in peak transmission, with efficiency roughly doubling that of the single-aperture design, as illustrated in Figure 4-1(c). The complex near-field interactions—involving mechanisms such as surface plasmon polaritons (SPP), localised surface plasmon resonances (LSPR), and Wood's anomalies—may provide an additional ~3% boost in transmission, although this effect is relatively modest. Moreover, the interference phase shift contributing to the transmission spectrum is partly governed by the g parameter; variations in g induce wavelength-dependent changes

in phase, which can result in peak shifts. The trimer configuration, although capable of further improving transmission, also introduces higher-order diffraction sidebands, which appear in the visible range for red filters, as shown in 4-2. In contrast and to emphasise, the dimer structure exhibits superior NIR cut-off performance compared to the trimer. Therefore, I chose to focus further investigation on the dimer configuration.

Another critical factor is the etch depth into the substrate during aperture formation. The periodic apertures were defined in a 150 nm-thick metal layer and were intentionally over-etched by an additional 100 nm into the substrate. Although substrate etching has been discussed in earlier work [54], in this study the etch depth was extended beyond the SPP penetration depth in the substrate material to further narrow the transmission linewidth.

The penetration depth of SPP into a dielectric for a continuous substrate dielectric-metal interface without apertures can be estimated using the following equation[226]:

$$\delta_d = \frac{1}{k_0}\left|\frac{\varepsilon'_m + \varepsilon_d}{{\varepsilon_d}^2}\right|^{\frac{1}{2}} \tag{4.1}$$

where ε'_m represents the real part of the permittivity of the metal (aluminium in this case), and ε_d refers to the permittivity of dielectric, which is silicon dioxide. For 530 nm wavelength, δ_d will be approximately 260 nm. Figure 4-3 a show the SPP depth into the substrate is approximately 150 nm under TM illumination. It is found that within this length-scale, substrate etching can reduce the linewidth. From the depth-transmission spectrum, it can be observed that the linewidth decreases with increasing substrate etching depth, while the peak transmission varies within a 5% range. When the substrate etching depth exceeds 100 nm, the linewidth reduction plateaus. A substrate etching depth of 100 nm is therefore sufficient to achieve the desired effect.

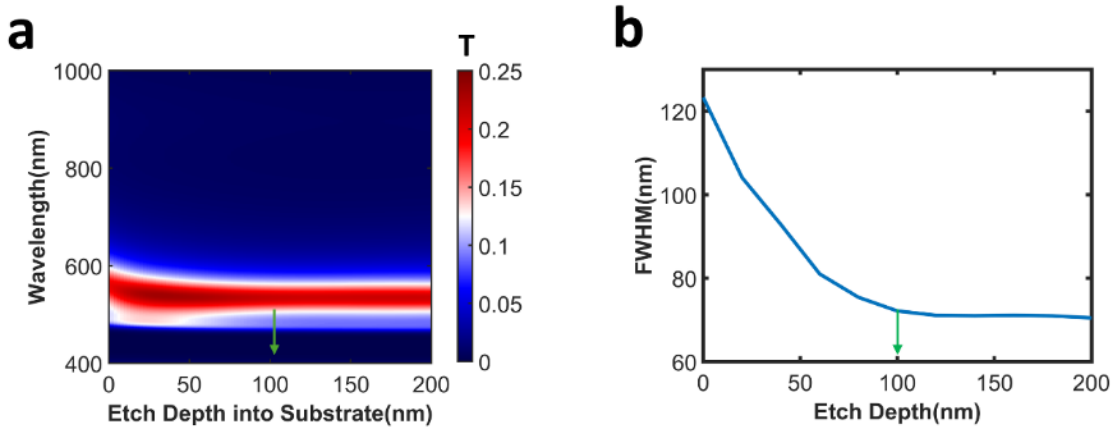

Figure 4-3 a. green filter transmission spectrum vs substrate etch depth. **b.** FWHM of the filtering peak vs etch depth.

4.2.3 **Polarisation selection**

It has been previously demonstrated that the excitation of SPPs is strongly dependent on the polarisation of the incident electromagnetic field[70-72, 216, 219], and in the context of extraordinary optical transmission (EOT), SPP formation primarily occurs at the edges of the apertures. Consequently, asymmetric or anisotropic shapes of the metal apertures resulting in unequal edge lengths in the x-y plane, or arrays anisotropic lattice cause the transmission spectrum to become sensitive to the polarisation direction of the incident wave.

As shown in Figure 4-4 (a) and (b), field enhancement is localised at the edges of the apertures, with strong excitation observed only when the magnetic field is aligned along the major axis of the elliptical apertures, i.e., perpendicular to the minor axis. By altering the orientation of the elliptical aperture's major axis, the polarisation direction of the filter can therefore be tuned accordingly. Increasing the metal thickness enhances these mechanisms

but also leads to greater Ohmic losses. Taking this trade-off into consideration, a metal thickness of 150 nm was selected, where the peak transmission remains above 20 %.

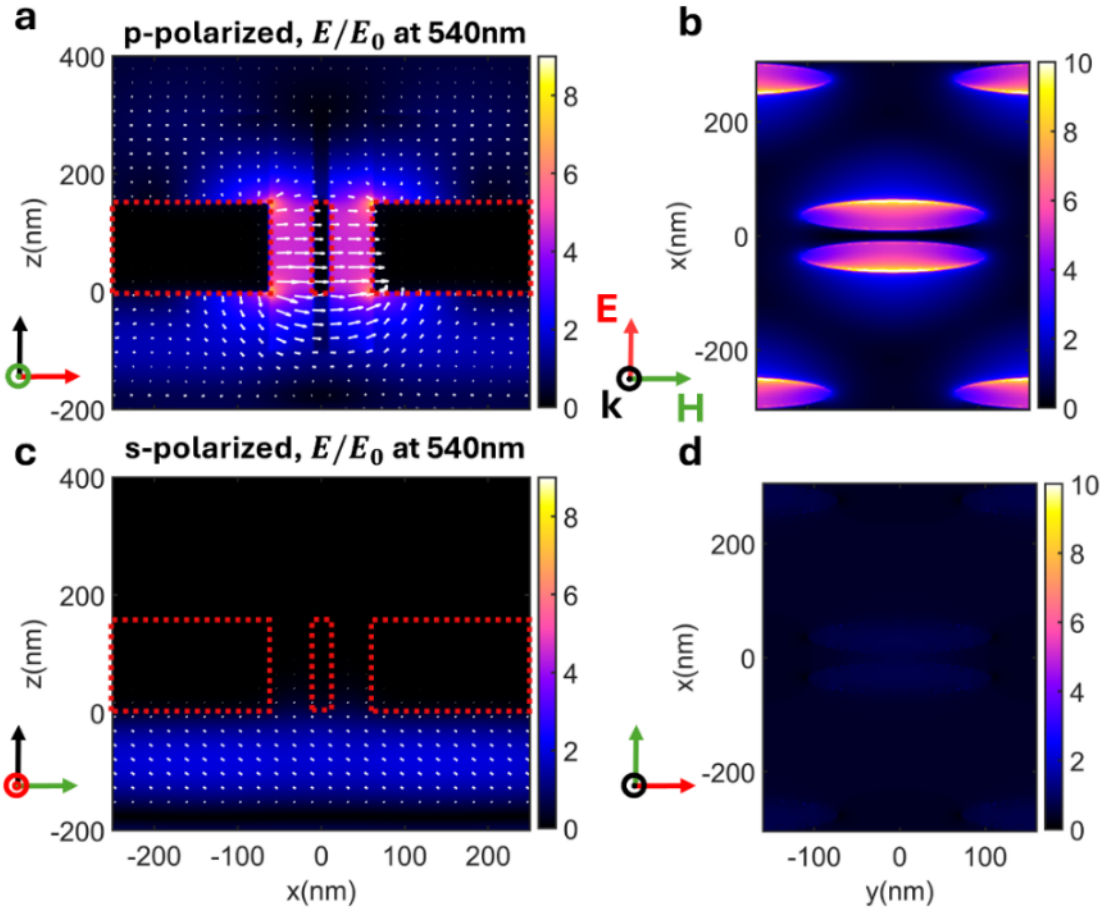

Figure 4-4. x-z view (sideview) and y-x view (top view of the dielectric-metal interface) of the normalized electric field distribution for green filter for normal incidence. The orientation of the electric field, magnetic field and the wavevector of the incident light is noted in red, green and black respectively. **a & b**. With TM-polarised light incidence (w.r.t. x-z plane). A strong field enhancement exists at the edge of the ellipse largely as a consequence of SPP modes. **c & d**. With TE-polarised light incidence. Most light is blocked by the metal film, and no field enhancement is observed.

Elliptical apertures do not differ fundamentally from the commonly reported rectangular or other anisotropic structures in the literature mentioned above. The presence or absence of sharp corners primarily affects localised LSPR modes but has negligible impact on the spectral features associated with nonlocal characteristics, which mainly depend on lattice constant and fill factor. However, in fabrication—particularly for potential wafer-scale production via nanoimprint or photolithography—the precise definition of sharp corners requires highly controlled PEC processes. Otherwise, corners naturally round off, forming

shapes closer to ellipses, and even variations in the area can shift the resonance peak position and amplitude. For this reason, an elliptical design was adopted at the design stage.

4.3 Results and discussion

4.3.1 Sample fabrication and spectrum characterisation

The fused quartz substrate was initially cleaned in sequence using acetone and IPA (isopropyl alcohol) solvents, each subjected to 5 minutes of ultrasonic cleaning in a water bath. Subsequently, 150 nm of aluminium was deposited via thermal evaporation. A 150 nm SiO_2 layer was then deposited on top as a capping and adhesion-promoting layer using plasma-enhanced chemical vapour deposition (PECVD). After another round of solvent cleaning as described previously, and a 10-minute bake at 180 °C on a hotplate, a 200 nm layer of CSAR resist was spin-coated onto the cooled substrate.

To prevent charging during electron-beam lithography (EBL), a 60 nm conductive Electra 92 layer was sputtered as a charge dissipation layer on top of the resist. The metasurface patterns were then exposed using a Raith EBPG 5200 EBL system operated at 100 keV acceleration voltage and 1 nA beam current. Following exposure, the samples were developed using n-Amyl acetate and IPA, each for 90 seconds.

The dimer aperture structures were etched using an Oxford Instruments Plasmalab RIE 80 Plus system (for the SiO_2 layer using CH_3F gas) and a Plasmalab System100 ICP 180 system (for the Al layer, using a Cl_2/Ar gas mixture) for dry etching.

A simplified schematic of the fabrication process is shown below, in which the final step of substrate etch is not shown:

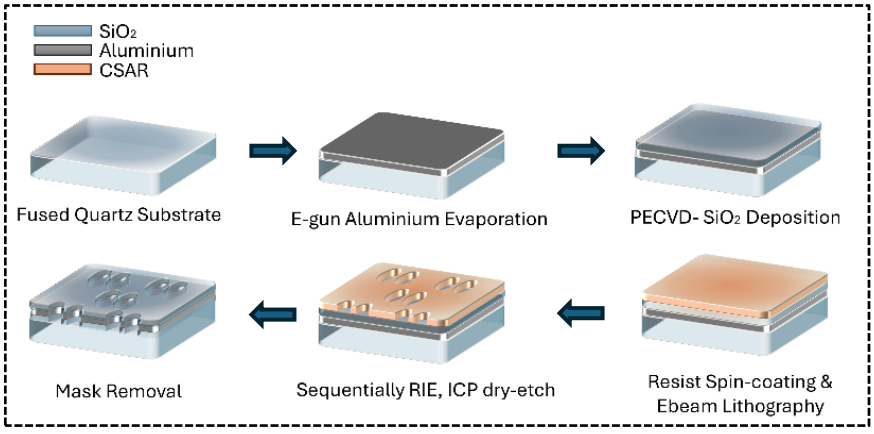

Figure 4-5 Simplified fabrication workflow for the proposed device.

For sample characterisation, a Foster + Freeman micro-spectrophotometer was employed to optically measure the spectral response of the fabricated structures. Condensers with a fixed numerical aperture (NA) of 0.5 (corresponding to f/# = 1) were used to evaluate the filter performance under different objective lenses. A wire grid polariser (Thorlabs WP25M-VIS) was inserted into the optical path to generate linearly polarised illumination. A standard halogen light source was used for illumination, and both the measured spectrum and colour output were normalised relative to the source spectrum.

4.3.2 Finite size and incident Angle tolerance analysis

To demonstrate the viability of employing the proposed structure as a focal plane array polarisation-colour filter layer for imaging purposes, its filtering performance at varying pixel sizes is of particular importance. As the device operates based on the surface plasmon polariton (SPP) mechanism, which is inherently a non-local resonance, it is anticipated that the filtering performance will degrade as the number of unit cell periods decreases.

To assess this effect, filters with finite dimensions were fabricated and characterised Specifically, square pixels of approximately 2 μm and 4 μm that corresponds to approximately 3 and 6 periods, respectively, for the red filters was made. (In fabrication, the number of periods for each pixel was rounded down to the nearest integer.) The red filter was selected the as the reference, since its wavelength (~640 nm) corresponds to the largest period, and is thus expected to experience finite-size effects more significantly than the green or blue filters at small pixel dimensions.

As shown in **Figure 4-6**(a), it was observed some degradation appeared in the spectral response for the 2 μm pixel, yet the structure still demonstrated clear red wavelength filtering behaviour. This level of performance is considered adequate for integration with typical industrial CMOS camera pixel sizes[227]. Furthermore, the design can be integrated with high-performance detectors such as single-photon avalanche diode (SPAD) detectors, which have been demonstrated with minimum pixel dimensions of approximately 8 μm, enabling simultaneous polarisation and colour sensing even under low-light conditions.

For imaging applications, the angular response of a colour filter is of critical importance. Accordingly, I have examined the performance of the proposed filter under varying angles of incidence, as illustrated in Figure 4-6(b). The analysis specifically considered the case in which the magnetic field component and the Poynting vector lie in a plane that is parallel to

the major axis of the elliptical aperture. This configuration corresponds to the condition that yields the maximum polarisation-dependent transmission.

As shown in the oblique angle response of the green filter in Figure 4-6(c), (d), and (e), the structure retains robust spectral filtering performance within the 0°–10° range of incidence, regardless of whether the incident light is TM-polarised (relative to the xz-plane) or TE-polarised (relative to the yz-plane). However, when the angle of incidence exceeds 15°, a redshift in the peak wavelength is observed, along with the emergence of higher-order resonances in the shorter wavelength region.

Notably, up to an incidence angle of 15°, the polarisation extinction ratio of the transmitted light remains above 10^5 in simulations. Because of the shown off-axis characteristics, the

proposed filter design is well-suited for imaging systems operating with focusing lenses, enabling use at an F-number as low as f/2 without introducing significant colour distortion.

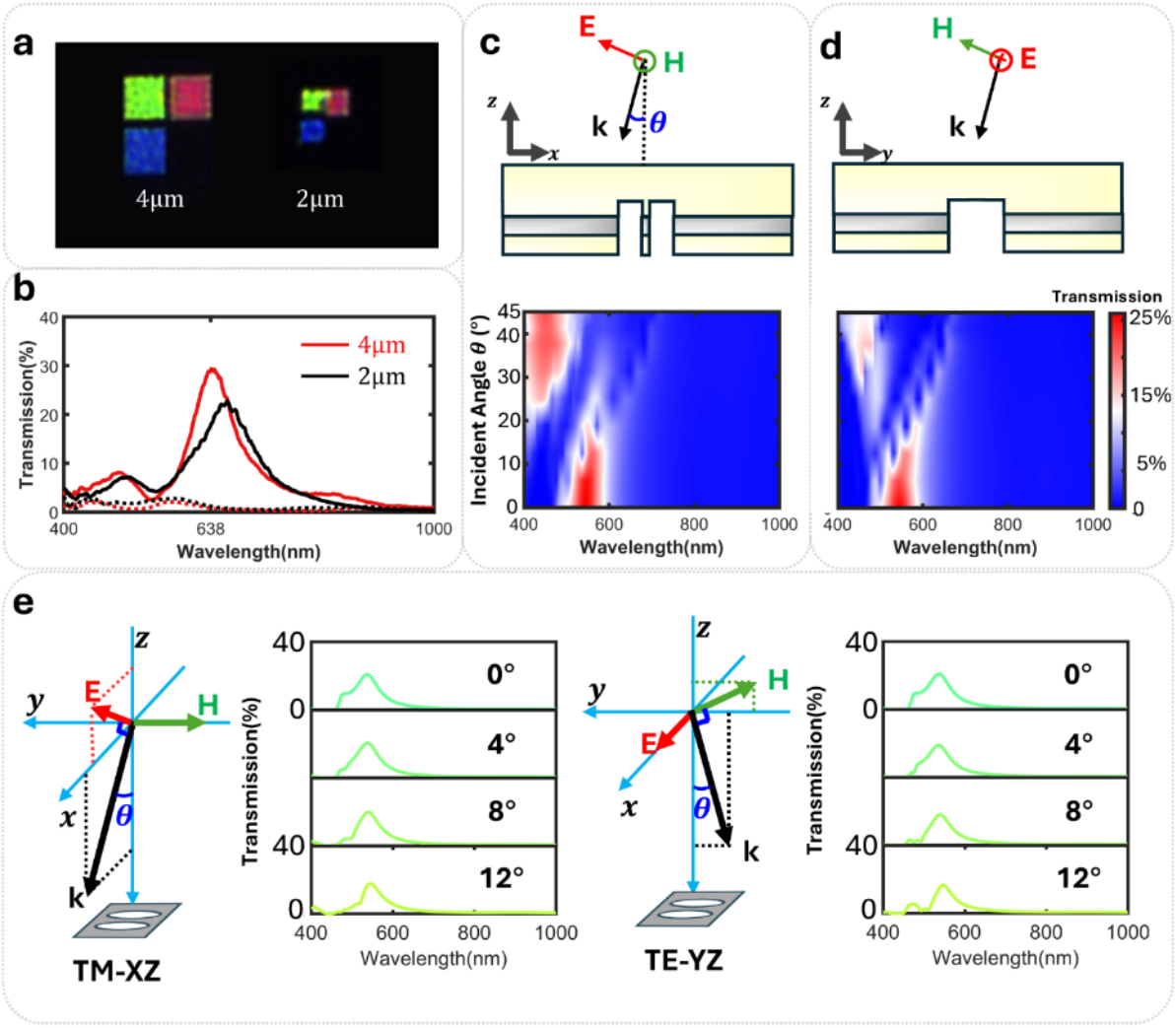

Figure 4-6 Finite sized array and angled incidence tolerance check. **a. & b.** Photomicrographs of fabricated 4 ***μm*** and 2 ***μm*** sized filter pixels and the measured spectrum for red filters. Dashed lines show TM-polarised incidence (w.r.t. x-z plane) while and solid lines show TE-polarised incidence. **c.** The effect of changing the angle of incidence ***θ*** for TM-polarised incidence with respect to x-z plane and in the wavelength range 400 – 1000 nm. **d.** The effect of changing ***θ*** for TE-polarised incidence with respect to y-z plane. **e.** The detailed transmission spectrum for angle of incidence within 12 degrees.

4.3.3 Colour – Polarisation Palette

Based on the colour-polarisation filtering principles outlined in Section 2, 20 μm × 20 μm RGB filters were fabricated as a proof-of-concept demonstration. The filtering characteristics and corresponding polarisation extinction ratios of the fabricated elements

are presented in Figure 4-7(b) and (c). The designed dimensions used for RGB pixels are listed in table 4-1.

Table 4-1 Period and corresponding dimension of the designed RGB pixels

(nm)	Period	Major length	Minor length	**Δd**
Red	420	256	64	126
Green	350	210	52	105
Blue	270	162	41	81

Spectral measurements were conducted using the optical setup illustrated in Figure 4-7(a), where a microscope coupled to a fibre-based spectrometer was used to characterise the microscale metasurface region.

The experimentally obtained transmission spectra of the RGB filters under normal incidence showed peak transmission values of approximately 25% (blue), 30% (green), and 30% (red) at central wavelengths of 465 nm, 540 nm, and 638 nm, respectively. The full width at half maximum (FWHM) for the blue, green, and red filters was approximately 75 nm, 90 nm, and 110 nm, respectively. Additionally, when the polarisation of the incident light was rotated from 0° to 90° relative to the minor axis of the elliptical apertures, the filters exhibited polarisation extinction ratios exceeding 150 (blue), 100 (green), and 20 (red). The corresponding spectral extinction ratio curves are shown in Figure 4-7(c). The E.R. here is defined as the transmission of the one linear-polarisation state divided by its orthogonal states.

In the green and red channels, the higher-than-simulated transmission coefficients and lower-than-simulated extinction ratios may be attributed to fabrication deviations and measurement techniques, as discussed later. To demonstrate the geometric tunability of the proposed structure in colour filtering, 20 filters were fabricated by scaling the periodicity while maintaining proportional consistency in other geometric parameters. The periods of these filters ranged from 240 nm to 440 nm in 10 nm increments. The associated simulation and experimental results are presented in Figure 4-7(e). Under illumination at the polarisation angle corresponding to peak transmission, the resulting spectra covered approximately 76% of the sRGB colour space in the CIE 1931 chromaticity diagram. A colour palette with a finer step size (8 nm, ranging from 270 nm to 430 nm) was also fabricated to visually illustrate the polarisation-dependent colour filtering performance, as shown in Figure 4-7(h).

A broader white-light polarisation filter can be achieved by increasing the relative length of the ellipse's major axis.

4.3.4 Image Encryption

To visually demonstrate the polarisation filtering capabilities of the proposed metasurface, I applied the encoding process shown in the Figure to orthogonally polarised letters ‘JWNC’ (James Watt Nanofabrication Centre) and ‘UOFG’ (University of Glasgow). In the final layout, the numbers 0, 1, 2, and 3 represent pixels with no pattern (transmission = 0), pixels oriented at 0° linear polarisation, 45° linear polarisation, and 90° linear polarisation, respectively. Each pixel was 8 μm x 8 μm. Light transmitted through the 45° linear polarisation filter will be seen at the same intensity for 0 and 90° incidence. After fabrication, the layout reveals different patterns when illuminated with orthogonally polarised light. **Figure 4-8**(c) shows the cross-polarised microscopic image of the letters. Using a polarizer set at 0° orientation for illumination and an analyser set at 90° orientation, only 45° filters could be imaged.

The same encoding and fabrication process can be used for two-dimensional orthogonal polarisation encoding, which could be applied to anti-counterfeiting displays operating in transmission mode using QR codes. I experimentally fabricated a polarisation encrypted bar-code shown in Figure 5(b) to demonstrate this concept. As before, the size of each functional filter pixel was 8 μm x 8 μm. The photograph of different pixels (noted as Diff. pixels) was taken using cross-polarised microscopy, where a polariser was set at 45° orientation, and an analyser was set at 135° orientation.

4.3.5 Simultaneous colour-polarisation filtering enabled micro-scale paintings

Finally, the simultaneous polarisation and colour filtering performance of the filters was demonstrated through micro-scale paintings, which may be considered the inverse process of polarisation-colour imaging. An RGB colour mixing strategy was applied to achieve full-colour micro-printing under a specific linearly polarised illumination. Each pixel in the original image was up sampled and decomposed into four subpixels: red, green, blue, and a

non-transmitting (black) subpixel. The RGB values for each subpixel were realised by rotating the polarisation orientation of the filters.

As the average extinction ratio of the three filters exceeds 20 within their respective spectral bands, intensity encoding based on polarisation angle was enabled using Malus' law. For instance, the polarisation orientation assigned to the red subpixel at the (i, j) pixel position can be described by:

$$\theta_{R(i,j)} = \arccos(I_R/I_0)^{-\frac{1}{2}} \tag{4.2}$$

where $I_R/I_0 = R_{\text{Value}}/255$. The normalised RGB values of the red pixel were selected, and the fourth subpixel was set to black instead of green to reduce EBL writing time and simplify the RGB encoding process, as the objective was to demonstrate the feasibility of colour mixing. Based on Equation (4.2) and the image encoding workflow illustrated in **Figure 4-8(e)**, two micro-painting images were produced: the **Hammermen Crest** (**Figure 4-8(f)**), representing the Incorporation of Hammermen of Glasgow, a trades guild of which James Watt was a member; the oil painting *Girl with a Pearl Earring* by Johannes Vermeer (**Figure 4-8(g)**); and the oil painting on canvas *Sunflowers* (F453) by Vincent van Gogh (**Figure 4-8(h)**). The scale bars for all images are 100 μm, with each colour subpixel measuring 2 μm. Compared to the original images, the micro printed images appear darker overall, which is expected since I intentionally up sampled the image and introduced one black subpixel in each 4-pixel RGB colour unit, significantly reducing the overall brightness. Nevertheless, as a demonstration, the outlines and shading variations in the images are still clearly visible. Figure 4-8(i) shows a zoomed-in view of the mixed-colour pixels, where the brightness variations of the RGB subpixels under 0° polarised light can be distinctly observed.

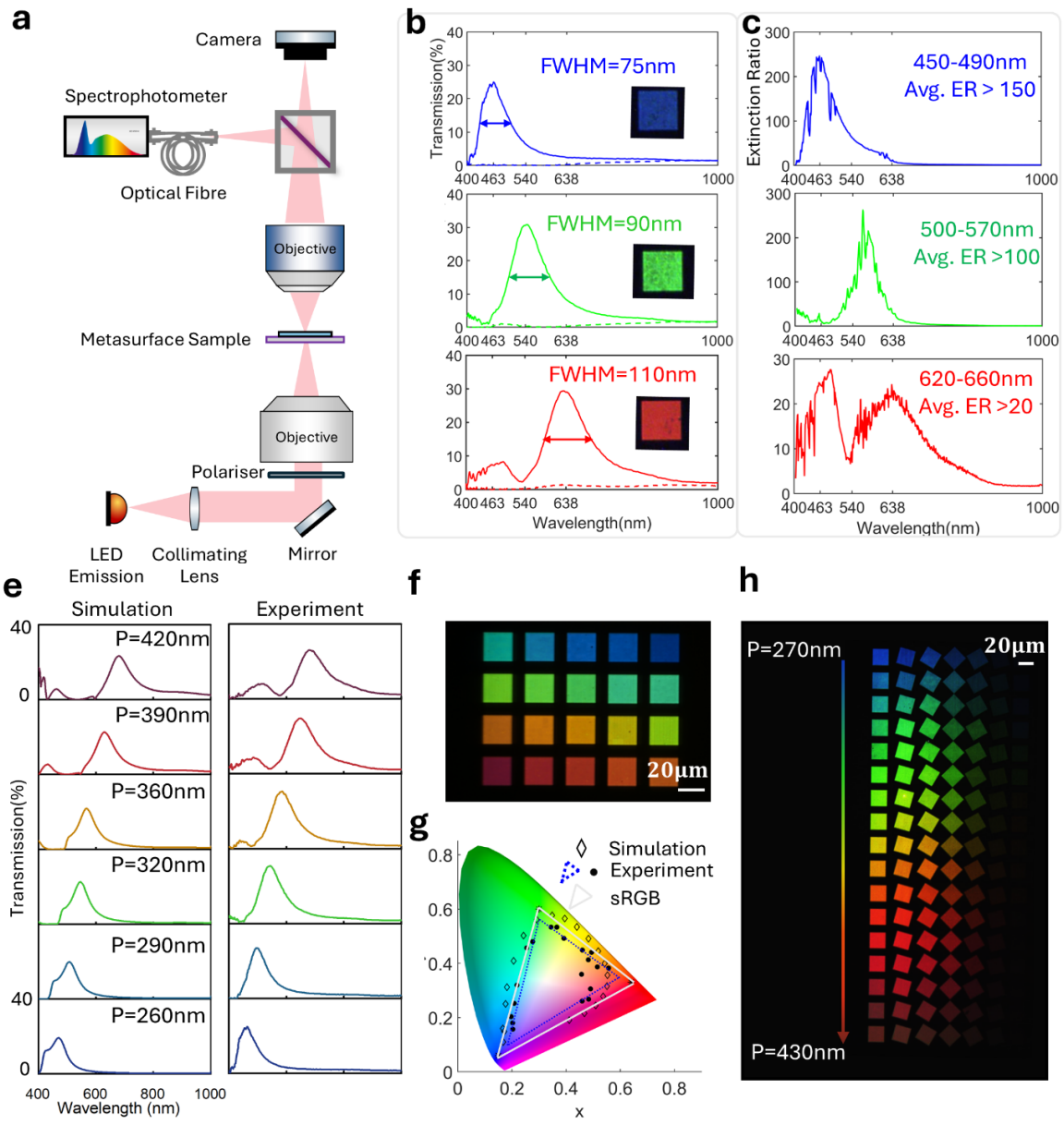

Figure 4-7 Spectral characterisation results of the fabricated dimer plasmonic metasurface sample. **a.** Optical path for sample spectral characterisation. The sample was tested in a micro-spectrophotometer in the Köhler illumination configuration, where a polarizer is settled underneath the condenser. The condenser has a numerical aperture of 0.5 and all spectra were obtained using an objective with 20x magnification. **b.** Transmission spectrum under X-polarised (E-component perpendicular to major axis, solid lines) and Y-polarised linear polarisation (E-component parallel to major axis, dashed lines) of RGB filters. **c.** Calculated extinction ratio within full spectrum. As the spectrometer readings got unstable for very low intensity illumination, I rounded all transmission smaller than 0.1% to 0.1% when calculating the extinction ratio. **e.** Simulated and tested transmission spectrum for filters with period ranging from 240 to 440nm, 6 out of 20 are shown here. **f & g.** Colour palette under microscope of the 20 filters and their calculated position on CIE 1931 axis. h. Colour-polarisation palette of 20 filters under X-polarisation illumination.

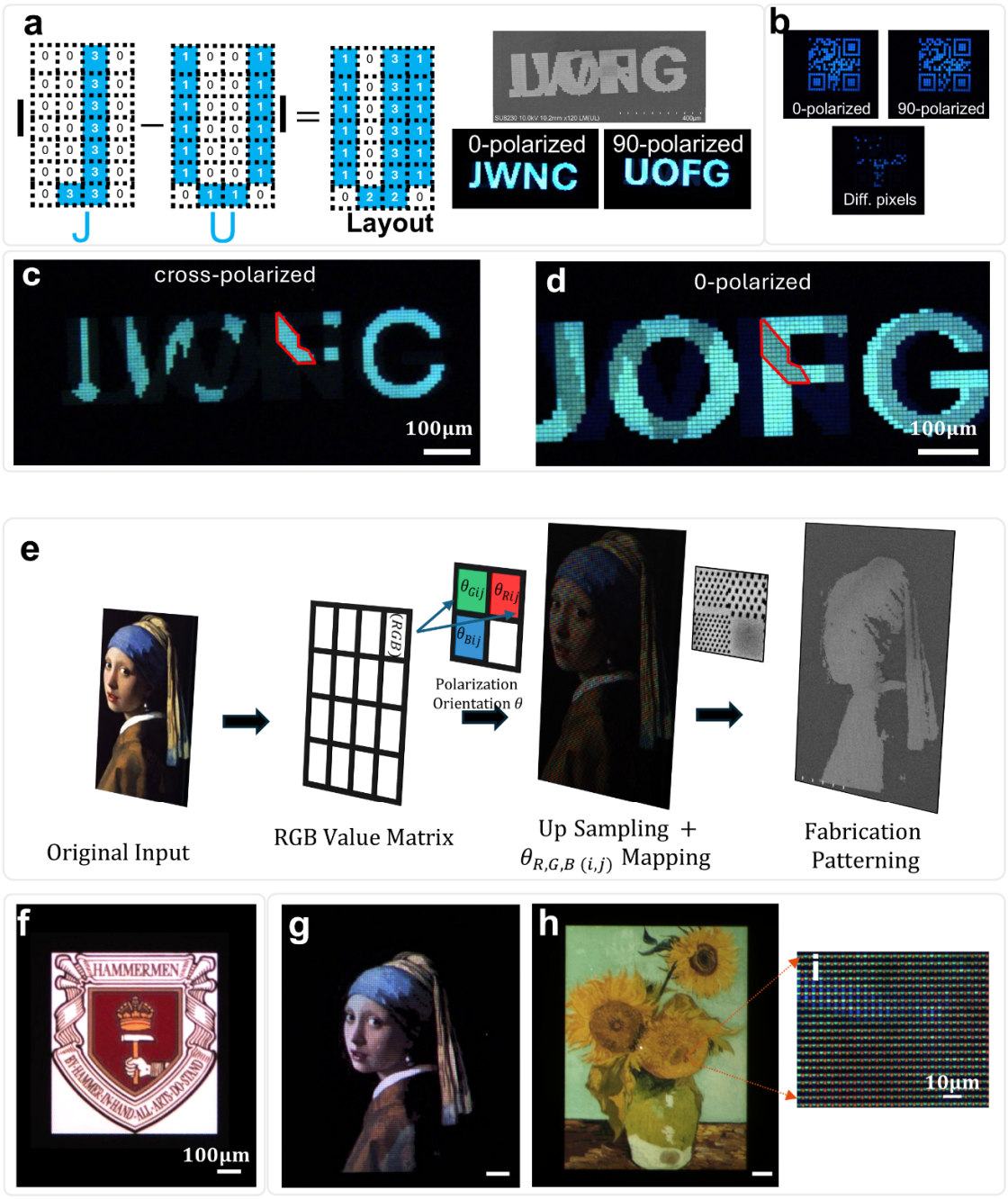

Figure 4-8 Demonstration of colour-polarisation filtering function of the proposed metasurface. **a.** Orthogonal linear-polarisation encrypted dual-state display. The pixels were encoded with (0,1,2,3) in final layout, representing no transmission, 0-degree polarisation angle, 45-degree polarisation angle, and 90-degree polarisation angle respectively. **b.** Polarisation-colour encrypted bar-coding. Two different bar-codes were encrypted in one layout, while only under blue illumination with 0-degree polarisation angle will the right bar-code appear. **c. & d**. A micrograph at higher magnification of the letters when viewed using cross-polarised imaging (polarizer and analyser aligned along 0- and 90-degree respectively) and 0-polarised imaging. The cross-polarised image shows the 45-degree polarisation filters, which resemble the area showing weaker intensity in **d**. **e.** Working principle for producing micro-scale paintings based on colour-mixing with proposed colour-polarisation filter. The RGB value of the original input was read, and each pixel were up sampled to a 2x2 block, respectively representing R, G, B channel and a black channel (no transmission). Then the RGB

values were normalized and mapped by polarisation angles, which are then fabricated through E-beam lithography and dry-etch. **f., g. & h**. Photomicrograph of the fabricated micro-paintings under polarised illumination. The scale bars are 100 μm for all paintings (The crest of the Hammermen of Glasgow in f, Girl with a Pearl Earring in g, Sunflower in h). i. Zoom-in view of the upper-right part of painting e, each colour pixel was in 2x2 μm format.

4.4 Conclusion

In conclusion, an aluminium dimer-aperture array plasmonic metasurface was proposed and fabricated to exploit the extraordinary optical transmission (EOT) effect, enabling efficient polarisation–colour filtering using CMOS-compatible materials. To validate the simultaneous polarisation–colour filtering capability of the structure, its application to structural colour generation was demonstrated. The resulting colour palette covered approximately 76% of the sRGB colour gamut, with blue (centred at 465 nm), green (centred at 540 nm), and red (centred at 638 nm) filters exhibiting full width at half maximum (FWHM) values of approximately 75 nm, 90 nm, and 110 nm, respectively, and average polarisation extinction ratios exceeding 150, 100, and 20, respectively.

Furthermore, orthogonal linear polarisation-encoded image encryption and microscale full-colour reproduction of colour-rich images were demonstrated using RGB colour mixing, based on the proposed structure. The dimer configuration demonstrated here shows strong potential for applications in display technology and imaging systems, particularly in multidimensional light-field detection when integrated with focal plane arrays.

4.5 Further discussion and future work

4.5.1 Influence of geometrical parameter e and g

In geometric dimensions, the axial ratio $e = r1/r2$ primarily affects the anisotropic response of the metasurface to incident light. When the major axis, r1, of the ellipse remains unchanged (i.e., the ratio of $r1$ to the lattice constant P is constant), as shown in Figure 4-9(a), the influence of e within the range from 3.5 to 4.5 on the transmission spectrum at the maximum (TM illumination with respect to the X-Z plane) is small, with the peak transmission and line shape remaining largely unchanged. However, Figure S.I. 1(b) demonstrates that when I take the average extinction ratio (E.R.) in the green channel range

(500–570nm), *e* has a significant impact on the extinction ratio. A higher *e* corresponds to a larger extinction ratio, which is primarily due to the increased difference in the grating-SPP interaction region under orthogonally polarised illumination.

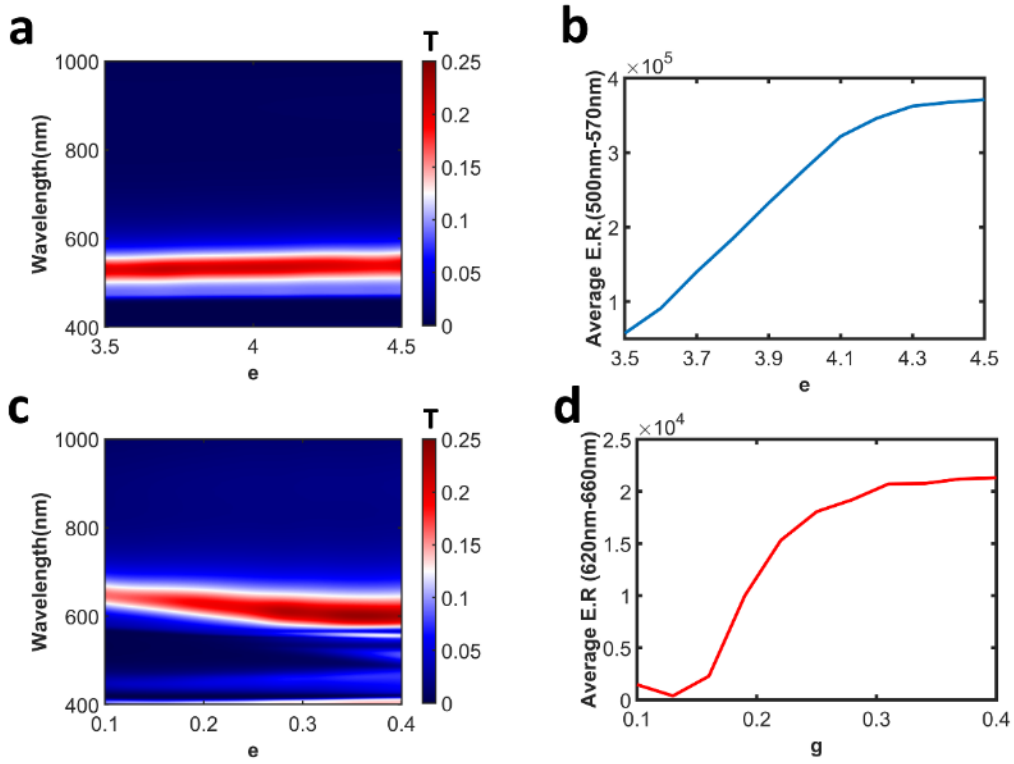

Figure 4-9 a. green channel filter transmission vs ***e***. **b.** green channel filter average E.R. (within spectral range 500-570nm) vs ***e***. **c.** red channel filter transmission vs ***g***. **d.** red channel filter average E.R. (within spectral range 620-660nm) vs ***g***.

As shown in Figures 4-9 (c) and (d), the spacing between dimer-apertures has a notable effect. Taking the red channel as an example, smaller spacing results in a lower peak transmission and a significantly reduced extinction ratio. Increasing *g* leads to a higher extinction ratio and greater peak transmission but also results in a broader linewidth, enhanced higher-order modes, and a blue shift in the peak wavelength.

The blue shift of the peak wavelength associated with the structure implies that larger structures are required for the red channel, which in turn increases the minimum compatible pixel size for red filters. As a demonstration, I select g = 0.2, which corresponds to a relatively narrow linewidth while ensuring at least three complete cycles in the x-y direction, respectively, within a 2-micron sized pixel.

4.5.2 **Efficiency enhancement with silver**

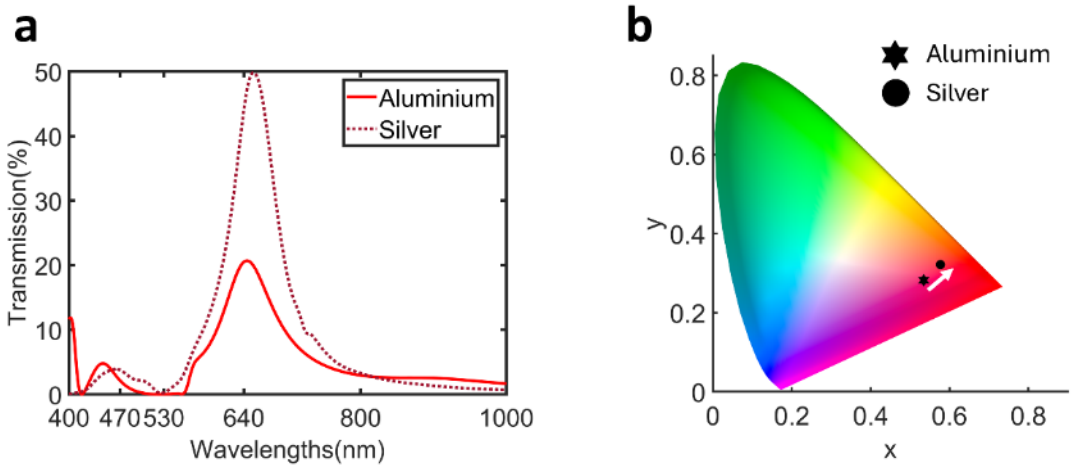

Figure 4-10 a. red channel filter transmission for comparison between aluminium aperture configuration and silver aperture configuration **b.** converted results of the transmission spectrum in a on CIE 1931 colour gamut.

Because of the lower loss features of silver compared to aluminium, a direct transmission coefficient enhancement method would be to replace the metal structure with silver. It can be clearly seen that the transmission can be enhanced to over 40% using same structure but using different dimensions compared to the structure in this work. However, silver suffers from the incompatibility to CMOS fabrication process, limiting its practical realisation.

4.5.3 Fabrication Errors

The peak transmission and linewidth are larger than simulation results for filters. This is attributed to both excessive exposure doses and overly long development times, which result in enlarged apertures. When the aperture size increases, the non-frequency-selective direct transmission also increases, whereas SPP-related modes do not increase proportionally. Consequently, although the peak transmission increases, the frequency selectivity of the filter decreases. This leads to brighter images but a narrower colour gamut. However, insufficient exposure or development can cause the apertures to remain unopened. Therefore, as a conceptual demonstration, it would be better to use slightly higher doses and longer development times to ensure the basic function of the sample. Larger apertures correspond to a smaller extinction ratio. The extinction ratio is highly influenced by the axis ratio between long and short axis. For aperture shape, it would tend to be over-etched more in the

direction along short axis (with narrower dimension) than along long axis (with wider dimension). Consequently, axis ratio between long and short axis are much smaller, as is shown in 4-11(b). The design ratio should be 4 while the fabricated sample shows a ratio of approximately 3.1. Another major factor which contributes to the reduced extinction ratio is the spectrometer detection limit. We've set the illumination LED light at maximum, while the tool still cannot obtain stable readings for TE incidence. All readings smaller than 0.1% were therefore rounded to be 0.1%, which means the E.R. ratio listed in the main text are only lower-limit estimates.

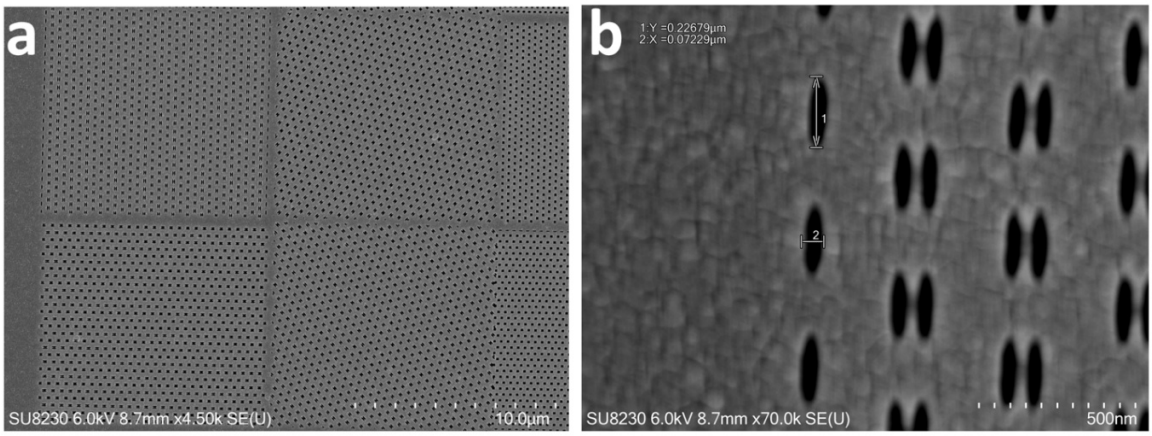

Figure 4-11 a. × **50**k magnification SEM photo of the fabricated filters. **b.** × **70**k magnification SEM photo of the fabricated red filters. The designed dimensions are 252nm and 63nm (ratio = 4) for long and short axis respectively, while the fabricated samples are 226 and 72nm (ratio=3.13) respectively.

In addition, as shown in **Figure 4-11(b)** and **Figure 4-12**, the aluminium films deposited by e-gun evaporation exhibited pronounced small grains and multiple grain boundaries. The gaps between these grains are either filled with air (sealed by a surface alumina layer) or filled with aluminium oxide, that consequently increase ohmic loss. However, the Q factor

of Al-based plasmonic filters is intrinsically low, and the corresponding resonance linewidth is already broad; this degradation is therefore not a critical limitation in practice.

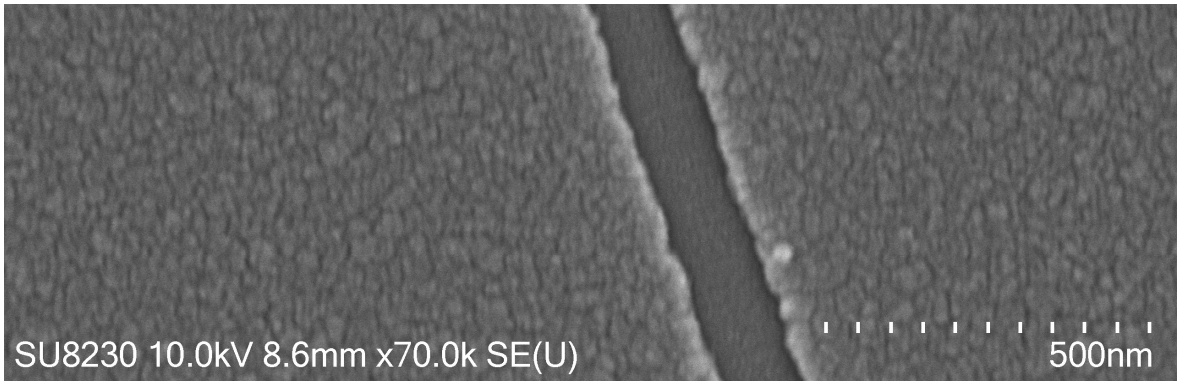

Figure 4-12 A SEM photo of E-gun evaporated Aluminium film

Grain size can be effectively increased through post-deposition annealing or high-temperature evaporation, and the use of single-crystalline aluminium via epitaxial growth could further mitigate this issue. However, aluminium inevitably exhibits higher loss compared with noble metals such as silver. Since aluminium is primarily chosen for its low cost and fabrication practicality, introducing additional processing overhead at the deposition stage is not particularly justified. In this study, room-temperature e-beam evaporation is therefore adopted, while the inclusion of an annealing step is left as a possible direction for future optimisation.

4.5.4 Cavity effects

For both back-illuminated[53] and front-illuminated[228] configurations in the integration of metamaterials with photodetectors, the intrinsic material properties of the detector must be taken into account. Using the widely adopted silicon photodetector (Si-PD) as an example, a large refractive-index mismatch between silicon and the metasurface substrate or contact layer can introduce substantial reflection because of Fresnel reflectance at the Si–metasurface substrate interface.

Consequently, the incorporation of a refractive-index-matched spacer layer often improves the quantum efficiency at a target wavelength. In practice, broadband reflection suppression can be achieved either by introducing an index-matching layer in the substrate design or by depositing an additional anti-reflection coating system between the metasurface and the

silicon detector, thereby alleviating cavity effects induced by multiple reflections. This consideration is not unique to metasurfaces; conventional thin-film optical filters similarly require careful refractive-index matching between the underlying layers and the detector.

4.5.5 Future work

The proposed approach can, following methods similar to those in ref, combine a filter with a SPAD to realise multimodal imaging—polarisation, colour, and depth. This work is in collaboration with the Strathclyde group. On this basis, several prototype samples were fabricated, one of which is shown in Figure 4-13. The format follows the common Bayer layout, except each supercell is 4×4 to cover four polarisations. Pixel size and placement are fully compatible with the pixel layout reported in ref[229].

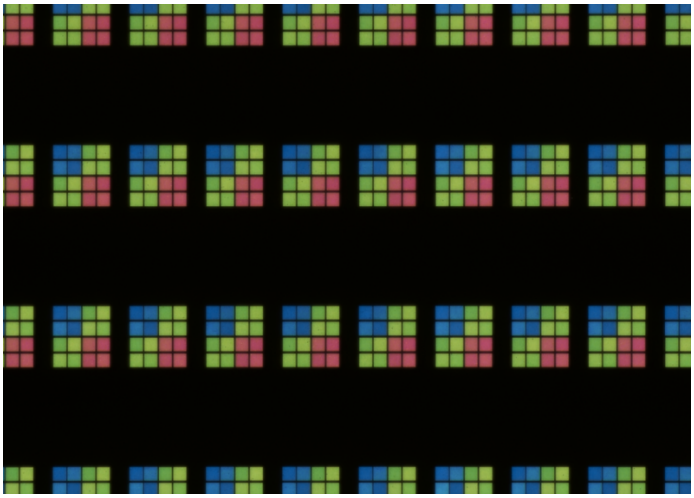

Figure 4-13 Colour-polarisation metasurface filter array for multimodal imaging.

Chapter 5 A linear-to-linear cross-polarisation conversion q-BIC metasurface for transmission mode mid-infrared spectral filtering

5.1 Introduction and motivation

High quality-factor (Q-factor) resonances are crucial in many applications, including surface emitting lasering, nonlinear enhancement and spectroscopic detection, etc. [38, 43, 83, 230-233]. Bound states in the continuum (BICs), are lossless embedded eigenstates that are perfectly confined within the continuum spectrum of radiative states[84, 85]. BICs are widely found across various physical systems and have attracted significant interest. While originating in quantum systems, BICs have also been experimentally demonstrated in macroscopic platforms such as photonic crystals and optical metasurfaces[36, 40, 41, 123, 234, 235].

Metasurfaces, composed of periodic subwavelength units[29, 67, 236], have drawn extensive attention owing to their novel electromagnetic properties. By engineering the geometry of these units, it is possible to tailor the eigenmodes of the metasurface array, thereby enabling diverse optical mode responses, including the BIC modes. In practical applications, slight perturbations are often introduced into the geometry of the metasurfaces that support BICs, converting them into leaky quasi-BIC (q-BIC) modes that can be observed as finite high-Q resonances. These high-Q, narrow-linewidth responses are particularly suited for electromagnetic wave manipulation from the visible to terahertz regimes, enabling functionalities such as narrowband perfect absorption, field enhancement and resonance coupling. Metasurfaces exhibiting such behaviour are therefore ideal for spectroscopic sensing applications [39, 42, 43, 97, 146].

In recent years, q-BIC modes supported by metasurfaces have gained significant attention for mid-infrared spectroscopic sensing. This is largely because the mid-infrared region encompasses fundamental vibrational absorption bands of many chemical molecules—so-called characteristic absorption bands[93, 237]. Detection of these spectral characteristic bands allows for both qualitative and quantitative chemical molecular analysis. Several studies have reported mid-IR spectroscopic detection using q-BIC modes supported by symmetry-broken zigzag metasurfaces[43, 97, 139, 147, 238]. However, the high-Q resonances in these structures typically operate in reflection mode, which complicates integration with detectors

and often requires additional optical elements like beam splitters to set up a reflective optical path. Q-BICs can be utilized in transmission mode by interfering with low-Q resonances to produce a narrow transparency window akin to electromagnetically induced transparency (EIT), although such EIT-like spectral response has sidelobes [36, 39, 239-241]. Without resorting to computational reconstruction or post-processing, direct spectroscopic detection remains challenging for filters with EIT-like spectral response. Many q-BIC metasurfaces that break C2 symmetry support narrowband circular cross-polarisation conversion from left-handed circular polarisation (LCP) to right-handed circular polarisation (RCP,) or vice versa [40, 59, 242-244]. By examining the T_{LR} (LCP in, RCP out) or T_{RL} term under cross-polarisation optical path, one can leverage the high-Q features of q-BICs in transmission mode—for instance, for wavelength-selective focusing under circular polarisation illumination. However, the illumination source is often broadband in mid-infrared (MIR) spectral sensing. Achieving broadband circular polarisation generation requires broadband quarter-wave plates in the mid-infrared that are difficult to realize in practice. Even when using total internal reflection instead of the principle of birefringence, its design and fabrication remain challenging and costly[245].

In this work, a dual-perturbation q-BIC metasurface design is proposed to achieve q-BIC excitation and linear-to-linear polarisation conversion, enabling transmission-mode operation of q-BIC in the mid-infrared region. Specifically, off-centre holes was introduced in a nano-disk unit cell to break geometrical symmetry and excite leaky q-BIC modes. Opening off-centre holes in resonators that support various Mie-type modes to realize high quality factor resonances has been widely reported [87, 246, 247]. Such resonators with off-centre holes, because of symmetry breaking, support high-Q leaky modes such as q-BICs that can be directly excited under normal incidence, enable strong near-field enhancement, and produce ultra-narrow spectral features. These features can be applied to nonlinear-effect enhancement[87], light-emission manipulation[248], and wavefront phase control[243, 249], etc. Single off-centre-hole structures have been demonstrated for chiral polarisation conversion[243, 249], however, the preservation of mirror symmetry of either XZ or YZ plane forbids the orthogonal linear-to-linear polarisation conversion channel, which is determined by the invariance of the Jones matrix under a mirror operation. The dual off-centre holes along the orthogonal axes simultaneously break the symmetries of both the XZ and YZ planes, and support identical responses for s-polarised and p-polarised illumination under normal incidence[250] for same amount of symmetry breaking. Because both symmetry planes are broken, it can open linear-to-linear cross-polarisation channels and achieve a

maximal polarisation conversion efficiency of 25%[191, 251, 252]. By varying the hole size, effectively tuning the duty cycle of the scattering element within a unit cell, a cross-polarisation efficiency of over 25% and high-quality factor narrow-linewidth transmission was achieved. The narrowband transmission peaks generated can be used for spectroscopic sensing in transmission mode. The reconstruction of the butane absorption spectrum in the 3200-3700 nm band using a transmission imaging setup was demonstrated. The proposed metasurface can be further integrated into polarisation sensitive infrared focal-plane-array (FPA) for multi-spectral imaging purposes.

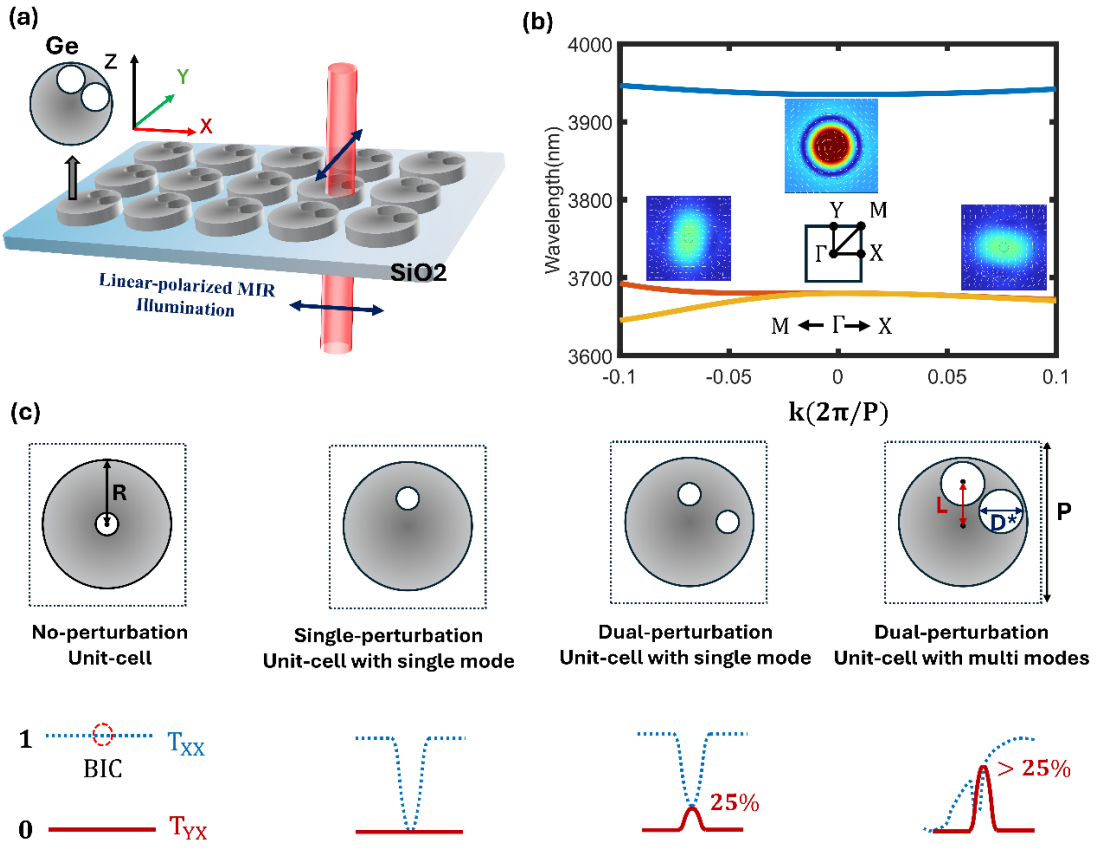

Figure 5-1 (a)(c) Schematic conceptual and geometrical design of the proposed linear polarisation conversion metasurface. (b) Eigen mode analysis of the no-perturbation unit-cell structure. The insets are the magnetic field intensity distribution of the respective modes, while the white arrows show the electric field vector distribution. Central inset corresponds to the blue curved line (TE-like modes), left side and right-side insets correspond to orange/yellow line (TM-like modes) respectively.

5.2 Design and modelling

Figure 5-1 illustrates the schematic geometry and design concept of the proposed metasurface. The structure consists of Ge nano-disks patterned on low refractive index (RI) substrate with a period of $P = 1400$ nm. CaF_2 would be a good choice since it has a low RI (1.4) and high transparency in the MWIR range. However, dry etching of CaF_2 releases contaminant hence its use is deprecated in some cleanrooms. SiO_2 was therefore used to demonstrate the principles under investigation and mainly interested below 4000 nm where IR grade SiO_2 remain low loss. The radius of the nano disk is 500nm. As shown in Figure 5-1(c), each Ge nano-disk contains a pair of holes along the X and Y axes, with each hole offset by a distance of L from the centre of the disk and having a diameter of D. These holes are introduced to break mirror symmetry along the XZ and YZ planes, thereby transforming symmetry-protected bound states in the continuum (SP-BICs) at high-symmetry points into leaky q-BICs both for x-polarised (s-polarised) incidence and y-polarised (p-polarised) incidence. The hole diameter and the disk diameter satisfy the relation $D = \mathrm{j} \cdot 2R$, where j represents the ratio between the two. In this work, $\mathrm{j} = 0.15$ was initially considered to reveal the characteristics of the q-BIC supported by the structure.

Figure 5-1(b) presents the mode supported by the structure when $L = 0$ and $\mathrm{j} = 0.1$. The magnetic field intensity and electric field vector distributions of the mode supported around 3930 nm as well as other two low-Q modes are shown in the inset of Figure 5-1(b). The inset shows a polarisation singularity enclosed by vortex linear polarisations for the mode at around 3930 nm. This mode exhibits a theoretically infinite Q-factor at the high-symmetry **Γ** point, indicating a symmetry-protected BIC (SP-BIC), as illustrated in Figure 5-2(a). Figures 5-2(b) and **2(e)** demonstrate by simulation the relation between the Q-factor and the symmetry-breaking parameters. A non-zero offset L leads to the transition from BIC to q-BIC, with its Q-factor varying as L or j increases (i.e., as the degree of symmetry-breaking increases). The Q-factor does not follow a conventional inverse square relation with L for SP-BICs[88] because at $L = 0$ and $L = D/2 + R$ there exist two fully decoupled SP-BIC. As the displacement perturbation parameter L increases from 0 to $R + D/2$, the system geometry gradually evolves from one symmetry-protected state to another. Consequently, the Q-factor of the q-BIC mode first decreases, then converges to a value that corresponds to the lower-bound of the Q-factor of the resonator, and subsequently increases to infinity, transiting to another SP-BIC state. This behaviour can be understood as a transition between SP-BICs, which raises the lower bound of the q-BIC Q-factor. In the vicinity of the two SP-

BIC states in real space, i.e., near $L = 0$ and $L = R + D/2$ system geometry configurations, the inverse-square proportionality law holds for single-perturbation and same-hole size case, consistent with the observations reported in Ref [253]. In the dual-perturbation case, there is overlap of the holes near $L = 0$, so the total hole area changes. The perturbation to the eigen field, i.e., the degree of symmetry breaking of the system, does not vary linearly with L in this region; therefore, the dependence of Q-factor on L does not follow an inverse-square relationship in this region. Figure 5-2(e) shows the dependence of the Q-factor of the q-BIC mode at Γ point on the hole-size parameter j for $L = 250$ and 300 nm, respectively. As j increases, the area increases in proportion to j^4. The perturbation to the eigen field (leading to an increase in asymmetry of the eigen field) therefore also increases. When the defect is located at different positions of the eigen field, even with the same area it produces different influences on the eigen field profile [254, 255]. Figure 5-2(c) and 2(d) show the in-plane electric-field distributions of the q-BIC mode for different hole positions (corresponding to $L = 250$ and 300 nm, respectively).

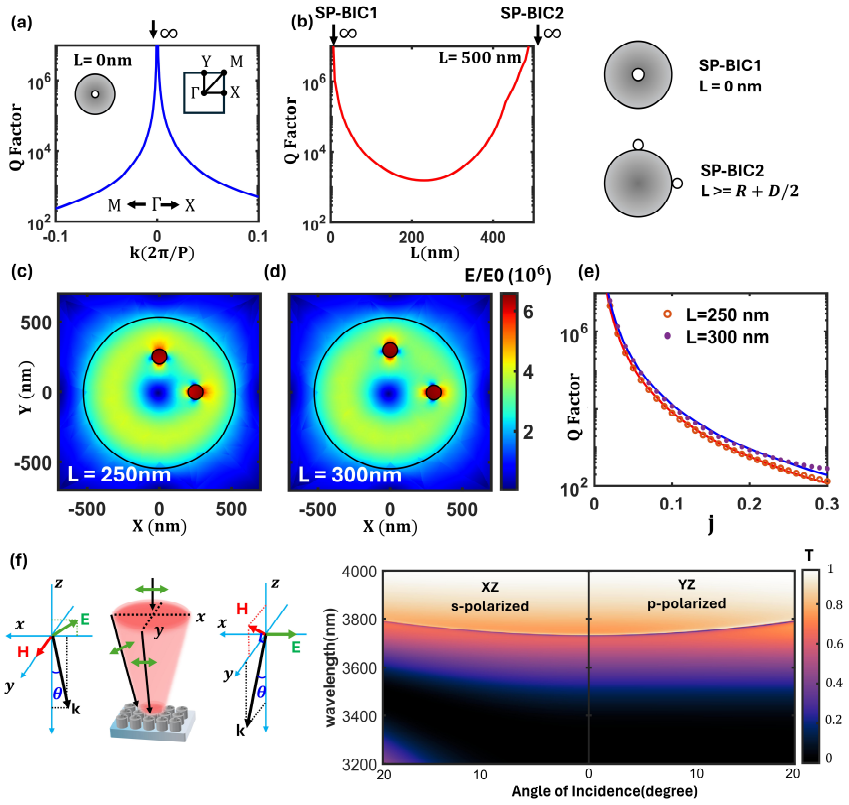

Figure 5-2 (a) Q-factor vs wavevector $\boldsymbol{k}$ for no-perturbation metasurface. Eigen frequency only contains real part, i.e. a mode that has infinite Q-factor is supported at $\boldsymbol{\Gamma}$ point, indicating a SP-BIC. (b) Q-factor vs non-zero asymmetric perturbation parameter $\boldsymbol{L}$, the righthand insets illustrate the two geometry configuration supporting SP-BICs. (c)(d) In-plane electric field distribution of q-BIC eigenmode for $\boldsymbol{L = 250}$ and $\boldsymbol{300}$ nm respectively. (e) Q-factor vs asymmetric perturbation parameter $\boldsymbol{j}$. Blue and red solid line represent fitting curve

for $\boldsymbol{L = 250}$ and $\mathbf{300}$ nm case respectively. (f) Illustration of the p-polarised w.r.t XZ plane and s-polarised w.r.t YZ plane for focused beam. The right-side plot shows the angle-resolved total transmission spectrum of p- and s-polarised incidence.

In Figure 5-2(e), the red solid line and the blue solid line respectively correspond to the fitted curves of Q-factor with respect to j for $L = 250$ and 300 nm; the fitting function used is:

$$Q = a * j^{-k} \tag{1}$$

The fitting results for (a, k) are $(1.12, -3.865)$ and $(1.932, -3.829)$ for $L = 250$ and 300 nm respectively, confirming that applied local perturbations at different positions of the eigen field leads to different regularities of influence , i.e. different scaling laws , on the q-BIC Q-factor value; this observation is consistent with the existing report in Ref[254].

Since the perturbations are introduced along both the X and Y axes with same parameters, the system maintains effective 90° rotational invariance from local field perturbation point of view. The transmission coefficients therefore satisfy $T_{xx} = T_{yy}$ and $T_{xy} = T_{yx}$, rendering the transmission spectra under s-polarised and p-polarised illumination identical. Notably, the q-BIC generated exhibits minimal angular dispersion over a broad range of incident angles for both s- and p- polarisations. For instance, within an incidence angle range of 0° to 10°, the shift in resonant centre wavelength is less than 15 nm. This characteristic is particularly important for applications involving incoherent or focused illumination[256], since even when linearly polarised light is used in an optical system, the actual incidence inherently includes both s-polarised w.r.t YZ plane and p-polarised w.r.t XZ plane. As illustrated in Figure 5-2(f), the identical s- and p- polarisation responses and low angular dispersion ensure spectral purity when using focused light illumination within 10°.

Although the proposed metasurface simultaneously shows narrow linewidths associated with the q-BIC and cross-polarisation conversion in transmission mode, the conversion efficiency has a fundamental limitation. For single-layer, ultra-thin passive metasurfaces, it can be theoretically shown that the coupling efficiency between orthogonal polarisations supported by a single-mode resonance has an upper limit, making complete polarisation conversion (CPC) impossible[251, 252]. This limitation can be derived using a four-port model:

$$\left|S_{yx}\right|^2 = \mathrm{Re}|S_{xx}| - |S_{xx}|^2 \quad (2)$$

$\left|S_{yx}\right|^2$ will reach maximum value of 25% when S_{xx} = 0.5 for positive $\left|S_{yx}\right|^2$ solutions of equation (1). In our structure, when linearly polarisation of the incidence light is along either the x-axis or y-axis, it satisfies $\mathrm{Re}|S_{xx}| = 0.5$ around q-BIC resonance frequency**,** while $\mathrm{Re}|S_{xx}| = 1$ when away from q-BIC frequency. Consequently, non-zero values of $\left|S_{yx}\right|^2$ only occur in the vicinity of the q-BIC resonance. The conclusion is derived in detail using temporal coupled-mode theory (TCMT) in Appendix TCMT derivation.

To overcome the 25% limit on cross-polarisation conversion at **Γ** point in a single-layer, ultra-thin metasurface, it is necessary to break the constraint of single-excitation or single-mode. To maintain simplicity in our system, the breaking was achieved by introducing an additional low-Q mode that couples with the q-BIC mode. As shown in Figure 5-3(a), by adjusting the hole size or the offset L, the relative spectral position between the low-Q magnetic dipole (MD) mode and the q-BIC mode can be tuned. In this demonstration, $L = 250$ nm was fixed and the hole diameter D was varied; the corresponding maximum of T_{yx} is also shown in Figure 5-3(a). It can be observed that as the hole diameter increases, the central wavelengths of q-BIC mode and low-Q MD mode were gradually tuned to be closer. The critical point for T_{yx} to go beyond 25% is around $j = 0.13$. At the sampling points in Fig. 5- 3(a), the width of the 'error bar' indicates the magnitude of the linewidth of the q-BIC mode derived from the imaginary part of the eigen-frequency solutions. As j is increased, however, the q-BIC mode becomes more leaky and therefore couples more easily to other modes. Around $j = 0.38$, the maximum unidirectional (transmission port) enhancement for the cross-polarisation channel can be achieved, and at the resonant centre wavelength the reflected cross-polarisation channel is nearly forbidden, as shown in Fig. 5-3(a) and 5-3(f). Through further multipolar expansion analysis, this phenomenon is attributed to the interference enhancement between the multipoles that contribute to the far-field scattering cross-polarisation channel. The reallocation of the multipole components was caused by mode coupling, which makes the scattering field lose symmetry and realizes unidirectional enhancement of the scattered energy, i.e., the Kerker effect (KE)[257, 258]. In this case, the unidirectional enhancement is mainly because of the interference between the electric dipole (ED) with even parity and the magnetic dipole (MD) with odd parity multipole components that respectively support the q-BIC and MD modes. Taking normal incidence and considering only s-polarised input (x-polarisation) and p-polarised output (y-

polarisation) as an example, the multipole components contributing to this cross-polarisation channel, expanded up to the quadrupole, can be written as:

$$t_{yx} = K \cdot \left(\mathrm{ED}_y - \frac{1}{c}\mathrm{MD}_x - k^2 \mathrm{TD}_y - \frac{ik}{6}\mathrm{EQ}_{zy} + \frac{ik}{2c}\mathrm{MQ}_{zx} \right) \quad (3)$$

Where t_{yx} denotes the complex amplitude of the far-field forward scattering; the power transmittance therefore is $T_{yx} = \mathrm{abs}|t_{yx}|^2$. The abbreviations of the multipoles are Electric Dipole (ED), Magnetic Dipole (MD), Toroidal Dipole (TD), Electric Quadrupole (EQ), and Magnetic Quadrupole (MQ). K is a normalisation parameter that is related to the amplitude of the incident field and unit cell area of the periodic resonator. From Fig. 3(b), it can be observed that the far-field scattering energy reconstructed from **equation (3)** agrees well with the transmittance obtained from the S parameters. The parts that do not match can be attributed to a slight asymmetric background refractive index and the presence of higher-order multipoles. In short, Figure 5-3(b) demonstrates the validity of this decomposition. The expressions of multipole expansions and the choice of components are provided in Appendix Multipole expansion. Figure 5-3 (h)–(i) show the relative magnitudes of each multipole; it can be observed that the relative magnitudes of ED and MD in the hybrid mode rapidly approach each other and reach a maximum at $j = 0.38$. At this point, the in-phase ED_y and MD_x amplitudes are nearly equal, which satisfied the requirement of KE, achieving the maximum unidirectional transmission enhancement. When j is further increased, the relative amplitude of MD_x decreases, leading to a reduction in unidirectional enhancement.

It is worth mentioning that the calculations for the eigenmode analysis, quality factors and multi-polar expansion were conducted using COMSOL Multiphysics 6.2 wave-optics module. The angle-resolved transmission spectrum was calculated using the rigorous coupled-wave analysis (RCWA) method. In the simulations, the real part of the refractive index of the substrate and Ge were set to be 1.4 and 4.03 respectively, while both materials can be viewed as transparent in the spectral range of interest. Periodic conditions were applied to both X and Y directions of the unit cell. Two ports, flow-in port and flow-out port, were respectively placed 5000 nm below and above the germanium layer to eliminate near-field influences. Perfectly matched layers were applied in Z direction as an absorbing material and to cut off the simulation region. All the calculated data were post-processed and plotted using MATLAB.

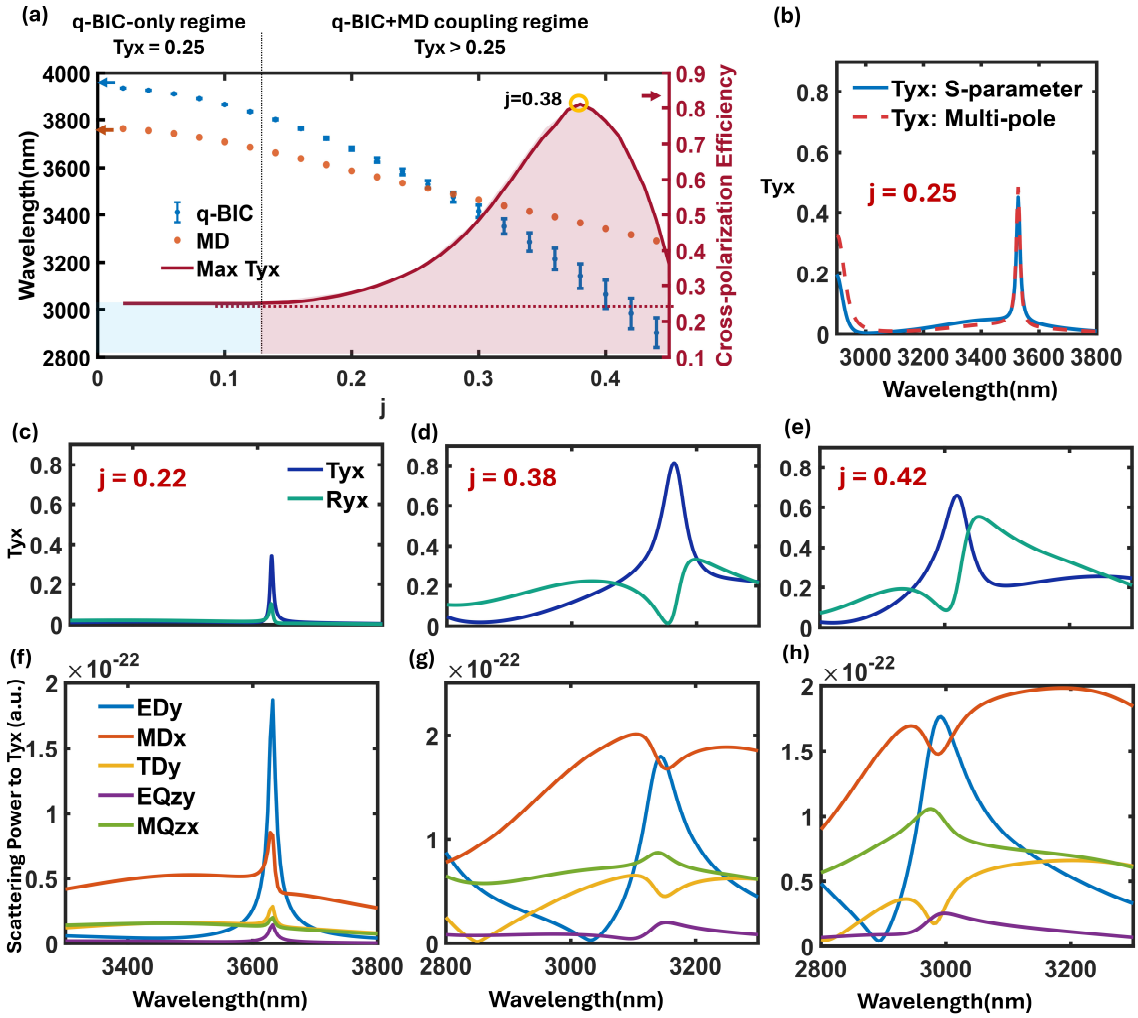

Figure 5-3 Illustration of mode coupling and unidirectional scattering enhancement. (a) Left-axis: eigen-wavelength vs $\boldsymbol{j}$ for q-BIC mode and low Q-factor MD mode respectively. The vertical bar at each point represents the bandwidth of the mode derived from the imaginary part of the eigen frequency. Right-axis: peak cross-polarisation efficiency vs j, where around $\boldsymbol{j} > 0.13$, $\boldsymbol{T_{yx}}$ surpass the limitation of 0.25. (b) Comparison of Tyx extracted from S-parameter of the resonator and derived from multipolar-expansion components that contributes to cross-polarised transmission port for $\boldsymbol{j = 0.25}$. (e) – (g) Tyx and Ryx with different j parameters, (h) – (j) shows their corresponding multi-polar expansion (to quadrupole components).

Considering the linewidth and transmission, a parameter of $j = 0.25$ was chosen, which gives a peak $T_{yx} > 40\%$ as well as a linewidth$<$ 20 nm in simulation.

5.3 Fabrication and results

A 25x25 mm IR-grade (water-free) fused silica substrate was first cleaned using acetone and IPA in an ultrasonic water bath. It was then deposited with 700($\pm$20) nm amorphous Ge using electron beam evaporation in a Plassys MEB 550s. An extra 30($\pm$5) nm silicon nitride layer was evaporated on top to enhance adhesion of the electron beam resists using plasma-enhanced chemical vapor deposition (PECVD) in an Oxford Instruments PlasmaPro system. After further solvent cleaning and drying on a hotplate, the sample was spin-coated with 200 nm ZEP520A electron-beam resist. The resist was patterned in a Raith EBPG5200 electron beam writer and developed successively in amyl acetate for 1 minute and o-xylene for 5 seconds. The sample was rinsed in IPA for 1 minute to remove any residual resist. The developed sample was then placed in the KLA-SPTS Rapier Deep Reactive Ion Etching tool for pattern transfer into the Ge layer, using C_4F_8/SF_6 etch gases with an 86/34 sccm flow rate. Finally, the sample was cleaned in oxygen to remove the last remaining resist. The silicon nitride layer was left as a protection layer to the upper surface, as it has nearly no spectral influence on the performance.

Sixteen metasurface regions were fabricated with varying scaling factors (ranging from 0.88 to 1.03 with step size 0.1) using the methods mentioned above, to cover the absorption band of butane. Scanning Electron Microscope (SEM) images of the fabricated sample are shown in **Figure 5-4(a)**. It can be seen from the SEM image that vertical sidewall was achieved. The Fourier Transform Infrared (FTIR) testing setup is presented in Figure 5-4(b). A pair of NA = 0.4 Cassegrain objectives with 18-degree centre angle of incidence was used as the condenser and imaging objectives, respectively, forming a rigorous Köhler illumination optical imaging path. A customized aperture was used to block half of the Cassegrain objective and reduce azimuth angle of incidence. The sample was either tested under 18-degree angle of incidence or tilted 18 degrees to form normal incidence. Characterisation was performed on 200 × 200 μm functional region. It is shown in Figure 5-4(c) that the fabricated sample showed identical spectral response in transmission for s-/p- polarisation illumination even under angled incidence, which is consistent with Figure 5-2. To evaluate cross-polarisation conversion efficiency, a pair of linear polarizers was placed before the condenser and after the imaging objective. As shown in Figure 5-4(d), The peak transmission efficiency of the sample reaches approximately 30%, with a linewidth narrower than 60 nm, corresponding to a Q-factor of approximately 60 in the mid-infrared range. These data are comparable with transmission or modulation depth results reported in the literature for

experimentally fabricated metasurfaces[96, 138, 139]. The Q-factor is, however, lower owing to the relatively high defect density in the amorphous electron beam evaporated Ge available. Another important cause of the lower Q-factor observed is that the existence of ranged angle of incidence even when the aperture was applied. A better result both in terms of peak transmission and linewidth would be obtained using rigorous parallel incidence setup, e.g. using a highly collimated tuneable Laser. The experimental results that have been obtained demonstrate the scaling capability of the design. Simply multiply all geometrical parameters by a scaling factor S will shift the centre wavelength correspondingly. The centre wavelength of T_{yx} increased linearly along with the scaling factor, as derived and shown in Figure 5-4(e) and (f).

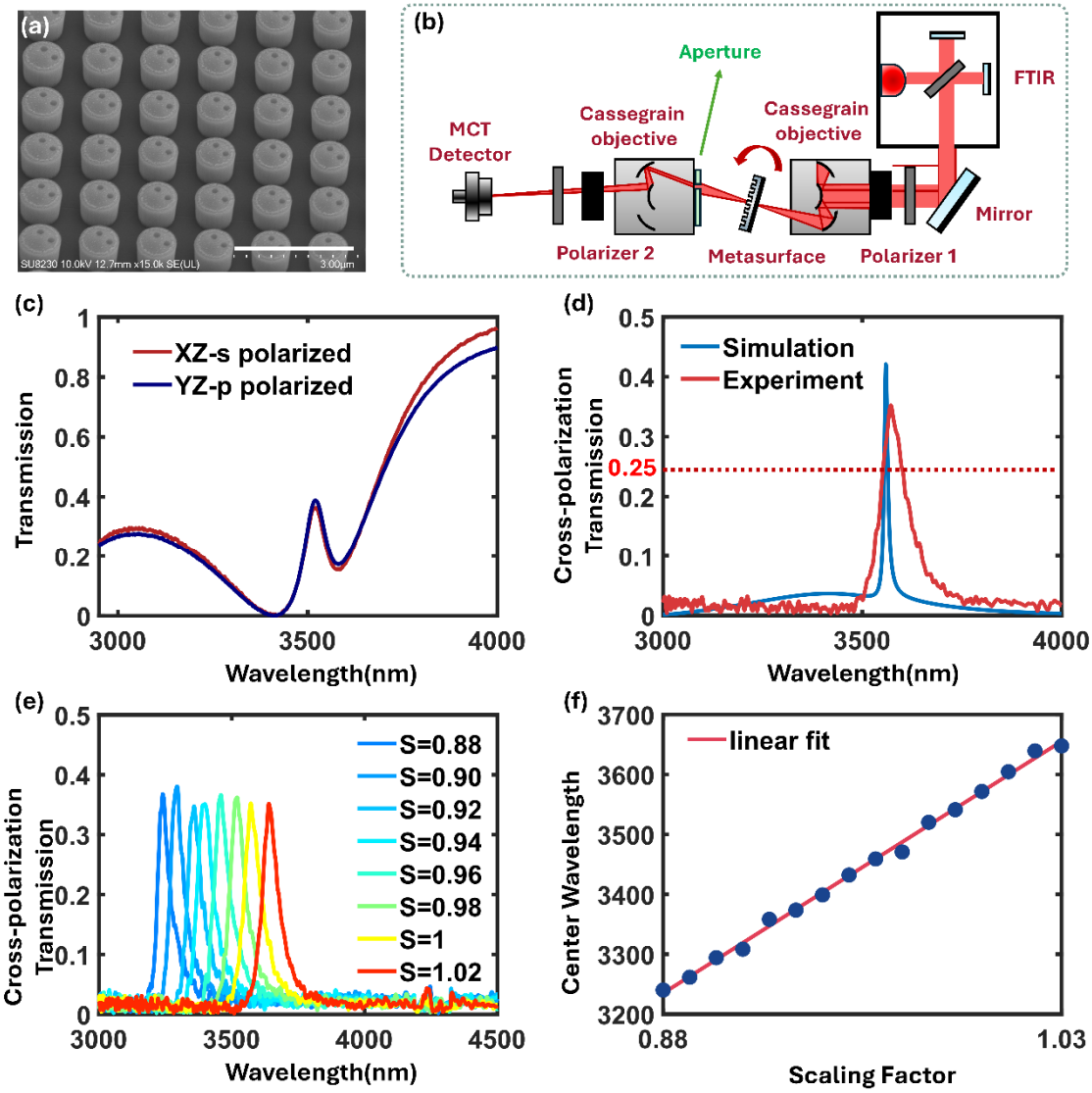

Figure 5-4 Characterisation of the fabricated metasurface samples. (a) Tilted view SEM photo of the fabricated metasurface. The sample was coated with 30 nm of Cr to enhance the imaging quality in SEM. (b) Illustration of the optical path for transmission spectrum tests with microscopy-FTIR. (c) Experimental transmission data

for p-polarised incidence (dark red) and s-polarised incidence (dark blue) under 18-degree angle of incidence without aperture. (d) Experimental cross-polarisation transmission data in simulation (blue) and experiment (red) with normal incidence (red) for scaling factor $\mathbf{S} = \mathbf{1}$ sample. The simulation data demonstrated was under normal incidence. (e) Tested transmission spectra of the fabricated samples with different scaling factors. (f) Derived centre wavelength of the $\boldsymbol{T_{yx}}$ versus scaling factor.

All infrared transmission spectra of the metasurfaces were tested using a Bruker FTIR Vertex 80v and a Hyperion 1000 microscope equipped with a liquid-nitrogen cooled MCT detector. The background tests were conducted in the air. The polarizer and analyser were both Thorlabs WP25M-IRC that were orthogonally oriented at the input port and output port respectively. The transmission-axes of the polarizers were either along the X-direction or Y-direction with respect to the sample. It is worth noting that a customised aperture was applied to form normal incidence as shown in Figure 5-4 (b). To reduce the range of the angle of incidence, holes were drilled on a metal plate to form an aperture. A tape was used to stick the aperture on the reflective objective entrance pupil. The radius of the plate is the same as parameters A shown in Fig. 5-5 (a) model 50105-01. The aperture position is designed to be cantered at 18-degree angle of incidence, which corresponds to 7.79 mm from centre. The length of the aperture is 1 mm, which allows [16.9,19.2] degree angle of incidence. When the sample is tilted to 18-degree, the allowing AOI is [-1.1,1.2] degree. The parameters in (a) are quoted from https://www.newport.com/p/50105-01.

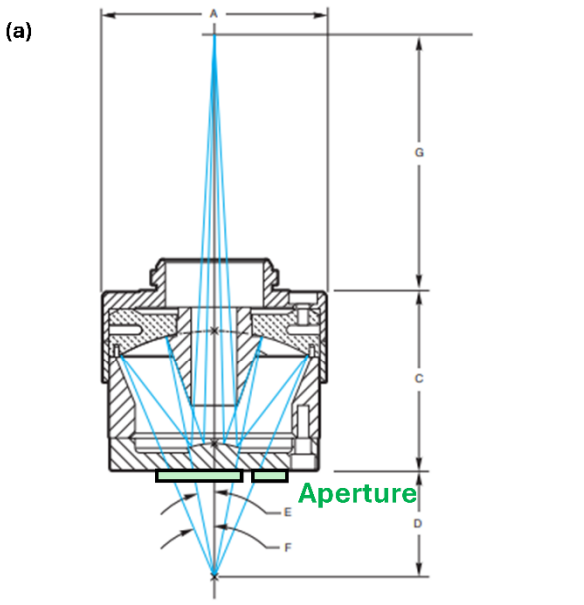

Dimensions [in.(mm)]

Model	A	B	C	D	E	F	G
50105-01	1.94 (49.3)	N/A	1.52 (38.6)	0.94 (24.0)	12.0°	23.6°	6.30 (160.0)
50105-02	1.94 (49.3)	0.383 (9.72)	1.52 (38.6)	0.94 (24.0)	12.0°	23.6°	N/A
50102-01	1.94 (49.3)	N/A	1.52 (38.6)	0.41 (10.4)	15.0°	30°	6.30 (160.0)
50102-02	1.94 (49.3)	0.212 (5.3)	1.52 (38.6)	0.41 (10.4)	15.0°	30°	N/A

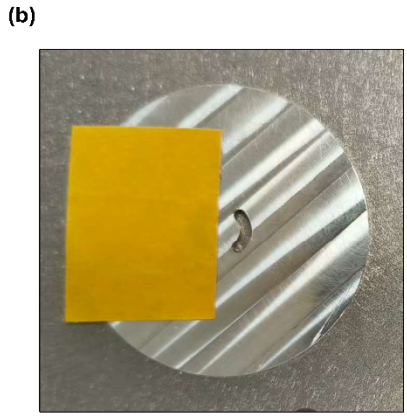

Figure 5-5 (a) Parameters of the reflective objective and (b) Photo of the aperture with drilled hole.

The cross-polarisation sensitive transmission characteristic enables a possible form of binary image encoding or even more complex encryption. Here a 21 × 21 Quick Response code (QR code) format is shown as an example in **Figure 5-6**. A 50 × 50 μm metasurface region was deined as a single pixel and constructed a QR code matrix using two types of pixels corresponding to $L = 0$ nm and $L = 250$ nm, both with $j = 0.25$. The $L = 0$ pixels support a lossless BIC and a low-Q MD mode, resulting in near-zero broadband transmission in the cross-polarisation imaging (note as cross-polarisation path) path and non-zero broadband transmission in the parallel polarizer-analyser path (note as co-polarisation path). In contrast, the regions composed of $L = 250$ nm units exhibit slightly weaker broadband transmission under co-polarisation illumination path (because of the transmission dip from the q-BIC), while maintaining non-zero broadband transmission in the orthogonal path. The correct QR code therefore only appeared under infrared illumination that includes the designed transmitting bands (around 3600 nm here) and using an active cross-polarisation imaging system, as shown in Figure 5-6 (f). The FLIR MWIR cooled camera worked in both passive and active imaging modes. The image of the sample taken in the passive mode, when the thermal emitter was shut off, is shown in Figure 5-6 (c). Images taken in active mode are shown in Figure 5-6 (d) and (e) with different polarisation and illumination wavelength

selective filters in place. The correct QR-code showed for T_{yx} setup only in Figure 5-6 (f) that matches with design in Figure 5-6 (b). When applying a 4.26 μm bandpass filter (Thorlabs FB4260-105) to the thermal emitter, the active imaging picture shown in Figure 5-6 (d) had nearly identical features to passive imaging, indicating zero transmission.

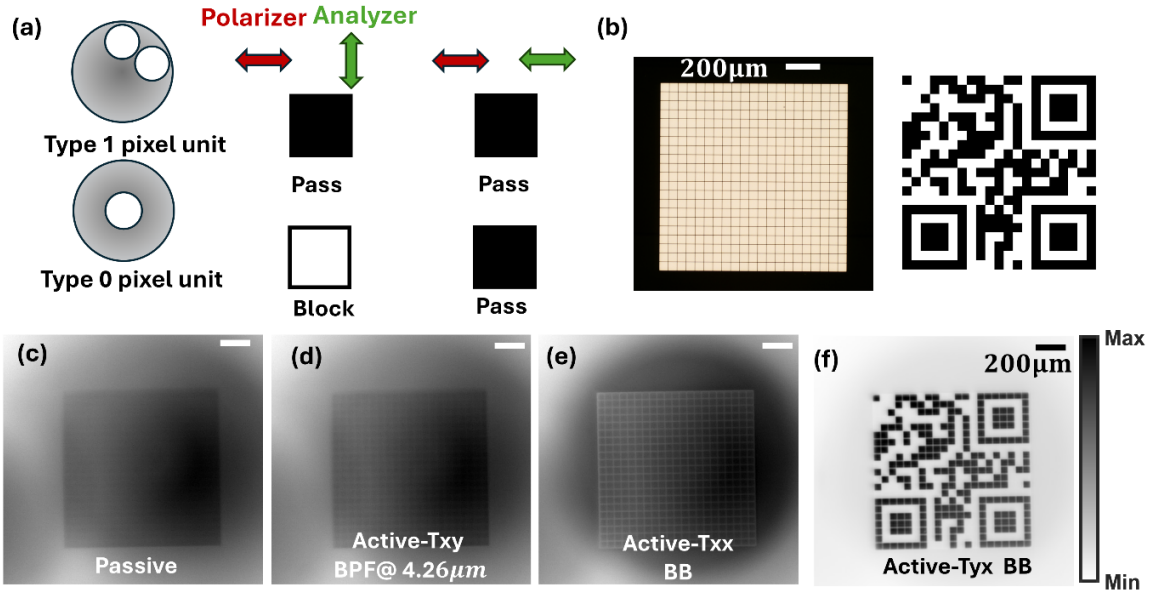

Figure 5-6 (a) QR-code binary encryption pixel unit design. Type 1 pixel will allow light transmission for both non-orthogonal polarizer-analyser (co-polarisation) path and orthogonal (cross-polarisation) path. Type 0 pixels will only allow light transmission in co-polarisation path. (b) Optical photo of the fabricated 21×21 formatted Quick-response (QR)-code encryption sample and its pattern design. (c) Thermal photo of the sample in passive imaging mode without a thermal emitter. (d) BPF: Bandpass Filter. Cross-polarisation active imaging photo of the sample with band-pass illumination centred at 4260 nm and FWHM ~ 100 nm. (e) BB: Broadband MWIR illumination [3000-5000 nm]. Active imaging photo taken under non-orthogonal path. An attenuator was applied in (e) to avoid saturation. (f) Cross-polarisation image under active imaging mode and broadband illumination that includes 3600 nm band. The colormap only applies to (f). All the scale bars shown in Figure 5 represent 200 μm.

Finally, the fabricated 16 metasurface filters was applied with different scaling factors to reconstruct the absorption spectrum of butane in the MIR region. The optical setup of the reconstruction experiment is the same as the optical path shown in **Figure 5-7(a)**. Butane gas was sprayed and applied near the light source; MIR radiation emitted from the thermal emitter was therefore spectrally altered by butane absorption. The transmitted light was then used as the illumination source to image the metasurface array. A focal plane array FLIR A6750sc infrared camera was placed at the image plane for data collection. By analysing the

relative change of the intensity of individual metasurface regions (each corresponding to a different central wavelength as shown in Figure 6(b)) with and without butane gas, the normalized transmission spectrum of butane at room temperature and pressure was reconstructed as described in experimental section. The reconstructed result was in good agreement with the NIST data as shown in Figure 6(c) in terms of the absorption bands (around 3400 nm in wavelength). A video that was recorded at a 25 Hz frame rate. By analysing such video data, continuous monitoring of the gas spectrum was achieved, allowing observation of the sudden release and gradual dispersion and dilution of butane gas. This approach can be applied as a novel method for real-time, non-dispersive infrared gas sensing. The design can be extended to different infrared wavelength ranges by scaling the pixel design and replacing the substrate with calcium fluoride.

The intensity in each region of Figure 5-7(b) is calculated using MATLAB. The input video was first converted to grey scale to directly analyse intensity. Each metasurface region was sampled and averaged with a square region smaller than the metasurface size. Frames without butane influence were averaged as a reference. Then, the relative transmission intensity can be calculated for each frame. The scripts can be found with the open source following link to analyse the video input built by me.

https://github.com/FrankBiscuit/PolXY_conversion/tree/main

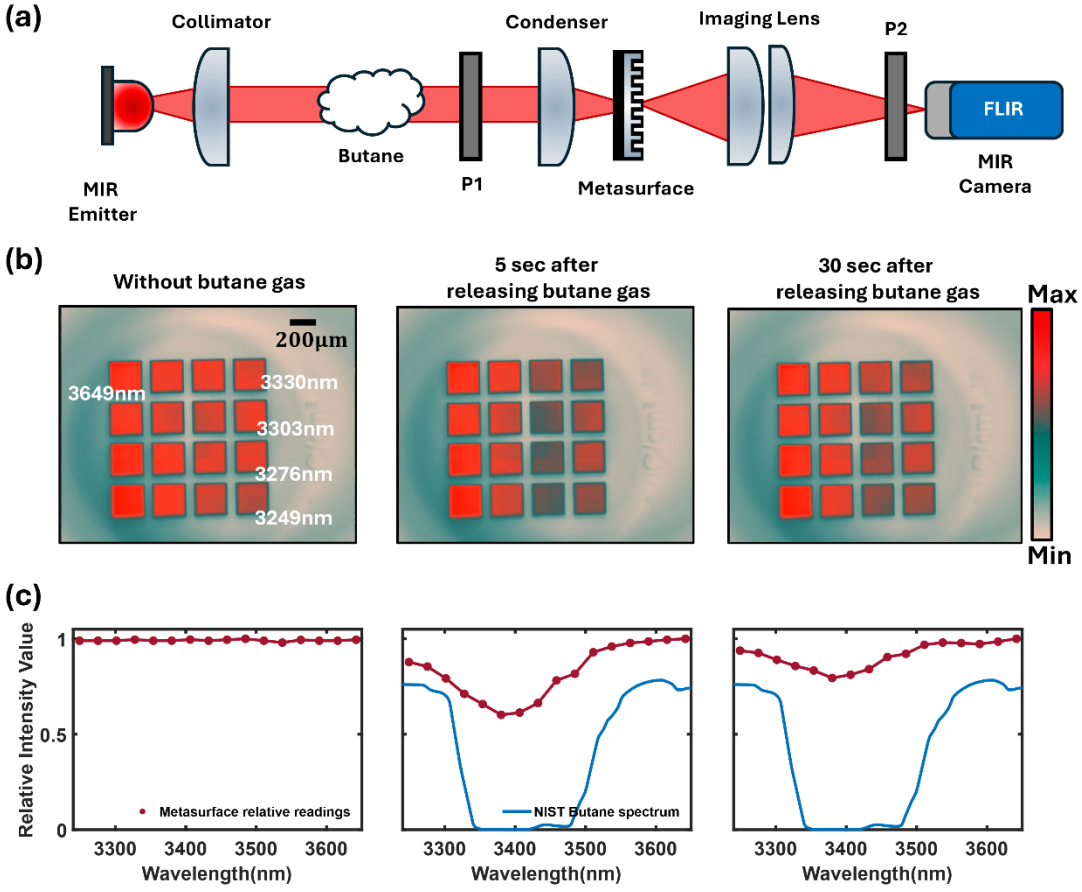

Figure 5-7 Video-rate gas absorption spectrum monitoring. (a) An imaging optical path with butane gas released in the optical path. (b) Thermal image of the 16-metasurface region in active cross-polarisation imaging mode. The colour palette was using the built-in grey-red palette in FLIR system, where red implies larger readings. The scale bar is 200 microns for the images and the centre wavelengths of the metasurface filters were partially marked to show the scaling orientation. (c) Derive relative intensity values from thermal image (red-dots) and ground-truth butane spectrum taken from NIST database (blue-lines) versus wavelength. Three frames in the video are shown here, respectively corresponds to no butane releasing, 5 seconds after releasing butane gas and 30 seconds after releasing butane gas.

5.4 Conclusion

In summary, a metasurface that supports linear-to-linear cross-polarisation conversion was proposed. A resonance-induced cross-polarisation conversion efficiency of 30% along with a Q-factor of approximately 60 was experimentally demonstrated. The metasurface is capable of narrow linewidth spectral filtering and polarisation conversion in the transmission mode within the mid-infrared spectral range. It is shown that the introduction of an additional low-Q mode is the key to surpassing the 25% limit typically associated with single-layer

metasurfaces for resonance-induced cross-polarisation conversion. In this work, such a mechanism was achieved by enlarging the off-centre holes, which tuned the relative spectral position of the high-Q q-BIC mode and low-Q magnetic dipole mode. Two modes were tuned spectrally close to each other, enhancing the coupling, and in turn helped to surpass the 25% limit. The linear-to-linear polarisation conversion characteristics of the proposed metasurface was leveraged to realise infrared QR code encryption using linear polarizers only. Furthermore, the device's narrowband filtering capability was exploited to reconstruct the absorption spectrum of butane in transmission mode. The proposed metasurface can be applied to various applications in mid infrared, including polarisation conversion, generalized Huygens sources, image encryption, as well as spectral sensing and detection.

5.5 Discussion and future work

5.5.1 Geometrical Phase of the proposed metasurface

The proposed structure nevertheless exhibits resonance-induced chiral cross-polarisation conversion as a consequence of the symmetry-breaking perturbations. By so doing the structure is suitable for further applications, such as wavelength selective wavefront control.

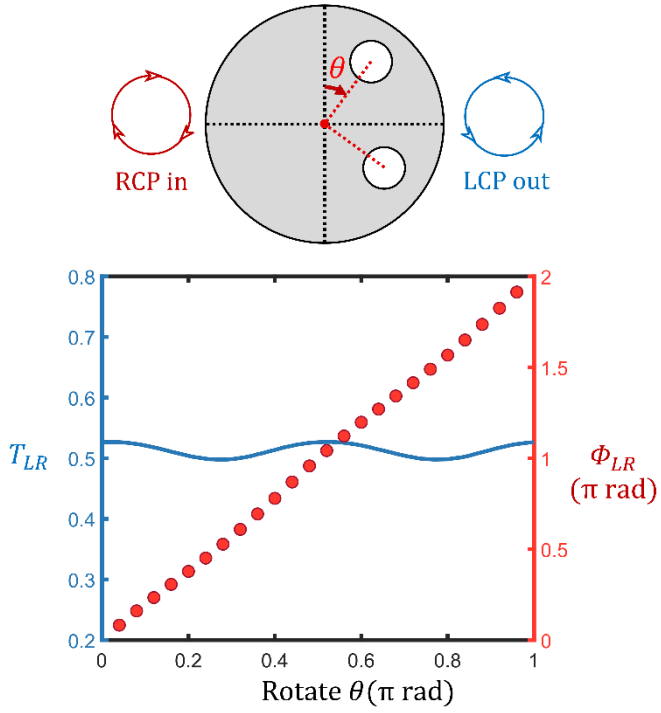

Figure 5-8 Non-local Huygens metasurface phase and amplitude illustration. Here the incidence light is 3473nm RCP light while the output monitored is LCP light at same wavelength.

As the C2 rotational symmetry of our structure is broken, it still supports resonance-induced circular polarization conversion. As an example, a structure with parameters $j = 0.28$ and $L = 250\ nm$ under right-handed circularly polarised (RCP) illumination is considered. Such configuration will give a centre wavelength at 3473nm with linewidth smaller than 30nm. The corresponding transmission coefficient T_{LR} and phase response Φ_{LR} for centre wavelength 3473nm illumination are shown in **Figure 5-8**. I planned to conduct more experiments evolving wavelength-selective beam focusing.

It can be observed that, as the pair of off-centre holes rotates an angle of θ from 0 to π w.r.t. the z-axis, the structure provides a full 2π phase coverage because of Pancharatnam–Berry phase. In the meantime, the peak cross-polarization transmission efficiency remained at around 50% for the entire space. This enables its functionality as an ultranarrow band Huygens-type source, suitable for applications such as narrow-band metalenses and beam steering[242, 243]

5.5.2 Target Gases

In this work, butane is selected as a demonstration gas because it has absorption lines nearly identical to those of CH_4, and a small batch of demonstration spray-type canisters purchased previously were available in the microsystem techonolgy group laboratory. It can therefore serve as a practical demonstration for CH_4 detection and reconstruction. The filters proposed in this study, operating in the mid-wave infrared with a linewidth of approximately 70 nm, are particularly useful for resolving gases with closely spaced absorption peaks.

For example, Figure 5-9 illustrates several gases with absorption peaks close to each other in the mid-wave infrared, with data obtained from the NIST Chemistry WebBook[259]. These include common greenhouse gases such as CO_2, N_2O, and CH_4, as well as toxic gases like formaldehyde (HCHO) and CO. As shown in Figure 5-9(a), the absorption peaks of N_2O and CO_2 are extremely close—separated by only about 300 nm. Consequently, spectral sampling with a full width at half maximum (FWHM) greater than ~300 nm would be unable to distinguish between these two gases. Similarly, the non-overlapping portion of the CO absorption peak is roughly 120 nm wide. In Figure 5-9(b), the absorption peaks of HCHO and CH_4 overlap extensively; accurate discrimination in this case requires either

simultaneous use of two corresponding filter signals or the scaling-array spectral reconstruction method proposed in this study.

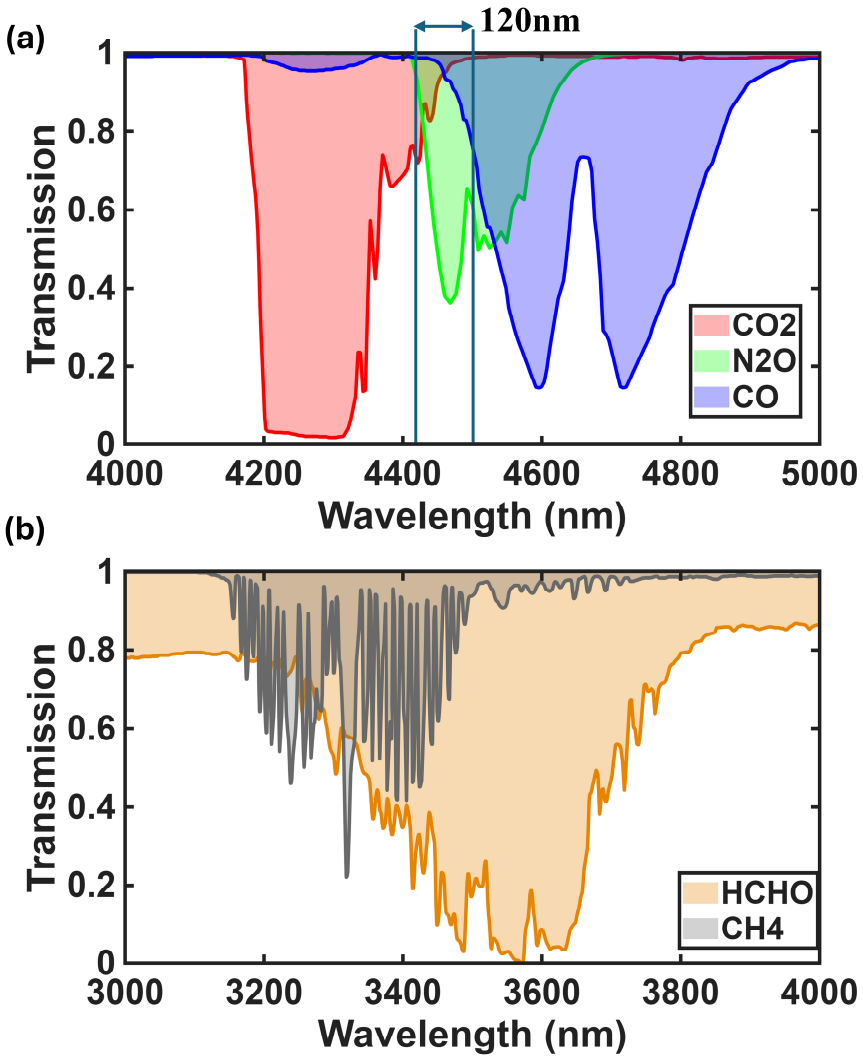

Figure 5-9 Examples of targeted gases in the MWIR range.

5.5.3 Germanium deposition

The deposition of germanium film in this research was made through E-gun evaporation, the film was therefore amorphous-Ge. Although it still shows low loss feature in the MWIR range, the increased imaginary part of the material refractive index will degrade the Q factor of the device. Figure 5-10 shows the changing of Q factor of the eigenmode at gamma point in response to the increasing imaginary index. It can be seen that the Q-factor falls dramatically when imaginary index increases. The performance of the device is therefore expected to be largely improved with high quality c-Ge deposition.

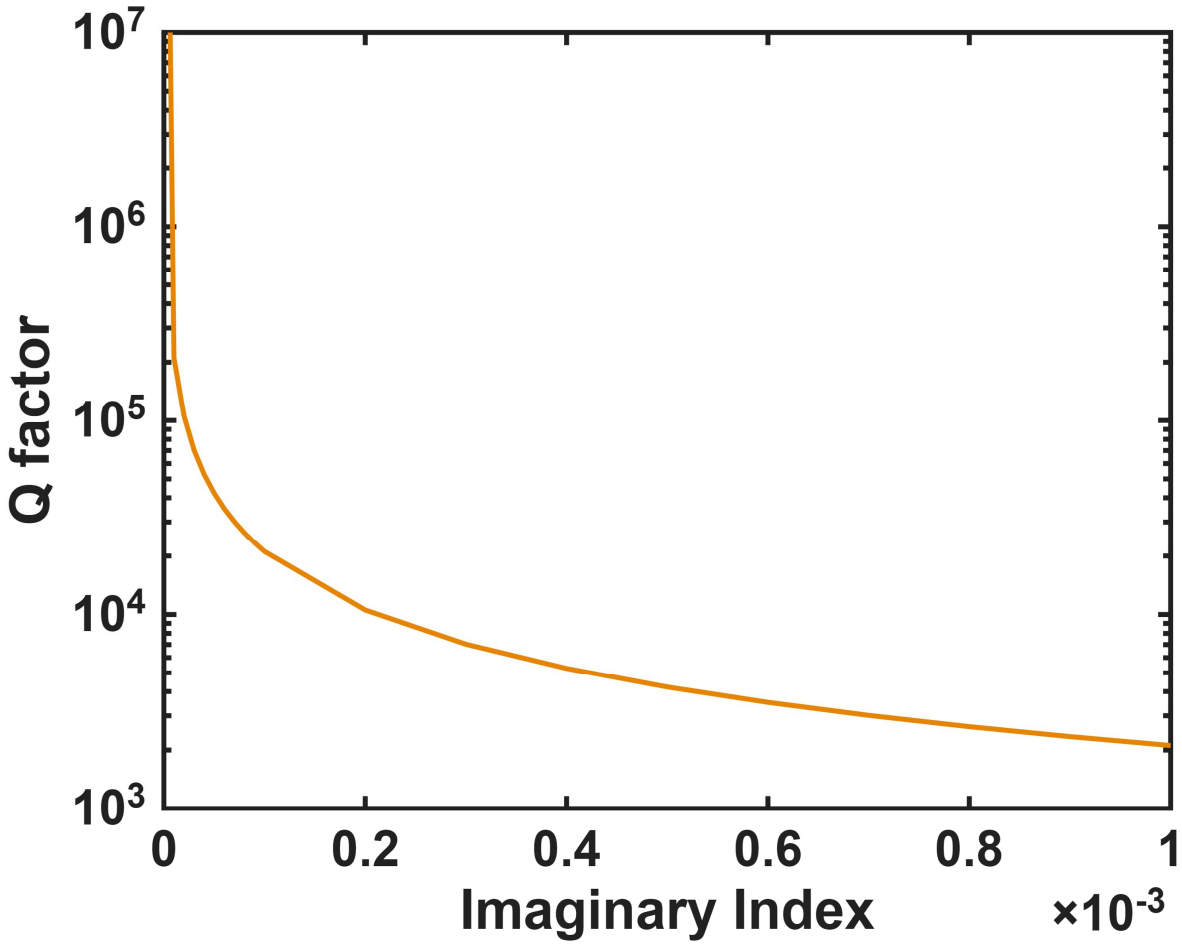

Figure 5-10 Q-factor vs assigned imaginary index of Ge layer in simulation.

Chapter 6 Metasurface Enabled High-Q Photonic Flatband in the Mid-infrared

6.1 Introduction and motivation

Long lifetimes and high quality-factor (Q-factor) resonances are very important for many applications that involves light-matter interactions, such as laser cavities, optical nonlinear effects enhancement, and on-resonance chemical molecular sensing[22, 83, 231]. Bound states in the continuum (BIC) with theoretically infinite Q-factors have therefore attracted widespread attention. BICs in photonics are eigen electromagnetic modes embedded in the radiation continuum that do not radiate energy into free space[46, 82, 85, 89, 260]. Metasurfaces, composed of quasi-two-dimensional nanostructures, serve as an ideal platform for realising and observing electromagnetic BICs since metasurfaces can achieve flexible control of electromagnetic mode responses at the subwavelength scale[46, 83]. In practical applications, to make BICs observable, perturbations are introduced into the system to convert non-radiative BIC into leaky modes, radiating into free space. Such resonant modes are called quasi-BIC (q-BIC) modes that show narrow reflection/transmission peaks in the spectrum and are accompanied by strong near-field enhancement. They are therefore widely used in spectroscopic applications[35, 39, 43, 141].

The mid-infrared (MIR) spectral region is crucial for spectroscopic applications because the MIR region includes many fundamental vibrational absorption bands of chemical molecules[149]. High quality factor metasurfaces like q-BIC metasurfaces working in the MIR region are therefore of great importance and have been widely investigated in recent years[39, 97, 147, 171]. Typical optical systems incorporating metasurfaces use a lens to intensify the light to a point. If the lens has a high numerical aperture (NA), the angular dispersion of the resonance wavelength of the metasurface at off- Γ will lead to a broadening of the spectral characteristic. It is therefore desirable to design and make metasurfaces with a flatband characteristic at the Γ-point in order to reduce dispersive effects that lead to spectral broadening and to increase density of states. Equally interesting is how to keep a high Q value at off- high symmetry point **Γ**. Although the BIC or quasi-BIC at **Γ** has an extremely high Q value, the Q values of the modes containing q-BIC usually drops fast as the $k_{\parallel}$ component increases[83, 84, 261]. One possible flat-band high-Q metasurface solution is to tune system parameters or introduce an asymmetric perturbation that supports strong coupling at the design frequency, between two modes with opposite band-dispersion trends. Strong

coupling causes band anti-crossing, realising compensation of the positive and negative dispersion trends, giving a flat band among certain $k_{\parallel}$ range.

At the same time, if there is another off-**Γ** BIC mode near the anti-crossing point, the high Q-value can be kept within a certain range, further increasing density of states. Most current reports use comb-like or asymmetric (with respect to z=0 plane) structures. They convert two crossing modes, which are odd/even mismatched with respect to the z=0 plane, into odd-like and even-like modes. With an asymmetric parameter added, strong coupling between the two modes is realised and anti-crossing phenomenon appears[158, 165, 167, 169, 262]. These reports are inspiring, however, the fabrication is relatively complex, because the comb-like or displaced structures must introduce z-direction asymmetry, which requires careful design and multiple steps in fabrication.

The key to this type of flat-band control is to create crossing modes and produce strong coupling. Here, a metasurface with a diatomic single-layer structure, i.e., a flat-optic structure, that can generate a flat-band high-Q mode by structural fine tuning is proposed. Generation of the flat-band high-Q mode relies on Brillouin-zone folding (BZF) and coupling between modes in this design. With a mechanism that I named as *dual-parametric period-doubling perturbation (DPPD)*, flexible band control is realised. Without a comb-like structure, the anti-crossing effect and band flattening can still be readily achieved. Because of the BZF-induced BIC at **Γ** and the FW-BIC at off- **Γ**, this band shows a flat band and ultra-high Q value within about a 15° along the k_y direction shown in **Fig. 6-1 a**.

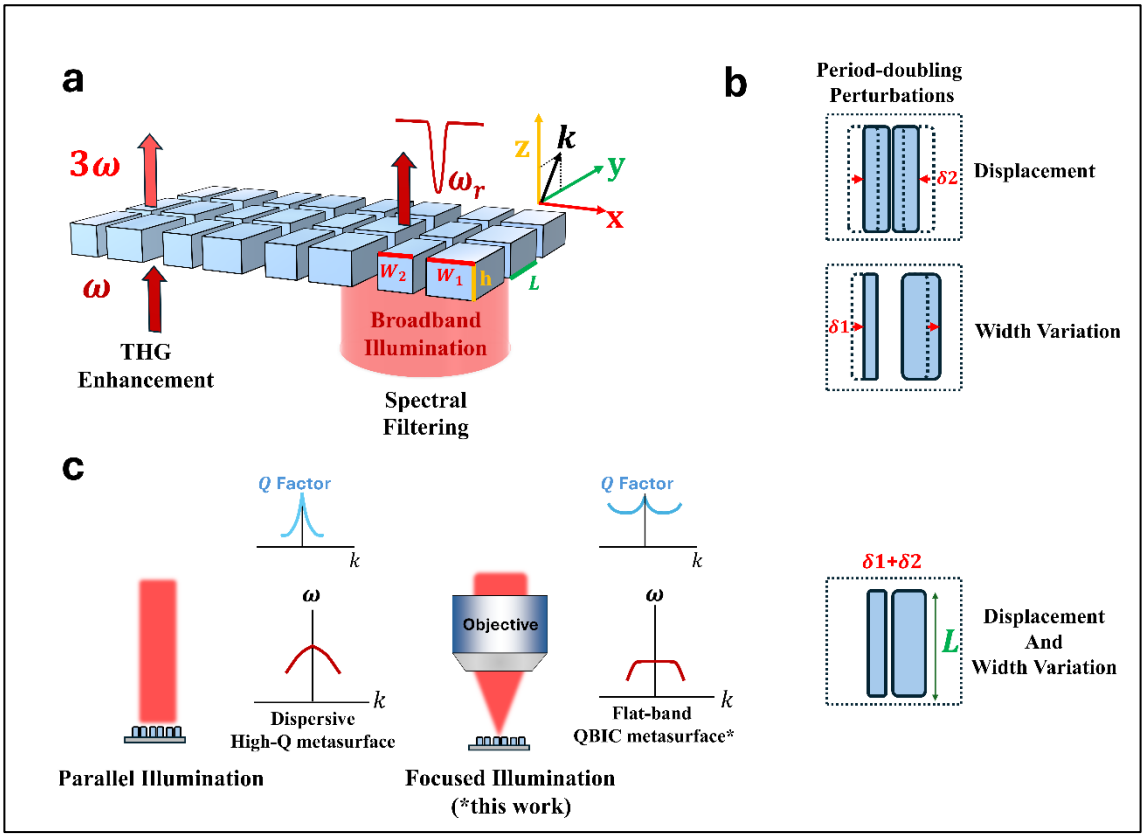

Figure 6-1 Schematic illustration of the flat optics enabled flatband and its applications.

Fig. 6-1 **b**, **c** shows the proposed flat-band high-Q metasurface and its mechanism. A relative shift δ_2 between the germanium bricks in two adjacent identical units, or a width variation δ_1 between the two bricks will both double the effective period of the unit. This type of perturbation therefore can be called a period-doubling perturbation. Combining the two period-doubling perturbations together can produce the DPPD on the right-hand side of Fig. 6-1**c.** By finely tuning the magnitudes of δ_1 and δ_2, a flat-band effect can be produced. Compared with a high-Q dispersive metasurface, this flat-band high-Q metasurface within a specific $k_{\parallel}$ range can keep the resonant wavelength unchanged under focused illumination that will greatly benefit applications such as infrared nonlinear enhancement and on-resonance sensing. It is worth mentioning that the concept diagram in Fig. 6-1(a) omits the low-refractive-index substrate that is used to support the nanobricks.

6.2 Design and modelling

Band analysis and angle-resolved transmission-spectrum simulations were conducted to clarify the generation mechanisms of the two high-Q flat bands. Unless stated otherwise,

band analysis was performed with COMSOL Multiphysics 6.2 (Wave Optics Module), and transmission spectra were computed with the RCWA package in Ansys Lumerical. The model comprised a three-layer stack: a CaF_2 substrate (refractive index = 1.4); a metasurface of periodic two-dimensional rectangular nanobricks (refractive index 4.033); and air above (refractive index 1).

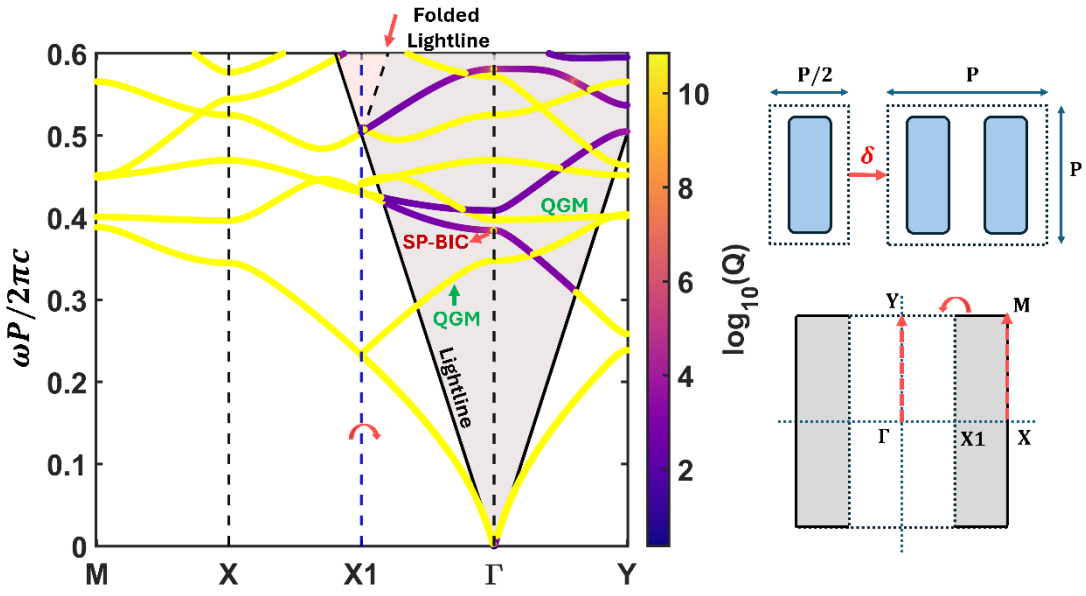

Figure 6-2 Illustration of band-folding caused by period-doubling perturbation.

Fig. 6-2 demonstrated the band-folding mechanism of the proposed metasurface. First, consider a single meta-atom array with period $\boldsymbol{P/2}$ along $\boldsymbol{x}$ direction and $\boldsymbol{P}$ along $\boldsymbol{y}$-direction (here lower case x, y represents directions in real space). Its band structure is shown in Fig. 6-2 $\boldsymbol{\Gamma - X}$ region. With period doubling perturbation, the effective period changes from $\boldsymbol{P/2}$ to $\boldsymbol{P}$, therefore the high-symmetry point $\mathbf{X}$ will be folded with respect to $k = \mathbf{X_1} = \mathbf{X/2}$. Bands along $\mathbf{X - M}$ mirror-fold into the newly formed $\mathbf{\Gamma - Y}$ path. Guided modes originally below the light line are folded above it, inherit the infinite-Q property of the parent bands, and become quasi-guided modes (QGM)[132, 263, 264]. The position of the QGM bands in momentum space is defined by the rectangle's long axis L and thickness H. In general, a larger long side corresponds to a higher frequency, with a higher effective refractive index. Here a parameter group of $L = 2500\text{nm}$ and $H = 700\text{nm}$ is chosen as a demonstration. Other parameters are set to be $\boldsymbol{P} = 2800\text{nm}, W = 1100\text{nm}$. The dimensionless frequency $\omega a/2\pi c$ is kept below 0.5 wherever possible, to reduce higher-order diffraction influence.

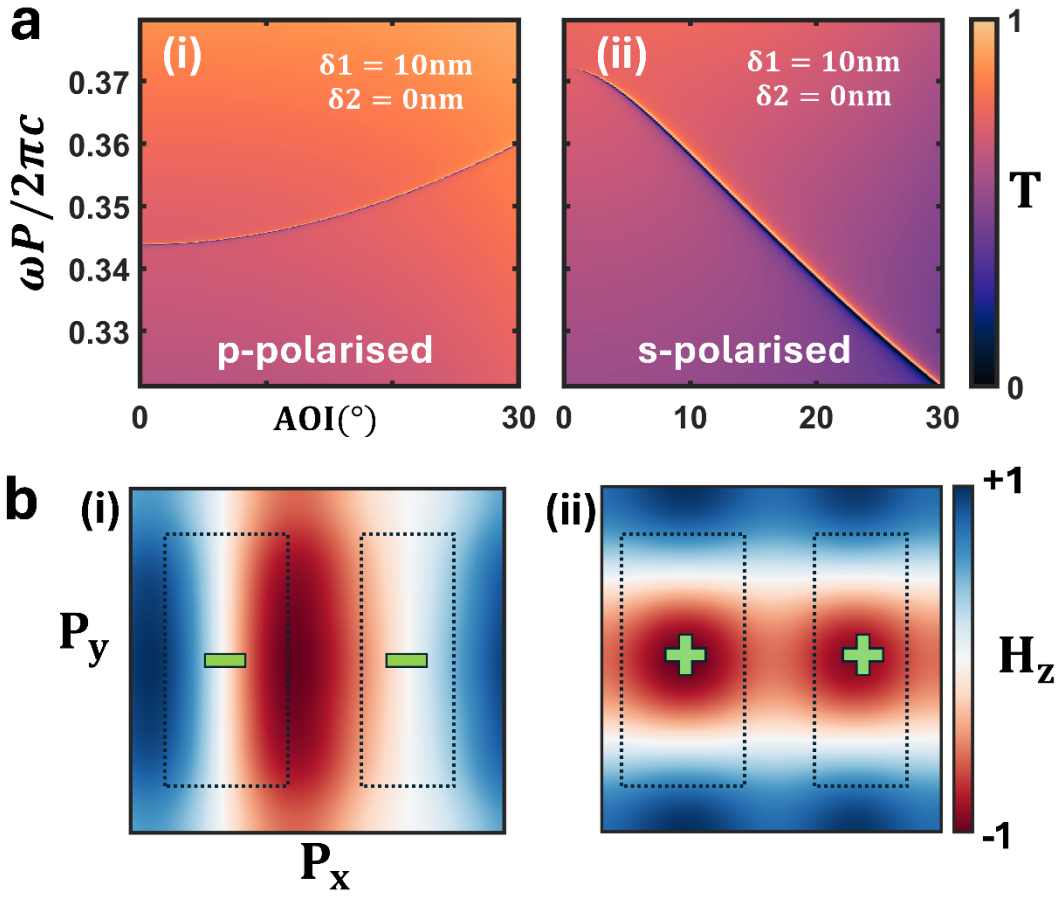

Figure 6-3 a. Angle-resolved transmission spectrum of the metasurface with single period doubling perturbation. **b.** The H_z component of eigen mode profile in z = 0 plane.

Fig. 6-3 shows the angle-resolved transmission spectra under a tilt along the y direction after introducing δ_1 into the proposed metasurface, together with the corresponding eigenmode profiles. Two bands appear around normalised angular frequency of [0.33 0.39], respectively referring to SP quasi-BIC and the folded QGM for p-polarised and s-polarised excitation. With the width variation δ_1 , the centres of the two bricks remain symmetry centre points. The **Hz** components in the $z = 0$ plane for the two modes is shown, marked with plus/minus signs to indicate symmetry or anti-symmetry. It can be seen that the two eigenmodes are respectively symmetric and antisymmetric. The odd–even mismatch prevents any mutual coupling between the two modes. In the transmission spectra, they can therefore only be excited by p- or s-polarised light, respectively. In the band structure, they appear as two crossing bands, as in Fig. 6-4**a.**

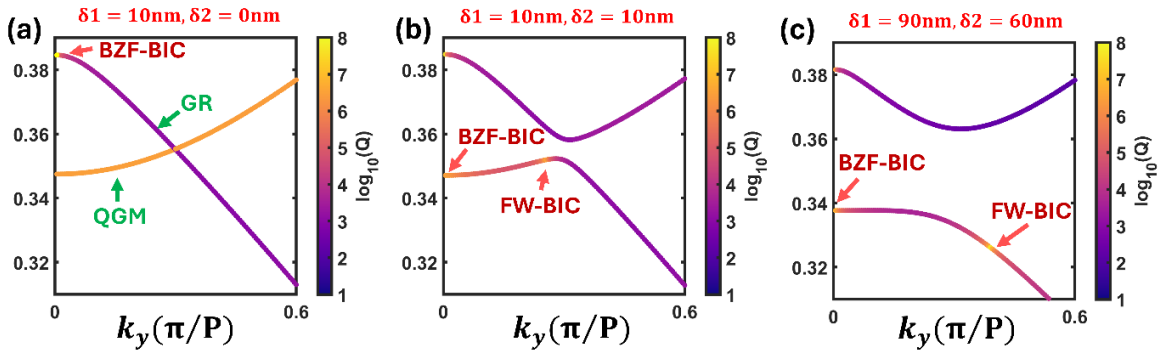

Figure 6-4 Band structure of the proposed metasurface with different PD perturbation.

Once a relative displacement δ_2 is introduced, the symmetry points at the brick centres are lost. The two modes therefore couple strongly, producing hybridisation and energy exchange, as shown in Fig. 6-5. In the spectra, both s- and p-polarised light can excite the hybrid modes. Meanwhile, the quasi-guided-mode band evolves into a band containing multiple BICs. It hosts an SP-BIC at **Γ** because of Brillouin-zone folding[143], and an interference-induced FW-BIC[260] near the off- **Γ** crossing point in Fig. 6-4 (a). Formation of this FW-BIC depends entirely on coupling and energy exchange between the original quasi-guided mode and the new one. As the coupling strength increases (i.e., larger perturbations), the FW-BIC position shifts. The strong anti-crossing between the two modes also alters the band slopes. For the upper band (the original guided resonances modes containing the BZF-BIC), the effect shifts it toward larger frequency; for the lower band, the effect is opposite. By finely tuning the ratio and magnitude of the two perturbations, the FW-BIC position and the shape of the lower band can be controlled. Here the optimised DPPD parameter is found to be $\delta_1 = 90\text{nm}$, $\delta_2 = 60$ nm. The resulting flat band lies between two BICs in momentum space[162] and therefore retains a high Q factor larger than 10^4. A metasurface with both flatband in certain k range and high Q factor is then obtained, as shown in Fig. 6-4 (c).

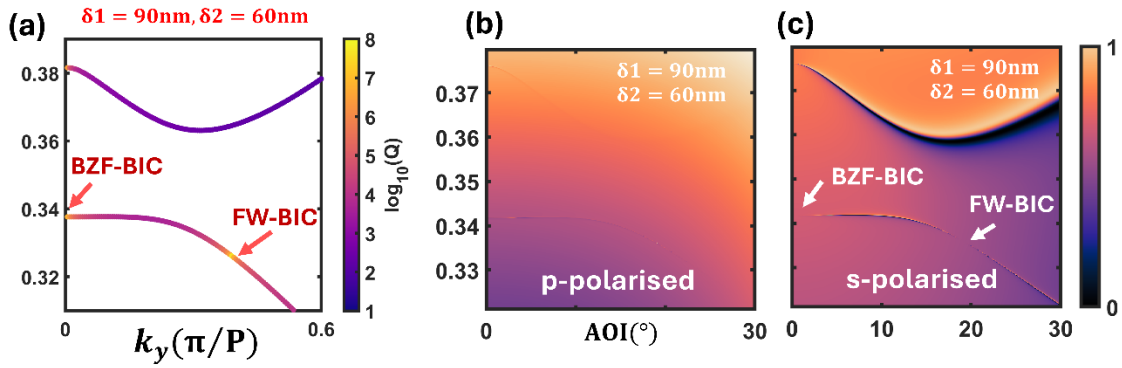

Figure 6-5 Illustration of the flatband formation and modes hybridisation.

6.3 Conclusion and future work

A new flat band metasurface formation mechanism DPPD (dual-parametric period-doubling perturbations) is proposed. It arises explicitly from band folding and symmetry breaking, which induce band anti-crossing, enable BIC-position tuning, simultaneously yielding flatband and high quality factor. The band folding and symmetry breaking originate from the DPPD (width variation δ_2 and relative translation δ_2). Band-structure analysis shows angle-independent resonance over 0-15°with a Q factor exceeding 10^4. Notably, the mechanism is implemented on a planar structure or so-called flat optics, greatly simplifying fabrication.

Future work will proceed along three directions.

1. Deeper understanding of the mechanism

The formation of the FW-BIC and the tuning of the relative positions of the two BICs depend on the inter-mode coupling strength and on system parameters, as in ref[165]. In this study, the "optimal" parameters were obtained by brute-force enumeration, which is not ideal. A complementary approach is to analyse the evolution from a topological viewpoint and via the system Hamiltonian. This should enable more effective modelling of such systems and a more efficient assessment of how DPPD parameters shape the band structure.

2. Fabrication

This planar structure can be readily fabricated using exactly the same steps as in Chapter 5.3, and with larger feature sizes. The key consideration is that a CaF_2 substrate is not permitted by most JWNC dry-etch processes due to the presence of calcium. Alternative process routes should be considered, such as lift-off, or outsourcing to a fabrication facility that allows this element.

3. Applications

Beyond the previously noted uses—nonlinear-effect enhancement and on-resonance sensing—a direct and widely discussed application is in lasing. This area has attracted substantial recent attention. Future work will focus on this direction, with the practical realisation of low-threshold lasing in flat-band metasurfaces set as a postdoctoral research topic.

Chapter 7 Conclusions

This thesis introduces the principles of metasurfaces, especially non-local metasurfaces, together with their applications. In particular, it focuses on two representative non-local metasurfaces—surface-plasmon-polariton (SPP) based resonant metasurfaces and bound-states-in-the-continuum (BIC) based resonant metasurfaces—as well as the dispersion control for high-Q resonant metasurfaces.

The design of the metasurfaces is based on finite-element methods (FEM), finite-difference time-domain (FDTD) and rigours-coupled mode analysis (RCWA) that help with the spectral transmission/reflection analysis, eigenmode analysis and angle-resolved spectral response analysis. These simulation methods were therefore comprehensively reviewed in the thesis, and it is concluded that three methods are respectively suitable for different tasks, e.g. FEM – eigenmode analysis and circular-polarised illumination spectral response analysis, FDTD – broadband spectral transmission/reflection analysis, RCWA – angle resolved transmission spectrum analysis.

Building on the reviewed state of the art, three new devices or mechanism are respectively proposed across three subfields. Here the most important contributions of the proposed devices/mechanism are concluded as follows, while the detailed description can be found in conclusion section in each chapter:

1. In plasmonic metasurface filters, a novel unit-cell design of dimeric aperture is introduced, yielding a transmission structural-colour filter with a broad gamut (76% sRGB coverage) while maintaining a high polarisation extinction ratio (>150 for the blue channel). The design can be readily applied to wavelength-selective and polarisation-selective display. A series of micro-scale artwork were also demonstrated to show the capability of simultaneous colour-polarisation control of the proposed structure.

2. In the mid-infrared spectral range, a q-BIC metasurface operating in transmission is demonstrated. The proposed mode of operation is enabled by two symmetry-breaking perturbations that realise linear-to-linear cross-polarisation coupling. A coupling efficiency that exceeds the ~25% limit of conventional single-layer resonant metasurfaces for cross-polarisations is obtained using multi-pole interference engineering and Kerker-effect enabled unidirectional scattering enhancement. The design was both wavelength selective and polarisation sensitive

that can be used for wavelength-selective and polarisation encoded display. A demonstration of using the proposed device for mid-infrared gas spectrum reconstruction has been shown.

3. A new mechanism for flat-band engineering in metasurfaces is proposed. In the novel proposed novel design, it does not require out-of-plane (z=0) symmetry breaking that was conventionally used for photonic flatband engineering; instead, in-plane parity breaking is used to induce strong coupling between otherwise uncoupled modes, enabling band-structure control. The in-plane symmetry mismatch of two eigenmodes respectively has even/odd symmetry mode profile were broken by introducing dual parametric period doubling (DPPD) perturbation to the periodic nano-bricks array. The DPPD can control the coupling strength of the modes, as well as tune the relative place of the BICs in momentum space. This mechanism is of practical relevance for high-Q infrared metasurfaces.

Chapter 8 Future Work

These foundational studies open many avenues for extension and application. A few planned directions are outlined below; more detailed descriptions are presented in the corresponding sections of Chapters 4, 5, and 6.

Dimeric aperture plasmonic filter (multimodal imaging).

This will be developed for imaging, termed "multimodal imaging". The future project integrates physics (metasurface features), hardware (metasurface + SPAD), and software algorithms (advanced deep-learning methods). The proposed metasurface design will serve as a functional surface layer to the detector and be integrated onto a depth-sensing single-photon avalanche diode (SPAD) via UV-glue flip-chip bonding, enabling polarisation–colour–depth, what I would like to call *information-super-rich* imaging that greatly expands the informational content of an image. A collaboration with the Heriot-Watt team is planned.

Linear-to-linear cross-polarisation conversion metasurface.

Its use for real-time spectral reconstruction has been demonstrated. With improved thin-film deposition of the functional metasurface layer, the linewidth and maximum transmittance of the proposed device can be further optimised to approach the designed performance. This likely requires higher-cost atomic-layer deposition of Ge films, though the cost can be mitigated by switching to an Si platform. The current real-time reconstruction is qualitative; future work will formalise it into a quantitative experiment using a mass-flow controller, and progress towards a manufacturable device.

Flat band metasurface*.

A new design method for flat band metasurfaces has been presented. The focus on this topic stems from the practical limitations imposed by angular dispersion in my research. The study introduces an in-plane symmetry-breaking route to form strong coupling and band-structure control for flat-band engineering. Future efforts will emphasise completing and formalising the theoretical framework, strengthening the mathematical treatment, and developing compatible fabrication processes that will be a central theme of my future research career. Currently, I am working on grant applications in this area. I have completed a new design and published the work in *EPJ Applied Metamaterials*. What is now required is precise

fabrication. This work shows considerable promise for enhancing light–matter interactions, and the platform has the potential to make significant contributions to applications involving such interactions, including low-threshold lasers, nonlinear effects, and strong coupling regimes.

BIBLIOGRAPHY

[1] M. L. Rubin, Spectacles - Past, Present, and Future*, Surv Ophthalmol* **1986**, *30*, 321-327. https://doi.org/Doi 10.1016/0039-6257(86)90064-0.

[2] N. I. Landy, S. Sajuyigbe, J. J. Mock, D. R. Smith, W. J. Padilla, Perfect metamaterial absorber*, Phys Rev Lett* **2008**, *100*. https://doi.org/10.1103/PhysRevLett.100.207402.

[3] T. J. Cui, S. Zhang, A. Alù, M. Wegener, S. J. Pendry, J. Luo, Y. Lai, Z. J. Wang, X. Lin, H. S. Chen, P. Chen, R. X. Wu, Y. H. Yin, P. F. Zhao, H. Y. Chen, Y. Li, Z. H. Zhou, N. Engheta, V. Asadchy, C. Simovski, S. Tretyakov, B. Yang, S. D. Campbell, Y. Hao, D. H. Werner, S. L. Sun, L. Zhou, S. Xu, H. B. Sun, Z. Zhou, Z. L. Li, G. X. Zheng, X. Z. Chen, T. Li, S. N. Zhu, J. X. Zhou, J. X. Zhao, Z. W. Liu, Y. C. Zhang, Q. M. Zhang, M. Gu, S. M. Xiao, Y. M. Liu, X. Z. Zhang, Y. T. Tang, G. X. Li, T. Zentgraf, K. Koshelev, Y. Kivshar, X. Li, T. Badloe, L. L. Huang, J. Rho, S. M. Wang, D. P. Tsai, A. Y. Bykov, A. V. Krasavin, A. V. Zayats, C. McDonnell, T. Ellenbogen, X. G. Luo, M. B. Pu, F. J. Garcia-Vidal, L. L. Liu, Z. Li, W. X. Tang, H. F. Ma, J. J. Zhang, Y. Luo, X. R. Zhang, H. C. Zhang, P. H. He, L. P. Zhang, X. Wan, H. T. Wu, S. Liu, W. X. Jiang, X. G. Zhang, C. W. Qiu, Q. Ma, C. Liu, L. Li, J. Q. Han, L. L. Li, M. Cotrufo, C. Caloz, Z. L. Deck-Léger, A. Bahrami, O. Céspedes, E. Galiffi, P. A. Huidobro, Q. Cheng, J. Y. Dai, J. C. Ke, L. Zhang, V. Galdi, M. di Renzo, Roadmap on electromagnetic metamaterials and metasurfaces*, J Phys-Photonics* **2024**, *6*. https://doi.org/10.1088/2515-7647/ad1a3b.

[4] A. Ali, A. Mitra, B. Aïssa, Metamaterials and Metasurfaces: A Review from the Perspectives of Materials, Mechanisms and Advanced Metadevices*, Nanomaterials-Basel* **2022**, *12*. https://doi.org/10.3390/nano12061027.

[5] J. B. Pendry, Negative refraction makes a perfect lens*, Phys Rev Lett* **2000**, *85*, 3966-3969. https://doi.org/DOI 10.1103/PhysRevLett.85.3966.

[6] G. Yoon, I. Kim, J. Rho, Challenges in fabrication towards realization of practical metamaterials*, Microelectronic Engineering* **2016**, *163*, 7-20. https://doi.org/https://doi.org/10.1016/j.mee.2016.05.005.

[7] H. T. Chen, A. J. Taylor, N. F. Yu, A review of metasurfaces: physics and applications*, Rep Prog Phys* **2016**, *79*, 076401. https://doi.org/10.1088/0034-4885/79/7/076401.

[8] J. P. B. Mueller, N. A. Rubin, R. C. Devlin, B. Groever, F. Capasso, Metasurface Polarization Optics: Independent Phase Control of Arbitrary Orthogonal States of Polarization*, Phys Rev Lett* **2017**, *118*. https://doi.org/10.1103/PhysRevLett.118.113901.

[9] A. H. Dorrah, N. A. Rubin, A. Zaidi, M. Tamagnone, F. Capasso, Metasurface optics for on-demand polarization transformations along the optical path*, Nat Photonics* **2021**, *15*, 287-296. https://doi.org/10.1038/s41566-020-00750-2.

[10] Y. Q. Hu, X. D. Wang, X. H. Luo, X. N. Ou, L. Li, Y. Q. Chen, P. Yang, S. Wang, H. G. Duan, All-dielectric metasurfaces for polarization manipulation: principles and emerging applications*, Nanophotonics-Berlin* **2020**, *9*, 3755-3780. https://doi.org/10.1515/nanoph-2020-0220.

[11] S. M. Wang, P. C. Wu, V. C. Su, Y. C. Lai, M. K. Chen, H. Y. Kuo, B. H. Chen, Y. H. Chen, T. T. Huang, J. H. Wang, R. M. Lin, C. H. Kuan, T. Li, Z. L. Wang, S. N. Zhu,

D. P. Tsai, A broadband achromatic metalens in the visible, *Nat Nanotechnol* **2018**, *13*, 227-232. https://doi.org/10.1038/s41565-017-0052-4.

[12] W. T. Chen, A. Y. Zhu, V. Sanjeev, M. Khorasaninejad, Z. J. Shi, E. Lee, F. Capasso, A broadband achromatic metalens for focusing and imaging in the visible, *Nat Nanotechnol* **2018**, *13*, 220-+. https://doi.org/10.1038/s41565-017-0034-6.

[13] S. Y. Xiao, J. R. Wang, F. Liu, S. Zhang, X. B. Yin, J. S. Li, Spin-dependent optics with metasurfaces, *Nanophotonics-Berlin* **2017**, *6*, 215-234. https://doi.org/10.1515/nanoph-2016-0121.

[14] W. M. Ye, F. Zeuner, X. Li, B. Reineke, S. He, C. W. Qiu, J. Liu, Y. T. Wang, S. Zhang, T. Zentgraf, Spin and wavelength multiplexed nonlinear metasurface holography, *Nat Commun* **2016**, *7*. https://doi.org/10.1038/ncomms11930.

[15] G. Kim, Y. Kim, J. Yun, S. W. Moon, S. Kim, J. Kim, J. Park, T. Badloe, I. Kim, J. Rho, Metasurface-driven full-space structured light for three-dimensional imaging, *Nat Commun* **2022**, *13*. https://doi.org/10.1038/s41467-022-32117-2.

[16] W. C. Hsu, C. H. Chang, Y. H. Hong, H. C. Kuo, Y. W. Huang, Metasurface- and PCSEL-Based Structured Light for Monocular Depth Perception and Facial Recognition, *Nano Lett* **2024**, *24*, 1808-1815. https://doi.org/10.1021/acs.nanolett.3c05002.

[17] *New Samsung Metalens Promises Thinner Phones and XR Headsets*, https://www.androidheadlines.com/2025/08/new-samsung-metalens-promises-thinner-phones-and-xr-headsets.html

[18] Z. B. Fan, Y. F. Cheng, Z. M. Chen, X. Liu, W. L. Lu, S. H. Li, S. J. Jiang, Z. Qin, J. W. Dong, Integral imaging near-eye 3D display using a nanoimprint metalens array, *Elight* **2024**, *4*. https://doi.org/10.1186/s43593-023-00055-1.

[19] Z. T. Tian, X. L. Zhu, P. A. Surman, Z. D. Chen, X. W. Sun, An achromatic metasurface waveguide for augmented reality displays, *Light-Sci Appl* **2025**, *14*. https://doi.org/10.1038/s41377-025-01761-w.

[20] M. Miyata, H. Hatada, J. Takahara, Full-Color Subwavelength Printing with Gap-Plasmonic Optical Antennas, *Nano Lett* **2016**, *16*, 3166-3172. https://doi.org/10.1021/acs.nanolett.6b00500.

[21] A. Pors, O. Albrektsen, I. P. Radko, S. I. Bozhevolnyi, Gap plasmon-based metasurfaces for total control of reflected light, *Sci Rep-Uk* **2013**, *3*. https://doi.org/10.1038/srep02155.

[22] K. Shastri, F. Monticone, Nonlocal flat optics, *Nat Photonics* **2023**, *17*, 36-47. https://doi.org/10.1038/s41566-022-01098-5.

[23] S. Pancharatnam, Generalized theory of interference, and its applications, *Proceedings of the Indian Academy of Sciences - Section A* **1956**, *44*, 247-262. https://doi.org/10.1007/BF03046050.

[24] M. V. Berry, Quantal phase factors accompanying adiabatic changes, *Proceedings of the Royal Society of London. A. Mathematical and Physical Sciences* **1984**, *392*, 45-57. https://doi.org/doi:10.1098/rspa.1984.0023.

[25] E. D. Walsby, S. Wang, J. Xu, T. Yuan, R. Blaikie, S. M. Durbin, X. C. Zhang, D. R. S. Cumming, Multilevel silicon diffractive optics for terahertz waves, *J Vac Sci Technol B* **2002**, *20*, 2780-2783. https://doi.org/10.1116/1.1518021.

[26] P. Lalanne, S. Astilean, P. Chavel, E. Cambril, H. Launois, Design and fabrication of blazed binary diffractive elements with sampling periods smaller than the structural cutoff, *J Opt Soc Am A* **1999**, *16*, 1143-1156. https://doi.org/Doi 10.1364/Josaa.16.001143.

[27] Z. Bomzon, V. Kleiner, E. Hasman, Pancharatnam-Berry phase in space-variant polarization-state manipulations with subwavelength gratings, *Opt Lett* **2001**, *26*, 1424-1426. https://doi.org/Doi 10.1364/Ol.26.001424.

[28] M. V. Berry, The Adiabatic Phase and Pancharatnam's Phase for Polarized Light, *Journal of Modern Optics* **1987**, *34*, 1401-1407. https://doi.org/10.1080/09500348714551321.

[29] N. F. Yu, F. Capasso, Flat optics with designer metasurfaces, *Nat Mater* **2014**, *13*, 139-150. https://doi.org/10.1038/nmat3839.

[30] N. F. Yu, P. Genevet, M. A. Kats, F. Aieta, J. P. Tetienne, F. Capasso, Z. Gaburro, Light Propagation with Phase Discontinuities: Generalized Laws of Reflection and Refraction, *Science* **2011**, *334*, 333-337. https://doi.org/10.1126/science.1210713.

[31] A. Arbabi, Y. Horie, M. Bagheri, A. Faraon, Dielectric metasurfaces for complete control of phase and polarization with subwavelength spatial resolution and high transmission, *Nat Nanotechnol* **2015**, *10*, 937-U190. https://doi.org/10.1038/Nnano.2015.186.

[32] B. H. Chen, P. C. Wu, V. C. Su, Y. C. Lai, C. H. Chu, I. C. Lee, J. W. Chen, Y. H. Chen, Y. C. Lan, C. H. Kuan, D. P. Tsai, GaN Metalens for Pixel-Level Full-Color Routing at Visible Light, *Nano Lett* **2017**, *17*, 6345-6352. https://doi.org/10.1021/acs.nanolett.7b03135.

[33] Q. Chen, D. R. S. Cumming, High transmission and low color cross-talk plasmonic color filters using triangular-lattice hole arrays in aluminum films, *Opt Express* **2010**, *18*, 14056-14062. https://doi.org/10.1364/Oe.18.014056.

[34] Z. Zheng, D. Smirnova, G. Sanderson, Y. Cuifeng, D. C. Koutsogeorgis, L. J. Huang, Z. X. Liu, R. Oulton, A. Yousefi, A. E. Miroshnichenko, D. N. Neshev, M. O'Neill, M. Rahmani, L. Xu, Broadband infrared imaging governed by guided-mode resonance in dielectric metasurfaces, *Light-Sci Appl* **2024**, *13*. https://doi.org/10.1038/s41377-024-01535-w.

[35] S. Han, M. V. Rybin, P. Pitchappa, Y. K. Srivastava, Y. S. Kivshar, R. Singh, Guided-Mode Resonances in All-Dielectric Terahertz Metasurfaces, *Adv Opt Mater* **2020**, *8*. https://doi.org/10.1002/adom.201900959.

[36] L. M. Berger, M. Barkey, S. A. Maier, A. Tittl, Metallic and All-Dielectric Metasurfaces Sustaining Displacement-Mediated Bound States in the Continuum, *Adv Opt Mater* **2024**, *12*. https://doi.org/10.1002/adom.202301269.

[37] T. Shi, Z. L. Deng, G. Z. Geng, X. Z. Zeng, Y. X. Zeng, G. W. Hu, A. Overvig, J. J. Li, C. W. Qiu, A. Alù, Y. S. Kivshar, X. P. Li, Planar chiral metasurfaces with maximal and tunable chiroptical response driven by bound states in the continuum, *Nat Commun* **2022**, *13*. https://doi.org/10.1038/s41467-022-31877-1.

[38] N. Bernhardt, K. Koshelev, S. J. U. White, K. W. C. Meng, J. E. Fröch, S. Kim, T. T. Tran, D. Y. Choi, Y. Kivshar, A. S. Solntsev, Quasi-BIC Resonant Enhancement of Second-Harmonic Generation in WS- Monolayers, *Nano Lett* **2020**, *20*, 5309-5314. https://doi.org/10.1021/acs.nanolett.0c01603.

[39] S. Rosas, W. Adi, A. Beisenova, S. K. Biswas, F. Kuruoglu, H. Y. Mei, M. A. Kats, D. A. Czaplewski, Y. S. Kivshar, F. Yesilkoy, Enhanced biochemical sensing with high-Q transmission resonances in free-standing membrane metasurfaces, *Optica* **2025**, *12*, 178-189. https://doi.org/10.1364/Optica.549393.

[40] J. Yao, F. X. Lai, Y. B. Fan, Y. H. Wang, S. H. Huang, B. R. Leng, Y. Liang, R. Lin, S. F. Chen, M. K. Chen, P. C. Wu, S. M. Xiao, D. P. Tsai, Nonlocal meta-lens with

Huygens' bound states in the continuum, *Nat Commun* **2024**, *15*. https://doi.org/10.1038/s41467-024-50965-y.

[41] Z. J. Liu, Y. Xu, Y. Lin, J. Xiang, T. H. Feng, Q. T. Cao, J. T. Li, S. Lan, J. Liu, High-Q Quasibound States in the Continuum for Nonlinear Metasurfaces, *Phys Rev Lett* **2019**, *123*. https://doi.org/10.1103/PhysRevLett.123.253901.

[42] F. Yesilkoy, E. R. Arvelo, Y. Jahani, M. K. Liu, A. Tittl, V. Cevher, Y. Kivshar, H. Altug, Ultrasensitive hyperspectral imaging and biodetection enabled by dielectric metasurfaces, *Nat Photonics* **2019**, *13*, 390-+. https://doi.org/10.1038/s41566-019-0394-6.

[43] A. Tittl, A. Leitis, M. K. Liu, F. Yesilkoy, D. Y. Choi, D. N. Neshev, Y. S. Kivshar, H. Altug, Imaging-based molecular barcoding with pixelated dielectric metasurfaces, *Science* **2018**, *360*, 1105-+. https://doi.org/10.1126/science.aas9768.

[44] G. Li, S. Zhang, T. Zentgraf, Nonlinear photonic metasurfaces, *Nat Rev Mater* **2017**, *2*. https://doi.org/10.1038/natrevmats.2017.10.

[45] J. Yao, W. L. Hsu, Y. Liang, R. Lin, M. K. Chen, D. P. Tsai, Nonlocal metasurface for dark-field edge emission, *Sci Adv* **2024**, *10*. https://doi.org/10.1126/sciadv.adn2752.

[46] Y. Liang, D. P. Tsai, Y. Kivshar, From Local to Nonlocal High-Q Plasmonic Metasurfaces, *Phys Rev Lett* **2024**, *133*. https://doi.org/10.1103/PhysRevLett.133.053801.

[47] P. Lalanne, P. Chavel, Metalenses at visible wavelengths: past, present, perspectives, *Laser Photonics Rev* **2017**, *11*. https://doi.org/10.1002/lpor.201600295.

[48] J. R. Nolen, A. C. Overvig, M. Cotrufo, A. Alù, Local control of polarization and geometric phase in thermal metasurfaces, *Nat Nanotechnol* **2024**, *19*. https://doi.org/10.1038/s41565-024-01763-6.

[49] J. Y. Ma, J. H. Zhang, J. Horder, A. A. Sukhorukov, M. Toth, D. N. Neshev, I. Aharonovich, Engineering Quantum Light Sources with Flat Optics, *Adv Mater* **2024**, *36*. https://doi.org/10.1002/adma.202313589.

[50] J. Kim, H. Chung, S. Lee, G. Boehm, M. A. Belkin, J. Lee, Local-to-Nonlocal Second-Harmonic Generation from Electrically Tunable Intersubband Polaritonic Metasurfaces, *Adv Sci* **2025**. https://doi.org/10.1002/advs.202518776.

[51] Y. G. Ma, Y. B. Gao, Metasurfaces: Design Principles and Application Challenges (Invited), *Chin J Lasers* **2024**, *51*. https://doi.org/10.3788/Cjl231405.

[52] S. T. Ha, Q. T. Li, J. K. W. Yang, H. V. Demir, M. L. Brongersma, A. I. Kuznetsov, Optoelectronic metadevices, *Science* **2024**, *386*. https://doi.org/10.1126/science.adm7442.

[53] Y. Horie, S. Han, J. Y. Lee, J. Kim, Y. Kim, A. Arbabi, C. Shin, L. L. Shi, E. Arbabi, S. M. Kamali, H. S. Lee, S. Hwang, A. Faraon, Visible Wavelength Color Filters Using Dielectric Subwavelength Gratings for Backside-Illuminated CMOS Image Sensor Technologies, *Nano Lett* **2017**, *17*, 3159-3164. https://doi.org/10.1021/acs.nanolett.7b00636.

[54] Y. D. Shah, P. W. R. Connolly, J. P. Grant, D. Hao, C. Accarino, X. M. Ren, M. Kenney, V. Annese, K. G. Rew, Z. M. Greener, Y. Altmann, D. Faccio, G. S. Buller, D. R. S. Cumming, Ultralow-light-level color image reconstruction using high-

efficiency plasmonic metasurface mosaic filters, *Optica* **2020**, *7*, 632-639. https://doi.org/10.1364/Optica.389905.

[55] S. Wu, P. W. R. Connolly, V. Pusino, G. S. Buller, D. R. S. Cumming, Polarization-Controlled Transmissive Plasmonic Color Filter Using a Dimer-Aperture Array, *Adv Sci* **2025**, *12*, 2501941. https://doi.org/https://doi.org/10.1002/advs.202501941.

[56] I. Javed, A. J. Satti, J. Katrib, H. Cho, H. Park, K. M. Almustafa, M. Ebrahim, F. Alzhouri, M. Q. Mehmood, I. Kim, MetaScope: Metasurface Based Multimodal Imaging System, *Adv Funct Mater* **2025**. https://doi.org/10.1002/adfm.202524783.

[57] Q. Liu, Y. L. Liu, W. W. Liu, H. Cheng, S. Q. Chen, Metasurfaces-Enabled Advanced Multidimensional Imaging: Principle and Applications, *Ann Phys-Berlin* **2025**, *537*. https://doi.org/10.1002/andp.202400230.

[58] Z. C. Shen, F. Zhao, C. Q. Jin, S. Wang, L. C. Cao, Y. M. Yang, Monocular metasurface camera for passive single-shot 4D imaging, *Nat Commun* **2023**, *14*. https://doi.org/10.1038/s41467-023-36812-6.

[59] J. Yao, Y. B. Fan, Y. H. Gao, R. Lin, Z. H. Wang, M. K. Chen, S. M. Xiao, D. P. Tsai, Nonlocal Huygens' meta-lens for high-quality-factor spin-multiplexing imaging, *Light-Sci Appl* **2025**, *14*. https://doi.org/10.1038/s41377-024-01728-3.

[60] J. Sardana, S. Devinder, S. Kaassamani, W. Q. Zhu, A. Agrawal, J. Joseph, Polarization Specific Edge Enhancement Enabled by Compact Dielectric Metasurface Imaging System, *Acs Photonics* **2025**, *12*, 2380-2388. https://doi.org/10.1021/acsphotonics.4c01776.

[61] T. T. Liu, J. M. Qiu, L. Xu, M. B. Qin, L. P. Wan, T. B. Yu, Q. G. Liu, L. J. Huang, S. Y. Xiao, Edge Detection Imaging by Quasi-Bound States in the Continuum, *Nano Lett* **2024**, *24*, 14466-14474. https://doi.org/10.1021/acs.nanolett.4c04543.

[62] C. Zhou, Y. J. Chen, Y. Li, J. J. Li, R. Z. Zhao, C. D. Tao, C. B. Liu, Y. Bai, X. Li, Y. T. Wang, L. L. Huang, Laplace Differentiator Based on Metasurface with Toroidal Dipole Resonance, *Adv Funct Mater* **2024**, *34*. https://doi.org/10.1002/adfm.202313777.

[63] M. Cotrufo, S. Singh, A. Arora, A. Majewski, A. Alu, Polarization imaging and edge detection with image-processing metasurfaces, *Optica* **2023**, *10*, 1331-1338. https://doi.org/10.1364/Optica.500121.

[64] A. Mischok, B. Siegmund, F. Le Roux, S. Hillebrandt, K. Vandewal, M. C. Gather, Breaking the angular dispersion limit in thin film optics by ultra-strong light-matter coupling, *Nat Commun* **2024**, *15*. https://doi.org/10.1038/s41467-024-54623-1.

[65] J. X. Zhang, L. D. Zhang, W. Xu, Surface plasmon polaritons: physics and applications, *J Phys D Appl Phys* **2012**, *45*. https://doi.org/10.1088/0022-3727/45/11/113001.

[66] C. U. Hail, G. Schnoering, M. Damak, D. Poulikakos, H. Eghlidi, A Plasmonic Painter's Method of Color Mixing for a Continuous Red-Green-Blue Palette, *Acs Nano* **2020**, *14*, 1783-1791. https://doi.org/10.1021/acsnano.9b07523.

[67] P. Genevet, F. Capasso, F. Aieta, M. Khorasaninejad, R. Devlin, Recent advances in planar optics: from plasmonic to dielectric metasurfaces, *Optica* **2017**, *4*, 139-152. https://doi.org/10.1364/Optica.4.000139.

[68] T. Xu, Y. K. Wu, X. G. Luo, L. J. Guo, Plasmonic nanoresonators for high-resolution colour filtering and spectral imaging, *Nat Commun* **2010**, *1*. https://doi.org/10.1038/ncomms1058.

[69] M. S. Bin-Alam, O. Reshef, Y. Mamchur, M. Z. Alam, G. Carlow, J. Upham, B. T. Sullivan, J. M. Ménard, M. J. Huttunen, R. W. Boyd, K. Dolgaleva, Ultra-high-Q resonances in plasmonic metasurfaces, *Nat Commun* **2021**, *12*. https://doi.org/10.1038/s41467-021-21196-2.

[70] H. T. Liu, P. Lalanne, Microscopic theory of the extraordinary optical transmission, *Nature* **2008**, *452*, 728-731. https://doi.org/10.1038/nature06762.

[71] C. Genet, T. W. Ebbesen, Light in tiny holes, *Nature* **2007**, *445*, 39-46. https://doi.org/10.1038/nature05350.

[72] J. R. DiMaio, J. Ballato, Polarization-dependent transmission through subwavelength anisotropic aperture arrays, *Opt Express* **2006**, *14*, 2380-2384. https://doi.org/Doi 10.1364/Oe.14.002380.

[73] L. Martín-Moreno, F. J. García-Vidal, H. J. Lezec, K. M. Pellerin, T. Thio, J. B. Pendry, T. W. Ebbesen, Theory of extraordinary optical transmission through subwavelength hole arrays, *Phys Rev Lett* **2001**, *86*, 1114-1117. https://doi.org/DOI 10.1103/PhysRevLett.86.1114.

[74] T. W. Ebbesen, H. J. Lezec, H. F. Ghaemi, T. Thio, P. A. Wolff, Extraordinary optical transmission through sub-wavelength hole arrays, *Nature* **1998**, *391*, 667-669. https://doi.org/Doi 10.1038/35570.

[75] Y. D. Shah, J. Grant, D. Hao, M. Kenney, V. Pusino, D. R. S. Cumming, Ultra-narrow Line Width Polarization-Insensitive Filter Using a Symmetry-Breaking Selective Plasmonic Metasurface, *Acs Photonics* **2018**, *5*, 663-+. https://doi.org/10.1021/acsphotonics.7b01011.

[76] M. H. Jiang, S. Y. Siew, J. Y. E. Chan, J. Deng, Q. Y. S. Wu, L. Jin, J. K. W. Yang, J. H. Teng, A. Donner, C. W. Qiu, Patterned resist on flat silver achieving saturated plasmonic colors with sub-20-nm spectral linewidth, *Mater Today* **2020**, *35*, 99-105. https://doi.org/10.1016/j.mattod.2019.10.020.

[77] M. W. Song, L. Feng, P. C. Huo, M. Z. Liu, C. Y. Huang, F. Yan, Y. Q. Lu, T. Xu, Versatile full-colour nanopainting enabled by a pixelated plasmonic metasurface, *Nat Nanotechnol* **2023**, *18*, 71-+. https://doi.org/10.1038/s41565-022-01256-4.

[78] B. Y. Zheng, Y. M. Wang, P. Nordlander, N. J. Halas, Color-Selective and CMOS-Compatible Photodetection Based on Aluminum Plasmonics, *Adv Mater* **2014**, *26*, 6318-6323. https://doi.org/10.1002/adma.201401168.

[79] K. Li, J. W. Wang, W. F. Cai, H. L. He, J. X. Liu, Z. Yin, D. Luo, Q. Q. Mu, D. Gérard, Y. J. Liu, Electrically switchable structural colors based on liquid-crystal-overlaid aluminum anisotropic nanoaperture arrays, *Opt Express* **2022**, *30*, 31913-31924. https://doi.org/10.1364/Oe.461887.

[80] F. Cheng, J. Gao, L. Stan, D. Rosenmann, D. Czaplewski, X. D. Yang, Aluminum plasmonic metamaterials for structural color printing, *Opt Express* **2015**, *23*, 14552-14560. https://doi.org/10.1364/Oe.23.014552.

[81] S. I. Azzam, A. Kildishev, Photonic Bound States in the Continuum: From Basics to Applications, *Adv Opt Mater* **2021**, *9*. https://doi.org/10.1002/adom.202001469.

[82] D. C. Marinica, A. G. Borisov, S. V. Shabanov, Bound states in the continuum in photonics, *Phys Rev Lett* **2008**, *100*. https://doi.org/10.1103/PhysRevLett.100.183902.

[83] J. B. Yu, W. Z. Yao, M. Qiu, Q. Li, Free-space high-Q nanophotonics, *Light-Sci Appl* **2025**, *14*, 174. https://doi.org/10.1038/s41377-025-01825-x.

[84] M. Kang, T. Liu, C. T. Chan, M. Xiao, Applications of bound states in the continuum in photonics, *Nat Rev Phys* **2023**, *5*, 659-678. https://doi.org/10.1038/s42254-023-00642-8.

[85] B. Zhen, C. W. Hsu, L. Lu, A. D. Stone, M. Soljacic, Topological Nature of Optical Bound States in the Continuum, *Phys Rev Lett* **2014**, *113*. https://doi.org/10.1103/PhysRevLett.113.257401.

[86] Z. J. Yu, X. K. Sun, Acousto-optic modulation of photonic bound state in the continuum, *Light-Sci Appl* **2020**, *9*. https://doi.org/10.1038/s41377-019-0231-1.

[87] L. Xu, K. Z. Kamali, L. J. Huang, M. Rahmani, A. Smirnov, R. Camacho-Morales, Y. X. Ma, G. Q. Zhang, M. Woolley, D. Neshev, A. E. Miroshnichenko, Dynamic Nonlinear Image Tuning through Magnetic Dipole Quasi-BIC Ultrathin Resonators, *Adv Sci* **2019**, *6*. https://doi.org/10.1002/advs.201802119.

[88] K. Koshelev, S. Lepeshov, M. K. Liu, A. Bogdanov, Y. Kivshar, Asymmetric Metasurfaces with High-Q Resonances Governed by Bound States in the Continuum, *Phys Rev Lett* **2018**, *121*, 193903. https://doi.org/10.1103/PhysRevLett.121.193903.

[89] H. Friedrich, D. Wintgen, Interfering Resonances and Bound-States in the Continuum, *Phys Rev A* **1985**, *32*, 3231-3242. https://doi.org/DOI 10.1103/PhysRevA.32.3231.

[90] P. D. Imesch, I. H. L. Wallow, D. M. Albert, The color of the human eye: A review of morphologic correlates and of some conditions that affect iridial pigmentation, *Surv Ophthalmol* **1997**, *41*, S117-S123. https://doi.org/DOI:10.1016/S0039-6257(97)80018-5.

[91] D. Comaniciu, P. Meer, Robust analysis of feature spaces: Color image segmentation, *Proc Cvpr Ieee* **1997**, 750-755. https://doi.org/Doi 10.1109/Cvpr.1997.609410.

[92] Q. Chen, X. Hu, L. Wen, Y. Yu, D. R. S. Cumming, Nanophotonic Image Sensors, *Small* **2016**, *12*, 4922-4935. https://doi.org/10.1002/smll.201600528.

[93] M. Vainio, L. Halonen, Mid-infrared optical parametric oscillators and frequency combs for molecular spectroscopy, *Phys Chem Chem Phys* **2016**, *18*, 4266-4294. https://doi.org/10.1039/c5cp07052j.

[94] J. Haas, B. Mizaikoff, Advances in Mid-Infrared Spectroscopy for Chemical Analysis, *Annu Rev Anal Chem* **2016**, *9*, 45-68. https://doi.org/10.1146/annurev-anchem-071015-041507.

[95] A. I. López-Lorente, B. Mizaikoff, Mid-infrared spectroscopy for protein analysis: potential and challenges, *Anal Bioanal Chem* **2016**, *408*, 2875-2889. https://doi.org/10.1007/s00216-016-9375-5.

[96] W. Adi, S. Rosas, A. Beisenova, S. K. Biswas, H. Y. Mei, D. A. Czaplewski, F. Yesilkoy, Trapping light in air with membrane metasurfaces for vibrational strong coupling, *Nat Commun* **2024**, *15*, 10049. https://doi.org/10.1038/s41467-024-54284-0.

[97] A. Leitis, A. Tittl, M. K. Liu, B. H. Lee, M. B. Gu, Y. S. Kivshar, H. Altug, Angle-multiplexed all-dielectric metasurfaces for broadband molecular fingerprint retrieval, *Sci Adv* **2019**, *5*. https://doi.org/10.1126/sciadv.aaw2871.

[98] S. Rosas, S. K. Biswas, W. Adi, F. Kuruoglu, A. Beisenova, M. S. Patankar, F. Yesilkoy, Mass-Manufactured Gradient Plasmonic Metasurfaces for Enhanced Mid-IR Spectrochemical Analysis of Complex Biofluids, *Adv Mater* **2025**, e04355. https://doi.org/10.1002/adma.202504355.

[99] A. Pors, M. G. Nielsen, R. L. Eriksen, S. I. Bozhevolnyi, Broadband Focusing Flat Mirrors Based on Plasmonic Gradient Metasurfaces, *Nano Lett* **2013**, *13*, 829-834. https://doi.org/10.1021/nl304761m.

[100] Q. Chen, D. Chitnis, K. Walls, T. D. Drysdale, S. Collins, D. R. S. Cumming, CMOS Photodetectors Integrated With Plasmonic Color Filters, *Ieee Photonic Tech L* **2012**, *24*, 197-199. https://doi.org/10.1109/Lpt.2011.2176333.

[101] W. J. Wu, J. B. Yang, D. B. Chen, Plasmonic Beam Deflector and Optical Coupler, *Ieee Photonic Tech L* **2017**, *29*, 1592-1595. https://doi.org/10.1109/Lpt.2017.2737779.

[102] T. Xu, C. T. Wang, C. L. Du, X. G. Luo, Plasmonic beam deflector, *Opt Express* **2008**, *16*, 4753-4759. https://doi.org/Doi 10.1364/Oe.16.004753.

[103] L. Verslegers, P. B. Catrysse, Z. F. Yu, J. S. White, E. S. Barnard, M. L. Brongersma, S. H. Fan, Planar Lenses Based on Nanoscale Slit Arrays in a Metallic Film, *Nano Lett* **2009**, *9*, 235-238. https://doi.org/10.1021/nl802830y.

[104] M. Kang, T. H. Feng, H. T. Wang, J. S. Li, Wave front engineering from an array of thin aperture antennas, *Opt Express* **2012**, *20*, 15882-15890. https://doi.org/10.1364/Oe.20.015882.

[105] X. Z. Chen, L. L. Huang, H. Mühlenbernd, G. X. Li, B. F. Bai, Q. F. Tan, G. F. Jin, C. W. Qiu, S. Zhang, T. Zentgraf, Dual-polarity plasmonic metalens for visible light, *Nat Commun* **2012**, *3*. https://doi.org/10.1038/ncomms2207.

[106] D. Wintz, P. Genevet, A. Ambrosio, A. Woolf, F. Capasso, Holographic Metalens for Switchable Focusing of Surface Plasmons, *Nano Lett* **2015**, *15*, 3585-3589. https://doi.org/10.1021/acs.nanolett.5b01076.

[107] X. J. Ni, A. V. Kildishev, V. M. Shalaev, Metasurface holograms for visible light, *Nat Commun* **2013**, *4*. https://doi.org/10.1038/ncomms3807.

[108] L. L. Huang, X. Z. Chen, H. Mühlenbernd, H. Zhang, S. M. Chen, B. F. Bai, Q. F. Tan, G. F. Jin, K. W. Cheah, C. W. Qiu, J. S. Li, T. Zentgraf, S. Zhang, Three-dimensional optical holography using a plasmonic metasurface, *Nat Commun* **2013**, *4*. https://doi.org/10.1038/ncomms3808.

[109] I. Freestone, N. Meeks, M. Sax, C. Higgitt, The Lycurgus Cup - A Roman nanotechnology, *Gold Bull* **2007**, *40*, 270-277. https://doi.org/Doi 10.1007/Bf03215599.

[110] K. M. Mayer, J. H. Hafner, Localized Surface Plasmon Resonance Sensors, *Chem Rev* **2011**, *111*, 3828-3857. https://doi.org/10.1021/cr100313v.

[111] K. Kumar, H. G. Duan, R. S. Hegde, S. C. W. Koh, J. N. Wei, J. K. W. Yang, Printing colour at the optical diffraction limit, *Nat Nanotechnol* **2012**, *7*, 557-561. https://doi.org/10.1038/Nnano.2012.128.

[112] Y. Li, J. Hu, Y. Zeng, Q. Song, C.-W. Qiu, S. Xiao, Recent progress on structural coloration, *Photonics Insights* **2024**, *3*, R03. https://doi.org/10.3788/pi.2024.R03.

[113] B. Yang, W. W. Liu, D. Y. Choi, Z. C. Li, H. Cheng, J. G. Tian, S. Q. Chen, High-Performance Transmission Structural Colors Generated by Hybrid Metal-Dielectric Metasurfaces, *Adv Opt Mater* **2021**, *9*. https://doi.org/10.1002/adom.202100895.

[114] S. Yokogawa, S. P. Burgos, H. A. Atwater, Plasmonic Color Filters for CMOS Image Sensor Applications, *Nano Lett* **2012**, *12*, 4349-4354. https://doi.org/10.1021/nl302110z.

[115] A. Wang, Y. P. Dan, Mid-infrared plasmonic multispectral filters, *Sci Rep-Uk* **2018**, *8*. https://doi.org/10.1038/s41598-018-29177-0.

[116] J. Grant, I. J. H. McCrindle, D. R. S. Cumming, Multi-spectral materials: hybridisation of optical plasmonic filters, a mid infrared metamaterial absorber and a terahertz metamaterial absorber, *Opt Express* **2016**, *24*, 3451-3463. https://doi.org/10.1364/Oe.24.003451.

[117] I. J. H. McCrindle, J. Grant, T. D. Drysdale, D. R. S. Cumming, Multi-Spectral Materials: Hybridisation of Optical Plasmonic Filters and a Terahertz Metamaterial Absorber, *Adv Opt Mater* **2014**, *2*, 149-153. https://doi.org/10.1002/adom.201300408.

[118] K. Li, J. W. Wang, W. F. Cai, H. L. He, M. J. Cen, J. X. Liu, D. Luo, Q. Q. Mu, D. Gérard, Y. J. Liu, Electrically Switchable, Polarization-Sensitive Encryption Based on Aluminum Nanoaperture Arrays Integrated with Polymer-Dispersed Liquid Crystals, *Nano Lett* **2021**, *21*, 7183-7190. https://doi.org/10.1021/acs.nanolett.1c01947.

[119] Z. B. Li, A. W. Clark, J. M. Cooper, Dual Color Plasmonic Pixels Create a Polarization Controlled Nano Color Palette, *Acs Nano* **2016**, *10*, 492-498. https://doi.org/10.1021/acsnano.5b05411.

[120] A. F. Kaplan, T. Xu, L. J. Guo, High efficiency resonance-based spectrum filters with tunable transmission bandwidth fabricated using nanoimprint lithography, *Appl Phys Lett* **2011**, *99*. https://doi.org/10.1063/1.3647633.

[121] S. Sun, Z. X. Zhou, C. Zhang, Y. S. Gao, Z. H. Duan, S. M. Xiao, Q. H. Song, All-Dielectric Full-Color Printing with TiO2 Metasurfaces, *Acs Nano* **2017**, *11*, 4445-4452. https://doi.org/10.1021/acsnano.7b00415.

[122] W. H. Yang, S. M. Xiao, Q. H. Song, Y. L. Liu, Y. K. Wu, S. Wang, J. Yu, J. C. Han, D. P. Tsai, All-dielectric metasurface for high-performance structural color, *Nat Commun* **2020**, *11*, 1864. https://doi.org/10.1038/s41467-020-15773-0.

[123] Z. G. Dong, L. Jin, S. D. Rezaei, H. Wang, Y. Chen, F. Tjiptoharsono, J. F. Ho, S. Gorelik, R. J. H. Ng, Q. F. Ruan, C. W. Qiu, J. K. W. Yang, Schrodinger's red pixel by quasi-bound-states-in-the-continuum, *Sci Adv* **2022**, *8*. https://doi.org/10.1126/sciadv.abm4512.

[124] Y. Zuo, B. Ni, Y. R. Zhou, J. H. Guo, H. B. Ni, X. Y. Zhou, S. J. Haque, J. H. Chang, Inverse design of polarization-independent structural color based on a coding metasurface via a bidirectional artificial neural network, *J Opt Soc Am B* **2024**, *41*, 2220-2227. https://doi.org/10.1364/Josab.530686.

[125] C. H. Lee, S. K. Lee, J. Seong, D. Y. Park, J. Rho, Inverse-designed metasurfaces for highly saturated transmissive colors, *J Opt Soc Am B* **2024**, *41*, 151-158. https://doi.org/10.1364/Josab.505444.

[126] C. Liu, J. L. Zhang, Y. P. Zhao, B. Ai, Inverse Design of Plasmonic Nanohole Arrays by Combing Spectra and Structural Color in Deep Learning, *Adv Intell Syst-Ger* **2023**, *5*. https://doi.org/10.1002/aisy.202300121.

[127] Z. Huang, X. Liu, J. F. Zang, The inverse design of structural color using machine learning, *Nanoscale* **2019**, *11*, 21748-21758. https://doi.org/10.1039/c9nr06127d.
[128] R. Y. Shen, R. He, L. Y. Chen, J. P. Guo, Inverse design of hybrid metal-dielectric guided mode resonance optical filters with a deep learning neural network and Fano function matching, *Opt Mater Express* **2022**, *12*, 3600-3613. https://doi.org/10.1364/Ome.461634.
[129] X. Qi, J. J. Wu, F. Wu, M. N. Ren, Q. Wei, Y. F. Wang, H. T. Jiang, Y. H. Li, Z. W. Guo, Y. P. Yang, W. H. Zheng, Y. Sun, H. Chen, Steerable merging bound states in the continuum on a quasi-flatband of photonic crystal slabs without breaking symmetry, *Photonics Res* **2023**, *11*, 1262-1274. https://doi.org/10.1364/Prj.487665.
[130] C. Saadi, S. Cueff, L. Ferrier, A. Benamrouche, M. Gayrard, E. Drouard, X. Letartre, H. S. Nguyen, S. Callard, Tailoring Flatband Dispersion in Bilayer Moiré Photonic Crystals, *Laser Photonics Rev* **2025**, *19*. https://doi.org/10.1002/lpor.202501038.
[131] S. M. Trushin, T. Ito, Y. Ishii, S. Iwamoto, Y. Ota, Flatband localization in 1D moiré bilayer photonic crystals with staggered potential, *Opt Lett* **2025**, *50*, 2405-2408. https://doi.org/10.1364/Ol.558564.
[132] G. D. Wang, E. Maqbool, Z. H. Han, High-Q optical resonances with robustness based on the quasi-guided modes in waveguide moiré gratings, *Opt Express* **2024**, *32*, 4720-4727. https://doi.org/10.1364/Oe.516194.
[133] T. Wenger, R. E. Muller, D. W. Wilson, A. Soibel, Mid-infrared plasmonic filter arrays using nanoholes in gold and silver films, *Opt Lett* **2023**, *48*, 3925-3928. https://doi.org/10.1364/Ol.492934.
[134] J. Xu, A. Wang, Y. P. Dan, Plasmonic micropipe spectral filters in mid-infrared, *Opt Lett* **2019**, *44*, 4479-4482. https://doi.org/10.1364/Ol.44.004479.
[135] J. R. Zhang, Z. J. Chen, Z. J. Su, Y. P. Dan, High-performance plasmonic mid-infrared bandpass filters by inverse design, *Nanotechnology* **2024**, *35*. https://doi.org/10.1088/1361-6528/ad1b99.
[136] W. S. Yue, Z. H. Wang, Y. Yang, J. Q. Li, Y. Wu, L. Q. Chen, B. Ooi, X. B. Wang, X. X. Zhang, Enhanced extraordinary optical transmission (EOT) through arrays of bridged nanohole pairs and their sensing applications, *Nanoscale* **2014**, *6*, 7917-7923. https://doi.org/10.1039/c4nr01001a.
[137] S. G. Rodrigo, L. Martín-Moreno, A. Y. Nikitin, A. V. Kats, I. S. Spevak, F. J. García-Vidal, Extraordinary optical transmission through hole arrays in optically thin metal films, *Opt Lett* **2009**, *34*, 4-6. https://doi.org/Doi 10.1364/Ol.34.000004.
[138] F. U. Richter, I. Sinev, S. L. Zhou, A. Leitis, S. H. Oh, M. L. Tseng, Y. Kivshar, H. Altug, Gradient High-Q Dielectric Metasurfaces for Broadband Sensing and Control of Vibrational Light-Matter Coupling, *Adv Mater* **2024**, *36*. https://doi.org/10.1002/adma.202314279.
[139] A. Aigner, T. Weber, A. Wester, S. A. Maier, A. Tittl, Continuous spectral and coupling-strength encoding with dual-gradient metasurfaces, *Nat Nanotechnol* **2024**, *19*, 1804-1812. https://doi.org/10.1038/s41565-024-01767-2.
[140] H. He, F. Lai, Y. Zhang, X. Zhang, C. Tian, X. Li, Y. Wang, S. Xiao, L. Huang, Spectro-polarimetric detection enabled by multidimensional metasurface with quasi-bound states in the continuum, *Opto-Electronic Advances* **2025**, *8*, 250015-250011-250015-250011. https://doi.org/10.29026/oea.2025.250015.

[141] R. D. Wang, R. Hao, D. X. Li, L. J. Huang, R. D. Jiang, X. B. Zhang, X. Yang, L. Wang, S. M. Wang, Y. Kivshar, C. Chang, Multifunctional Terahertz Biodetection Enabled by Resonant Metasurfaces, *Adv Mater* **2025**, *37*. https://doi.org/10.1002/adma.202418147.

[142] I. Sinev, F. U. Richter, I. Toftul, N. Glebov, K. Koshelev, Y. Hwang, D. G. Lancaster, Y. Kivshar, H. Altug, Chirality encoding in resonant metasurfaces governed by lattice symmetries, *Nat Commun* **2025**, *16*. https://doi.org/10.1038/s41467-025-61221-2.

[143] W. H. Wang, Y. K. Srivastava, T. C. Tan, Z. M. Wang, R. Singh, Brillouin zone folding driven bound states in the continuum, *Nat Commun* **2023**, *14*, 2811. https://doi.org/10.1038/s41467-023-38367-y.

[144] S. R. Furkan Kuruoglu, Jin-Woo Cho, David A. Czaplewski, Yuri Kivshar, Mikhail Kats, Filiz Yesilkoy, Dynamically Tunable Membrane Metasurfaces for Infrared Spectroscopy, *arXiv* **2025**, *2506.10115*. https://doi.org/https://doi.org/10.48550/arXiv.2506.10115.

[145] J. Kühne, J. Wang, T. Weber, L. Kühner, S. A. Maier, A. Tittl, Fabrication robustness in BIC metasurfaces, *Nanophotonics-Berlin* **2021**, *10*, 4305-4312. https://doi.org/10.1515/nanoph-2021-0391.

[146] M. Luo, Y. Zhou, X. Y. Zhao, Z. H. Guo, Y. X. Li, Q. Wang, J. J. Liu, W. Luo, Y. Z. Shi, A. Q. Liu, X. Wu, High-Sensitivity Optical Sensors Empowered by Quasi-Bound States in the Continuum in a Hybrid Metal-Dielectric Metasurface, *Acs Nano* **2024**, *18*, 6477-6486. https://doi.org/10.1021/acsnano.3c11994.

[147] S. K. Biswas, W. Adi, A. Beisenova, S. Rosas, E. R. Arvelo, F. Yesilkoy, From weak to strong coupling: quasi-BIC metasurfaces for mid-infrared light-matter interactions, *Nanophotonics-Berlin* **2024**, *13*, 2937-2949. https://doi.org/10.1515/nanoph-2024-0043.

[148] A. John-Herpin, A. Tittl, L. Kühner, F. Richter, S. H. Huang, G. Shvets, S. H. Oh, H. Altug, Metasurface-Enhanced Infrared Spectroscopy: An Abundance of Materials and Functionalities, *Adv Mater* **2023**, *35*, 2110163. https://doi.org/10.1002/adma.202110163.

[149] J. Kozuch, K. Ataka, J. Heberle, Surface-enhanced infrared absorption spectroscopy, *Nat Rev Method Prime* **2023**, *3*. https://doi.org/10.1038/s43586-023-00253-8.

[150] S. Liu, M. B. Sinclair, S. Saravi, G. A. Keeler, Y. M. Yang, J. Reno, G. M. Peake, F. Setzpfandt, I. Staude, T. Pertsch, I. Brener, Resonantly Enhanced Second-Harmonic Generation Using III-V Semiconductor All-Dielectric Metasurfaces, *Nano Lett* **2016**, *16*, 5426-5432. https://doi.org/10.1021/acs.nanolett.6b01816.

[151] R. Kolkowski, T. K. Hakala, A. Shevchenko, M. J. Huttunen, Nonlinear nonlocal metasurfaces, *Appl Phys Lett* **2023**, *122*. https://doi.org/10.1063/5.0140483.

[152] J. Yang, Y. Z. Li, Y. M. Yang, X. R. Xie, Z. J. Zhang, J. L. Yuan, H. Cai, D. W. Wang, F. Gao, Realization of all-band-flat photonic lattices, *Nat Commun* **2024**, *15*. https://doi.org/10.1038/s41467-024-45580-w.

[153] Y. Yang, C. Roques-Carmes, S. E. Kooi, H. N. Tang, J. Beroz, E. Mazur, I. Kaminer, J. D. Joannopoulos, M. Soljacic, Photonic flatband resonances for free-electron radiation, *Nature* **2023**, *613*, 42-+. https://doi.org/10.1038/s41586-022-05387-5.

[154] D. Leykam, S. Flach, Perspective: Photonic flatbands, *Apl Photonics* **2018**, *3*. https://doi.org/10.1063/1.5034365.

[155] B. Sutherland, Localization of Electronic Wave-Functions Due to Local Topology, *Phys Rev B* **1986**, *34*, 5208-5211. https://doi.org/DOI 10.1103/PhysRevB.34.5208.
[156] M. Arai, T. Tokihiro, T. Fujiwara, M. Kohmoto, Strictly Localized States on a Two-Dimensional Penrose Lattice, *Phys Rev B* **1988**, *38*, 1621-1626. https://doi.org/DOI 10.1103/PhysRevB.38.1621.
[157] J. Li, T. P. White, L. O'Faolain, A. Gomez-Iglesias, T. F. Krauss, Systematic design of flat band slow light in photonic crystal waveguides, *Opt Express* **2008**, *16*, 6227-6232. https://doi.org/Doi 10.1364/Oe.16.006227.
[158] H. S. Nguyen, F. Dubois, T. Deschamps, S. Cueff, A. Pardon, J. L. Leclercq, C. Seassal, X. Letartre, P. Viktorovitch, Symmetry Breaking in Photonic Crystals: On-Demand Dispersion from Flatband to Dirac Cones, *Phys Rev Lett* **2018**, *120*. https://doi.org/10.1103/PhysRevLett.120.066102.
[159] J. W. Yang, K. Y. Cui, Y. D. Huang, W. Zhang, X. Feng, F. Liu, Angle-Insensitive Spectral Imaging Based on Topology-Optimized Plasmonic Metasurfaces, *Laser Photonics Rev* **2024**, *18*. https://doi.org/10.1002/lpor.202400255.
[160] X. Y. Zhang, Q. Li, F. F. Liu, M. Qiu, S. L. Sun, Q. He, L. Zhou, Controlling angular dispersions in optical metasurfaces, *Light-Sci Appl* **2020**, *9*, 76. https://doi.org/10.1038/s41377-020-0313-0.
[161] C. Y. Yang, W. D. Shen, J. Zhou, X. Fang, D. Zhao, X. Zhang, C. G. Ji, B. Fang, Y. G. Zhang, X. Liu, L. J. Guo, Angle Robust Reflection/Transmission Plasmonic Filters Using Ultrathin Metal Patch Array, *Adv Opt Mater* **2016**, *4*, 1981-1986. https://doi.org/10.1002/adom.201600397.
[162] G. C. Sun, Y. Wang, Y. H. Li, Z. J. Cui, W. S. Chen, K. Zhang, Tailoring topological nature of merging bound states in the continuum by manipulating structure symmetry of the all-dielectric metasurface, *Phys Rev B* **2024**, *109*. https://doi.org/10.1103/PhysRevB.109.035406.
[163] M. Kang, L. Mao, S. P. Zhang, M. Xiao, H. X. Xu, C. T. Chan, Merging bound states in the continuum by harnessing higher-order topological charges, *Light-Sci Appl* **2022**, *11*. https://doi.org/10.1038/s41377-022-00923-4.
[164] M. Kang, S. P. Zhang, M. Xiao, H. X. Xu, Merging Bound States in the Continuum at Off-High Symmetry Points, *Phys Rev Lett* **2021**, *126*.
[165] N. D. Le, P. Bouteyre, A. Kheir-Aldine, F. Dubois, L. Berguiga, X. Letartre, P. Viktorovitch, T. Benyattou, H. S. Nguyen, Super Bound States in the Continuum on a Photonic Flatband: Concept, Experimental Realization, and Optical Trapping Demonstration, *Phys Rev Lett* **2024**, *132*, 173802. https://doi.org/10.1103/PhysRevLett.132.173802.
[166] C. U. Hail, L. Michaeli, H. A. Atwater, Third Harmonic Generation Enhancement and Wavefront Control Using a Local High-Q Metasurface, *Nano Lett* **2024**, *24*, 2257-2263. https://doi.org/10.1021/acs.nanolett.3c04476.
[167] C. Munley, A. Manna, D. Sharp, M. Choi, H. A. Nguyen, B. M. Cossairt, M. Li, A. W. Barnard, A. Majumdar, Visible Wavelength Flatband in a Gallium Phosphide Metasurface, *Acs Photonics* **2023**, *10*, 2456-2460. https://doi.org/10.1021/acsphotonics.3c00175.
[168] M. Choi, C. Munley, J. E. Fröch, R. Chen, A. Majumdar, Nonlocal, Flat-Band Meta-Optics for Monolithic, High-Efficiency, Compact Photodetectors, *Nano Lett* **2024**, *24*, 3150-3156. https://doi.org/10.1021/acs.nanolett.3c05139.

[169] T. T. H. Do, Z. Y. Yuan, E. G. Durmusoglu, H. K. Shamkhi, V. Valuckas, C. Y. Zhao, A. I. Kuznetsov, H. V. Demir, C. Dang, H. S. Nguyen, S. T. Ha, Room-Temperature Lasing at Flatband Bound States in the Continuum*, Acs Nano* **2025**, *19*, 19287-19296. https://doi.org/10.1021/acsnano.5c01972.

[170] S. Eyvazi, E. A. Mamonov, R. Heilmann, J. Cuerda, P. Törmä, Flat-Band Lasing in Silicon Waveguide-Integrated Metasurfaces*, Acs Photonics* **2025**, *12*, 1570-1578. https://doi.org/10.1021/acsphotonics.4c02332.

[171] K. L. Sun, Y. J. Cai, L. J. Huang, Z. H. Han, Ultra-narrowband and rainbow-free mid-infrared thermal emitters enabled by a flat band design in distorted photonic lattices*, Nat Commun* **2024**, *15*. https://doi.org/10.1038/s41467-024-48499-4.

[172] K. Sun, K. Wang, W. Wang, Y. Cai, L. Huang, A. Alù, Z. Han, High-Q photonic flat-band resonances for enhancing third-harmonic generation in all-dielectric metasurfaces*, Newton* **2025**, *1*. https://doi.org/10.1016/j.newton.2025.100057.

[173] C. Kim, B. Lee, TORCWA: GPU-accelerated Fourier modal method and gradient-based optimization for metasurface design*, Comput Phys Commun* **2023**, *282*. https://doi.org/10.1016/j.cpc.2022.108552.

[174] M. G. Moharam, E. B. Grann, D. A. Pommet, T. K. Gaylord, Formulation for Stable and Efficient Implementation of the Rigorous Coupled-Wave Analysis of Binary Gratings*, J Opt Soc Am A* **1995**, *12*, 1068-1076. https://doi.org/Doi 10.1364/Josaa.12.001068.

[175] M. G. Moharam, T. K. Gaylord, Rigorous Coupled-Wave Analysis of Metallic Surface-Relief Gratings*, J Opt Soc Am A* **1986**, *3*, 1780-1787. https://doi.org/Doi 10.1364/Josaa.3.001780.

[176] M. G. Moharam, T. K. Gaylord, Rigorous Coupled-Wave Analysis of Planar-Grating Diffraction*, J Opt Soc Am* **1981**, *71*, 811-818. https://doi.org/Doi 10.1364/Josa.71.000811.

[177] J. J. Hench, Z. Strakos, The Rcwa Method - a Case Study with Open Questions and Perspectives of Algebraic Computations*, Electron T Numer Ana* **2008**, *31*, 331-357.

[178] Y. Kane, Numerical solution of initial boundary value problems involving maxwell's equations in isotropic media*, IEEE Transactions on Antennas and Propagation* **1966**, *14*, 302-307. https://doi.org/10.1109/TAP.1966.1138693.

[179] A. Taflove, Application of the Finite-Difference Time-Domain Method to Sinusoidal Steady-State Electromagnetic-Penetration Problems*, Ieee T Electromagn C* **1980**, *22*, 191-202. https://doi.org/Doi 10.1109/Temc.1980.303879.

[180] *What is Finite-Difference Time-Domain (FDTD)?*,

[181] D. E. McCoy, A. Shneidman, A. L. Davis, J. Aizenberg, Finite-difference Time-domain (FDTD) Optical Simulations: A Primer for the Life Sciences and Bio-Inspired Engineering*, Micron* **2021**, *151*. https://doi.org/10.1016/j.micron.2021.103160.

[182] S. D. Gedney, *Introduction to the Finite-difference Time-domain (FDTD) Method for Electromagnetics,P 52-55 Vol.*, Morgan & Claypool Publishers, **2011**.

[183] A. Calà Lesina, A. Vaccari, P. Berini, L. Ramunno, On the convergence and accuracy of the FDTD method for nanoplasmonics*, Opt Express* **2015**, *23*, 10481-10497. https://doi.org/10.1364/Oe.23.010481.

[184] *Selecting the best mesh refinement option in the FDTD simulation object*, https://optics.ansys.com/hc/en-us/articles/360034382614-Selecting-the-best-mesh-refinement-option-in-the-FDTD-simulation-object

[185] Y. M. Yang, I. I. Kravchenko, D. P. Briggs, J. Valentine, All-dielectric metasurface analogue of electromagnetically induced transparency*, Nat Commun* **2014**, *5*. https://doi.org/10.1038/ncomms6753.

[186] *GPU Acceleration in AI: How Graphics Processing Units Drive Deep Learning*, https://gcore.com/blog/deep-learning-gpu

[187] W. Jeon, G. Ko, J. Lee, H. Lee, D. Ha, W. W. Ro, Deep learning with GPUs*, Adv Comput* **2021**, *122*, 167-215. https://doi.org/10.1016/bs.adcom.2020.11.003.

[188] M. G. Moharam, D. A. Pommet, E. B. Grann, T. K. Gaylord, Stable Implementation of the Rigorous Coupled-Wave Analysis for Surface-Relief Gratings - Enhanced Transmittance Matrix Approach*, J Opt Soc Am A* **1995**, *12*, 1077-1086. https://doi.org/Doi 10.1364/Josaa.12.001077.

[189] S. Spiridonov, A. A. Shcherbakov, Reformulated Fourier Modal Method with improved near field computations*, J Comput Sci-Neth* **2023**, *67*. https://doi.org/10.1016/j.jocs.2022.101936.

[190] A. Rahimzadegan, T. D. Karamanos, R. Alaee, A. G. Lamprianidis, D. Beutel, R. W. Boyd, C. Rockstuhl, A Comprehensive Multipolar Theory for Periodic Metasurfaces*, Adv Opt Mater* **2022**, *10*. https://doi.org/10.1002/adom.202102059.

[191] A. Hassanfiroozi, P. S. Huang, S. H. Huang, K. I. Lin, Y. T. Lin, C. F. Chien, Y. Z. Shi, W. J. Lee, P. C. Wu, A Toroidal-Fano-Resonant Metasurface with Optimal Cross-Polarization Efficiency and Switchable Nonlinearity in the Near-Infrared*, Adv Opt Mater* **2021**, *9*. https://doi.org/10.1002/adom.202101007.

[192] P. D. Terekhov, V. E. Babicheva, K. V. Baryshnikova, A. S. Shalin, A. Karabchevsky, A. B. Evlyukhin, Multipole analysis of dielectric metasurfaces composed of nonspherical nanoparticles and lattice invisibility effect*, Phys Rev B* **2019**, *99*. https://doi.org/10.1103/PhysRevB.99.045424.

[193] R. W. Millar, K. Gallacher, U. Griskeviciute, L. Baldassarre, M. Sorel, M. Ortolani, D. J. Paul, Low Loss Germanium-on-Silicon waveguides for integrated Mid-infrared Photonics*, Proc Spie* **2019**, *10923*. https://doi.org/10.1117/12.2510009.

[194] K. Gallacher, R. W. Millar, V. Giliberti, E. Calandrini, L. Baldassarre, J. Frigerio, A. Ballabio, E. Sakat, G. Pellegrini, G. Isella, M. Ortolani, P. Biagioni, D. J. Paul, Mid-Infrared n-Ge on Si Plasmonic Based Microbolometer Sensors*, Ieee Int Conf Group* **2017**, 3-4.

[195] P. Pal, V. Swarnalatha, A. V. N. Rao, A. K. Pandey, H. Tanaka, K. Sato, High speed silicon wet anisotropic etching for applications in bulk micromachining: a review*, Micro and Nano Systems Letters* **2021**, *9*, 4. https://doi.org/10.1186/s40486-021-00129-0.

[196] P. Pal, K. Sato, A comprehensive review on convex and concave corners in silicon bulk micromachining based on anisotropic wet chemical etching*, Micro and Nano Systems Letters* **2015**, *3*, 6. https://doi.org/10.1186/s40486-015-0012-4.

[197] A. H. Nuttall, Some Windows with Very Good Sidelobe Behavior*, Ieee T Acoust Speech* **1981**, *29*, 84-91. https://doi.org/Doi 10.1109/Tassp.1981.1163506.

[198] G. Horváth, *Polarized Light and Polarization Vision in Animal Sciences, 2nd Edition,P 2*, **2014**.

[199] N. J. Marshall, A Unique Color and Polarization Vision System in Mantis Shrimps, *Nature* **1988**, *333*, 557-560. https://doi.org/DOI 10.1038/333557a0.
[200] F. Liu, Y. Wei, P. L. Han, K. Yang, L. Bai, X. P. Shao, Polarization-based exploration for clear underwater vision in natural illumination, *Opt Express* **2019**, *27*, 3629-3641. https://doi.org/10.1364/Oe.27.003629.
[201] X. Huang, J. Bai, K. W. Wang, Q. Liu, Y. J. Luo, K. L. Yang, X. J. Zhang, Target enhanced 3D reconstruction based on polarization-coded structured light, *Opt Express* **2017**, *25*, 1173-1184. https://doi.org/10.1364/Oe.25.001173.
[202] L. H. Shen, Y. Q. Zhao, Q. N. Peng, J. C. W. Chan, S. G. Kong, An Iterative Image Dehazing Method With Polarization, *Ieee T Multimedia* **2019**, *21*, 1093-1107. https://doi.org/10.1109/Tmm.2018.2871955.
[203] C. He, H. H. He, J. T. Chang, B. G. Chen, H. Ma, M. J. Booth, Polarisation optics for biomedical and clinical applications: a review, *Light-Sci Appl* **2021**, *10*. https://doi.org/10.1038/s41377-021-00639-x.
[204] S. J. Wen, Y. Q. Zheng, F. Lu, Q. P. Zhao, Convolutional demosaicing network for joint chromatic and polarimetric imagery, *Opt Lett* **2019**, *44*, 5646-5649. https://doi.org/10.1364/Ol.44.005646.
[205] Y. Y. Sun, J. C. Zhang, R. G. Liang, Color polarization demosaicking by a convolutional neural network, *Opt Lett* **2021**, *46*, 4338-4341. https://doi.org/10.1364/Ol.431919.
[206] Y. D. Luo, J. C. Zhang, D. Tian, Sparse representation-based demosaicking method for joint chromatic and polarimetric imagery, *Opt Laser Eng* **2023**, *164*. https://doi.org/10.1016/j.optlaseng.2023.107526.
[207] J. Liu, J. Duan, Y. F. Hao, G. Q. Chen, H. Zhang, Y. Zheng, Polarization image demosaicing and RGB image enhancement for a color polarization sparse focal plane array, *Opt Express* **2023**, *31*. https://doi.org/10.1364/Oe.494836.
[208] Z. J. Xu, N. X. Li, Y. Dong, Y. H. Fu, T. Hu, Q. Z. Zhong, Y. Y. Zhou, D. D. Li, S. Y. Zhu, N. Singh, Metasurface-based subtractive color filter fabricated on a 12-inch glass wafer using a CMOS platform, *Photonics Res* **2021**, *9*, 13-20. https://doi.org/10.1364/Prj.404124.
[209] M. ElKabbash, N. Hoffman, A. R. Lininger, S. A. Jalil, T. Letsou, M. Hinczewski, G. Strangi, C. L. Guo, Fano resonant optical coatings platform for full gamut and high purity structural colors, *Nat Commun* **2023**, *14*. https://doi.org/10.1038/s41467-023-39602-2.
[210] H. Zheng, H. Hu, T. Weber, J. Wang, L. Nan, B. Zou, S. A. Maier, A. Tittl, All-dielectric structural coloration empowered by bound states in the continuum, *Nanophotonics-Berlin* **2024**, *13*, 4327-4335. https://doi.org/10.1515/nanoph-2024-0367.
[211] B. Yang, W. W. Liu, Z. C. Li, H. Cheng, D. Y. Choi, S. Q. Chen, J. G. Tian, Ultrahighly Saturated Structural Colors Enhanced by Multipolar-Modulated Metasurfaces, *Nano Lett* **2019**, *19*, 4221-4228. https://doi.org/10.1021/acs.nanolett.8b04923.
[212] W. J. Yue, S. Gao, Y. Li, C. W. Zhang, X. Q. Fu, D. Y. Choi, Polarization-encrypted high-resolution full-color images exploiting hydrogenated amorphous silicon nanogratings, *Nanophotonics-Berlin* **2020**, *9*, 875-884. https://doi.org/10.1515/nanoph-2019-0500.
[213] J. Proust, F. Bedu, B. Gallas, I. Ozerov, N. Bonod, All-Dielectric Colored Metasurfaces with Silicon Mie Resonators, *Acs Nano* **2016**, *10*, 7761-7767. https://doi.org/10.1021/acsnano.6b03207.

[214] M. Hentschel, K. Koshelev, F. Sterl, S. Both, J. Karst, L. Shamsafar, T. Weiss, Y. Kivshar, H. Giessen, Dielectric Mie voids: confining light in air*, Light-Sci Appl* **2023**, *12*. https://doi.org/10.1038/s41377-022-01015-z.

[215] J. S. Lee, J. Y. Park, Y. H. Kim, S. Jeon, O. Ouellette, E. H. Sargent, D. H. Kim, J. K. Hyun, Ultrahigh resolution and color gamut with scattering-reducing transmissive pixels*, Nat Commun* **2019**, *10*. https://doi.org/10.1038/s41467-019-12689-2.

[216] H. F. Ghaemi, T. Thio, D. E. Grupp, T. W. Ebbesen, H. J. Lezec, Surface plasmons enhance optical transmission through subwavelength holes*, Phys Rev B* **1998**, *58*, 6779-6782. https://doi.org/DOI 10.1103/PhysRevB.58.6779.

[217] P. W. R. Connolly, J. Valli, Y. D. Shah, Y. Altmann, J. Grant, C. Accarino, C. Rickman, D. R. S. Cumming, G. S. Buller, Simultaneous multi-spectral, single-photon fluorescence imaging using a plasmonic colour filter array*, J Biophotonics* **2021**, *14*. https://doi.org/10.1002/jbio.202000505.

[218] D. Yao, P. W. R. Connolly, A. J. Sykes, Y. D. Shah, C. Accarino, J. Grant, D. R. S. Cumming, G. S. Buller, S. Mclaughlin, Y. Altmann, Rapid single-photon color imaging of moving objects*, Opt Express* **2023**, *31*, 26610-26625. https://doi.org/10.1364/Oe.493172.

[219] R. Gordon, A. G. Brolo, A. McKinnon, A. Rajora, B. Leathem, K. L. Kavanagh, Strong polarization in the optical transmission through elliptical nanohole arrays*, Phys Rev Lett* **2004**, *92*. https://doi.org/10.1103/PhysRevLett.92.037401.

[220] Y. Jung, H. Jung, H. Choi, H. Lee, Polarization Selective Color Filter Based on Plasmonic Nanograting Embedded Etalon Structures*, Nano Lett* **2020**, *20*, 6344-6350. https://doi.org/10.1021/acs.nanolett.0c01738.

[221] V. R. Shrestha, S. S. Lee, E. S. Kim, D. Y. Choi, Polarization-tuned Dynamic Color Filters Incorporating a Dielectric-loaded Aluminum Nanowire Array*, Sci Rep-Uk* **2015**, *5*. https://doi.org/10.1038/srep12450.

[222] N. Nakazaki, H. Matsumoto, H. Tsuda, Y. Takao, K. Eriguchi, K. Ono, Surface smoothing during plasma etching of Si in Cl*, Appl Phys Lett* **2016**, *109*. https://doi.org/10.1063/1.4967474.

[223] T. Guo, 2025.

[224] S. H. Chang, S. K. Gray, G. C. Schatz, Surface plasmon generation and light transmission by isolated nanoholes and arrays of nanoholes in thin metal films*, Opt Express* **2005**, *13*, 3150-3165. https://doi.org/Doi 10.1364/Opex.13.003150.

[225] D. B. Mazulquim, K. J. Lee, J. W. Yoon, L. V. Muniz, B. H. Borges, L. G. Neto, R. Magnusson, Efficient band-pass color filters enabled by resonant modes and plasmons near the Rayleigh anomaly*, Opt Express* **2014**, *22*, 30843-30851. https://doi.org/10.1364/Oe.22.030843.

[226] W. L. Barnes, Surface plasmon-polariton length scales: a route to sub-wavelength optics*, J Opt a-Pure Appl Op* **2006**, *8*, S87-S93. https://doi.org/10.1088/1464-4258/8/4/S06.

[227] R. Turchetta, N. Guerrini, I. Sedgwick, Large area CMOS image sensors*, J Instrum* **2011**, *6*. https://doi.org/10.1088/1748-0221/6/01/C01099.

[228] L. Frey, P. Parrein, J. Raby, C. Pellé, D. Hérault, M. Marty, J. Michailos, Color filters including infrared cut-off integrated on CMOS image sensor*, Opt Express* **2011**, *19*, 13073-13080. https://doi.org/10.1364/Oe.19.013073.

[229] I. Gyongy, A. T. Erdogan, N. A. W. Dutton, G. M. Martin, A. Gorman, H. N. Mai, F. M. Della Rocca, R. K. Henderson, A Direct Time-of-Flight Image Sensor With In-

Pixel Surface Detection and Dynamic Vision, *Ieee J Sel Top Quant* **2024**, *30*. https://doi.org/10.1109/Jstqe.2023.3238520.

[230] A. Kodigala, T. Lepetit, Q. Gu, B. Bahari, Y. Fainman, B. Kanté, Lasing action from photonic bound states in continuum, *Nature* **2017**, *541*, 196-199. https://doi.org/10.1038/nature20799.

[231] L. J. Huang, R. Jin, C. B. Zhou, G. H. Li, L. Xu, A. Overvig, F. Deng, X. S. Chen, W. Lu, A. Alu, A. E. Miroshnichenko, Ultrahigh-Q guided mode resonances in an All-dielectric metasurface, *Nat Commun* **2023**, *14*. https://doi.org/10.1038/s41467-023-39227-5.

[232] Y. Akahane, T. Asano, B. S. Song, S. Noda, High-Q photonic nanocavity in a two-dimensional photonic crystal, *Nature* **2003**, *425*, 944-947. https://doi.org/10.1038/nature02063.

[233] C. Huang, C. Zhang, S. M. Xiao, Y. H. Wang, Y. B. Fan, Y. L. Liu, N. Zhang, G. Y. Qu, H. J. Ji, J. C. Han, L. Ge, Y. Kivshar, Q. H. Song, Ultrafast control of vortex microlasers, *Science* **2020**, *367*, 1018-+. https://doi.org/10.1126/science.aba4597.

[234] L. L. Wang, C. B. Zhou, Y. Zhang, H. X. He, H. Duan, Y. Y. Wang, Y. F. Yi, C. G. Gao, Polarization-Independent High Q-Factor Resonance Achieved by Efficiently Selecting and Perturbing the Unit Cell of Nanostructure, *J Lightwave Technol* **2025**, *43*, 757-763. https://doi.org/10.1109/Jlt.2024.3452668.

[235] C. B. Zhou, L. J. Huang, R. Jin, L. Xu, G. H. Li, M. Rahmani, X. S. Chen, W. Lu, A. E. Miroshnichenko, Bound States in the Continuum in Asymmetric Dielectric Metasurfaces, *Laser Photonics Rev* **2023**, *17*, 2200564. https://doi.org/10.1002/lpor.202200564.

[236] A. V. Kildishev, A. Boltasseva, V. M. Shalaev, Planar Photonics with Metasurfaces, *Science* **2013**, *339*. https://doi.org/10.1126/science.1232009.

[237] I. E. Gordon, L. S. Rothman, C. Hill, R. V. Kochanov, Y. Tan, P. F. Bernath, M. Birk, V. Boudon, A. Campargue, K. V. Chance, B. J. Drouin, J. M. Flaud, R. R. Gamache, J. T. Hodges, D. Jacquemart, V. I. Perevalov, A. Perrin, K. P. Shine, M. A. H. Smith, J. Tennyson, G. C. Toon, H. Tran, V. G. Tyuterev, A. Barbe, A. G. Császár, V. M. Devi, T. Furtenbacher, J. J. Harrison, J. M. Hartmann, A. Jolly, T. J. Johnson, T. Karman, I. Kleiner, A. A. Kyuberis, J. Loos, O. M. Lyulin, S. T. Massie, S. N. Mikhailenko, N. Moazzen-Ahmadi, H. S. P. Müller, O. V. Naumenko, A. V. Nikitin, O. L. Polyansky, M. Rey, M. Rotger, S. W. Sharpe, K. Sung, E. Starikova, S. A. Tashkun, J. Vander Auwera, G. Wagner, J. Wilzewski, P. Wcislo, S. Yu, E. J. Zak, The HITRAN2016 molecular spectroscopic database, *J Quant Spectrosc Ra* **2017**, *203*, 3-69. https://doi.org/10.1016/j.jqsrt.2017.06.038.

[238] K. L. Sun, M. Sun, Y. J. Cai, U. Levy, Z. H. Han, Strong coupling between quasi-bound states in the continuum and molecular vibrations in the mid-infrared, *Nanophotonics-Berlin* **2022**, *11*, 4221-4229. https://doi.org/10.1515/nanoph-2022-0311.

[239] Z. X. Liao, Q. C. Ma, L. X. Wang, Z. Yang, M. Q. Li, F. Deng, W. Y. Hong, Guiding-mode-assisted double-BICs in an all-dielectric metasurface, *Opt Express* **2022**, *30*, 24676-24688. https://doi.org/10.1364/Oe.463340.

[240] R. L. Chern, T. J. Hsu, Bound states in the continuum in divided triangular hole metasurfaces, *Sci Rep-Uk* **2024**, *14*. https://doi.org/10.1038/s41598-024-63912-0.

[241] B. J. Russell, J. J. Cadusch, J. J. Meng, D. D. Wen, K. B. Crozier, Mid-infrared spectral reconstruction with dielectric metasurfaces and dictionary learning, *Opt Lett* **2022**, *47*, 2490-2493. https://doi.org/10.1364/Ol.448858.
[242] S. C. Malek, A. C. Overvig, A. Alu, N. F. Yu, Multifunctional resonant wavefront-shaping meta-optics based on multilayer and multi-perturbation nonlocal metasurfaces, *Light-Sci Appl* **2022**, *11*, 246. https://doi.org/10.1038/s41377-022-00905-6.
[243] X. Ouyang, Y. X. Zeng, Z. Wang, B. C. Bo, F. X. Lai, C. Zhang, C. W. Qiu, Q. H. Song, S. H. Yu, Y. Kivshar, S. M. Xiao, Ultra narrowband geometric-phase resonant metasurfaces, *P Natl Acad Sci USA* **2025**, *122*. https://doi.org/10.1073/pnas.2420830122.
[244] A. C. Overvig, S. C. Malek, N. F. Yu, Multifunctional Nonlocal Metasurfaces, *Phys Rev Lett* **2020**, *125*, 017402. https://doi.org/10.1103/PhysRevLett.125.017402.
[245] G. G. Kang, Q. F. Tan, X. L. Wang, G. F. Jin, Achromatic phase retarder applied to MWIR & LWIR dual-band, *Opt Express* **2010**, *18*, 1695-1703. https://doi.org/10.1364/Oe.18.001695.
[246] V. R. Tuz, V. V. Khardikov, A. S. Kupriianov, K. L. Domina, S. Xu, H. Wang, H. B. Sun, High-quality trapped modes in all-dielectric metamaterials, *Opt Express* **2018**, *26*, 2905-2916. https://doi.org/10.1364/Oe.26.002905.
[247] C. B. Zhou, L. J. Huang, R. Jin, L. Xu, G. H. Li, M. Rahmani, X. S. Chen, W. Lu, A. E. Miroshnichenko, Bound States in the Continuum in Asymmetric Dielectric Metasurfaces, *Laser Photonics Rev* **2023**, *17*. https://doi.org/10.1002/lpor.202200564.
[248] C. C. Cui, C. B. Zhou, S. Yuan, X. Z. Qiu, L. Q. Zhu, Y. X. Wang, Y. Li, J. W. Song, Z. Huang, Y. Wang, C. Zeng, J. S. Xia, Multiple Fano Resonances in Symmetry-Breaking Silicon Metasurface for Manipulating Light Emission, *Acs Photonics* **2018**, *5*, 4074-4080. https://doi.org/10.1021/acsphotonics.8b00754.
[249] B. R. Matsudo, B. Sain, L. Carletti, X. Zhang, W. L. Gao, C. de Angelis, L. L. Huang, T. Zentgraf, Efficient Frequency Conversion with Geometric Phase Control in Optical Metasurfaces, *Adv Sci* **2022**, *9*. https://doi.org/10.1002/advs.202104508.
[250] W. B. Ma, C. B. Zhou, Quasi-symmetry-protected BICs in a double-notched silicon nanodisk metasurface, *Opt Lett* **2023**, *48*, 2158-2161. https://doi.org/10.1364/Ol.486552.
[251] F. Monticone, N. M. Estakhri, A. Alù, Full Control of Nanoscale Optical Transmission with a Composite Metascreen, *Phys Rev Lett* **2013**, *110*. https://doi.org/10.1103/PhysRevLett.110.203903.
[252] M. Kang, Z. Y. Zhang, T. Wu, X. Q. Zhang, Q. Xu, A. Krasnok, J. G. Han, A. Alù, Coherent full polarization control based on bound states in the continuum, *Nat Commun* **2022**, *13*. https://doi.org/10.1038/s41467-022-31726-1.
[253] X. Q. Luo, Y. Y. Han, X. Du, S. Chen, G. Y. Li, Robust Ultrahigh-Q Quasi-Bound States in the Continuum in Metasurfaces Enabled by Lattice Hybridization, *Adv Opt Mater* **2023**, *11*. https://doi.org/10.1002/adom.202301130.
[254] M. M. Zhou, S. J. You, J. Liu, K. Qin, J. Wang, Y. Zhang, H. Xiang, C. B. Zhou, D. Z. Han, Selective Perturbation of Eigenfield Enables High-

Quasi-Bound States in the Continuum in Dielectric Metasurfaces, *Acs Photonics* **2024**, *11*, 2413-2421. https://doi.org/10.1021/acsphotonics.4c00319.

[255] L. J. Huang, S. L. Li, C. B. Zhou, H. Z. Zhong, S. J. You, L. Li, Y. Cheng, A. E. Miroshnichenko, Realizing Ultrahigh-Q Resonances Through Harnessing Symmetry-Protected Bound States in the Continuum, *Adv Funct Mater* **2024**, *34*. https://doi.org/10.1002/adfm.202309982.
[256] Z. Wang, Y. Liang, J. Q. Qu, M. K. Chen, M. J. Cui, Z. Cheng, J. C. Zhang, J. Yao, S. F. Chen, D. P. Tsai, C. Y. Yu, Plasmonic bound states in the continuum for unpolarized weak spatially coherent light, *Photonics Res* **2023**, *11*, 260-269. https://doi.org/10.1364/Prj.477385.
[257] Z. Jing, S. L. Li, S. Y. Ouyang, J. J. Lu, Y. K. Wang, L. J. Huang, L. Li, T. Sang, Observation of the Generalized Kerker Effect Mediated by Quasi-Bound States in the Continuum, *Nano Lett* **2024**, *25*, 522-528. https://doi.org/10.1021/acs.nanolett.4c05421.
[258] W. Liu, Y. S. Kivshar, Generalized Kerker effects in nanophotonics and meta-optics [Invited], *Opt Express* **2018**, *26*, 13085-13105. https://doi.org/10.1364/Oe.26.013085.
[259] 2025.
[260] W. J. Zhou, G. C. Sun, Y. Y. Yuan, Y. X. Wang, S. N. Burokur, Y. Wang, K. Zhang, Bound States in the Continuum in Photonics and Metasurfaces: From Phenomena to Applications, *Ann Phys-Berlin* **2025**, *537*, 2400250. https://doi.org/10.1002/andp.202400250.
[261] W. J. Wang, S. J. Liang, J. Q. Zou, Y. Y. Huo, T. Y. Ning, Symmetry-protected and Brillouin zone folding driven bound states in the continuum in dielectric nanorod arrays for efficient third harmonic generation, *Chinese Phys B* **2025**, *34*. https://doi.org/10.1088/1674-1056/ada2f0.
[262] Y. J. Zang, R. H. Chai, W. W. Liu, Z. C. Li, H. Cheng, J. G. Tian, S. Q. Chen, Enhanced wide-angle third-harmonic generation in flat-band-engineered quasi-BIC metagratings, *Sci China Phys Mech* **2024**, *67*, 244212. https://doi.org/10.1007/s11433-023-2299-9.
[263] K. L. Sun, Y. J. Cai, U. Levy, Z. H. Han, Quasi-guided modes resulting from the band folding effect in a photonic crystal slab for enhanced interactions of matters with free-space radiations, *Beilstein J Nanotech* **2023**, *14*, 322-328. https://doi.org/10.3762/bjnano.14.27.
[264] K. L. Sun, H. Wei, W. J. Chen, Y. Chen, Y. J. Cai, C. W. Qiu, Z. H. Han, Infinite-Q guided modes radiate in the continuum, *Phys Rev B* **2023**, *107*. https://doi.org/10.1103/PhysRevB.107.115415.

APPENDIX

Temporal Coupled Mode Theory and cross-polarization conversion limit

The proposed structure is an ultrathin metasurface with a thickness of 700 nm, operating at wavelengths on the order of 3000 nm. It is therefore a non-magnetic, planar system that supports only zero-order transmission. The substrate used is low-refractive-index material (RI=1.4), which approximately preserves mirror symmetry with respect to the z-axis.

Considering the system supports only one single resonant mode $A(t)$ with single excitation port, the amplitude will be governed by:

$$\frac{dA}{dt} = (i\omega_0 - \gamma)A + K\, s^+ \tag{S1}$$

$$s^- = C\, s^+ + D\, A \tag{S2}$$

Where:
- ω_0: Eigen angular frequency of the resonant mode
- γ : Total decay rate including all loss channels
- s_+, s_-: Input and output wave amplitude vectors, such $\pm$ subscripts indicates the direction
- K: Coupling matrix from input to the resonator
- D: Coupling matrix from resonator to output
- C: Direct (no resonance involved) transmission coupling matrix

The resonant can be described in the steady-state regime by:

$$A = \frac{K^T s^+}{[i(\omega_0 - \omega) + \gamma]} \tag{S3}$$

$$s^- = C\, s^+ + \frac{D\, K^T s^+}{[i(\omega_0 - \omega) + \gamma]} \tag{S4}$$

From (S1) to (S4), the total S matrix can be derived as:

$$\mathrm{S}(\omega) = C + \frac{D\, K^T}{[i(\omega_0 - \omega) + \gamma]} \tag{S5}$$

Considering a four port (x-pol in, y-pol out, y-pol in, x-pol out), $\mathrm{T_{yx}}$ at resonance is given by $|\mathrm{S}_{21}|^2$, focusing on the expression of S_{21} at q-BIC eigen frequency. Because of the energy conservation, reciprocity, and time-reversal symmetry requirements, the system satisfies $CK^\dagger + K^T = 0$ and $D = K$. Then the expression of S_{21} (cross-polarization term) can be written as:

$$\mathrm{S}_{21} = \frac{K_2 K_1^T}{\gamma} \tag{S6}$$

Energy conservation condition requires $|K_2|^2 + |K_1|^2 = \gamma$, hence

$$\mathrm{T_{yx}} = |\mathrm{S}_{21}|^2 = \frac{|K_2|^2(\gamma - |K_2|^2)}{\gamma^2} \leq \frac{1}{4}$$

And the maximum $\mathrm{T_{yx}}$ of 25% is obtained when $|K_2|^2 = \gamma/2$ for a lossless system.

Multipole expansion expression

The multi-pole expansion to quadrupole order presented in Figure 2(f) in the main text were calculated using following expression in integral form, which includes electric dipole

(ED) moment, magnetic dipole (MD) moment, toroidal dipole (TD) moment, electric quadrupole (EQ) moment, and magnetic quadrupole (MQ) moment.

$$\vec{p} = \frac{1}{i\omega}\int \vec{j}\, d^3r \qquad (\textbf{ED S7})$$

$$\vec{m} = \frac{1}{2c}\int \left(\vec{r} \times \vec{j}\right) d^3r \qquad (\textbf{MD S8})$$

$$\vec{T} = \frac{1}{10c}\int \left[\left(\vec{r}\cdot\vec{j}\right)\vec{r} - 2r^2\vec{j}\right] d^3r \qquad (\textbf{TD S9})$$

$$Q_{\alpha\beta}^{(e)} = \frac{1}{2i\omega}\int \left[r_\alpha j_\beta + r_\beta j_\alpha - \frac{2}{3}\left(\vec{r}\cdot\vec{j}\right)\delta_{\alpha,\beta}\right] d^3r \qquad (\textbf{EQ S10})$$

$$Q_{\alpha\beta}^{(m)} = \frac{1}{3c}\int \left[\left(\vec{r}\times\vec{j}\right)_\alpha r_\beta + \left(\vec{r}\times\vec{j}\right)_\beta r_\alpha\right] d^3r \qquad (\textbf{MQ S11})$$

where c and ω are the speed and angular frequency of electromagnetic field(light), respectively. The subscripts α, β represent x, y, z in Cartesian coordinate. $\vec{j}$ is the current density distribution in a unit cell which has the expression:

$$\vec{j} = -i\omega\varepsilon_0(n^2-1)\vec{E}$$

The far-field scattered power of them can be expressed by the following formulas[239]:

$$I_P = \frac{2\omega^4}{3c^3}\left|\vec{p}\right|^2, \qquad (\textbf{ED power S12})$$

$$I_M = \frac{2\omega^4}{3c^3}\left|\vec{m}\right|^2, \qquad (\textbf{MD power S13})$$

$$I_T = \frac{2\omega^6}{3c^5}\left|\vec{T}\right|^2, \qquad (\textbf{TD power S14})$$

$$I_{Q^{(e)}} = \frac{\omega^6}{5c^5}\sum\left|\vec{Q}_{\alpha\beta}^{(e)}\right|^2, \qquad (\textbf{EQ power S15})$$

$$I_{Q^{(m)}} = \frac{\omega^6}{40c^5}\sum\left|\vec{Q}_{\alpha\beta}^{(m)}\right|^2. \qquad (\textbf{MQ power S16})$$

The integral area was set to be the germanium nano disk with holes. The total scattering power in the far field were calculated using following expression:

$$I_{total} = I_P + I_M + \frac{4\omega^5}{3c^4}\left(\vec{P}\cdot\vec{T}\right) + I_T + I_{Q^{(e)}} + I_{Q^{(m)}} + O\left(\frac{1}{c^5}\right) \qquad (\textbf{Total power})$$

Such scattering power is calculated and integrated using COMSOL Multiphysics. For incidence along the z direction, the y-polarized component (electric field) of the output after the resonator has the following contributions from each multipole:

The component of $\vec{p}$ along $\vec{y}$ direction: E (ED) $\propto \vec{y} \cdot \vec{p}$, take the subscript p_y, i.e. ED_y

The component of $\vec{m}$ along $\vec{y}$ direction: E (MD) $\propto \vec{y} \cdot \left(\vec{z} \times \vec{m}\right) = \vec{m} \cdot \left(\vec{y} \times \vec{z}\right) = \vec{m} \cdot \vec{x}$, take the subscript m_x, i.e. MD_z.

The component of $\vec{Q^{(e)}}$ along $\vec{y}$ direction: E (EQ) $\propto ik \cdot \vec{y} \cdot \left(\vec{Q^{(e)}} \cdot \vec{z}\right)$, take the subscript $Q^{(e)}{}_{zy}$, i.e. EQ_{zy}.

Similarly, take TD_y and MQ_{zx}.

Tips for Optimising Large periodic arrays (Based on personal experience):

1. **Automate layout/pattern generation.** This can save a significant amount of time when arranging array lattice constants and meta-unit dimensions. A basic example is provided in the Appendix. At the 2023 JWNC mini-conference, I emphasised the advantages of this approach where the slides can be found on JWNC wiki. Automation can also be extended to simulations: although defining individual meta-units in a metasurface is conceptually straightforward, it is highly repetitive. Such tasks are ideal for scripting and coding. Lumerical provides a Python API, and in the current AI era, this has become even easier than three years ago. Consequently, inverse design and optimisation workflows can be accelerated considerably.

2. **File format optimisation for large-scale EBL work.** In JWNC EBL projects, Beamer software typically uses GDSII as the standard tutorial file format. However, the arrays in Chapter 4 of this study span millimetre-scale micro-/nano-arrays, causing GDSII file sizes to reach hundreds of megabytes, and sometimes exceeding 1 GB. This imposes a significant burden on reading, writing, and transferring files. By using open-source software such as KLayout or commercial alternatives, GDSII files can be converted to OASIS format without not information loss nor pattern compression, resulting in a tenfold or greater reduction in file size. This provides a substantial advantage for storage on shared academic servers and for Beamer read/write efficiency.

3. **Dose control in E-beam lithography.** The most critical parameter is the exposure dose. The primary positive resists used in this work include CSAR, ZEP520A, and PMMA. ZEP520A generally requires the lowest dose, but the difference relative to CSAR is not large. PEC (proximity effect correction) can help compensate for morphology differences between the centre and edges of an array due to back scattering of the electrons, but for large-array structures, this is generally of limited significance. In particular, for multi-period nonlocal modes, small differences at the edges have negligible effect on the overall transmission spectrum. PEC, however, can significantly increase Beamer memory usage and slightly extend EBL writing time. In practice, I optimise dose and beam current through dose tests to select the minimum acceptable dose, and do not use PEC. This approach can yield substantial reductions in EBL write time.

Example of code for GDS generation

Here an example of the code generating GDS patterns is shown, which corresponds to the case in Chapter 5.

```
import pya

import numpy as np

import math

import time

# import python pya api module


time_start = time.time()

# parameter definition

rec_w0 = 500

rec_l0 = 700

p0= 1400

g10 = 200

g20 = 120

j= 0.16

offset0 = 0

# Initialise

# define hex function

for i in range(1):

  layout=pya.Layout()

  top = layout.create_cell('top')

  hex_cell = layout.create_cell('hex')

  temp = layout.create_cell('temp')

  hex_layer = layout.layer(1,0)

  temp_layer = layout.layer(2,0)


  def draw_hex(a,offset1,offset2):

    nr_points = 20 #number of points
```

```
    angles = np.linspace(0,2*np.pi,nr_points+1)[0:-1]
    points = [] #array of point
    for angle in angles:
        points.append(pya.Point(a*np.cos(angle),a*np.sin(angle)))
    hex_unit = pya.SimplePolygon(points)
    hex_cell.shapes(hex_layer).insert(hex_unit.moved(offset1,offset2))
        return

def draw_rec(w,l,g1,g2,p):
    rec1 = pya.Box()
    rec1.left= -(w+g2)/2
    rec1.right = (w+g2)/2
    rec1.top =  l/2
    rec1.bottom = -l/2
    hex_cell.shapes(hex_layer).insert(rec1)
    rec1 = pya.Box()
    rec1.left= -(w-g2)/2
    rec1.right = (w-g2)/2
    rec1.top =  l/2
    rec1.bottom = -l/2
    hex_cell.shapes(hex_layer).insert(rec1.moved(p/2-g1,0))
    # hex_cell.shapes(hex_layer).insert(rec.moved(p*math.sqrt(3)/2,p/2))
    return

k = 1
rec_w = rec_w0*k
rec_l = rec_l0*k
p= p0*k
offset = offset0
g1 = g10*k
g2= g20*k
cell_pitchx = p
```

```
    cell_pitchy = p
    vec = cell_pitchx
## draw hex
    draw_hex(rec_w*j,offset,0)
    B = pya.Region(hex_cell.shapes(temp_layer))

    draw_hex(rec_w*j,0,offset)
    C= pya.Region(hex_cell.shapes(hex_layer))

    draw_hex(rec_w,0,0)
    A = pya.Region(hex_cell.shapes(hex_layer))
    D = A-(B+C)
    #### Lift-off/Negative version
    bg = pya.Box()
    bg.left= -cell_pitchx/2 + cell_pitchx/4  -205
    bg.right= cell_pitchx/2+ cell_pitchx/4  -200
    bg.top =  cell_pitchx/2
    bg.bottom = -cell_pitchx/2
    hex_cell.shapes(hex_layer).insert(bg)
    E = pya.Region(hex_cell.shapes(hex_layer))
    F = E-D

    temp.shapes(hex_layer).insert(F)




    # define x and y repeats
    x_repeat = np.floor(100*1000/cell_pitchx)
    y_repeat = np.floor(100*1000/cell_pitchy)

    # cell array
```

```
    array_hex = pya.CellInstArray(temp.cell_index(), pya.Trans(pya.Point(0,0)),
                          pya.Vector(0, vec),pya.Vector(vec, 0),
                          x_repeat,y_repeat)


    top.insert(array_hex)
    hex_cell.delete()


    layout.write(f"100umstate_0.gds")


end_time = time.time()
# execution_time = end_time - time_start
# print(f"Execution time: {execution_time:.8zf seconds")
##save as gds file
```